Technische Universität München
TUM School of Natural Sciences

TUM

Examination of the Mechanism and the Critical Parameters Governing the Coprecipitation Kinetics of Mixed-Metal Hydroxides

Rafael Benjamin Berk

Abstract

Layered lithium transition oxides are commercially employed as cathode active material (CAM) in lithium-ion battery (LIB) applications for electric vehicles. Current industrial manufacturing of layered transition metal oxides is conducted by coprecipitation of a mixed metal hydroxide precursor (referred to as pCAM) in a stirred tank reactor and subsequent calcination of the pCAM with a lithium compound at elevated temperatures in a kiln. The electrochemical performance and physical properties of the resulting CAM powders are highly contingent on the physical and microstructural properties of the associated pCAM utilized for synthesis. Further, a precise control of the pCAM and CAM powder's fluidity is necessary for an economical and efficient manufacturing of a CAM. In this context, an in-depth understanding of the mixed metal hydroxide particle formation mechanism during the coprecipitation reaction enables every degree of freedom to tailor the pCAM properties according to the requirements of cost-effective CAM production for a given LIB application.

Therefore, the scope of this thesis was to gain mechanistic insights into the coprecipitation process of mixed metal hydroxides. Typically, a hydroxide pCAM is coprecipitated by simultaneous feeding of a mixed metal sulfate, a sodium hydroxide and an ammonia solution into a stirred tank reactor under inert atmosphere. As a first step of this work, a reactor setup was developed and optimized to study the coprecipitation of nickel-rich mixed metal hydroxides as a model system.

Subsequently, a two-stage particle formation mechanism comprising of initial seeding of agglomeration and subsequent polycrystallisation during coprecipitation was identified. In this regard, the degree of turbulence governs the initial agglomerate size and number, which dictates the growth rate, final particle size, and particle sphericity.

In a second study, the impact of the coprecipitation pH-value on the course of particle development during coprecipitation of nickel-rich mixed metal hydroxides was investigated. Thereby, a pH-dependent sulfate adsorption equilibrium was revealed, which not only governs the crystallinity of formed metal hydroxide, but also the crystal growth of particles. This in turn affects the pCAM particle morphology and porosity.

The demonstrated relationships in this work allow formulating design strategies for the synthesis of hydroxide pCAMs in the context of industrial CAM manufacturing and according to the CAM requirements for LIB applications.

Zusammenfassung

Lithium Übergangsmetall Schichtoxide werden kommerziell eingesetzt als Kathodenaktiv Material (CAM) in Lithiumionen Batterien (LIB) für elektrische Fahrzeuge. Die aktuelle industrielle Herstellung von Lithium Übergangsmetall Schichtoxiden umfasst die Fällung von Mischmetallhydroxid Präkursoren (bezeichnet als pCAM) in einem Rührkessel Reaktor gefolgt von anschließender Kalzination des pCAMs mit einer Lithiumverbindung bei erhöhten Temperaturen in einem Röstofen. Die elektrochemische Leistung des resultieren CAM-Pulvers hängt maßgeblich von den physikalischen und mikrostrukturellen Eigenschaften des jeweiligen pCAMs ab, der zur Synthese eingesetzt worden ist. Weiterhin ist für eine ökonomische und effiziente Herstellung von einem CAM die präzise Kontrolle der Fluidität des pCAM und CAM-Pulvers notwendig. In diesem Kontext ermöglicht ein detailliertes Verständnis des Partikelbildungsmechanismus von Mischmetallhydroxiden während der Fällungsreaktion jeden Freiheitsgrad die Eigenschaften von einem pCAM gemäß der Anforderung einer kosteneffizienten CAM-Produktion als auch der entsprechenden LIB-Anwendung maßzuschneidern.

Deshalb ist es das Ziel dieser Doktorarbeit das mechanistische Verständnis über den Fällungsprozess von Mischmetallhydroxiden zu fördern. Typischerweise wird Hydroxid pCAM durch ein simultanes Einspeisen einer Mischmetallsulfatlösung, einer Natriumhydroxidlösung und Ammoniakwasser in einen Rührkessel Reaktor unter inerter Atmosphäre gefällt. Zunächst wurde in dieser Arbeit ein Reaktor Setup entwickelt, welches anschließend optimiert wurde für die Studie von nickelreichen Mischmetallhydroxiden als Modellsystem.

Anschließend wurde ein zweistufiger Partikelbildungsmechanismus bestehend aus einer initialen Keimbildung von Agglomeraten gefolgt von einer anschließenden Polykristallisation identifiziert. In diesem Zusammenhang regelt der Turbulenzgrad die Größe und Anzahl der gebildeten initialen Agglomerate, welcher die Wachstumsrate, finale Partikelgröße und Sphärizität der Partikel bestimmt.

In einer zweiten Studie wurde der Einfluss des Fällungs-pH-Wertes auf den Verlauf der Partikelentwicklung während der Fällung von nickelreichen Mischmetallhydroxiden untersucht. Dabei wurde ein pH-Wert abhängiges Sulfatadsorptionsgleichgewicht aufgedeckt, welches nicht nur die Kristallinität des gebildeten Metallhydroxids, sondern auch das Kristallwachstum der Partikel bestimmt. Dies wiederum beeinflusst die Partikelmorphologie und Porosität.

Die in dieser Arbeit aufgezeigten Zusammenhänge in dieser Arbeit erlauben die Herleitung von Design Strategien für Hydroxid-basierte pCAM in dem Kontext von industrieller CAM-Produktion und den Anforderungen an CAMs für LIB-Anwendungen.

Table of contents

List of abbreviations and symbols

Abbreviation	Meaning
BET	Brunauer-Emmet-Teller
BEV	battery electric vehicle
CAM	cathode active material
CS	cross section
CS-SEM	cross section-scanning electron microscopy
CSTR	continuous stirred tank reactor
DRC	Democratic Republic of Congo
EU	European Union
EV	electric vehicle
FIB	focused ion-beam
FI	flow indication
HAADF	high-angle annular dark field
HR-TEM	high resolution-transmission electron microscopy
ICE	internal combustion engine
ICP-OES	inductively coupled plasma-optical emission spectroscopy
LFP	lithium iron phosphate ($LiFePO_4$)
LIB	lithium-ion battery
LMO	lithium manganese oxide ($LiMn_2O_4$)
M	motor
MHP	mixed hydroxide precipitate
NUS	user choice multivariable switch
NCA	lithium nickel cobalt alumina oxide ($LiNi_{1-x-y}Co_xAl_yO_2$, $x+y < 1$)
NCM	lithium nickel cobalt manganese oxide ($LiNi_{1-x-y}Co_xMn_yO_2$, $x+y < 1$)
NDIR	non-dispersive infrared
NH_3/M	ammonia to metal ratio
OEM	original equipment manufacturer
P	pump
pCAM	precursor of cathode active material
PI	pressure indication
PID	process and instrumentation diagram
PIS+	pressure indication switch and safety regulation above threshold
$PP_{vert.}$	vertical primary particle size
PSD	particle size distribution
PXRD	powder X-ray diffraction
Q(pH)IR	quantity (pH-value) indication record
RHK	roller hearth kiln
SEM	scanning electron microscopy
SSA	specific surface area
STEM	scanning transmission electron microscopy
STR	stirred tank reactor
T	tank
TIRS+	temperature indication record switch and safety regulation above threshold
WIR	weight indication record
XRD	X-ray diffraction

List of abbreviations and symbols

Symbol	Meaning	Units
$A_{eq.\ circle}$	area of circle with equivalent perimeter	m^2
$A_{particle}$	area of segmented particle	m^2
$A_{segm.}$	Segmented area	m^2
c_{MSO4}	concentration of $MSO_{4(aq.)}$	mol/l
C	circularity	–
C_{50}	median circularity	–
$d_{eq.}$	equivalent diameter of circle with identical area	m
$d_{10},\ d_{50},\ d_{90}$	volume-based percentile particle diameter	m
$M_{M(OH)2}$	molar mass of $M(OH)_2$	g/mol
pk_a	acid dissociation constant	–
$P_{par.}$	perimeter of segmented particle	m
p/p_0	relative pressure	–
R	gas constant	J/(mol K)
r_K	Kelvin radius	m
T	temperature	K or °C
t_{run}	run time of coprecipitation reaction	h
$V_{N2,m}$	molar volume of liquid nitrogen	m^3/mol
$V_{N2,ads.}$	total volume of adsorbed nitrogen	m^3
$V_{N2,liquid}$	total volume of liquified nitrogen	m^3
$V_{M(OH)2}$	total volume of precipitated $M(OH)_2$	m^3
$V_{par.}$	volume of individual particle	m^3
V_{total}	total volume of the reaction suspensions	m^3
$\dot{V}_{in}$	total volumetric flow rate of reactants entering the reactor	m^3/h
$\dot{V}_{MSO4}$	volumetric flow rate of $MSO_{4(aq.)}$	m^3/h
$\dot{V}_{NaOH}$	volumetric flow rate of $NaOH_{(aq.)}$	m^3/h
$\dot{V}_{NH3}$	volumetric flow rate of $NH_{3(aq.)}$	m^3/h
$\dot{V}_{out}$	total volumetric flow rate of reaction suspension leaving the reactor	m^3/h
γ	surface tension	J/m^2
ε_{intra}	intra-particle porosity	–
$\rho_{cryst.}$	crystallographic density	g/m^3
$\rho_{N2,\ liquid}$	density of liquid nitrogen at 77 K	g/m^3
$\rho_{N2,\ STP.}$	density of nitrogen at standard temperature (= 273.15 K) and pressure (= 101325 Pa)	g/m^3
σ	span	–

1 Introduction

1.1 Electric mobility is a reality

"It's game over for the internal combustion engine in Europe," stated the green mobility NGO Transport and Environment about the historic decision of environment ministers from the European Union (EU) member states to cease the sale of internal combustion engine (ICE) vehicles in the EU by 2035.[1] This legislation is connected to a set of EU policies referred to as "Fit for 55", which aims at the reduction of the net greenhouse gas emissions from 1990 by at least 55% until 2030, and to eventually achieve carbon neutrality by 2050.[2] However, such developments are not only limited to the EU, as analogous policies have been adopted from legislative authorities worldwide.[3] This drives a growing replacement of ICE-based vehicles by battery electric vehicles (BEVs), because BEVs have the potential to significantly reduce CO_2 emissions if the electricity utilized for powering BEVs as well as for manufacturing the battery and its individual components is produced in a carbon-neutral fashion.[4] In this regard, lithium-ion batteries (LIBs) have solidified their status as current technology monopole to power electric vehicles (EVs).[5, 6] While to the current day original equipment manufacturers (OEMs) have already commercialized an impressive selection of EV models,[6] it is projected that the total global EV sales will expand from 2020 to 2030 by a factor of ~10, namely from 3 to 25 million cars, corresponding to a total vehicle stock share of nearly 8% and a market share of 15%.[3] To satisfy this exponential growth of EVs, an enormous quantity of LIBs in the range of 1.6 TWh will be required by 2030.[3]

The fundamental working principle of state-of-the-art LIBs is the reversible intercalation of lithium ions (Li^+) in host structures of the active materials in the electrodes, resulting in the conversion of chemical energy into electrical energy by spatial separation of oxidation and reduction reaction at the electrodes. Thereby, Li^+ migrates as charge carrier through the electrolyte and the porous separator between the electrodes, while electrons are transported through an external circuit between the electrodes.[7, 8] Independent of the cell chemistry, the active materials are not only the heaviest, but also the most expensive components in a battery pack (a battery pack is comprised of numerous battery cells).[5] Approximately 43% of the mass and 39% of the cost of a LIB pack corresponds to the active materials, whereby the cathode active material (CAM) exhibits with 26% the by far largest share in both properties among all pack components (see Figure 1).[9] Further, the CAM significantly affects the overall achievable energy and power density in a LIB cell.[10] Therefore, the development of high performing CAMs is essential to additionally decrease the cost of

BEVs while simultaneously increasing their range, both essential to further raise the market share of BEVs and meet the demands of legislative authorities worldwide.[11, 12]
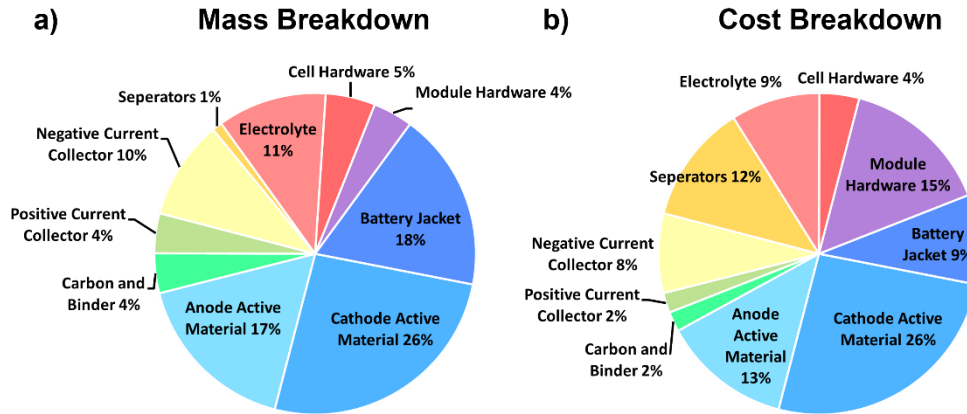
Figure 1: Mass (a) and cost (b) breakdown of a lithium-ion battery pack, comprised of $LiNi_{0.6}Co_{0.2}Mn_{0.2}O_2$-graphite 240 cells and divided in to 20 modules (the data to produce the figure were taken from Nelson et al,[9] based on the price for the respective components in the year 2018). The cost breakdown solely reflects the cost contributions of the components, while the manufacturing cost of the battery cell, module, and pack are not considered.

By now a variety of CAM chemistries are considered as promising for LIBs in BEVs applications. In a fundamental approach, Manthiram distinguishes between three major CAM material classes: layered oxides, spinel oxides, and polyanion oxide, each possessing distinctive advantages and disadvantages.[10] The most prominent representative for polyanion oxide-based CAM is lithium iron phosphate ($LiFePO_4$, referred to as LFP), which offers non-toxicity, low cost, high thermal stability, and a long lifetime at the expense of volumetric energy density. These features make LFP a viable choice for stationary applications, medium-range BEVs, or heavy duty.[10, 12] Spinel oxides present another alternative to polyanion oxides as non-toxic and inexpensive CAM. The most noteworthy spinel oxide CAM, is lithium manganese oxide ($LiMn_2O_4$, referred to as LMO). LMO displays an excellent rate-capability but suffers from a low capacity, which limits its practical application to predominantly being blended with other CAM classes.[10, 12] On the other hand, the class of layered oxide-based CAMs consists of an assortment of lithium-nickel-cobalt-manganese oxides and lithium-nickel-cobalt-aluminum-oxides, which can be generally defined by the formula $LiNi_{1-x-y}Co_xMn_yO_2$ or $LiNi_{1-x-y}Co_xAl_yO_2$, respectively (with x+y < 1, referred to as NCM or NCA, respectively). The ability to adjust the transition metal ratio, hence the properties of the CAM such as capacity and stability, endows

layered oxides with the unique flexibility to tailor the composition according to the requirements of a given LIB application.[6, 10] Impelled by the high driving range at low cost requirements of BEV manufacturers, the current development direction is towards layered oxides with a Ni-content above 80% (referred to as Ni-rich). This is owed to the fact that with increasing Ni-fraction,[13] the extractable quantity of Li increases and therefore, the attainable capacity and resulting energy density at a fixed operational voltage window increases.[14, 15] Overall, these features resulted in a market share of layered oxides as CAM in LIBs for EV applications in 2020 of approximately 90%, which is expected to virtually remain constant until at least 2030. Whereas the fraction of Ni-rich layered oxides will shift during that period from a market share of about 15% to 60%. This ultimately translates into a raw material demand for layered oxides for LIB-based EVs in 2030 of 650 kt for Ni corresponding to an 11-fold increase for CAM synthesis compared to 2020, 120 kt for Co (9-fold increase compared to 2020), and 92 kt for Mn (4-fold increase compared to 2020).[16]

Summarized, the transformation of the transportation sector to electrically powered vehicles requires a considerable quantity of raw materials. Focusing on the production of NCM CAMs for LIBs, the global distribution of Ni, Co, and Mn mineral deposits will be covered in the subsequent section.

1.2 Global distribution of nickel, cobalt, and manganese production

Powering the future fleet of LIB-based EVs with Ni-rich layered oxide CAMs incurs a significant demand of raw materials. This has sparked a race of OEMs, cell, and battery material manufacturers towards securing raw material supply chains worldwide.[17] In this context, the global production share of the five main producing nations of transition metals employed in NCMs is given in Figure 2.
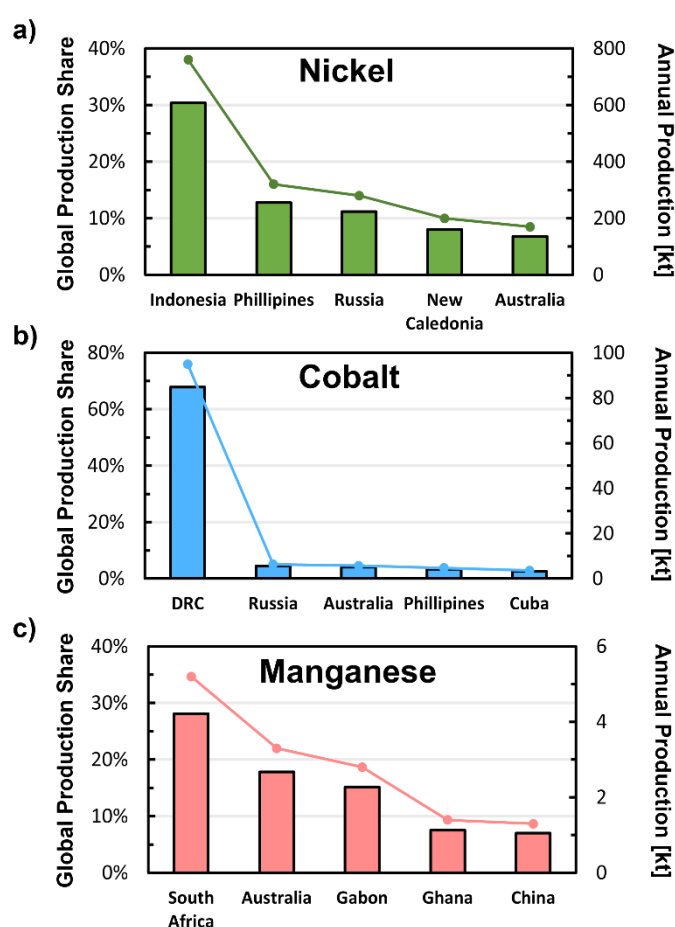
Figure 2: Global production share (bars) and absolute annual production in the year 2020 (data points) of metals employed in NCMs as cathode active materials for lithium-ion batteries, itemized after the five major producing nations of nickel (a), cobalt (b), and manganese (c). The nations were listed in descending sequence from left to right, where DRC = Democratic Republic of Congo. Note that the percentiles do not add up to 100%, as the remaining producing countries are not depicted, which make up in total 31% for Ni (775 kt), 18% for Co (25.2 kt), and 24% for Mn (4.44 kt). The data to produce the figure were taken from the United States Geological Survey, 2021.[18]

In the year 2020, at least 58% and therefore the majority of Ni originated from Australia and Oceania, with Indonesia leading by far with a percentage of 31% of the global annual production, which corresponds to 760 kt Ni manufactured. The only country that is not located in the Pacific Ocean but still has a significant Ni output is Russia, with a share of 11% equivalent to 280 kt Ni (Figure 2a).

The current Co production is heavily dominated by the Democratic Republic of Congo (DRC), with a share of 68% amounting to 95 kt Co produced in 2021, with the remaining "major" countries each exhibiting merely a respective production footprint of less than 5% (Figure 2b). Due to unethical and non-sustainable mining conditions in the DRC,[19] it is expected that the fraction of Co extracted from the DRC being employed for NCM manufacturing will decrease noticeably,[18] especially when considering that the transition metal content in NCMs is shifting towards Ni-rich compositions that contain much less to no Co at all.[16] Furthermore, approximately 30% of produced Co is a byproduct of Ni ore processing, since nickel ore deposits typically contain 0.01-0.1wt% Co (vs. 1-2wt% Ni).[20, 21] Thus, the Co obtainable only by Ni ore mining would be sufficient for manufacturing NCMs with a composition of $LiNi_{1-x-y}Co_xMn_yO_2$ with $x \leq 0.05$ and $y \leq 0.95$, compositions that would be compatibile with the current trend towards Ni-rich NCMs.[22]

Compared to Ni and Co, the Mn production is rather well distributed between Africa, Asia, and Austrialia (Figure 2c). Thereby, South Africa can be accounted for the largest production share of 28% equal to 5.2 kt Mn produced in 2020, followed by Australia with 18% corresponding to 3.3 kt Mn. Even though the current accesible total Mn reserves in the world are estimated to be sufficient with 1300 kt,[18] there seems to be a discrepancy between the projected Mn demand for LIB-based EVs of 92 kt by 2030[16] and the current total global annual Mn production of 18.5 kt.[18] Along with adressing this disparity, the mining industry will face investments in the coming future to step up the output of the remaining elements in employed NCMs.[23]

While based on the preceeding analysis, a leading role in providing raw materials for NCMs can be ascribed to several countries, Australia is not only in the unique position to be among the top five main producing countries of Ni (5th), Co (4th) and Mn (2nd) but also is the worldwide largest producer of Li and the 5th largest producer of aluminum (Al).[18] Therefore, Australia offers a comprehensive access to minerals required for the manufacturing of an extensive range of NCM and NCA CAM chemistries. Taken this in conjuction with the fact that Australia was according to The World Bank ranked as the 44th most stable nation in the

world in 2020 (vs. 56th for Germany),[24] it is reasonable that Australia is currently experiencing investments in the mining sector by companies related to LIB-based EVs such as Tesla[25], since it is capable of providing a stable and sustainable supply chain of raw materials required for the large-scale synthesis of NCMs.

However, the conversion of mined ores that contain Ni, Co, and/or Mn to NCM CAM powders that can be readily employed in a LIB requires numerous metallurgical operations in conjunction with complex chemical processes. The major processing routes from minable Ni, Co, and Mn minerals to NCMs as well as the advantages and disadvantages of distinctive commercially relevant NCM synthesis methods will be discussed in the next section.

1.3 From raw material to cathode active material

The transition metals employed in NCMs are harvested as natural minerals from the earth's crust by mining and subsequent refining to high-grade chemicals, which can be utilized for the synthesis of NCMs. The economically relevant deposits of Ni can be divided into two classes of ores: sulfidic and lateritic ones, whereas the latter can be characterized as a mixture of silicates and (hydro-)oxidic minerals. Lateritic ores make up 80% of the global Ni deposits, while sulfidic ores make up the remaining 20%.[21] While Co exists alongside with copper enriched in the form of sulfides in the DRC, it is also found in lateritic Ni deposits as mentioned above.[20, 21] In contrast to Ni and Co, Mn occurs naturally in high-grade oxidic ores with a striking Mn-content of above 40wt%, which renders the extraction of low-grade Mn ores economically unattractive.[26, 27] In addition to the primary Ni, Co, and Mn sources accessible by mining, spent active material powders from end-of-life LIBs, referred to as black mass, will become a secondary source of metals for NCMs in the future via by LIB recycling.[28-30] This can significantly reduce negative environmental consequences by establishing a circular economy, decreasing the life cycle impact of LIBs by 51%.[31] Therefore, it is only natural that various companies related to the LIB supply chain such as Sumitomo Metal Mining and Umicore are already operating LIB recycling plants, while others like Northvolt, Tesla, and BASF announced or initiated the construction of LIB recycling plants.[30, 32]

Having established the major sources of Ni, Co, and Mn, a schematic overview of the main production routes for NCMs starting from the previously discussed raw materials to the precursor compounds for NCM cathode active material (referred to as pCAM) and final NCM CAM are depicted in Figure 3. It is noteworthy that this topic is quite exhaustive. Each ore processing and refining method practiced from different companies varies in detail, which results in intermediate and raw material products which exhibit distinctive metal concentrations and prices. Therefore, the following discussion can be only understood as a simplified summary of the NCM production routes. Further, the yellow-red arrow illustrates the materials cost only in a relative manner. The exact prices of raw materials and products emerging from distinctive process routes, even if depicted in Figure 3 on the same level, may vary. Another take on the primary production route of NCMs starting from Ni and Co ores, considering only the current industrially applied synthesis method, can be found elsewhere.[33]
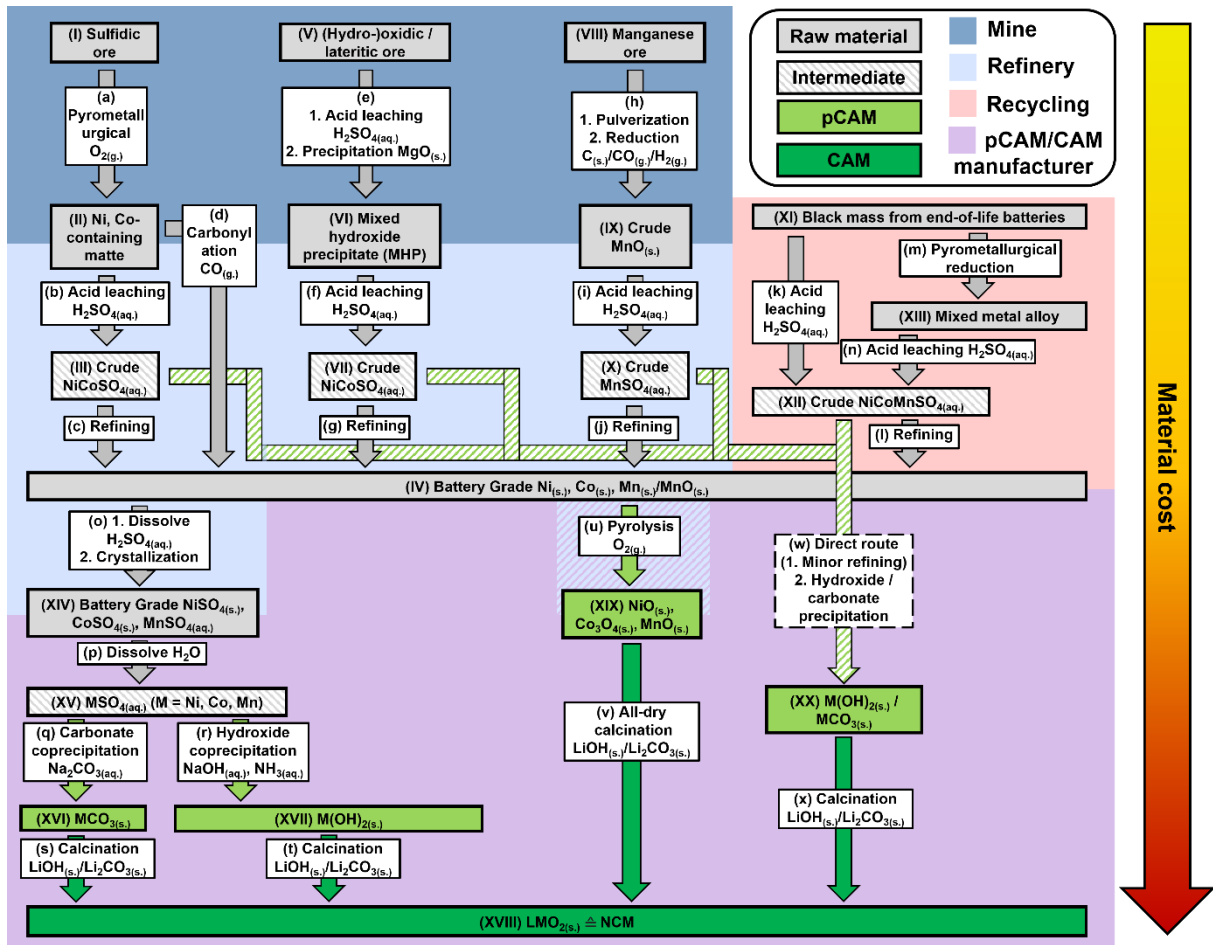
Figure 3: Schematic overview of the major production routes of layered lithium nickel cobalt manganese oxide (NCM)-based cathode active material (CAM), with emphasis on the nickel chain of production, starting from mineable ores or black mass extracted from end-of-life batteries. The raw materials, important intermediates, and products are numbered by roman numbers and are categorized by color: raw materials are given in grey boxes, important intermediates in grey striped boxes, precursor of cathode active material (referred to as pCAM) in light green boxes and CAM in dark green boxes. The grey arrows indicate the processing steps (colorless box, numbered by letters) of raw materials (grey), synthesis of pCAM (light green) and CAM (dark green). The light green striped arrow indicates the potential for direct synthesis of pCAM applying crude metal sulfate solutions after only minor or no refining at all. The arrow exhibiting a color gradient from yellow to red illustrates the relative cost of raw materials. The colored underlay denotes the business segment related to the respective process steps within the NCM supply chain itemized after mining (dark blue), refining (light blue), recycling (pink), and battery material manufacturing (purple). The scheme is based on the information available in the literature on the raw material supply chain of nickel,[21, 34-36] cobalt,[20] and manganese,[26, 27] as well as lithium-ion battery recycling.[28-30, 37, 38] The information about the distinctive CAM synthesis routes was taken from scientific and patent literature for the carbonate (q),[39-42] hydroxide (r),[15, 43, 44] all-dry (v),[45-51] and direct route (w).[52, 53]

In the following discussion, roman numbers indicate raw materials, intermediates, and products (pCAM and CAM), while letters indicate process operations. After the mining of sulfidic Ni minerals (I) from the earth's crust in the form of distinct grains within a complex
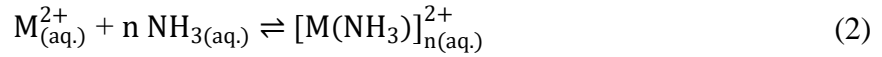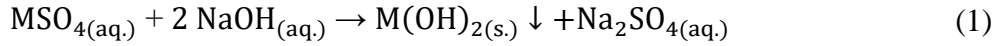
rock matrix (1.0-2.0wt% Ni), the ores are subjected to mechanical enrichment by comminution, froth flotation, and magnetic separation. Most of the thereby attained metal concentrates (5.0-12wt% Ni) are then beneficiated by a pyrometallurgical process (a) comprising of roasting, smelting, and converting to separate iron (Fe), which results in the formation of a Ni-enriched and Co-containing sulfide called matte (II). Matte (II) exhibits a metal grade range of 60-80wt% Ni and 0.1-1.0wt% Co. Since the obtained matte (II) is partially enriched with 5-25wt% copper (Cu), the metals are subsequently leached by sulfuric acid $H_2SO_{4(aq.)}$ and separated in a two-stage hydrometallurgical process (b). This yields an unrefined, aqueous Cu-free nickel cobalt sulfate solution $NiCoSO_{4(aq.)}$ (III) and leaves a Cu enriched leach residue.[21] The refinement (c) thereof is conducted by either electrowinning, electrorefining, hydrogen reduction, or solution purification. Thereby, elemental Ni and Co in the form of powders, pellets, briquettes, or cathodes is obtained, each metal exhibiting a grade of ≥99.7% (commonly referred to as battery grade) (IV).[21, 34, 35] Instead of wet process routes, Ni metal powders and pellets with an exceptionally high purity of ≥99.97% can be directly obtained by carbonylation (g) of Matte (II) with gaseous carbon monoxide $CO_{(g.)}$. By being a dry process method, acid leaching and refinement is effectively skipped during carbonylation (d), which averts wastewater generation during refining and ensuing treatment thereof.[21, 34, 35]

Alternatively, pure Ni and Co metal (IV) can be obtained starting from mined lateritic Ni ores (IV) that contain 1.0-3.0wt% Ni and 0.05-0.2wt% Co. A fraction of the mechanically upgraded (hydro-)oxidic Ni ores (V) are pyrometallurgically converted to either ferronickel or nickel pig iron, both as raw material for the steel stainless industry. However, the majority is immediately subjected to $H_2SO_{4(aq.)}$ leaching (e) because the high moisture content of 20-50% in lateritic Ni ores (V) incurs high energy consumption for the drying thereof for pyrometallurgical processing. The acid treatment leads to the coprecipitation of Fe and Al as sulfates, while at the same time dissolving Ni, Co, and magnesium (Mg). After solid/liquid separation, a caustic magnesia oxide slurry $MgO_{(s.)}$ is added to the crude metal sulfate (e), resulting in the formation of dissolved magnesium sulfate and a mixed hydroxide precipitate referred to as MHP (VI). This beneficiated resource exhibits a metal grade of 35-40wt% Ni and 1.0-2.0wt% Co. Subsequently, MHP (VI) is subjected to releaching in $H_2SO_{4(aq.)}$ (f) to attain a crude $NiCoSO_{4(aq.)}$ (VII), which is refined (g) to battery grade Ni and Co(IV).[21, 34, 35] The exploitation of Co concentrated sulfidic ores in the DCR are subjected analogously to a combination of pyro- and hydrometallurgical process like sulfidic Ni ores (I) to attain a crude cobalt sulfate solution that can be further refined to Co metal (process route not shown in Figure 3).[20, 21]

While oxidic Mn ores (VIII) naturally exhibit very high Mn concentrations of above 40wt%, the Mn minerals are almost exclusively encountered with Mn being in the highly insoluble +4 oxidation state. Therefore, after mechanical pulverization, Mn ores (VIII) are calcined in reductive atmosphere (h) to deliver Mn in the acid soluble +2 oxidation state. Resulting MnO (IX) is subsequently dissolved in $H_2SO_{4(aq.)}$ to give crude manganese sulfate solution $MnSO_{4(aq.)}$ (X). While a wide range of methods are applied for the refinement of Ni and Co, the refinement (j) of $MnSO_{4(aq.)}$ (X) mainly comprises electrowinning to generate elemental Mn metal (IV) in the form of flakes, granules, or powder, exhibiting a grade of ≥99.5%.[26, 27]

Another very important source on the horizon for metals employed in NCMs is black mass extracted from end-of-life lithium-ion batteries (XI). Currently, commercially prevailing processing of black mass comprises either hydrometallurgical (k), pyrometallurgical treatment (m), or combinations thereof. Even though the pyrometallurgically operation (m) affords a mixed metal alloy (XIII), an acid leaching with $H_2SO_{4(aq.)}$ (n) is applied to recover the respective elements in the following operations from a crude nickel cobalt manganese sulfate solution $NiCoMnSO_{4(aq.)}$ (XII).[28-30, 38]

So far it was demonstrated that independent of the raw material source, every processing route shares battery grade elemental Ni, Co, and Mn as a common intermediary substrate (IV). Starting from the respective metals in elemental form (IV), an assortment of options for the synthesis of NCMs unfolds. The most mature and currently industrially applied process route comprises the dissolution of the pure metals in $H_2SO_{4(aq.)}$ followed by recrystallisation (o) as the respective battery grade solid metal sulfate $NiSO_{4(s.)}$, $CoSO_{4(s.)}$, and $MnSO_{4(s.)}$ (XIV). These are shipped to battery material manufactures and dissolved in H_2O (p) in the desired transition metal ratio of the target NCM composition, yielding a mixed metal sulfate solution $MSO_{4(aq.)}$ (M consisting of Ni, Co, Mn) (XV). The ensuing production of the pCAM is conducted by feeding $MSO_{4(aq.)}$ in a stirred tank reactor (STR) concomitant with either sodium carbonate $Na_2CO_{3(aq.)}$ to precipitate a mixed metal carbonate $MCO_{3(s.)}$ (XVI), denoted as carbonate CO_3^{2-} coprecipitation (q),[39-42] or concomitant with sodium hydroxide solution $NaOH_{(aq.)}$ and ammonia solution $NH_{3(aq.)}$ to yield a mixed metal hydroxide $M(OH)_{2(s.)}$ (XVII), denoted as hydroxide OH^- coprecipitation (r).[15, 43, 44] During the OH^- coprecipitation (s), an equilibrium of the coprecipitation reaction of metal cations $M^{2+}_{(aq.)}$ with OH^- anions and of the complexation reaction of $M^{2+}_{(aq.)}$ with ammonia (for which especially Ni exhibits a high affinity) occurs, as presented in the following.[44]

$$MSO_{4(aq.)} + 2\,NaOH_{(aq.)} \rightarrow M(OH)_{2(s.)} \downarrow +Na_2SO_{4(aq.)} \tag{1}$$

$$M^{2+}_{(aq.)} + n\,NH_{3(aq.)} \rightleftharpoons [M(NH_3)]^{2+}_{n(aq.)} \tag{2}$$

Further, it is suggested that the coprecipitation of $M(OH)_{2(s.)}$ (XVII) might also occur from the metal ammonia complex, which enables controlled crystallization.[54] Accruing $NH_{3(aq.)}$ is typically recovered in gaseous state by raising the temperature of the wastewater in a stripping column to outgas $NH_{3(aq.)}$. The OH^- coprecipitation reaction is typically conducted close to, or in the solubility minimum of the respective metal hydroxides, ranging from pH-value of 10.0-13.0.[5, 41, 44, 55] Further, a reductive atmosphere, such as nitrogen gas, is maintained in the STR to suppress the oxidation of manganese hydroxide $Mn(OH)_2$ to manganese oxo hydroxide $MnOOH$ and/or manganese dioxide MnO_2. This prevents the formation of undesired side phases and reduces impurity uptake.[56, 57]

The underlying reaction of the CO_3^{2-} coprecipitation (q) is given by the ensuing expression.[39-42]

$$MSO_{4(aq.)} + Na_2CO_{3(aq.)} \rightarrow MCO_{3(s.)} \downarrow +Na_2SO_{4(aq.)} \tag{3}$$
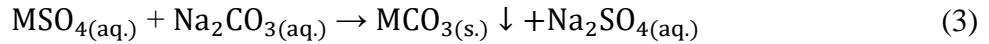
A reductive atmosphere is redundant during CO_3^{2-} coprecipitation as the oxidation of Mn^{2+} cannot occur from the carbonate, and for this reason is advantageous for the synthesis of phase-pure Mn-rich NCMs.[39-41] In contrast to the OH^- coprecipitation, the CO_3^{2-} coprecipitation is operated in pH-range of 7.5-9.0, which represents the solubility minimum of the respective metal carbonates.[40, 41] Since the pk_a-value of NH_3 at 23 °C is approximately 9.3, NH_3 exists below a pH-value of 9.3 in the protonated form as ammonium cation NH_4^+,[58, 59] which exhibits no complexation ability towards metal cations according to equation 2. In light of this, and in contrast to academic literature,[39-41] the CO_3^{2-} coprecipitation is industrially practiced in the absence of $NH_{3(aq.)}$.[42] Apart from morphology control of the resulting pCAM,[40] coprecipitation techniques allow the formation of a single-phase mixed metal compound, in which the elements are homogenously distributed on an atomic scale, since the metal cations are coprecipitated from liquid phase ($MSO_{4(aq.)}$) where the cations are homogenously dissolved.[56, 60] A phase-pure pCAM exhibiting a uniform metal distribution is an imperative prerequisite for ensuring consistently high product quality of NCM CAMs.

After the coprecipitation reaction, the attained pCAM slurries are filtered, washed, dried, and mixed with a lithium (Li) salt such as lithium hydroxide ($LiOH_{(s.)}$) or lithium

carbonate ($Li_2CO_{3(s.)}$). The solid mixture is then transferred to an industrial kiln and calcined at elevated temperatures to produce lithium transition metal oxides $LiMO_{2(s.)}$ ($\triangleq$ NCMs) (XVIII) by solid state synthesis (s, t). Accordingly, the following net reaction for the case of $M(OH)_{2(s.)}$ with $LiOH_{(s.)}$[61, 62] (equation 4) and $MCO_{3(s.)}$ with $LiOH_{(s.)}$[63] (equation 5), respectively, are occurring.

$$M(OH)_{2(s.)} + LiOH_{(s.)} + \frac{1}{4} O_{2(g.)} \rightarrow LiMO_{2(s.)} + \frac{3}{2} H_2O_{(g.)} \uparrow \tag{4}$$

$$MCO_{3(s.)} + LiOH_{(s.)} + \frac{1}{4} O_{2(g.)} \rightarrow LiMO_{2(s.)} + CO_{2(g.)} \uparrow + \frac{1}{2} H_2O_{(g.)} \uparrow \tag{5}$$
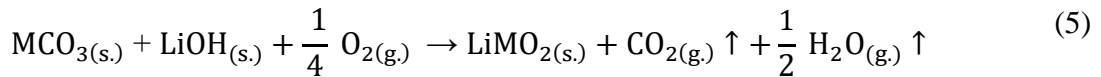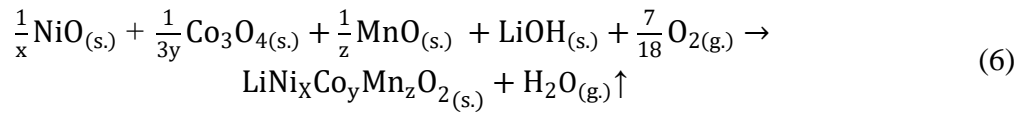
Based on equation 5, application of $MCO_{3(s.)}$ (XVI) as pCAM for the synthesis of NCMs results in a stoichiometric release of carbon dioxide $CO_{2(g.)}$, which entails the necessity for exhaust treatment to meet the standards of environmentally sustainable production of CAMs. Irrespective of the utilized pCAM, the same consideration has to be made if $Li_2CO_{3(s.)}$ is employed as lithium source for CAMs, because $Li_2CO_{3(s.)}$ decomposes to $CO_{2(g.)}$ at the commonly applied calcination temperatures for NCMs of above 700 °C.[64] Further, the individual coprecipitation routes each offer access to distinctive pCAM properties, as it is reported that carbonate pCAMs exhibit higher porosities than hydroxide pCAMs.[65] This may have a crucial role in the context of the final LIB application of the CAM,[66, 67] since the physical properties[68-73] and electrochemical performance[73-75] are affected by the pCAM that was utilized for the synthesis of the CAM.

Nevertheless, independent of the synthesis route starting from $MSO_{4(aq.)}$ (XV), large amounts of alkaline water contaminated with sodium sulfate $Na_2SO_{4(aq.)}$ are accrued as a byproduct (see equation 1 and 3) due to the aqueous coprecipitation feedstocks and downstream processes such was washing of the pCAM product. Combined with the fact that the industrial utilization of Na_2SO_4 is limited, costly wastewater treatment and disposal of Na_2SO_4 is necessary.[63] This questions the environmental sustainability of this traditional NCM manufacturing route, which recently has resulted in a surge of alternative synthesis methods.

In this context, instead of utilizing $MCO_{3(s.)}$ (XVI) or $M(OH)_{2(s.)}$ (XVII), a physical blend of the individual transition metal oxides $NiO_{(s.)}$, $CoO_{(s.)}$ and $MnO_{(s.)}$ (XIX) can be directly applied as pCAM for NCM (XVIII).[45-50] The oxides (XIX) can be attained by oxidation with $O_{2(g.)}$ (u) from the respective elemental metal (IV), or by calcination of other metal compounds (process route not shown in Figure 3).[21, 36] Even though the technique of synthesizing lithium nickel oxide (LNO), lithium cobalt oxide (LCO) and lithium manganese oxide (LMO) from the

respective metal oxide[76] as well as NCMs from a physical mixture of various transition metal precursors such as oxides, nitrates, and/or carbonates[77-79] has been known for more than 20 years, it regained attention as an alternative method for NCM synthesis by both academia[45, 46, 51] and industry.[47-50] Essentially, a dry powder blend of the respective individual transition metal oxides (XIX) in a desired molar ratio corresponding to the target NCM composition is mixed with a lithium compound and subsequently calcined at elevated temperatures (v) to yield NCM (XVIII). Not being dependent on solvents to produce pCAM from the dry oxide powders, this method was termed "all-dry".[46] It is assumed that the following solid state reaction is taking place during the calcination reaction of the metal oxide blend with $LiOH_{(s.)}$.

$$\frac{1}{x}NiO_{(s.)} + \frac{1}{3y}Co_3O_{4(s.)} + \frac{1}{z}MnO_{(s.)} + LiOH_{(s.)} + \frac{7}{18}O_{2(g.)} \rightarrow$$
$$LiNi_xCo_yMn_zO_{2_{(s.)}} + H_2O_{(g.)}\uparrow \tag{6}$$

where x, y and z present the mole fraction of Ni, Co, and Mn, respectively, in the target NCM $LiNi_xCo_yMn_zO_{2(s.)}$.

For the purpose of cost reduction, it is suggested to utilize class 2 $NiO_{(s.)}$ for the all-dry synthesis of Ni-rich NCMs,[45] since class 2 $NiO_{(s.)}$ is cheaper compared to the pure Ni metal (class 1), as class 2 Ni compounds are recovered earlier in the refining process and therefore, exhibit a lower metal grade. However, the production of class 2 $NiO_{(s.)}$ is currently limited to the Caron Process (process route not shown in Figure 3), which in total amounts to only 113 kt Ni produced per year.[21] This corresponds to ~5% of the total annual Ni production worldwide.[18] Therefore, an adaption of the all-dry synthesis method would require a change in the current refining infrastructure.

To obtain single-phase NCMs exhibiting a homogenous element distribution and spherical secondary particle shape, analogous to what is produced by the coprecipitation method (r, s),[68, 70-73] the irregular-shaped distinctive metal oxides are milled, physically mixed, and granulated prior to the calcination reaction within the all-dry route (w).[45, 47-50] However, these techniques are known to yield aspherical granulates with void fractions.[45, 80, 81] The latter might lead not only to pronounced capacity fade due to increased contact of the NCM particle with the electrolyte in the LIB application,[82, 83] but also excessive internal porosity in CAM particles that lowers the volumetric energy density of the LIB.[66, 67] Further, the irregular shape of particles decreases powder flowability,[84-89] which negatively affects powder production.[84]

Additionally, the elemental distribution achievable by mechanical mixing and ensuing calcination might not be sufficient and result in elemental inhomogeneities and/or phase separations in the CAM product. Both is detrimental for the electrochemical performance of the NCM in the LIB application.[56, 60] Further, it is claimed that a radially alignment of primary particles within an NCM secondary particle improves the mechanical integrity of secondary particles, which reduces secondary particle cracking and therewith related degradation mechanisms.[90-92] This particle architecture originates from the coprecipitation reaction of pCAM and can be transferred to the CAM after calcination.[90-92] In light of the preceding discussion, it might prove difficult to fulfil the requirements of hierarchically structured NCM secondary particles by an all-dry synthesis method (v).

However, an alternative particle design to the secondary particle architecture, namely a monolithic particle morphology exhibiting large single crystal domains (commonly referred to as single crystal or single crystalline NCM) offers reduction of degradation mechanisms and therefore, improvement of the capacity retention and overall LIB lifetime.[93-96] Since the hierarchally structured secondary particle architecture created during the pCAM coprecipitation process is in any case broken down during the synthesis of single crystalline NCMs due to the excessive particle agglomeration by high calcination temperatures and subsequent milling to the size of the irregular-shaped, single grains,[93, 94, 97] the all-dry process route (v) seems especially beneficial for the synthesis of single crystal materials, because the previously discussed drawbacks of this method for the synthesis of conventional NCMs become irrelevant. Further, the higher calcination temperatures required for the formation of single crystalline NCM facilitate the solid-state diffusion of the metals during the calcination reaction. This yields a uniform metal distribution in the single crystalline product,[46] which otherwise cannot be achieved at the lower calcination temperatures applied for the synthesis of conventional NCM materials by the all-dry method (v).[60] In light of these facts, the drawbacks of the all-dry method (v) can be overcome if utilized for the synthesis of single crystalline NCM, which renders the process route particularly suitable for the synthesis of single crystal materials.[46] Regardless, the main advantage of this process route remains to enable the production of NCM without accruing byproducts and wastewater. In addition, it has the potential to be a lower cost process compared to the conventional synthesis route, as it utilizes a cheaper feedstock, namely on metal oxides (XIX) instead of metal sulfates (XIV).[45, 46, 98]

Another possible process route for the synthesis of NCM (XVIII) on the horizon that likewise offers the potential for cost-reduction and amelioration from an ecological perspective, but in addition can utilize the current industrial infrastructure employed for the NCM

production is the "direct route" (w). Independent of the raw material source, natural (I, V, VIII) or secondary by recycling (XI), every process route shares crude metal sulfate solution $MSO_{4(aq.)}$ (M = Ni, Co for III and VII, M = Mn for X and M = Ni, Co, Mn for XII) as a common intermediate towards the synthesis of high-grade elemental metal substrates (IV) to produce NCMs (XVIII). Even though the exact composition (metal grade and impurity content) of the crude metal sulfate solutions is contingent on the individual processing route and starting material, the refinement thereof is conducted similarly by either electrowinning, electrorefining, hydrogen reduction, or solution purification.[20, 21, 26-30, 34, 35] If Ni, Co, and Mn are emerging from the same raw material source and therefore, are accrued together as a crude $MSO_{4(aq.)}$, it is pointless in the context of NCM production to isolate the metals separately and refine them individually to only mix (p) the elements (XIV) together again to give a battery grade $MSO_{4(aq.)}$ (XV) for the pCAM synthesis. To save cost, the metals can be purified simultaneously as a $MSO_{4(aq.)}$ and recovered earlier in the value chain. This will also limit the wastewater produced by the ensuing coprecipitation process for the synthesis of pCAM to the wastewater, which would be anyways produced by the refining process, independent of the downstream NCM synthesis method. Therefore, the environmental impact of the CO_3^{2-} (q) and OH^- coprecipitation (r) is also reduced. This is particularly true for LIB recycling, where in the case the black mass feedstock (XI) contains NCM in the target stoichiometric transition metal ratio, a separation of the metals for the synthesis of NCMs would be redundant. Further, an optimized minor refining for the synthesis of NCMs can be imagined that balances the maximum tolerable threshold of impurities in the feedstock, the performance, and the final cost of the resulting NCM. The thereby resulting metal sulfate $MSO_{4(aq.)}$ of minimum required grade can be employed as starting material for the OH^- coprecipitation or CO_3^{2-} coprecipitation (w) to produce $M(OH)_{2(s.)}$ or $MCO_{3(s.)}$, respectively (XX), as it is the case for the current NCM manufacturing process (r, s). The resulting pCAM (XX) can then be blended with a lithium compound and calcined (z) to produce an NCM CAM (XVIII). In this context, several studies benchmarked NCM111 CAM synthesized from an $MSO_{4(aq.)}$ solution derived from hydrometallurgically treated black mass against commercially available NCM111, demonstrating comparable electrochemical performances for 11 Ah cells.[68] This was also proven for other NCM chemistries such as NCM523,[99] NCM622,[99] and NCM811[100] for smaller cells. Further, the feasibility of applying mixed CAM chemistries in the black mass, ranging from NCM, NCA, LFP, and LMO as substrate is reported, which highlights the flexibility of this process.[52, 101, 102] The impact of common impurities that are present in an $MSO_{4(aq.)}$ feedstock derived from black mass, such as Al,[103] Cu,[104] Li,[105] and Mg[106] on the electrochemical performance was evaluated. Each of the

studies identified a maximum tolerable concentration of impurities above which the electrochemical performance of the NCMs deteriorates.[103-106] These approaches can also be transferred to crude metal sulfate solutions (III, VII, X and XII) recoverable during the upgrading of raw materials in order to optimize the refining process for the purpose of synthesizing of NCMs. Therefore, determining the sufficient purity required in feedstocks to manufacture NCMs will become an integral part of future CAM research - metaphorically speaking, finding out how much sawdust can be admixed to the flour until the taste of the resulting bread turns bad.

While the preceding discussion provides a simplified overview of the industrially relevant NCM manufacturing routes, it can only shed some light on the technical, economic, and ecological aspects of the distinctive production methods. For a fair comparison, a detailed analysis of the distinctive process routes in their entirety and the therewith associated technical infrastructure (e.g., if pure elemental metals are applied as substrate for the synthesis of a pCAM or CAM, this would require specially designed silos for the storage of ignitable powders, which would not be necessary for the storage of an aqueous solution)[107, 108] as well as the feedstock starting from the raw materials, including the economic and ecological aspects on every level is necessary. However, this would be beyond the scope of this work.

Since the currently practiced industrial synthesis method involves the coprecipitation of an NCM pCAM (q, r), a process that will likely also be practiced in the future due to its potential for backwards integration, ecological amelioration and inclusion of recycling feeds while at the same time making use of the current NCM production infrastructure, the next section will present a technical overview of the NCM manufacturing by utilizing the OH^- coprecipitation process (r) to produce $M(OH)_{2(s.)}$ (XVII) as pCAM for the synthesis of NCM (XVIII) by calcination (t).

1.4 Current manufacturing process of layered lithium nickel cobalt manganese oxides

The up to today predominantly practiced commercial method to produce NCMs is schematically presented in Figure 4 and comprises three principal process operations: the OH⁻ coprecipitation of pCAM particles (I),[15, 43, 44] their calcination with a lithium compound to yield a raw NCM product (II),[109-111] and the final posttreatment of the latter to give a treated NCM (III) that is ready to be used as CAM in a LIB application.[112]
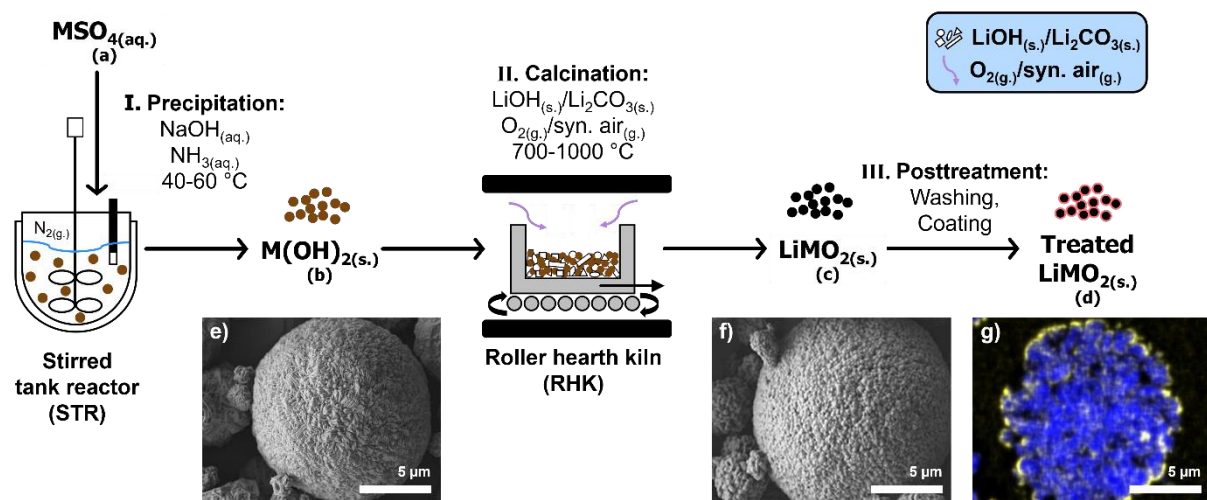
Figure 4: Schematic illustration depicting the industrial synthesis of layered lithium nickel cobalt manganese oxides (i.e., NCMs ≙ $LiMO_{2(s.)}$) as cathode active material (CAM) for lithium-ion batteries (LIBs). The manufacturing process can be divided into three major steps: (I) coprecipitation, (II) calcination and (III) posttreatment. During coprecipitation (I), an aqueous mixed metal sulfate $MSO_{4(aq.)}$ (a) is continuously fed alongside aqueous sodium hydroxide solution $NaOH_{(aq.)}$ and aqueous ammonia solution $NH_{3(aq.)}$ into a stirred tank reactor (STR) under nitrogen $N_{2(g.)}$ atmosphere to produce a mixed metal hydroxide $M(OH)_{2(s.)}$ (b). In the subsequent calcination step (II), the coprecipitated $M(OH)_{2(s.)}$ particle powder (b) is mixed with a lithium compound (lithium hydroxide $LiOH_{(s.)}$ or lithium carbonate $Li_2CO_{3(s.)}$) and calcined in a roller hearth kiln (RHK) at elevated temperatures in an oxygen $O_{2(g.)}$ or synthetic air$_{(g.)}$ atmosphere. In the end, the attained lithium metal oxide $LiMO_{2(g.)}$ particle powder (c) is subjected to posttreatments like washing and/or coating to yield treated lithium metal oxide $LiMO_{2(s.)}$ (d). The top view SEM images exemplarily depict $M(OH)_{2(s.)}$ (e) and $LiMO_{2(s.)}$ (f) secondary particles. The SEM-EDX image (g) exemplarily depicts a cross-sectionally sliced $LiMO_{2(s.)}$ secondary particle (blue) with a coating (yellow). The information about the NCM production process steps to create the figure was taken from scientific and patent literature for the OH⁻ coprecipitation,[15, 43, 44] the calcination,[109-111] and the posttreatment,[112] while the displayed SEM images present internal data from BASF SE.

The OH$^-$ coprecipitation (I) is conducted by simultaneously feeding MSO$_{4\text{(aq.)}}$ (a), NaOH$_\text{(aq.)}$, and NH$_{3\text{(aq.)}}$ into an STR operated under N$_{2\text{(g.)}}$ atmosphere. After the completed reaction, the solid slurry is collected, washed, and dried to obtain M(OH)$_{2\text{(s.)}}$ as a solid powder (b).[15, 43, 44] For a quantitative formation of M(OH)$_{2\text{(s.)}}$, the process is operated in the solubility minimum of the respective Ni, Co, and Mn hydroxides, ranging from pH-value of 10.0-13.0[5, 41, 44, 55] in order to favor the reactions given by equation 1 and 2.[15, 43, 44] The thereby attained secondary particles exhibit particle sizes in the lower micron range (4-16 µm) and are composed of numerous plate-like primary particles in the submicron range (exemplarily depicted in Figure 4e).[56, 74, 113-115] It is suggested that the primary particles consist of various crystallites[115] which are micro-structurally related to layered, hexagonal brucite-type β-Ni(OH)$_2$.[54, 113, 116-118] Further, an elemental mixing on an atomic scale in the M(OH)$_{2\text{(s.)}}$ particle is achieved since the metal cations are coprecipitated from liquid phase.[56, 60] The course of the coprecipitation (growth rate, nucleation rate, agglomeration, etc.) and the M(OH)$_{2\text{(s.)}}$ product properties (particle size, particle morphology, etc.) are highly contingent on the applied process parameters. The available process variables are the operational mode (semi-batch or continuous),[119] the reaction time,[113, 120-122] the coprecipitation pH-value,[43, 113, 114, 120, 121, 123] the temperature,[120, 121, 124] the NH$_{3\text{(aq.)}}$ concentration,[43, 114, 120, 122, 125] the flow rates,[126] the turbulence controllable by the stirring speed,[43, 114, 120, 121] and the composition of the reactor's gaseous atmosphere,[56, 127] with each parameter affecting in specific ways the complex solution chemistry of the coprecipitation reaction and thus the properties of the precipitate. On top of that, additives may be employed to tailor the pCAM properties[128-131] and/or heterogenous elements (commonly referred to as dopants) such as Al,[132, 133] Mg,[132, 134, 135] Ti,[134] Zr,[134, 135] W,[136-138] Nb,[134] and Mo[138] can be coprecipitated into M(OH)$_{2\text{(s.)}}$ particles to modify the microstructural and physical properties of the M(OH)$_{2\text{(s.)}}$ pCAM, which ultimately affects the electrochemical properties of the final NCM.

In the subsequent calcination process (II), the M(OH)$_{2\text{(s.)}}$ powder (b) is blended with a lithium compound such as LiOH$_\text{(s.)}$ or Li$_2$CO$_{3\text{(s.)}}$ and transferred into ceramic vessels, which are passed through a roller hearth kiln (RHK) at temperatures in the range of 700-1000 °C in an O$_{2\text{(g.)}}$ or synthetic air atmosphere in order to convert the powder mixture to LiMO$_{2\text{(s.)}}$ ($\triangleq$ NCM) powder (c).[109-111] The net solid-state reaction if LiOH$_\text{(s.)}$ is employed as lithium reagent is given by equation 4. It has been demonstrated that the actual underlying reaction comprises i) the dehydration of the M(OH)$_{2\text{(s.)}}$ to MO$_\text{(s.)}$ with a rock-salt crystal structure, ii) the decomposition of Li(OH)$_\text{(s.)}$ to lithium oxide Li$_2$O$_\text{(s.)}$, iii) the lithiation reaction to form layered NCM with a hexagonal α-NaFeO$_2$ crystal structure, and iv) finally growth of the individual NCM

crystallites.[61, 139] Despite several phase transitions occurring during the calcination reaction, the secondary particle structure of the $M(OH)_{2(s.)}$ pCAM is maintained after the calcination at high temperatures and is transferred to the NCM CAM.[69-72] Therefore, the $M(OH)_{2(s.)}$ pCAM can be considered as template for the final NCM, which is indicated by the SEM images depicting exemplarily an $M(OH)_{2(s.)}$ (Figure 4e) and an $LiMO_{2(s.)}$ CAM secondary particle (Figure 4f). Consequently, it is widely acknowledged that the NCM electrochemical performance is affected by the associated pCAM utilized for synthesis.[73-75] Analogous to the coprecipitation reaction (I), a vast assortment of process variables exists during the calcination (II) to control the solid-state reaction (crystal growth, lithiation kinetics, etc.) and to tailor the product properties (primary particle size, crystallinity, etc.). The most critical parameter is the temperature profile to which the powder mixture is subjected in the kiln, comprising the heating and cooling speed, the maximum temperature, and the overall dwell time.[61, 62, 69, 82] The employed lithium salt,[61] the Li equivalents per mol transition metal in $M(OH)_{(s.)}$,[62, 82] the atmosphere in the oven and the exchange thereof per time,[140] the total solid loading as well as the corresponding architecture of the powder bed in the ceramic vessels,[61, 141] and the kiln design present additional process parameters.[61, 142] Further, multi-step calcination profiles[61, 94, 143] and/or particle growth amplifiers[144] can be employed to improve the manufacturing throughput and/or tailor the product properties. Besides the coprecipitation reaction (I), the calcination (II) offers likewise an opportunity to incorporate dopant-elements such as Al,[145] B,[146, 147] F,[148] Mg,[145, 149] Ti,[145] Zr,[145, 150, 151] W,[152] Sn,[90] and Ta[145, 153] into the NCM in order to tune the product properties. Contingent on the solid-state diffusivity of the respective elements at given firing conditions in the kiln, either a surface accumulation of the dopant on the NCM secondary particle or uniform distribution across the secondary particle can be achieved.[132, 154-156] However, if a homogenous distribution is desired, the mobility of the doping element during the solid-state reaction might not be sufficient. Therefore, it might prove beneficial to already include the element during the coprecipitation reaction (I) instead in order to ensure a homogenously distribution of the respective dopant.[134, 135]

The raw NCM product (c) attained by calcination (II) is subsequently subjected to a posttreatment (III) like washing and/or coating in order to produce the final treated NCM particles (d).[112] Figure 4g exemplarily depicts a cross-sectionally sliced $LiMO_{2(s.)}$ secondary particle (blue) exhibiting a coating (yellow). The washing is conducted to remove Li residuals (e.g., $Li_2CO_{3(s.)}$) originating from the calcination reaction (II), which are residing in the porous network within the NCM secondary particles. This not only open pores and therefore increases the specific surface area of the NCM particles,[82, 157] but also prevents down-stream issues by Li

residuals such as ink-gelation during electrode casting[158] and detrimental side reactions in the LIB cell.[159] Additionally, washing induces a lithium-ion/proton Li^+/H^+-exchange in the layered structure in the near surface region of the NCM, which upon drying of the washed material results in the formation of oxygen depleted phases such as $NiO_{(s.)}$ in the near surface region of the NCM particles.[157, 160, 161] Notable process variables to control the washing procedure (degree of Li residual removal, Li^+/H^+-exchange, increase in porosity, etc.) are the washing intervals,[160] the water to CAM ratio,[157] the washing time,[157] and the washing temperature,[162] as well as the drying temperature of the washed NCM.[157, 160] Further, specialized washing techniques such as acid[163] or buffer washing[162] can be employed for specific NCM chemistries. To mitigate performance loss by material degradation during cycling in the LIB application,[5] a coating is applied on the NCM particles to form a protective layer and to stabilize the NCM surface against degradation reactions and/or to enhance the mechanical integrity of the secondary particle.[164] Additionally, if the coated material exhibits a high lithium ion conductivity, the lithium ion diffusion at the NCM surface is enhanced, which decreases the resistance build-up during cycling.[165] Commonly applied coating elements are W,[166] Ti,[167, 168] Zr,[156, 165, 169] Al,[155, 165, 170] La,[165] Co,[164] B,[164] and Nb.[171] Again, various process parameters exist to apply a coating and to modify the coating properties (coating thickness, homogeneity, etc.) such as coating substrate concentration,[171] wet or dry coating,[170] annealing temperature,[155] and reactivity of the coating element with Li compounds or Li residuals.[164, 169, 171]

In summary, while the underlying chemistry of NCM manufacturing might appear simple at first glance, the multiple and partially intertwined dependencies between the numerous synthesis parameters and structure performance relationships create a complex discipline of microstructural particle engineering. Quantifying the available process parameters of each process step, the coprecipitation (I) comprises 10 process parameters, while the calcination (II) and posttreatment (III) each have 13 process parameters (application of doping elements or additives during the coprecipitation (I) and calcination (II), respectively, were each reduced to one process parameter per process step). Overall, this gives 36 process parameters to prepare NCMs, each with their own distinctive impact on the product properties and performance in the LIB cell. Considering this, the synthesis of NCMs can be perceived more as art than science. However, such statement would underestimate the tremendous progress in the recent years to understand the synthesis process, the pCAM and CAM properties, and the behavior of NCM materials in the LIB cell of NCMs, such as the implications of the particle morphology on the electrochemical performance for various NCM chemistries[67, 94, 96] even including the calcination parameters,[61, 62] the lithiation mechanism occurring during the

calcination process reaction[61, 139] leading to the use of two-stage calcination profiles for optimized physical properties,[94, 143] or the transfer of the $M(OH)_{2(s.)}$ particle morphology to the NCM.[68-73] Despite this impressive work, a certain knowledge gap persists, especially regarding the OH^- coprecipitation to generate the $M(OH)_{2(s.)}$ pCAM for the synthesis of NCM CAM. So far, coprecipitation-parameter-product relationships have been mainly empirically studied to optimize the energy density of the resulting NCM in the final LIB.[39, 43, 121, 123] Since the coprecipitation reaction represents the first set-screw in the synthesis process of NCMs to adjust the physical properties and electrochemical performance of the product, thus the quality of the final LIB, a systematic understanding of the particle formation during the coprecipitation reaction is imperative to enable every degree of freedom available to tailor the material properties. Therefore, the scope of this thesis is to identify process-parameter-product-property relationships by detailed examination of the $M(OH)_{2(s.)}$ particle formation and growth during the coprecipitation reaction to contribute to an efficient manufacturing of excellent NCMs for high-performing LIBs with the aim in BEV applications.

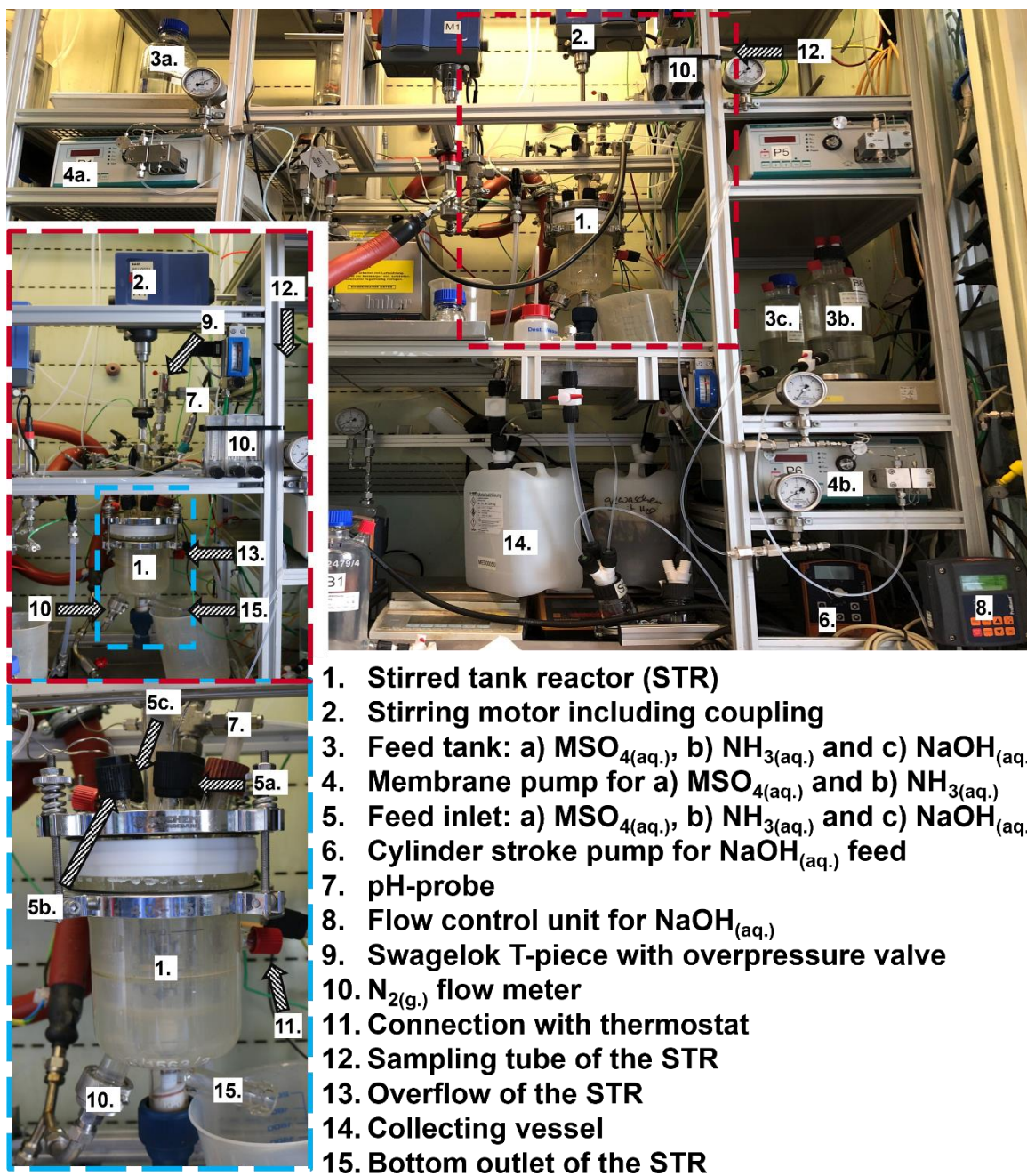# 2 Experimental section

2.1 Stirred tank reactor setup

The optimized coprecipitation setup – The coprecipitation of pCAM particles for NCM CAM particles, both OH^- and CO_3^{2-} coprecipitation[39-42], are commonly practiced in an STR. While a facile coprecipitation in beaker is principally possible, the thereby attained product properties vary drastically from that of pCAM particles synthesized in an STR (e.g., spherical secondary particle structure)[56] due to the lack of turbulence combined with imprecise control of the process conditions. This limits the use of beaker experiments to solely investigate thermodynamic properties relevant for the coprecipitation of an NCM pCAM such as the solubility of Ni^{2+}, Co^{2+}, and Mn^{2+}. Therefore, an STR setup suitable for the investigation of the $M(OH)_2$ coprecipitation mechanism was developed in this work. The piping and instrumentation diagram (PID) of the designed STR system is given in Figure 5.
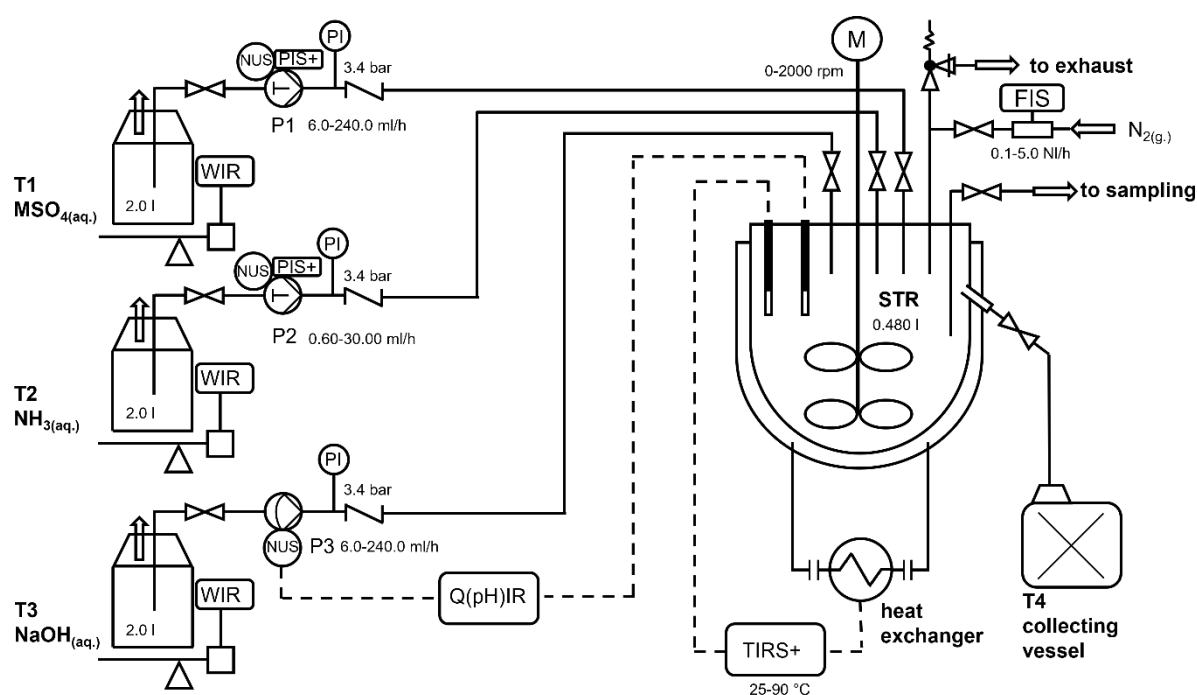
Figure 5: Piping and instrumentation diagram (PID) of the coprecipitation reactor setup utilized in this work, depicting the major constituents, where T = tank, P = pump, M = motor, STR = stirred tank reactor, WIR = weight indication record, NUS = user choice multivariable switch (here: volumetric flow rate), PIS+ = pressure indication switch and safety regulation above threshold value, PI = pressure indication, FI = flow indication, Q(pH)IR = quantity (pH-value) indication record and switch, and TIRS+ = temperature indication record switch and safety regulation above threshold value.

The center piece of the setup is a 480 ml jacketed STR equipped with a mechanical stirrer M to control the stirring speed between 0-2000 rpm and with an overflow. The STR can be fed with the reactants via three feed ports. The $MSO_{4(aq.)}$ and $NH_{3(aq.)}$ solutions are conveyed by the membrane pumps P1 (6.0-240.0 ml/h) and P2 (0.60-30.00 ml/h), respectively, from the respective feed storage tank T1 and T2 with a capacity of 2 l each. The feed tanks are positioned on balances, which allows monitoring the mass loss in the feed tank over time, thus the mass flow rate of the respective feeds. On the contrary, the $NaOH_{(aq.)}$ is fed into the reactor by a cylinder stroke pump P3 (6.0-240.0 ml/h) from the $NaOH_{(aq.)}$ feed storage tank T3, which is also positioned on a balance. The resulting flow is regulated by a flow control unit, which is connected to a pH-probe inserted into the reactor. This enables to automatically adjust the $NaOH_{(aq.)}$ flow conveyed by P3 according to the deviation of the set pH-value and the measured pH-value of the probe inside the STR. For all feeds, a safety valve with a threshold of 3.4 bar was installed. The temperature inside the stirred vessel can be controlled between 25-90 °C by a heat exchanger system, which is connected to a temperature sensor for tracking the temperature inside the reactor. This allows the regulation of the temperature of the heating fluid inside the double wall of the STR. Sampling reactor content for process analysis is possible by a tube inserted into the STR (denoted as "to sampling" in Figure 5). A $N_{2(g.)}$ atmosphere inside the reactor can be generated by a $N_{2(g.)}$ stream from the $N_{2(g.)}$ laboratory supply line, which can be controlled by a flow meter (0.1-5.0 Nl/h). As a security measure, a safety valve is connected to the STR, which in the case of excess pressure releases the reactor's atmosphere into the exhaust. Further, a collecting vessel T4 is attached to the reactor by an overflow line that provides the possibility to operate the system in continuous mode. In the case of any security measure being triggered, the power supply for the entire equipment is shut down.

Based on the presented PID in Figure 5, a coprecipitation reactor setup was developed, which is displayed in Figure 6. The photographs depict the overall equipment (upper photo, shown without a frame), a higher magnification of the STR (framed by the red dashed lines), and a detailed close-up view of the STR (framed by blue dashed lines). In each image the most important parts are labeled by numbers, which will be used in the following discussion. The 480 ml double-walled glass STR (1; BASF SE) was equipped with a three-stage 45° pitch-blade stirrer (BOLA), which was fixated through the center hole in the vessel's cap and anchored by a coupling to the stirrer motor (2; IKA Eurostar 20 digital).

1. **Stirred tank reactor (STR)**
2. **Stirring motor including coupling**
3. **Feed tank: a) $MSO_{4(aq.)}$, b) $NH_{3(aq.)}$ and c) $NaOH_{(aq.)}$**
4. **Membrane pump for a) $MSO_{4(aq.)}$ and b) $NH_{3(aq.)}$**
5. **Feed inlet: a) $MSO_{4(aq.)}$, b) $NH_{3(aq.)}$ and c) $NaOH_{(aq.)}$**
6. **Cylinder stroke pump for $NaOH_{(aq.)}$ feed**
7. **pH-probe**
8. **Flow control unit for $NaOH_{(aq.)}$**
9. **Swagelok T-piece with overpressure valve**
10. **$N_{2(g.)}$ flow meter**
11. **Connection with thermostat**
12. **Sampling tube of the STR**
13. **Overflow of the STR**
14. **Collecting vessel**
15. **Bottom outlet of the STR**

Figure 6: Photographs of the coprecipitation reactor setup utilized in this work, depicting the overall setup equipment (upper photo, depicted without frame), a higher magnification of the stirred tank reactor (framed by red dashed lines), and a detailed close-up view of the stirred tank reactor (framed by blue dashed lines). The major parts of the setup are labeled by numbers.

The reactants, $MSO_{4(aq.)}$ and $NH_{3(aq.)}$, were conveyed from the respective 2.0 l feed tanks (3a and b, respectively) by membrane pumps (4a and b, respectively; Bischoff, HDP Pump multitherm 200 for $MSO_{4(aq.)}$ and Bischoff, HDP Pump multitherm 3351 for $NH_{3(aq.)}$) through 0.5 mm Teflon tubes to the STR (1). These tubes entered the vessel through the respective feed inlets (5a and 5b). The $NaOH_{(aq.)}$ was conveyed from the respective feed tank (3c) by a cylinder

stroke pump (6; ProMinent, Gamma L), while the flow rate was regulated according to the deviation between the pH-value measured by the pH-probe (7; HA 405-DXK-S8, Mettler Toledo) inside the STR and the pH-setpoint value of a flow control unit (8; ProMinent, Dulcometer). In this regard, the $NaOH_{(aq.)}$ was fed through a 0.5 mm Teflon tube that entered the STR through the respective feed inlet (5c). The $N_{2(g.)}$ stream from the $N_{2(g.)}$ supply line of the laboratory was transported through a 0.5 mm Teflon tube and entered the STR by a Swagelok T-piece with an overpressure valve (9) and could be controlled by a flow meter (10). The temperature inside the STR was monitored by a temperature probe inserted into the STR through the Swagelok T-piece with overpressure valve (9) and its signal was fed back to a thermostat (Hubert, Ministat 125) that was connected to the jacket of the STR that contained the heating fluid (11). This provided temperature control in the vessel. Reaction suspension could be withdrawn from the reactor by a syringe attached to a 0.5 mm Teflon tube for sampling (12), which was inserted into the STR through the Swagelok T-piece with overpressure valve (9). During continuous operation of the STR, reaction suspension could leave the reactor through an overflow (13) and was collected in a container (14). Additionally, the reaction suspension could be collected from the bottom outlet of the STR (15).

For further details about the dimensions of the STR body, the geometry of the employed STR (a) and the corresponding cap of the STR (b) is schematically depicted in Figure 7
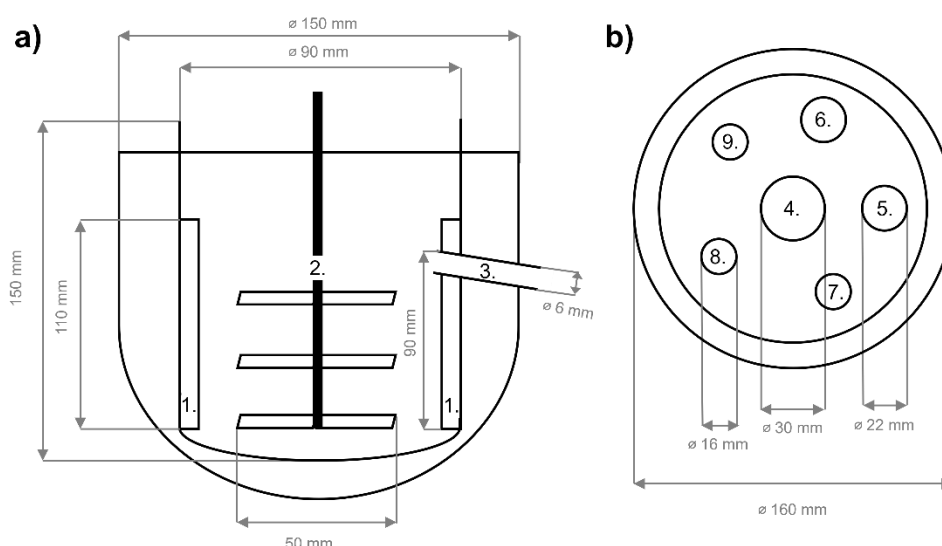
Figure 7: Schematic illustration of the STR cross section (a), and the corresponding STR cap from the top (b). The major parts of the STR and cap are labeled by numbers.

The vessel had an inner diameter of 90 mm, and the outer diameter of the jacket was 150 mm (see Figure 7a). Further, it was equipped with stainless steel baffles with a height of 110 mm (1), with a stainless steel three-stage 45° pitch-blade stirrer with a diameter of 5.0 cm (2), and with an overflow with a diameter of 6 mm located at a height of 90 mm (3). The latter was used to operate the vessel in continuous mode at a reactor volume of 250 ml. During a semi-batch coprecipitation, the overflow hole was closed, and a reactor volume of 480 ml was available. The reactor's lid had a diameter of 120 mm and exhibited six openings (see Figure 7b). The center aperture with a diameter of 30 mm (4) was utilized for fixing the three-stage 45° pitch-blade stirrer. Through one of the two openings with a diameter of 22 mm (5), the pH-probe was inserted, while through the other one the sampling tube, the temperature probe and the $N_{2(g.)}$ inlet tube were inserted by means of a Swagelok T-piece onto which the overpressure valve was installed (6). The feed inlets were placed through the remaining openings of the caps, having a diameter of 16 mm, and positioned 50 mm above the maximum liquid level (7-9). The $MSO_{4(aq.)}$ inlet (7) was located 40 mm from the $NH_{3(aq.)}$ inlet (8) and 80 mm from the $NaOH_{(aq.)}$ inlet (9).

In conclusion, the coprecipitation setup described above allowed to operate coprecipitation reactions in a continuous or in a semi-batch mode, in both cases under a nitrogen atmosphere, while providing a sufficient flow of $NH_{3(aq.)}$ and maintaining constant pH-value (±0.02-0.03).

Troubleshooting while setting up the coprecipitation setup – So far, the preceding discussion dealt with the optimized coprecipitation setup, which provided the experimental basis for this work. However, the process of setting up the coprecipitation facility itself presented diverse technical challenges and had various pitfalls, requiring the optimization of the equipment by trial and error. This was not discussed in the articles presented later in this work and therefore will be briefly addressed in the following.

In a first design of the coprecipitation equipment, it was intended to feed the reactants below the liquid level in a very close proximity to the upper blades of the three-stage 45° pitch-blade stirrer to enable a fast mixing of the reactants as well as to provide reactant dosing in the reactor zone experiencing the highest shear force. While this configuration is viable for larger vessels (>1 l), in smaller setups (<1 l), as employed in this work, it is unfavorable due to the very low absolute volumetric flow rates of the reactants for small STRs such that solid formation occurs at the $MSO_{4(aq.)}$ feed entry, because alkaline reaction suspension is being pushed into the feed inlet of the acidic $MSO_{4(aq.)}$ solution by the turbulent flow in the STR

induced by the mechanical stirring. This leads to plugging of the $MSO_{4(aq.)}$ feed inlet, thus generating pressure loss in the conveying system, which in turn then decreases the effective $MSO_{4(aq.)}$ flow rate and/or brings the feed flow entirely to a stop. Therefore, maintaining constant process conditions would not be possible in this case. Although it is in principle possible to mitigate this issue by decreasing the diameter of the feed tubes, thereby increasing the pressure of the feeds to prevent the backflow of reaction suspension into the feed tube, a tube diameter of 0.5 mm presents already the minimum for commercially available tubes. For larger STRs (>1 l) this problem is rarely encountered, as the absolute volumetric flow rates are intrinsically higher than for smaller STRs (<1 l), even though normalized by the reactor's volume the volumetric flow rates are identical. To overcome the problem, the feed inlets for all reactants were positioned above the liquid level, thus the reactants are dropped onto the surface of the reaction liquid/suspension.

Further, it is critical to avoid dead zones in the geometry of the STR, as these present areas in the reactor which not only suffer from a mixing and/or turbulence deficiency,[172] but in the case the formation of a solid reaction product can result in crystal fouling and the formation of undesired crystal deposits.[84] Both phenomena can lead to process failures, undefined product properties, and/or yield loss. In this work, for the initial design of the STR, the pH-probe was inserted through a concave extension at the side of the STR. However, this zone experienced a lower degree of turbulence compared to the reactor's bulk, which resulted in precipitated pCAM particles being pushed into the extension zone by the turbulent flow but were not pulled out again by the fluid flow throughout the bulk of the reactor. Therefore, the extension zone was quickly burrowed with particles exhibiting undefined properties. Additionally, crystal deposits started forming in this area of the reactor, which eventually were covering the pCAM particles and the pH-probe, so that the pH-probe would lose contact with the reaction suspension. This falsified the pH-value measurement, the therewith associated $NaOH_{(aq.)}$ flow, and eventually process failure occurred. This issue was solved by employing an STR vessel geometry that had no extensions of any sort and by inserting the pH-probe from the top through the cap of the STR.

Additional sensitivity in smaller setups (<1 l) might arise from the oversized proportions of the equipment (e.g., the pH-probe, sampling tube, etc.) compared to the reactor dimensions. A pH-probe inserted into a smaller STR could potentially influence the fluid flow and the turbulence inside the stirred vessel during operation, as the diameter of the pH-probe is relatively large compared to the diameter of the entire vessel. This is substantially less likely in

a larger setup, since the diameter of a pH-probe is significantly smaller than the diameter of a large STR (<1 l), thus this uncertainty can be readily ruled out.

In conclusion, the within the frame of this work developed coprecipitation equipment in its optimized state was well suited to study the pCAM particle formation mechanism. However, if the author would have to set up a coprecipitation equipment again, he would certainly not start below an STR size below 2 l, as this eliminates most of the above-described issues, facilitates troubleshooting, and provides more flexibility of adjusting the entire setup.

2.2 Coprecipitation process operation and control

Before describing the operation of the coprecipitation setup given in section 2.1, the analytical techniques utilized for monitoring the coprecipitation reaction, the determination of the particle size distribution (PSD) by light scattering, the pH-value measurement, and the visual evaluation of the reaction suspension will be discussed.

PSD by light scattering – Since the secondary particle size of a CAM is affected by the secondary particle size of the associated pCAM utilized for the synthesis thereof,[82] a precise control of the pCAM secondary particle size during the coprecipitation reaction is necessary. Further, monitoring the PSD throughout the course of the pCAM coprecipitations grants information about unexpected changes in the PSD, which indicate undesired process changes. This enables the possibility for process and recipe optimization by applying light scattering as a diagnostic tool. Therefore, monitoring the PSD provides indispensable process control.

During light scattering, a dispersion of suspended particles is irradiated by a combination of red and blue light.[173] This results in scattering, diffraction, and absorption of the incoming light, which is captured by a detector. The properties of the detected light, such as the intensity distribution, depend on the size distribution of the suspended particles. Two models for the transformation of the attained optical data into a PSD were examined, namely the Fraunhofer approximation and the Mie theory. As the name suggests, the Fraunhofer approximation can be only considered as an approximative determination of the PSD, since the investigated particles are assumed as opaque discs. This simplified assumption can result in systematic errors, especially for particles $<50\,\mu m$. In contrast, the Mie theory is based on spherical, transparent particles, which improves the accuracy of light scattering for the determination of PSDs in the range of $<50\,\mu m$. However, the application of the Mie theory requires information about the refractive index of the investigated material. Therefore, the Fraunhofer approximation might prove beneficial for the analysis of unknown materials and/or mixtures of different materials.[173]

Since the particle size of CAMs and pCAMs ranges from 2-20 µm, the Mie theory seems to be more suitable for the evaluation of the PSD of CAMs and pCAMs. This was experimentally verified by comparing the PSD attained by light scattering via the Fraunhofer approximation and the Mie theory. For this purpose, dry pCAM powder was homogenously dispersed in H_2O, and a small amount of the particle slurry was transferred into the particle size analyzer (Mastersizer 2000, Malvern Panalytical GmbH) until a light attenuation between 4.0-14.0% was achieved. The respective volume-based particle size distribution was

determined by laser scattering using either the Fraunhofer or the Mie theory. In both cases, a refractive index of 1.33 for H_2O as dispersant was selected, while for the Mie theory a refractive index of 2.19, identical to the refractive index of NiO, was assumed for the $Ni_{0.8}Co_{0.1}Mn_{0.1}(OH)_2$ particles. The intensity of the scattered laser beam was collected as a function of the scattering angle for particle sizes in the range of 0.05-70.0 µm by applying a combination of red and blue light. The resulting PSDs from the different optical models are compared to the PSD determined from a scanning electron microscopy SEM image taken at 1 k magnification of the $Ni_{0.8}Co_{0.1}Mn_{0.1}(OH)_2$ material in Figure 8 (for detailed information about the SEM method, see section 2.3).
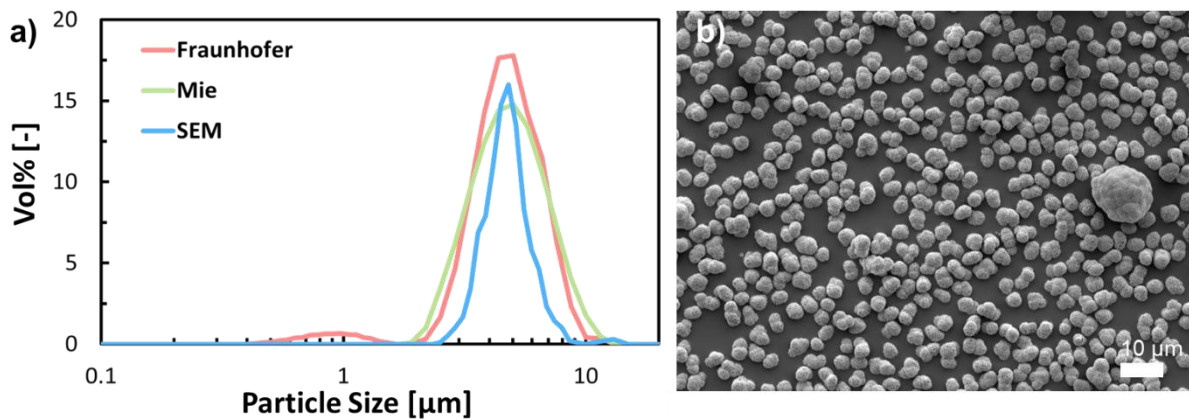
Figure 8: a) Comparison of particle size distributions (PSDs) attained by various techniques for an exemplary sample of $Ni_{0.8}Co_{0.1}Mn_{0.1}(OH)_2$ particles. The shown PSDs were obtained by light scattering using either the Fraunhofer approximation (red) or the Mie theory (green) or PSD obtained by manual determination of the particle size distribution from a b) SEM image of $Ni_{0.8}Co_{0.1}Mn_{0.1}(OH)_2$ particles taken at 1 k magnification by application of image J[174] (blue). (For detailed information about the SEM method, see section 2.3).

The PSD determined by light scattering based on the Fraunhofer approximation yields a bimodal PSD with a small modal in the particle size range of 0.4-1.5 µm and a large modal in the range of 3.4-12.0 µm. By comparison, the PSD determined by light scattering employing the Mie theory is monomodal agrees well with the monomodal PSD determined by SEM imaging. Since the small particles corresponding to modal in the range of 0.4-1.5 µm in the Fraunhofer based PSD are absent in the SEM image, this small modal is clearly an analysis artefact. Hence, the Fraunhofer approximation is inappropriate for the determination of pCAM PSDs by light scattering. Hackley et al. observed a similar artefact in their analysis of aluminum

oxide powders by light scattering, where the application of the Fraunhofer model yielded an apparent modal of particles in the submicron meter range, which were not existent.[173] In light of these results, the Mie theory was utilized as model for the evaluation of the PSD of pCAMs by light scattering.

When conducting a PSD analysis of reaction suspension samples from the operating STR containing mother liquor and $Ni_{0.8}Co_{0.1}Mn_{0.1}(OH)_2$ particles, the slurry was cooled down to room temperature prior to the measurements. The PSD was then determined by light scattering by applying the Mie theory. Based on three measurements per sample, the average volume-based percentile particle sizes d_{10}, d_{50}, and d_{90} were determined. The span σ was calculated according to the following equation.

$$\sigma = \frac{d_{90} - d_{10}}{d_{50}} \tag{7}$$

pH-value measurement – Besides light scattering for the determination of the PSD of the $Ni_{0.8}Co_{0.1}Mn_{0.1}(OH)_2$ pCAM particles inside the STR during the coprecipitation reaction, another essential tool for process control is measuring the pH-value of the sampled reaction suspension. The pH-value is defined as the negative decadic logarithm of the proton concentration. The higher the pH-value of a liquid, the lower is its proton concentration and in turn the higher is its OH⁻ concentration. Monitoring the pH-value during the coprecipitation reaction was performed in-situ and ex-situ. The installed internal pH-probe was employed for monitoring the pH-value at reaction temperature inside the STR, while the external pH-probe (InLab® SemI MIcro, Mettler Toledo) was used for measuring the reference pH-value at 23 °C by cooling the sampled reaction suspension down to 23 °C in a water bath for 5 min prior to the measurement. The external pH-electrode was calibrated at 23 °C, while the internal was calibrated at the applied reaction temperature, in both cases utilizing buffer solutions ($pH_{23\,°C} = 7.0$, $pH_{23\,°C} = 12.0$, Certipure, Merck KGaA).

Alternatively, a facile acid titration method can be employed for the determination of the OH⁻ concentration. For this purpose, the precipitated particles must be separated from the collected reaction suspension and the resulting solid-free mother liquor can then be titrated with an acid such as $HCl_{(aq.)}$. This approach proves especially beneficial for pH-values >12.7, where the so-called alkaline error can falsify the pH-probe measurement.[175] Additional error sources such as the falsification of the measured pH-value by changes in ionic strength and/or aging of the pH-

probe during the coprecipitation reaction can also be excluded by acid titration. The latter therefore gives more accurate information compared to a simple pH-value measurement but is more time consuming. Further, acid titration of mother liquor can be combined with Kjeldahl digestion[176] for monitoring the $NH_{3(aq.)}$ concentration during the coprecipitation as well as for deconvoluting the overall OH^- concentration into free OH^- and OH^- originating from $NH_{3(aq.)}$.

Visual evaluation of the reaction suspension – While a simple observation with the bare eye certainly does not allow to monitor the coprecipitation process in a quantitative manner, it can provide indirectly a qualitative information about the gaseous atmosphere inside the STR and the $NH_{3(aq.)}$ concentration in the mother liquor.
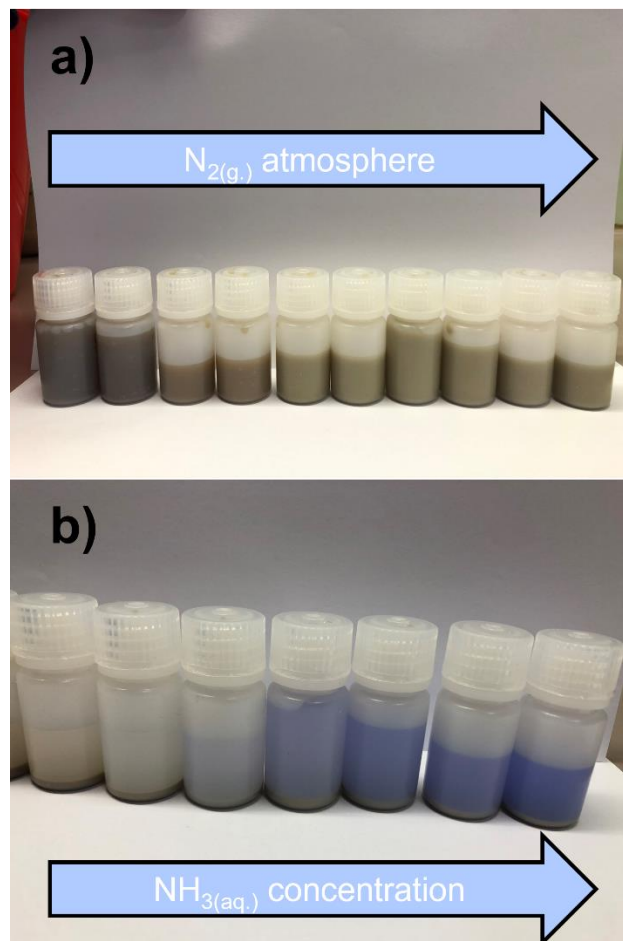
Figure 9: a) Illustration of the impact of the atmosphere inside the STR on the undesired oxidation of Mn^{2+} in $Ni_{0.8}Co_{0.1}Mn_{0.1}(OH)_2$, showing the coloring of the coprecipitated solid for a coprecipitation reaction where the initial $O_{2(g.)}$ atmosphere was gradually exchanged by a $N_{2(g.)}$ atmosphere. Note that the reaction suspension samples were homogenously suspended before taking the photo. (b) The influence of the $NH_{3(aq.)}$ concentration on the formation of the $[Ni(NH_3)_x]^{2+}_{(aq.)}$ complex that colors the mother liquor progressively blue with increasing $NH_{3(aq.)}$ concentration (here being increased from 0.0 mol/l to 0.7 mol/l). Note that the sampled reaction suspension the solid was allowed to settle before taking the photos.

In general it is desirable to prevent the oxidation of $Mn(OH)_{2(s.)}$ to $MnOOH_{(s.)}$ and/or $MnO_{2(s)}$ in the precipitated $M(OH)_{2(s.)}$ is prevented by conducting the coprecipitation reaction under inert atmosphere, typically $N_{2(g.)}$.[56, 127] Since $MnOOH_{(s.)}$ is a light brown solid and $MnO_{2(s)}$ is a dark brown/black solid while $Mn(OH)_{2(s.)}$ is a cream-colored/white solid,[27] the former two turn a mixed $NiCoMn(OH)_{2(s.)}$ precipitate brown/black (strictly speaking, it is no longer a pure hydroxide but rather an oxyhydroxide); on the other hand, while the hydroxide of Mn does not affect the intrinsically green color of $NiCoMn(OH)_{2(s.)}$, which originates from $Ni(OH)_{2(s.)}$.[177] Therefore, if the precipitated solid inside the reactor exhibits a brown color even though the coprecipitation reaction was conducted under a nominally inert atmosphere, this indicates that an inert atmosphere was not successfully established (e.g., due to a leak in the STR and/or the $N_{2(g.)}$ flow tube, etc.) and the oxidation of Mn^{2+} in the $M(OH)_{2(s.)}$ precipitate must have occurred inside the STR. This is exemplarily demonstrated in Figure 9a.

If the coprecipitation reaction of a Ni containing $NiCoMn(OH)_{2(s.)}$ is practiced in the presence of $NH_{3(aq.)}$, the complexation of $Ni^{2+}_{(aq.)}$ occurs, which results in the formation of an ammonia-nickel complex $[Ni(NH_3)_6]^{2+}_{(aq.)}$. The appearance of this complex colors the aqueous mother liquor blue.[178] Therefore, if $M(OH)_{2(aq.)}$ is precipitated at medium to high $NH_{3(aq.)}$ concentrations, a blue coloring of the mother liquor indicates the presence of $NH_{3(aq.)}$. This means in turn that the lack of a blue color at medium to high $NH_{3(aq.)}$ concentrations must be due to a loss of NH_3 from the reaction mixture (e.g., due to excessive $N_{2(g.)}$ flow removing NH_3 from the aqueous phase, etc.). This is exemplarily shown in Figure 9b. Based on the strong color of the $[Ni(NH_3)_6]^{2+}_{(aq.)}$ complex, the Ni^{2+} concentration can be also quantitatively determined by colorimetric determination.[178]

Coprecipitation process operation – The coprecipitation of pCAM particles in an STR can be generally conducted in a semi-batch or in a continuous mode, also referred to as continuous stirred tank reactor CSTR. The fundamental differences between both operational styles are schematically illustrated in Figure 10.
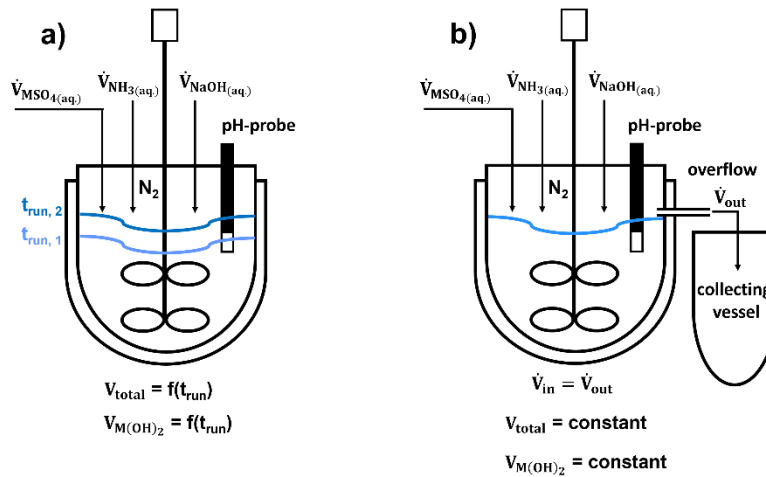
Figure 10: Schematic illustration of STR setups for the two major process operation modes for pCAM coprecipitation. a) Semi-batch and b) continuous operation (continuously stirred tank reactor, CSTR). During semi-batch operation, the reaction volume and therefore the coprecipitated $M(OH)_2$ volume and mass are a function of the batch run time t_{run}. In contrast, during continuous operation, the reaction volume and therefore the total coprecipitated $M(OH)_2$ volume and mass inside the reactor remain constant due to the overflow that enables a steady flow of reaction suspension leaving the reaction vessel.

During semi-batch operation (see Figure 10a), reactants are continuously added, while the reaction suspension is unable to leave the stirred vessel. This results in a steady increase of the total reaction volume V_{total} and of the volume of the formed $M(OH)_2$ $V_{M(OH)2}$ with progressing batch run time t_{run}. In contrast, during continuous operation (see Figure 10b), the summed-up volumetric flow rates of reactants $\dot{V}_{in}$ equals the volumetric flow rate of reaction suspension leaving the system $\dot{V}_{out}$ via the overflow. Thus, V_{total} and $V_{M(OH)2}$ remain constant throughout the process. The operation mode applied in this work was the semi-batch operation.

Prior to initiating a semi-batch coprecipitation, the free overflow of the STR was closed. The reactor atmosphere was then rendered inert with $N_{2(g)}$, charged with deionized H_2O, and $NH_{3(aq.)}$ was added to achieve the desired starting liquid volume and $NH_{3(aq.)}$ concentration in the reactor. The reaction temperature, the pH-value, and the stirring speed were set to the desired values. The reaction was then initiated by simultaneously feeding $MSO_{4(aq.)}$ and $NH_{3(aq.)}$ into the reactor, while the $NaOH_{(aq.)}$ flow was controlled by the mass-flow control unit linked to the internal pH-probe to maintain a constant pH-value throughout the reaction. In desired time intervals, the reaction progress was controlled by withdrawing reaction suspension from the reactor, cooling it to 23 °C, measuring the pH-value at 23 °C and determining the PSD of the precipitated solid by laser scattering. After a desired t_{run}, the reactant flows were stopped, the obtained product suspension was collected, filtered, washed with H_2O in a 10:1 weight ratio

of H_2O to precipitate and dried in air at 120 °C for 12 h in an oven (Universal Oven U, Memmert). The STR was cleaned between runs with diluted $H_2SO_{4(aq.)}$ at 55 °C and at a stirring speed of 1500 rpm for 10 min. This was repeated for additional three times by employing deionized H_2O instead of $H_2SO_{4(aq.)}$.

Tracking the development of the average volume-based percentile particle sizes d_{10}, d_{50}, and d_{90} over time as well as the pH-value during the semi-batch coprecipitation allows to monitor the progress of the coprecipitation reaction. This provides not only control of the product's physical properties such as the particle size, but also enables the possibility for process and recipe optimization.

2.3 Scanning electron microscopy

The morphological structure of particles has a significant impact of an NCM CAM on the efficiency in the field of application (e.g., on the electrochemical performance)[67, 82] as well as the processing thereof.[84] In this work, the morphology of coprecipitated $Ni_{0.8}Co_{0.1}Mn_{0.1}(OH)_2$ pCAM particles was characterized by scanning electron microscopy (SEM). This technique allows to visualize particles and to qualitatively evaluate the physical properties of particles such as secondary particle size,[43, 114] primary particle size,[127] orientation of primary particles,[91] secondary particle sphericity,[43, 114] porosity,[127] and/or the homogeneity within and/or between particles.[60] Additionally, some of these characteristics can be quantified from SEM images by analysis of a statistically representative number of particles and/or images via manual and/or automatic image analysis tools.[61, 82]

The samples for top view SEM imaging were prepared by fixing pCAM powder onto a SEM pin holder (Agar Scientific, Ltd.) that was covered with conducting carbon (Plano GmBH). Subsequently, a 6 nm platinum layer was coated on top of the sample by sputter deposition (SCD 500 Sputter Coater, Bal-Tec AG). The samples for cross section (CS) measurements were prepared by mixing 2 g of epoxy resin, 0.5 g of epoxy hardener (Buehler, ITW Test & Measurement GmbH) and adding a few drops of the blend to the respective pCAM powder in a gelatine capsule. The resulting suspension was cast onto an Al-foil using a manual coater with a gap size of 0.5 mm and then dried in an oven at 40 °C overnight. Small sections of the coated foil were transferred to an ion milling system (ArBlade 5000, Hitachi, Ltd) equipped with an Ar ion beam at an operating voltage of 6 kV. The SEM imaging was performed applying a thermal field emission cathode and an Everhat-Thornley secondary electron detector at an operating voltage of 5 kV (Ultra 55, Carl Zeiss Ag).

In section 3.1.1, quantitative information about circularity as indicator for sphericity of precipitated $Ni_{0.8}Co_{0.1}Mn_{0.1}(OH)_2$ pCAM particles was determined from SEM top view images by employing a segmentation model. The SEM images were taken at 1 k magnification and for each sample the circularity of approximately 80-100 particles was determined. The algorithm implemented for the automated image segmentation is based on a U-Net architecture neural network.[179] The proportions of the SEM image (such as lengths/areas) were captured in the dimension of pixels, which after the segmentation were converted back by applying a calibration factor from the image metadata. To increase the accuracy of the segmentation, the regions adjacent to the boundary of the image were rejected, since particles in this region might not be fully captured. Further, only particles were considered, which exhibited an area of above

200 pixels and a compactness (ratio between the particle's area and its convex hull) of ≥ 0.8. These filters ascertained that only particles that did not deviate excessively from a spherical shape were recognized. By two-dimensional approximation of particles, the circularity C of segmented particles that fulfilled the aforementioned criteria was then calculated according to the isoperimetric quotient, which is defined as.[180]

$$C = \frac{A_{particle}}{A_{eq.\ circle}} = \frac{4\pi A_{particle}}{P_{particle}^2} \tag{8}$$

where $A_{particle}$ is the area of the segmented particle based on a 2D projection of the particle, and $A_{eq.\ circle}$ is the area of a circle exhibiting the same equivalent perimeter $P_{particle}$ as the particle (C equals one for a perfect circle).

On average, 60-100 particles per $Ni_{0.8}Co_{0.1}Mn_{0.1}(OH)_2$ pCAM sample were analyzed. The validity of the segmentation model was verified by comparing algorithm-based circularity distributions of selected samples to distributions attained by manual segmentation via ImageJ,[174] which is exemplarily given in Figure 13.
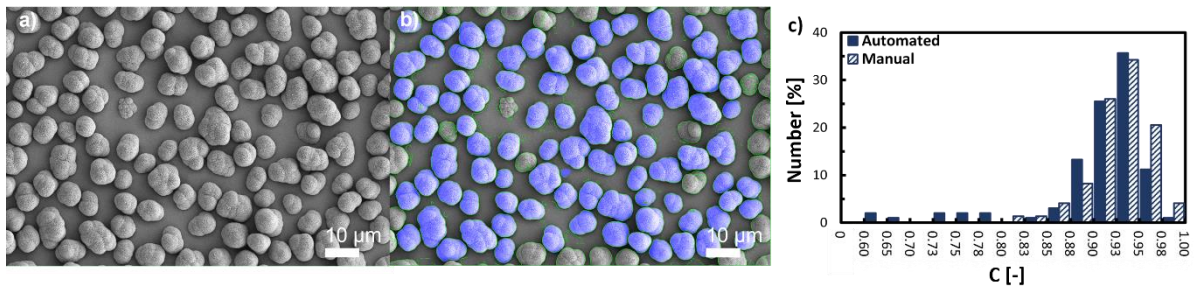
Figure 13: Quantification of particle circularity C as descriptor for the sphericity of $Ni_{0.8}Co_{0.1}Mn_{0.1}(OH)_2$ secondary particles by SEM image analysis. An exemplary top view SEM image at 1 k magnification of $Ni_{0.8}Co_{0.1}Mn_{0.1}(OH)_2$ secondary particles is shown a) before and b) after automated secondary particle segmentation. The segmented particles are highlighted with a blue overlay. c) Comparison of the corresponding number-based circularity distribution of $Ni_{0.8}Co_{0.1}Mn_{0.1}(OH)_2$ secondary particles determined by automated (filled) and manual segmentation (unfilled).

The identified secondary particles for which C was determined are encircled in green and are depicted with a blue overlay, while particles that were identified but were not considered by the model due to the employed filters are only encircled in green. Solely minor deviations can be observed when comparing the attained distributions by manual and automated segmentation (Figure 12c) for secondary particles exhibiting nearly perfect circularity (C > 0.95) and for rather non-circular particles (C < 0.80). The discrepancy for C > 0.95 might be ascribed to circular secondary particles which were not considered by the algorithm due to local brightness inhomogeneities across the secondary particle structure that results in a blending with the background brightness. The discrepancy for C < 0.80 might be due to improper segmentation of overlapping secondary particles by the model, which results in an underestimation of C for the particle being overlapped. These overlapped particles were not considered during manual segmentation. Overall, however, this amounts to an insignificant discrepancy of merely 2% when comparing the number median circularity C_{50} determined from C distributions obtained by both methods (data not shown). Therefore, it is demonstrated that reasonable results can be obtained by algorithm-based determination of secondary particle circularity as indicator for particle sphericity from SEM images.

Further, in section 3.1.1, the size of the secondary particle core was manually determined from CS-SEM images of $Ni_{0.8}Co_{0.1}Mn_{0.1}(OH)_2$ secondary particles at various magnifications by applying ImageJ.[174] Only those cross-sectionally sliced secondary particles were considered for which the particle core was readily exposed, as this ensures that the secondary particle was cut through its center. The corresponding equivalent diameter ($d_{eq.}$) of a circle with identical area as the determined area of the core ($A_{segm.\ area}$) was calculated according to the following.

$$d_{eq.} = 2\sqrt{\frac{A_{segm.\ area}}{\pi}} \qquad (9)$$

The area of approximately 50 secondary particle centers per $Ni_{0.8}Co_{0.1}Mn_{0.1}(OH)_2$ sample was determined. From the resulting $d_{eq.}$, volume-based PSD were derived. This approach is exemplarily displayed in Figure 14.
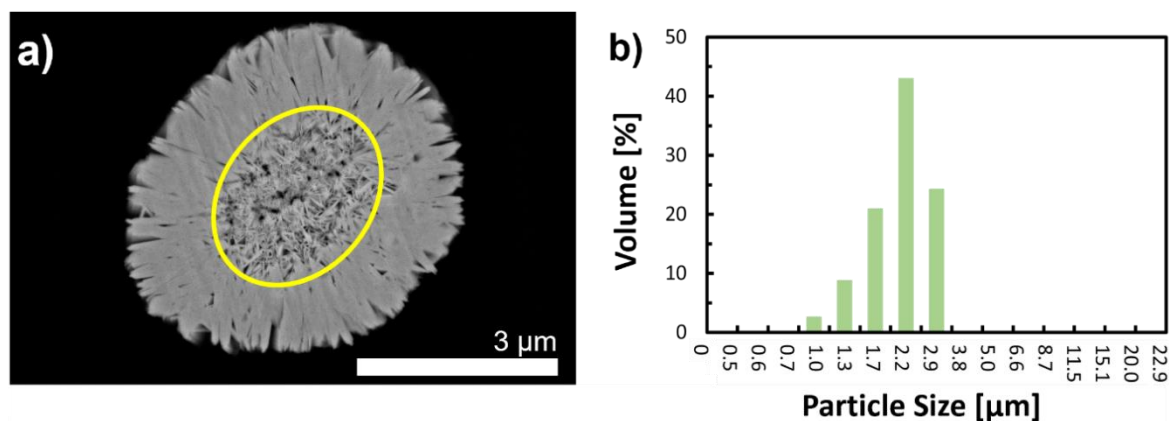
Figure 14: a) Exemplary CS-SEM image of a cross-sectionally sliced $Ni_{0.8}Co_{0.1}Mn_{0.1}(OH)_2$ secondary particle taken at 15 k magnification. The secondary particle center is encircled in yellow, illustrating how the particle core size was determined by SEM image segmentation via ImageJ.[174] b) Corresponding volume-based particle size distribution of $Ni_{0.8}Co_{0.1}Mn_{0.1}(OH)_2$ secondary particle centers obtained by the analysis of approximately 50 secondary particles by SEM image segmentation and determination of the size of the secondary particle center.

In section 3.1.2, the vertical size of primary particles was manually determined from top view SEM images of $Ni_{0.8}Co_{0.1}Mn_{0.1}(OH)_2$ secondary particles taken at 50 k magnification applying ImageJ software.[174] In this case, only primary particles were considered for which the vertical size was perpendicularly exposed, since the curvature of the spherical secondary particle could falsify the determined vertical primary particle size. Overall, the vertical size of 100 primary particles per $Ni_{0.8}Co_{0.1}Mn_{0.1}(OH)_2$ sample and average values formulated. This approach is exemplarily visualized in the SEM image shown in Figure 14, including the thereby attained vertical primary particle size distribution.
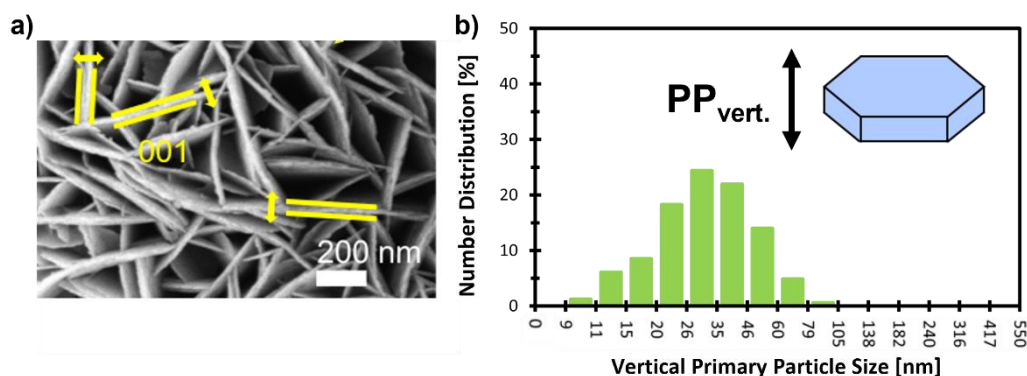
Figure 15: a) Exemplary SEM image of a $Ni_{0.8}Co_{0.1}Mn_{0.1}(OH)_2$ secondary particle taken at 50 k magnification. The yellow bars exemplarily depict the analyzed vertical primary particle size ($PP_{vert.}$) for selected primary particles via ImageJ.[174] b) Corresponding formulated number distribution histogram of vertical primary particle size in a $Ni_{0.8}Co_{0.1}Mn_{0.1}(OH)_2$ secondary

particle obtained by analysis of approximately 100 primary particles by SEM image segmentation.

In summary, SEM imaging is a valuable method to attain visual insights into a particle-based system and for the formulation of initial conclusions. Further, the observed qualitative trends can be quantitatively validated by image analysis. However, in some cases it might prove difficult to quantify physical properties of particles such as the specific surface area SSA or the porosity of particles. Therefore, SEM imaging can be complemented with a quantitative technique such as light scattering for PSD analysis or nitrogen physisorption for SSA and porosity analysis. The latter will be discussed in the subsequent section.

2.4 Nitrogen physisorption

Physical properties of particles such as the SSA and porosity are important characteristics for a wide range of material classes. Both properties can be determined by physisorption. This method is based on the physical adsorption of a fluid, typically an inert gas, (commonly referred to as adsorptive) on the interfacial region of a solid (commonly referred to as adsorbate) due to van der Waals interaction.[181] The most commonly employed adsorptive during physisorption is N_2, while other gases such as krypton can be applied if an exceptionally high accuracy is necessary.[82, 182] Typically, the adsorption is conducted at a constant temperature. Thus, the amount of gas adsorbed on the solid directly correlates with the equilibrium pressure of the gas, which can be expressed in the form of a sorption isotherm.[181] In section 3.1.1 and 3.1.2, N_2 physisorption was conducted by degassing the $Ni_{0.8}Co_{0.1}Mn_{0.1}(OH)_2$ powders at 120 °C for three hours and subsequently measuring N_2 physisorption isotherms at 77 K (ASAP2420, Micromeritics) for the quantification of the SSA and intra-particle porosity of $Ni_{0.8}Co_{0.1}Mn_{0.1}(OH)_2$ secondary particles. Figure 15 depicts exemplarily N_2 isotherms obtained for a porous and a dense $Ni_{0.8}Co_{0.1}Mn_{0.1}(OH)_2$ secondary particle powder. The volume of adsorbed N_2 ($V_{N2,ads}$) at standard temperature and pressure STP (273.15 K and 101325 Pa) is normalized to the sample mass, while the relative pressure p/p_0 corresponds to the actual gas pressure divided by the saturation vapor pressure of N_2 at 77 K. The obtained isotherms in Figure 15, both for the dense and porous material, can be classified as type IV isotherms. These exhibit a characteristic hysteresis feature corresponding to the gap between the adsorption and desorption isotherm, which is attributed to capillary condensation of $N_{2(g.)}$ into the mesoporous network of the sample.[181]

The SSA of particles in a powder can then be extracted from the obtained adsorption isotherm based on the Brunauer-Emmet-Teller (BET) model, which relies on the principle of multilayer adsorption. A linear fit of the adsorption data points in the range of $0.05 \leq p/p_0 \leq 0.20$-$0.30$ (see Figure 16) by applying the relationship $1/(V_{N2,ads} (p_0/p\text{-}1))$ against p/p_0 allows to determine the BET SSA.[181] The appropriate particle size corresponding to the SSA can then be calculated by using a spherical approximation of the particles if the density of the investigated material is known. Likewise, SSAs can be estimated if the particle size (secondary particle SSA and/or primary particle SSA, respectively) of the evaluated particle was determined by a complementary technique such as light scattering and/or SEM imaging, again using a spherical approximation.[67, 82]
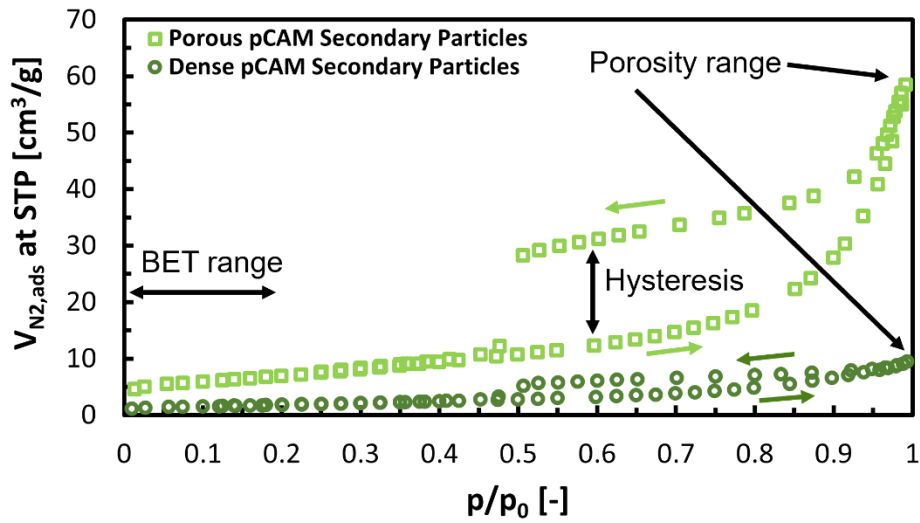
Figure 16: Exemplary adsorption and desorption isotherms for a pCAM with porous (squares, light green) or a pCAM with dense $Ni_{0.8}Co_{0.1}Mn_{0.1}(OH)_2$ secondary particles (circles, dark green) obtained by N_2 physisorption. The relevant relative pressure ranges p/p_0 for the determination of the SSA and for the intra-particle porosity are indicated by arrows and denoted as "BET range" and "Porosity range", respectively. Further, the adsorption hysteresis between the adsorption and desorption isotherm is highlighted for the porous material. Here, the dense $Ni_{0.8}Co_{0.1}Mn_{0.1}(OH)_2$ pCAM exhibited a BET SSA of 6.7 m^2/g and intra-particle porosity of 5.5%, while the porous $Ni_{0.8}Co_{0.1}Mn_{0.1}(OH)_2$ pCAM exhibited a BET SSA of 24.8 m^2/g and intra-particle porosity of 26.4%.

If the vapor pressure of a gas exceeds its saturation vapor pressure at any given temperature, a phase transition from gas to liquid occurs. However, gas can also readily liquify below the saturation vapor pressure by capillary condensation. This phenomenon can be utilized during N_2 physisorption for the determination of the porosity in materials, since at high relative pressure ranges p/p_0-values N_2 intrudes into the pores of the investigated material by capillary condensation. In this context, the Kelvin radius r_K describes the maximum pore size accessible by N_2 liquefaction at a given relative pressure and is given by the Kelvin equation.[183]

$$r_K = \frac{-2 \, \gamma \, V_{N2,m}}{R \, T \, \ln\left(\frac{p}{p_0}\right)} \tag{10}$$

where γ is the surface tension of liquid N_2 at 77 K ($= 8.85 \times 10^{-7}$ J/cm^2), $V_{N2,m}$ is the molar volume of liquid N_2 ($= 34.7$ cm^3/mol), R is the gas constant ($= 8.314$ J/(mol K)), and T is the boiling point of nitrogen ($= 77$ K).

For a relative pressure of $p/p_0 \geq 0.995$ (see Figure 16), N_2 liquefaction occurs in pores with a diameter below 380 nm. From the SEM image shown in Figure 15a, the pore size within the $Ni_{0.8}Co_{0.1}Mn_{0.1}(OH)_2$ secondary particle structure was estimated to be <200 nm. Therefore, the porous structure of the $Ni_{0.8}Co_{0.1}Mn_{0.1}(OH)_2$ secondary particles investigated in this work will be filled with liquid N_2 at a relative pressure of $p/p_0 = 0.995$, which allows the determination of the secondary particle porosity. The specific liquid volume condensed in the pores can then be determined by the following equation.[181]

$$V_{N2,liquid} = V_{N2,ads} \cdot \frac{\rho_{N2,STP}}{\rho_{N2,liquid}} \tag{11}$$

where $V_{N2,liquid}$ is the specific liquid N_2 volume intruded into the particles pores, $V_{N2,ads}$ is the total amount of the measured adsorbed N_2 at a relative pressure of $p/p_0 \approx 0.995$, $\rho_{N2,STP}$ is the density of N_2 at standard temperature 273.15 K and pressure 101325 Pa ($= 1.25$ mg/cm^3), and $\rho_{N2,liquid}$ is the density of liquid N_2 at 77 K ($= 0.809$ g/cm^3).

At relative pressure ranges of $p/p_0 \approx 0.995$, the determined intrusion volume of N_2 was entirely allocated to intra-particle porosity ε_{intra}, which then can be calculated according to the following expression.[184]

$$\varepsilon_{intra} = \frac{V_{N2,liquid}}{V_{N2,liquid} + \dfrac{1}{\rho_{cryst.}}} \tag{12}$$

where $\rho_{cryst.}$ is the crystallographic density of the investigated compound. In the case of $Ni_{0.8}Co_{0.1}Mn_{0.1}(OH)_2$, a molar averaged crystallographic density of 3.96 g/cm^3 was assumed,

based on the crystallographic density of Ni(OH)$_2$ (= 4.1 g/cm^3), Co(OH)$_2$ (= 3.6 g/cm^3) and Mn(OH)$_2$ (= 3.26 g/cm^3) and considering the transition metal ratio of 8/1/1.

Alternatively, the intra-particle porosity in powders can be determined by mercury intrusion porosimetry. While this method is very accurate, it suffers from the drawbacks of destroying the sample as well as of the toxicity of mercury. Further, the mechanical stability of the investigated material must be considered, since the intrusion of mercury into the porous network requires the application of an external pressure. This may alter the physical properties of the investigated sample and/or even destroy it during investigation, which may result in either non-representative and/or non-meaningful results. Therefore, N$_2$ physisorption provides a simple technique for the characterization of the intra-particle porosity in powders with a pore size domains of ≤380 nm,[185] which can be conveniently determined directly during the evaluation of the SSA of materials.

2.5 Further techniques

In the following, additional methods that were utilized in this work for material characterization are summarized. The metal composition in coprecipitated $Ni_{0.8}Co_{0.1}Mn_{0.1}(OH)_2$ particle powders as well as the content of impurities derived from the coprecipitation reaction was investigated in section 3.1.2. The Ni-, Co-, and Mn-content in coprecipitated pCAM was determined by ICP-OES. The S- and C-impurity content was investigated by catalytic combustion methods, while the N-impurity content was determined by a modified Kjeldahl digestion method.[176] The microstructural properties of synthesized $Ni_{0.8}Co_{0.1}Mn_{0.1}(OH)_2$ powders was investigated by PXRD in section 3.1.2, while applying by applying the Scherrer equation and using the DIFFRAC.EVA V6 software (Bruker AXS GmbH) for the determination of the crystallite sizes.[186] To visualize the degree of layer orientation on an atomic level in the crystals of synthesized $Ni_{0.8}Co_{0.1}Mn_{0.1}(OH)_2$ powders, HR-TEM was utilized in Section 3.1.2.

3 Results

The following chapter presents two published studies. The journal articles address the particle formation and growth mechanism during the coprecipitation reaction of Ni-rich pCAM, investigating distinctive coprecipitation-process-parameter-product-property relationships.

Section 3.1.1 demonstrates that the formation of $Ni_{0.8}Co_{0.1}Mn_{0.1}(OH)_2$ secondary particles during the coprecipitation reaction is governed by a two-stage mechanism comprising the generation of secondary particle agglomerates, which subsequently increase in size by crystal growth of distinctive primary particles. In this context, the degree of turbulence, controllable by the stirring speed, regulates the number and size of agglomerates formed during seeding, which in turn dictates the growth rate and sphericity of secondary particles.

In section 3.1.2, a pH-dependent SO_4^{2-} adsorption equilibrium during the coprecipitation reaction of $Ni_{0.8}Co_{0.1}Mn_{0.1}(OH)_2$ was identified, which determines the SO_4^{2-} uptake in $Ni_{0.8}Co_{0.1}Mn_{0.1}(OH)_2$, the crystallinity, and the vertical size of primary particles affecting the secondary particle porosity. Further, the implications of other anion systems (acetate CH_3COO^- and nitrate NO_3^-) on the secondary particle morphology due to distinctive anion adsorption affinities can be well understood based on the Fajans-Paneth-Hahn law for crystallization.[187]

3.1 Particle size distribution and secondary particle sphericity

This section presents the article "Investigation of Particle Formation Mechanism during Coprecipitation of Ni-rich Hydroxide Precursor for Li-Ion Cathode Active Material". The manuscript was submitted to the peer-reviewed Journal of the Electrochemical Society in August 2023 and published in November 2023. The article is published open access and distributed under the terms of the Creative Commons Attribution 4.0 License. The permanent web link is: https://iopscience.iop.org/article/10.1149/1945-7111/ad050b/meta. A summary of the article was presented by Rafael B. Berk as oral presentation (abstract number A02-0485) at the 243rd Meeting of the Electrochemical Society in Boston, Massachusetts, May 28th–June 2nd, 2023.

Layered lithium nickel cobalt manganese oxides (NCMs) are commercially employed as cathode active material (CAM) in lithium-ion battery applications for electric vehicles because NCMs can provide a sufficient driving range on a single charge at competitive costs.[5, 13] Current industrial manufacturing of NCMs is practiced by coprecipitation of mixed metal hydroxide ($M(OH)_2$) particles (M consisting mainly of Ni, Co, and Mn) as precursor for the preparation of a CAM (referred to as pCAM), which is afterwards fired with a lithium compound at high temperatures to afford the NCM product.[5, 43, 56] Thereby, the secondary particle structure of the pCAM is transferred to the CAM.[68, 70-72] In general, the physical properties such as the particle size, uniformity, and sphericity significantly affect the fluidity of powders. With decreasing particle size and uniformity as well as with a deviation from a spherical particle shape, the fluidity of powders suffers.[84-89] However, an effortlessly fluent form of the pCAM and CAM powders is essential for their industrial-scale production in order to prevent clogging of the powders in the technical equipment, which implicates frequent cleaning and/or extra pulverization between process steps to upheld powder fluidity. Both is expensive and impinges the production throughput.[84] Thus, a detailed understanding of the $M(OH)_2$ particle formation mechanism during the coprecipitation reaction allows to adjust the physical properties of the pCAM and CAM powders that are required for an economical manufacturing of NCMs.

In this work the particle development during the semi-batch coprecipitation reaction of $Ni_{0.8}Co_{0.1}Mn_{0.1}(OH)_2$ pCAM particles in a stirred tank reactor at different stirring speeds was studied. Thereby, independent of the applied stirring condition, a two-stage particle formation mechanism is identified. By means of light scattering, it is shown that during the initial seeding phase, the particle number increases at stagnating particle size, whereas in the ensuing growth

phase the particle size increases linearly with the third root of reaction time. Examination of the developing particle morphology by SEM imaging revealed that during the seeding phase aspherical secondary particle agglomerates are generated, which were enlarged in the growth period by the lateral crystal growth of distinctive plate-like shaped primary particles. This growth behavior leads to a progressive enhancement of the secondary particle sphericity with run time, which was quantified by extracting the secondary particle circularity distributions from SEM images. Additional evidence for a two-step particle formation mechanism was discovered by identification of core-shell secondary particle structures via SEM imaging of cross-sectionally sliced $Ni_{0.8}Co_{0.1}Mn_{0.1}(OH)_2$ secondary particles gathered after the completed coprecipitation reaction. Furthermore, it is demonstrated that the extent of turbulence, controllable by the stirring conditions, dictates the number and size of initial agglomerates formed during the seeding stage at otherwise constant process parameters. This governs the average growth rate and the ability of secondary particles to become spherical over the reaction time. In the end, the proposed two-stage particle formation mechanism consisting of agglomeration and polycrystallisation is juxtaposed to mechanisms reported in the literature.

Author contributions

R.B.B. carried out the coprecipitation experiments, the processing of data from analytical measurements as well as the calculations. All authors discussed and commented the data, as well as the conclusions. R.B.B. wrote the manuscript. T.B., L.M., and H.A.G. edited the manuscript.

Investigation of the Particle Formation Mechanism during Coprecipitation of Ni-Rich Hydroxide Precursor for Li-Ion Cathode Active Material

Rafael B. Berk,[1,2,*] Thorsten Beierling,[3] Lukas Metzger,[4] and Hubert A. Gasteiger[2,*]

[1] BASF SE, New Battery Materials and Systems, D-67056 Ludwigshafen, Germany
[2] Chair of Technical Electrochemistry, Department of Chemistry and Catalysis Research Center, School of Natural Sciences, Technical University of Munich, D-85748 Garching, Germany
[3] BASF SE, Battery Materials Process Technology, D-67056 Ludwigshafen, Germany
[4] BASF SE, Crystallization and Coprecipitation, D-67056 Ludwigshafen, Germany

Industrial production of cathode active material (CAM) for lithium-ion batteries is conducted by coprecipitation of a hydroxide $(Ni_xCo_yMn_z(OH)_2)$ precursor (referred to as pCAM) in a stirred tank reactor and subsequent high-temperature calcination of the pCAM with a lithium compound. The physical properties of the resulting CAM are significantly affected by the associated pCAM utilized for synthesis. For an economical manufacturing of pCAM and CAM, the pCAM particle size and sphericity during the coprecipitation reaction must be precisely controlled, requiring an in-depth understanding of the $Ni_xCo_yMn_z(OH)_2$ particle formation mechanism. Therefore, the development of the secondary particle size and morphology throughout the semi-batch coprecipitation of $Ni_{0.8}Co_{0.1}Mn_{0.1}(OH)_2$ at various stirring speeds was monitored by light scattering and SEM imaging, respectively. A two-stage particle formation mechanism was identified: In the initial seeding phase, irregular-shaped secondary particles agglomerates are formed, which in the subsequent growth phase linearly increase in size with the third root of time, governed by the growth of individual primary particles. Thereby, the degree of turbulence governs the initial agglomerate size and number formed during seeding, which dictates the growth rate and the secondary particle sphericity. Finally, the proposed particle formation mechanism is compared to mechanisms prevailing in the literature.

Layered lithium nickel cobalt manganese oxides $(LiNi_xCo_yMn_zO_2$, with $x + y + z = 1$ (NCMs)) are commercially employed as cathode active material (CAM) in lithium-ion battery (LiB) applications for electric vehicles, satisfying the demand for a long driving-range on a single charge due to their high energy density.[1,2] Currently, the industrial production of CAMs comprises two major synthesis steps: Initially, mixed metal hydroxide $(M(OH)_2)$ particles (M consisting mainly of Ni, Co, and Mn) are coprecipitated, serving as precursor for CAM synthesis (referred to as pCAM). The pCAM particles are subsequently blended with a lithium compound and calcined at elevated temperatures in a kiln to convert the powder mixture to the lithiated CAM (e.g., NCM) by solid-state reaction.[1,3,4]

The coprecipitation is conducted by simultaneous introduction of mixed metal sulfate solution $(MSO_{4(aq.)})$, sodium hydroxide solution $(NaOH_{(aq.)})$, and ammonia solution $(NH_{3(aq.)})$ in a stirred tank reactor under nitrogen atmosphere. In general, the following chemical reactions are occurring simultaneously: The coprecipitation of the $M(OH)_2$ with sodium sulfate accruing as byproduct (Na_2SO_4) (Eq. 1) and the complexation of metal cations (M^{2+}) by NH_3 (Eq. 2), for which particularly Ni^{2+} exhibits a high affinity.[5] Further, it is suggested that the coprecipitation of $M(OH)_2$ might also occur from the metal ammonia complex.[6]

$$MSO_4 + 2\,NaOH \rightarrow M(OH)_2 + Na_2SO_4 \quad [1]$$

$$M^{2+} + n\,NH_3 \rightleftharpoons [M(NH_3)]_n^{2+} \quad [2]$$

The thereby attained secondary particles exhibit particle sizes in the lower micron range ($\sim$4–16 μm) and are composed of numerous plate-like primary particles in the submicron range.[4,7–11] After calcination at high temperatures, not only the secondary particle structure of the pCAM is preserved and reflected in the CAM structure,[12–15] but also the electrochemical performance of the CAM

in the LiB is significantly affected by the morphology of the associated pCAM that was used for the CAM synthesis.[8,16,17] Furthermore, the physical properties such as the secondary particle size, uniformity, and sphericity of particles significantly affect the filterability and flowability of the pCAM and CAM powders, which is crucial for their efficient processing on an industrial scale.

In general, after the coprecipitation reaction, the attained pCAM particles are filtrated and washed with H_2O and $NaOH_{(aq.)}$ in order to minimize the amount of remaining mother liquor and impurities, such as SO_4^{2-}, from the crystallization reaction.[7] Additionally, synthesized CAMs are being subjected to a washing step to remove undesired residual lithium impurities (e.g., Li_2CO_3) formed during calcination reaction,[18,19] to increase the specific surface area of the CAM particles,[20] as well as to prevent ink gelation during electrode manufacturing[21] and deteriorating side-reactions in the final LiB application.[22] In this context, it is generally accepted that powders comprising of large, uniform, and spherical particles exhibit the lowest filtration resistance and display the least tendency for caking during washing. This significantly enhances the production throughput by increasing filtration rates. In contrast, small, non-uniform, and irregular-shaped particles show the poorest filtrability.[23–26] Analogously, uniformity, size and shape of particles affects the fluidity of powders, which is considerably reduced with decreasing particle size and uniformity as well as with a progressive deviation from a spherical particle shape.[23,27–31] In industrial-scale production of CAM, a free-flowing form of the pCAM and CAM powders is necessary, as this facilitates their processability in tonnage quantities. It is required that powders readily flow out of containers, can be easily transferred between various apparatuses for different process operations, and effortlessly packed for transportation and storage. However, lumping of the powder in technical apparatuses, pipes, or simply during storage entails the necessity for additional pulverization between process steps to maintain sufficient powder fluidity as well as excessively-frequent cleaning runs of the equipment; both is cost-intensive and lowers productivity.[23]

A control of CAM particle size and uniformity is furthermore required for the popular strategy to increase the press density of
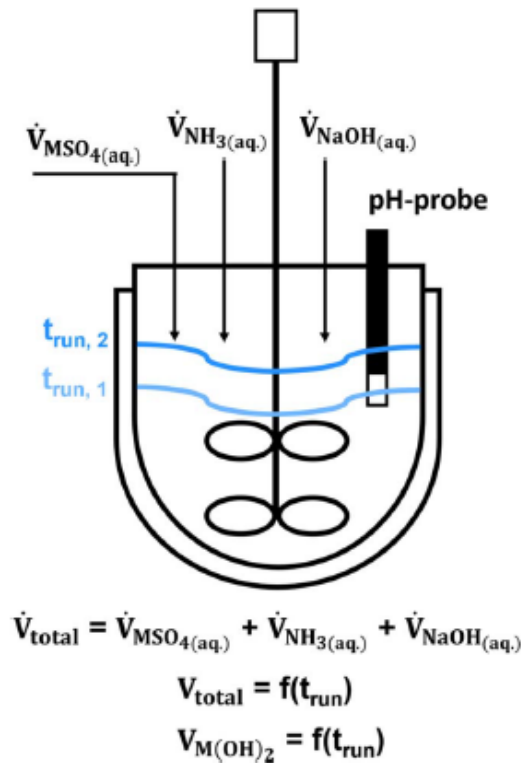
Figure 1. Schematic illustration of the stirred tank reactor setup used here for semi-batch coprecipitation of $Ni_{0.8}Co_{0.1}Mn_{0.1}(OH)_2$ secondary particles. For constant volumetric flow rates of the reactants ($\dot{V}_{total}$), the reaction volume (V_{total}) and thus the precipitated $Ni_{0.8}Co_{0.1}Mn_{0.1}(OH)_2$ volume ($V_{M(OH)2}$) and mass are a linear function of the run time (t_{run}), as indicated by the distinctive liquid levels at $t_{run,\,1}$ (light blue) and $t_{run,\,2}$ (dark blue).

CAM powders and thus the volumetric energy density of cathode electrodes for LIBs, namely the blending of CAMs with distinctively different particle sizes (large and small) in a desired mass ratio.[32,33] This is based on the de Larrard model that predicts that the maximum packing density can be achieved with a sphere size ratio of 4, in which case the optimal CAM blend would have a small-sphere mass fraction of 0.25.[34] For this reason, the control of particle size and shape is a substantial prerequisite for realizing optimized blend packings. Finally, the relevance of the physical attributes of the pCAM and CAM powders is not only limited to the CAM production process. In the subsequent manufacturing of electrode tapes from CAM powders, the physical property of the CAM affects the subsequent electrode coating procedure and the final electrode properties.[35,36]

Based on the above discussion in conjunction with the objective to manufacture CAMs for LiB applications in an economic manner, a precise control of the physical properties of the pCAM and CAM powders is necessary. Therefore, an in-depth knowledge of the $M(OH)_2$ pCAM particle formation mechanism during coprecipitation would enable a high degree of freedom to tailor pCAM and CAM properties according to the requirements for the cost-effective, large-scale manufacturing of CAMs as well as for a given LiB application. This study seeks to develop a mechanistic understanding of the $M(OH)_2$ pCAM particle formation by monitoring the development of the secondary particle size (via light scattering analysis) and morphology (via SEM imaging) throughout the semi-

batch coprecipitation of $Ni_{0.8}Co_{0.1}Mn_{0.1}(OH)_2$ at various stirring speeds. Using laser scattering analysis and a mass-balance model, it is demonstrated that the particle growth can be divided into two distinctive stages: An initial seeding phase, where the particle number increases while the particle size remains roughly constant, and a subsequent growth phase, where the number of particles remains roughly constant while the particle size increases. Investigation of the particle morphology at selected stages of particle growth is done by monitoring the secondary particle circularity via automated SEM image segmentation and by SEM imaging of cross-sectionally sliced $Ni_{0.8}Co_{0.1}Mn_{0.1}(OH)_2$ secondary particles after completed semi-batch coprecipitation. The latter reveals a core–shell pCAM structure, with the core consisting of loosely and randomly arranged primary particles. The validity of the two-stage coprecipitation mechanism is examined by comparing the pCAM size at the transition of the seeding to the growth stage with the core size of the pCAM particles after the semi-batch synthesis. Furthermore, by conducting semi-batch synthesis at different stirring speeds, the effect of turbulence (quantified by the Reynolds number and the average volume specific energy input) on the number/size of particles during the seeding phase and on the particle sphericity versus particle size of the final pCAM will be examined. In the end, a two-stage particle formation mechanism during the coprecipitation of $Ni_{0.8}Co_{0.1}Mn_{0.1}(OH)_2$ consisting of an agglomeration and a polycrystallization step is proposed, which is at variance with the coprecipitation mechanisms prevailing in the literature.

Theoretical Considerations

The fundamental characteristics of a semi-batch coprecipitation in a stirred tank reactor are schematically illustrated in Fig. 1. Reactants are continuously added, with the reaction suspension accumulating in the stirred vessel. This results in a steady increase of the total reaction volume (V_{total}) and mass of formed mixed metal hydroxide, so that of the volume of the formed mixed metal hydroxide ($V_{M(OH)2}$) increases with progressing batch run time (t_{run}). Due to low solubilities of the respective metal hydroxides of <200 ppm at the coprecipitation pH-range of 11.0–13.0,[5,37] an essentially complete conversion of the aqueous mixed metal sulfate solution ($MSO_{4(aq.)}$, M = Ni/Co/Mn in a molar ratio of 8/1/1) can be assumed. Furthermore, considering that over the entire run time the total volumetric flow rate ($\dot{V}_{total}$) and the concentration of all input streams remained constant, then $V_{M(OH)2}$ of the formed $Ni_{0.8}Co_{0.1}Mn_{0.1}(OH)_2$ particles is a simple linear function of t_{run}:

$$V_{M(OH)_2} = \frac{\dot{V}_{MSO4}\, t_{run}\, c_{MSO4}\, M_{M(OH)2}}{\rho_{cryst.}} \quad [3]$$

Here, $\dot{V}_{MSO4}$ is the volumetric flow rate of $MSO_{4(aq.)}$ (=18.0 ml h^{-1}), c_{MSO4} is the concentration of the $MSO_{4(aq.)}$ solution (=2.6 mol l^{-1}), $M_{M(OH)2}$ is the molar mass of $Ni_{0.8}Co_{0.1}Mn_{0.1}(OH)_2$ (=91.93 g mol^{-1}), and $\rho_{cryst.}$ is the crystallographic density of $Ni_{0.8}Co_{0.1}Mn_{0.1}(OH)_2$. For the latter, a molar composition averaged crystallographic density of 3.96 g cm^{-3} is assumed, based on the crystallographic density of $Ni(OH)_2$ (=4.1 g cm^{-3}), $Co(OH)_2$ (=3.6 g cm^{-3}), and $Mn(OH)_2$ (=3.26 g cm^{-3}) as well as on the molar transition metal ratio of Ni/Co/Mn = 8/1/1.

By assuming an approximately spherical shape for the $Ni_{0.8}Co_{0.1}Mn_{0.1}(OH)_2$ particles, the volume of individual $Ni_{0.8}Co_{0.1}Mn_{0.1}(OH)_2$ particles (V_{par}) can be estimated as the volume of a sphere with a diameter that corresponds to the volume median particle size (d_{50}) that can be determined by light scattering.

$$V_{par} = \frac{4}{3}\pi \left(\frac{d_{50}}{2}\right)^3 \quad [4]$$

Due to mass conservation, the total volume of all particles inside the reactor is equal to $V_{M(OH)2}$, so that the particle number (N_{par}) at

any given t_{run} value can be approximated by:

$$N_{par.} = \frac{V_{M(OH)_2}}{V_{par.}} \qquad [5]$$

When combined with Eqs. 3 and 4, the following relationship between the measured volume median particle size and the reaction run time holds *if* the number of particles remains constant (i.e., during the above postulated growth phase):

$$d_{50} = \sqrt[3]{\frac{6}{\pi} \cdot \frac{V_{MSO4} \, c_{MSO4} \, M_{M(OH)2}}{\rho_{cryst.}}} \cdot \sqrt[3]{\frac{t_{run}}{N_{par.}}}$$
$$\propto \sqrt[3]{t_{run}} \quad (\text{for } N_{par.} = \text{constant}) \qquad [6]$$

This would imply that during the growth phase, the d_{50} value would have to increase with the third root of the run time. Furthermore, with the constraint that the particle number throughout the run remains constant, the following equation is valid, which is frequently utilized for seeded batch crystallization reactions and relates the solid volume at the onset ($V_{s,initial}$) and at the end of the growth period ($V_{s,final}$) to the respective diameter of spherical particles (d_{final} and $d_{initial}$):[38–40]

$$\left(\frac{d_{final}}{d_{initial}}\right)^3 = \frac{V_{s,final}}{V_{s,initial}} \qquad [7]$$

The mean growth rate (G) of particles in a certain interval of t_{run} between $t_{run,1}$ and $t_{run,2}$ with corresponding volume median particle sizes $d_{50,1}$ and $d_{50,2}$, respectively, can be defined by the following expression.

$$G = \frac{d_{50,2} - d_{50,1}}{t_{run,2} - t_{run,1}} \qquad [8]$$

Experimental

Materials and methods.—The following aqueous transition metal solutions were obtained from BASF SE ($\geqslant$99.0% purity): Nickel(II) sulfate solution (2.6 mol l^{-1} NiSO$_{4(aq.)}$), cobalt(II) sulfate solution (2.6 mol l^{-1} CoSO$_{4(aq.)}$), and manganese(II) sulfate solution (2.6 mol l^{-1} MnSO$_{4(aq.)}$). From these, a mixed metal sulfate solution (MSO$_{4(aq.)}$) was prepared by combining the respective transition metal salt solutions in a molar ratio of M = Ni/Co/Mn = 8/1/1 to achieve an overall metal concentration of c_{MSO4} = 2.6 mol l^{-1}. Furthermore, sodium hydroxide solution (25 wt% NaOH$_{(aq.)}$ ($\equiv$7.9 mol l^{-1}), $\geqslant$99.0% purity) and ammonia solution (25 wt% NH$_{3(aq.)}$ ($\equiv$13.2 mol l^{-1}), $\geqslant$99.0% purity) were obtained from Bern Kraft GmbH (Germany). All solutions were used as they arrived from the chemical suppliers without any further purification.

Semi-batch coprecipitation of Ni$_{0.8}$Co$_{0.1}$Mn$_{0.1}$(OH)$_2$.—The Ni$_{0.8}$Co$_{0.1}$Mn$_{0.1}$(OH)$_2$ particle formation was investigated during semi-batch coprecipitation reactions in a 480 ml stirred tank reactor under nitrogen atmosphere (with a N$_2$ purge flow of 2.0 l h^{-1}), equipped with a temperature control unit and a pH-probe (HA 405-DXK-S8, Mettler Toledo) for monitoring the internal pH-value of the solution (for a sketch of the reactor setup see our previous work).[7] The glass vessel with a double jacket for circulating a heating fluid had an inner diameter of 8 cm, a height of 15 cm, and an outer diameter of 15 cm; it was equipped with baffles, a three-stage 45° pitch-blade stirrer with a diameter of 5 cm, and three dosing tubes for the respective reactant solutions, namely for the mixed metal solution (MSO$_{4(aq.)}$), the sodium hydroxide solution (NaOH$_{(aq.)}$), and the ammonia solution (NH$_{3(aq.)}$). The three dosing tubes (1 mm inner and 2 mm outer diameter) were introduced through the sealed top of the reactor, separated from each other by 4 cm each (with a total distance of 8 cm between the MSO$_{4(aq.)}$ and the

NaOH$_{(aq.)}$ inlets); the tube outlets were positioned in the reactor 3 cm above the maximum liquid level, which corresponds to 12 cm from the bottom of the reactor.

Before starting the coprecipitation reaction, the vessel was charged with 200 ml deionized and degassed H$_2$O as well as with 4.0 ml of 25 wt%NH$_{3(aq.)}$ solution to achieve an overall NH$_{3(aq.)}$ concentration in the reactor of 0.25 mol l^{-1}. The temperature was set to 55 °C via circulation of tempered silicon oil through the double jacket and the stirring speed was set to the desired value. The internal reaction pH-value measured at the solution temperature of 55 °C was referenced to an external pH-value measured at 23 °C (pH$_{23 °C}$; via an InLab$^\circ$ SemI MIcro, Mettler Toledo) by taking solution samples from the reactor and measuring the pH-value at 23 °C. The internal pH electrode was calibrated at 55 °C, while the external electrode was calibrated at 23 °C; in both cases, buffer solutions with pH$_{23 °C}$ = 7.0 and pH$_{23 °C}$ = 12.0 were employed (Certipure, Merck KGaA).

The semi-batch coprecipitation was initiated by simultaneously feeding the MSO$_{4(aq.)}$ solution at a volumetric flow rate of 18.0 ml h^{-1} and the NH$_{3(aq.)}$ solution at a volumetric flow rate 1.8 ml h^{-1} into the reactor. The NaOH$_{(aq.)}$ solution flow was controlled by a flow control-unit (Dulcometer, Prominent) linked to the internal pH-probe to maintain a constant pH-value throughout the reaction; the actual flow was close to the predicted volumetric flow rate of 12.0 ml h^{-1}. The stirring speed was varied between 550, 950, and 1350 rpm, while other remaining process parameters remained unchanged. In desired time intervals, the reaction progress was controlled by withdrawing 4–5 ml of reaction suspension from the reactor, cooling it to 23 °C, measuring the pH-value at 23 °C and determining the particle size distribution by laser diffraction (see below). For investigation of particle morphology by scanning electron microscopy (see below), the particle slurry was filtered, washed with H$_2$O in a 10:1 precipitate:H$_2$O weight ratio, and dried in air at 120 °C for 12 h in an oven (universal Oven U, Memmert). After 8.75 h reaction run time, the total solution volume was 480 ml, and the reactant flows were stopped. The obtained product suspension was collected and identically processed.

Particle size distribution by laser scattering.—The reactor suspension sample was homogenously dispersed, and a small amount of the particle slurry was transferred into the particle size analyzer (Mastersizer 2000, Malvern Panalytical GmbH) until a light obscuration between 4.0%–14.0% was achieved. The respective volume-based particle size distribution (PSD) was determined by laser diffraction based on Mie's scattering theory. A refractive index of 1.33 for H$_2$O as dispersant was selected, while a refractive index of 2.19, identical to the refractive index of NiO, was assumed for the Ni$_{0.8}$Co$_{0.1}$Mn$_{0.1}$(OH)$_2$ particles. The intensity of the scattered laser beam was collected as a function of the scattering angle for particle sizes in the range of 0.05–70.0 μm by applying a combination of red and blue light. Based on three measurements per sample, the average volume-based percentile particle sizes d_{10}, d_{50}, and d_{90} were determined. The span (σ) of the PSD was calculated according to the following equation.

$$\sigma = \frac{d_{90} - d_{10}}{d_{50}} \qquad [9]$$

Scanning electron microscopy (SEM).—The morphology of the obtained pCAM particles was characterized by attaching the Ni$_{0.8}$Co$_{0.1}$Mn$_{0.1}$(OH)$_2$ powder on a SEM pin holder (Agar Scientific, Ltd.), which is covered with conducting carbon (Plano GmBH). Subsequently, the sample was coated with a 6 nm platinum layer (SCD 500 Sputter Coater, Bal-Tec AG). Top-view SEM imaging was performed with a thermal field emission cathode and an Everhat-Thornley secondary electron detector at an operating voltage of 5 kV (Ultra 55, Carl Zeiss Ag).
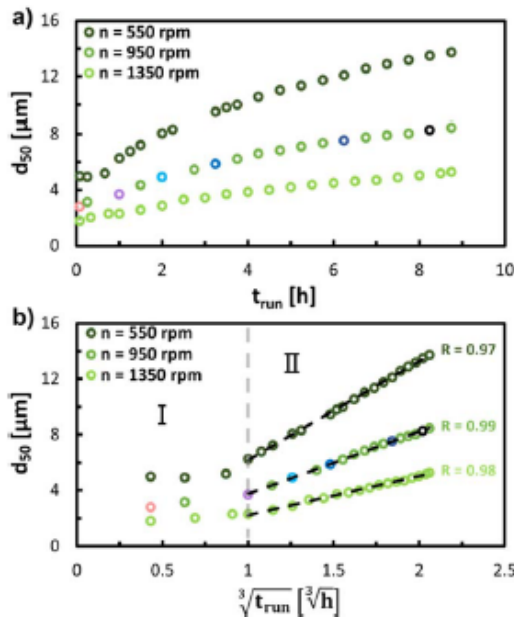
Figure 2. Evolution of the volume median particle size d_{50} obtained by light scattering during the semi-batch coprecipitation of $Ni_{0.8}Co_{0.1}Mn_{0.1}(OH)_2$ at a stirring speed of n = 550 rpm (dark green), n = 950 rpm (green) and n = 1350 rpm (light green), plotted versus: (a) the run time t_{run} and (b) the third root of the run time, $\sqrt[3]{t_{run}}$. The gray dashed line divides the course of coprecipitation reaction into a seeding stage I ($t_{run} > 1.0$ h) and a growth stage II ($t_{run} \leqslant 1.0$ h). The black dashed lines represent linear regressions of the d_{50} values in the growth stage between $\sqrt[3]{t_{run}} = 1.0 \sqrt[3]{h}$ and $\sqrt[3]{t_{run}} = 2.06 \sqrt[3]{h}$, listing also the respective correlation coefficients R. The differently colored data points for the experiment at 950 rpm indicate exemplary particle suspensions for which volume-based PSD and SEM images of the coprecipitated particles are depicted in Fig. 3.

Samples for cross-section measurements were prepared by mixing 2 g of epoxy resin and 0.5 g of epoxy hardener (Buehler, ITW Test & Measurement GmbH) and then adding a few drops of the mixture to the respective $Ni_{0.8}Co_{0.1}Mn_{0.1}(OH)_2$ precursor sample in a gelatine capsule (Plano GmbH). The resulting slurry was cast onto an Al-foil using a manual coater with a gap size of 0.5 mm and dried in an oven at 40 °C overnight. Small sections thereof were transferred to an ion milling system (ArBlade 5000, Hitachi, Ltd.) equipped with an Ar-ion beam at an operating voltage of 6 kV. Images were taken as described above for the top-view measurements.

Particle circularity by SEM image segmentation.—Quantitative information about particle circularity as a two-dimensional descriptor for the particle sphericity of $Ni_{0.8}Co_{0.1}Mn_{0.1}(OH)_2$ particles, which is a three-dimensional property, was determined from SEM top-view images at 1 k magnification by employing a segmentation model. The underlying algorithm implemented for automated image segmentation is based on a convolutional neural network utilizing the U-Net architecture,[41] which is analogous to the model applied by other authors for the segmentation of primary particles in polycrystalline lithium nickel oxide.[20,42] The as-measured lengths/areas from two-dimensional projected particles from the original SEM image were captured in the dimension of pixels and converted back to actual lengths/areas after segmentation by using a calibration factor from the image metadata. Additionally, several filters for the segmentation were employed to increase the accuracy of the process.

Particles touching the boundary of the image were not evaluated, since particles in this region might not be fully captured. Further, only particles were considered, which exhibited an area of above 200 pixels and a solidity (=ratio between the particle's area and the area of the convex hull that encloses the particle) of $\geqslant 0.8$.[43] These conditions ascertained that only particles that did not deviate excessively from a spherical shape were recognized. The circularity (C) of the segmented particles that fulfilled the aforementioned criteria was then calculated according to the isoperimetric quotient, which is defined as:[44]

$$C = \frac{A_{particle}}{A_{eq.circle}} = \frac{4\pi A_{particle}}{P_{particle}^2} \quad [10]$$

Here, $A_{particle}$ is the area and $P_{particle}$ is the perimeter of the segmented particle based on a 2D projection of the particle and $A_{eq.circle}$ is the area of a perfect circle that would have the equivalent perimeter as that measured for the segmented particle (= $P_{particle}$); note that C equals one for a perfect circle.

Overall, for each sample, the circularity of approximately 60–100 particles was determined to obtain the circularity distribution for each sample. For each circularity distribution the median number-based percentile circularities C_{10}, C_{50}, and C_{90} were determined. The validity of the segmentation model was verified by comparing algorithm-based circularity distributions of selected samples to distributions attained by manual segmentation via ImageJ.[45] Further, similar to the span σ that is used to represent the width of the particle size distribution determined by light scattering (see Eq. 9), the width of the here obtained circularity distributions (C_{span}) was calculated according to the following equation.

$$C_{span} = \frac{C_{90} - C_{10}}{C_{50}} \quad [11]$$

Particle core size by cross-section SEM image segmentation.— The size of secondary particle cores was manually determined from cross-section SEM images of $Ni_{0.8}Co_{0.1}Mn_{0.1}(OH)_2$ secondary particles at various magnifications by applying ImageJ.[45] For this analysis, only those secondary particles were considered as representative which had been sliced perfectly through the equator of the secondary particle during the SEM sample preparation to ensure fault-free quantification of the core size. This is assured by only selecting particles, which have a similar particle size as was determined by light scattering and for which the core was readily exposed. This prevents falsification of the analysis by in e.g., secondary particles that were sliced through the upper or lower quarter and therefore would result in a non-representative secondary particle core size.

The corresponding equivalent diameter (d_{eq}) of a circle with identical area as the determined area of the core (A_{core}) was calculated according to the following.

$$d_{eq.} = 2 \cdot \sqrt{\frac{A_{core}}{\pi}} \quad [12]$$

Nitrogen physisorption measurements.—The internal secondary particle porosity of $Ni_{0.8}Co_{0.1}Mn_{0.1}(OH)_2$ particles were determined by measuring nitrogen physisorption isotherms at 77 K (ASAP2420, Micromeritics). Prior to the measurements, pCAM powders were degassed at 120 °C for three hours. It was demonstrated in a previous work that the internal secondary particle porosity of pCAM particles can be determined via N_2 capillary condensation in these pores at a high relative pressure p/p_0 value of 0.995.[7] The SEM imaging analysis of the pCAM particles showed that internal pores were smaller than ~300–400 nm, which is below the pore diameter below which according to the Kelvin equation liquid N_2 can be formed in these pores at a relative pressure p/p_0 value of 0.995.

Table I. Volume median particle size d_{50} and span σ (see Eq. 9) of the corresponding PSDs at selected stages of particle growth during coprecipitation of $Ni_{0.8}Co_{0.1}Mn_{0.1}(OH)_2$ in semi-batch mode conducted at various stirring speeds (n) as well as the mean growth rate (G) in stage II of the corresponding run calculated by Eq. 8.

Run #	n [rpm]	$d_{50,\ 5\ min}$ [μm]	$\sigma_{5\ min}$ [-]	$d_{50,\ 1.0\ h}$ [μm]	$\sigma_{1.0\ h}$ [-]	$d_{50,\ 8.75\ h}$ [μm]	$\sigma_{8.75\ h}$ [-]	G [μm/h]
1	550	5.0	1.5	6.2	1.4	13.7	0.73	0.96
2	950	2.8	1.4	3.7	1.2	8.4	0.76	0.62
3	1350	1.9	1.4	2.3	1.3	5.3	0.77	0.38

The intra-particle porosity ε_{intra} of $Ni_{0.8}Co_{0.1}Mn_{0.1}(OH)_2$ secondary particles can be calculated according to:[46]

$$\varepsilon_{intra} = \frac{V_{N2,liquid}}{V_{N2,liquid} + \dfrac{1}{\rho_{cryst.}}} \qquad [13]$$

where $V_{N2,liquid}$ is the specific liquid N_2 volume condensed in the pCAM secondary particle pores and $\rho_{cryst.}$ is the crystallographic density of $Ni_{0.8}Co_{0.1}Mn_{0.1}(OH)_2$. Here, a molar averaged crystallographic density of 3.96 g cm^{-3} is assumed, based on the crystallographic density of $Ni(OH)_2$ (=4.10 g cm^{-3}), $Co(OH)_2$ (=3.60 g cm^{-3}), and $Mn(OH)_2$ (=3.26 g cm^{-3}) and the transition metal ratio of Ni/Co/Mn = 8/1/1.

Results and Discussion

Analysis of particle growth during coprecipitation of $Ni_{0.8}Co_{0.1}Mn_{0.1}(OH)_2$—The particle growth during semi-batch operation was monitored by sampling the reaction suspension at desired time intervals and determining the corresponding particle size distribution (PSD) by light scattering. The development of the obtained volume median particle sizes (d_{50}) throughout the semi-batch run time (t_{run}) for coprecipitations conducted with different stirring speeds (n) are depicted in Fig. 2a. Furthermore, Table I lists the d_{50} values of the $Ni_{0.8}Co_{0.1}Mn_{0.1}(OH)_2$ particles formed after 5 min, 1.0 h, and 8.75 h as well as the span (σ) values that represent the width of the corresponding PSD for each semi-batch experiment. The d_{50} values of the initial particles generated after a t_{run} of 5 min depend inversely on the applied stirring speed, while the spans of the corresponding PSDs are similar in each run and indicate a broad PSD. During the first hour of the coprecipitation reaction, the particle size increases only slightly (by $\sim$20%–30% between 5 min and 1.0 h, see Table I), accompanied by a minor decrease in PSD span ($\sim$10%–15%). After this early phase, the particle growth over each run appears to follow a power function (see Fig. 2a), as observed by other authors during hydroxide pCAM coprecipitation,[47,48] which is characteristic for the growth of spherical particles independently of the material class.[49,50] The final d_{50} values achieved at the end of each experiment, i.e., after t_{run} = 8.75 h is roughly inversely proportional to the stirring speed (see Table I). In contrast, independent of the applied stirring speed, the PSD of the particles continuously narrows over the course of the coprecipitation reaction, and the PSD span after 8.75 h of run time is approximately halved compared to the PSD of the initial particles formed after 5 min. A similar behavior, namely an extremely broad span of particles formed throughout the first 45 min of the semi-batch coprecipitation of $Ni_{0.35}Mn_{0.65}(OH)_2$ that is followed by a continuous decrease in span throughout the proceeding particle growth phase was observed by Liu et al., without, however, conducting any further investigations in this phenomenon.[47]

To gain further insights into the growth mechanism, the particle growth curves depicted in Fig. 2a were scaled by plotting the determined d_{50} as a function of the third root of the batch run time ($\sqrt[3]{t_{run}}$) (see Eq. 6). The thus attained particle growth profiles for each of the applied stirring speeds (n) are shown in Fig. 2b. As already indicated above, independent of the stirring speed, the course of particle growth can be divided into two distinct stages: For $\sqrt[3]{t_{run}}$ < 1.0 h ($\hat{=}$ t_{run} < 1.0 h), the particle size remains fairly constant and only marginally increases, delineating stage I. After this initial phase, for $\sqrt[3]{t_{run}}$ ≥ 1.0 h ($\hat{=}$ t_{run} ≥ 1.0 h), the d_{50} values for each stirring speed increase perfectly linearly with $\sqrt[3]{t_{run}}$, illustrated by correlation factors (R) of the linear regression lines of close to one, delineating stage II. The slope of these linear regression lines are a function of the mean particle growth rates (G, defined by Eq. 8) during the respective coprecipitation, which are listed in Table I, and which are roughly inversely proportional to the applied n in the respective semi-batch run.

This analysis suggests that new particles are still being generated during stage I, because the overall volume of coprecipitated solid $V_{M(OH)2}$ is increasing with run time (see Eq. 3) while the particle size barely increases (see Fig. 2b). In contrast, in stage II, the increase of the d_{50} values with $\sqrt[3]{t_{run}}$ suggests that the continuously coprecipitated solid mass is solely deposited on already existing particles, without any further increase in particle number ($N_{par.}$, see Eq. 6). This growth behavior in stage II is characteristic for seeded batch crystallization processes, whereby nucleation and formation of new particles is suppressed by charging the reactor with seed particles before initiating the reaction.[38-40] Hence, after stage I, the semi-batch coprecipitation conducted in this work behaves analogous to a seeded crystallization reaction. Interestingly, despite different applied stirring speeds, the transition from stage I to stage II in the here conducted semi-batch experiments occurs at similar t_{run} values. This suggests that the cessation of nucleation (i.e., the end of stage I) and the concomitant onset of particle growth (i.e., the beginning of stage II) seems to be mainly dependent on the solid mass fraction in the reactor. It is rationalized that this can be justified by the feedback effect of the existing solid mass in the reactor on the nucleation kinetics, namely by decreasing the existing supersaturation as driving force for nucleation in the system because lattice ions (for the formation of $M(OH)_2$, the lattice ions are M^{2+} and OH^-) are contributing to crystal growth on already available solid mass instead to the supersaturation.[51,52] This is consistent with the observation of a critical seed loading reported for seeded batch crystallization syntheses of various compounds, above of which the formation of new particles is effectively suppressed.[53,54]

Table I also shows that the span values (σ) of the PSDs for the three runs conducted at different stirring speeds decrease with run time. It is rationalized, that the narrowing of the PSD with progressing particle growth implies that the particle size increase of particles *within* each run is independent of their size, and therefore, nearly the surface mass specific uptake nearly identical for every particle. Consequently, smaller particles "catch up" in mass and volume to larger ones with proceeding t_{run}, since an equal increase in diameter for particles of varying size denotes a larger gain in volume for smaller particles compared to larger ones. This overall results in a particle size independent growth rate *within* each run. Please note that the growth rate *between* each run is different (see G in Table I), which will be explained below.

By Eq. 5 determined values for $N_{par.}$ of the coprecipitated $Ni_{0.8}Co_{0.1}Mn_{0.1}(OH)_2$ particles inside the reactor after 5 min, 1.0 h, and 8.75 h for each semi-batch experiment are given in Table II. The particle number during each run was increased within stage I by factor of $\sim$5–6 (i.e., between t_{run} of 5 min and 1.0 h, see Fig. 2b), which implies that new particles are formed by nucleation. During

Results

Table II. Particle number ($N_{par.}$) in the reactor at selected stages of particle growth during the semi-batch coprecipitation of $Ni_{0.8}Co_{0.1}Mn_{0.1}(OH)_2$ conducted at various stirring speeds (n), calculated according to Eq. 5. The subsequent columns give the theoretically resulting particle size at t run = 8.75 h for an assumed constant number of particles during stage II ($d_{50,8.75 h}^{theo}$, based on Eq. 13), and the particle number ($N_{par.,8.75 h}^{*}$) determined on the basis of the intra-particle porosity (ε_{intra})-corrected density in Eq. 3. ε_{intra} was determined by nitrogen physisorption.

Run #	n [rpm]	$N_{par., 5 min}$ [-]	$N_{par., 1.0 h}$ [-]	$N_{par., 8.75 h}$ [-]	$d_{50,8.75 h}^{theo}$ [μm]	$N_{par.,8.75 h}^{*}$ [-]	ε_{intra} [-]
1	550	1.4×10^9	8.3×10^9	7.1×10^9	12.9	8.2×10^9	17.1%
2	950	7.9×10^9	4.1×10^{10}	3.1×10^{10}	7.6	3.8×10^{10}	18.1%
3	1350	2.5×10^{10}	1.7×10^{11}	1.2×10^{11}	4.7	1.5×10^{11}	17.4%

the subsequent growth phase, i.e., in stage II, the initial particle number at t_{run} = 1.0 h in each run decreases by 14%–29% until the end of the experiment at t_{run} = 8.75 h. A decrease in particle number throughout the course of the coprecipitation reaction can be rationalized by the following scenarios: (a) agglomeration of secondary particles throughout the process; (b) a significant secondary particle porosity, which would lower the assumed crystallographic density (ρ_{cryst}) applied for the calculation of the particle volume according to Eq. 3, and thus would result in an underestimation of particle number; and/or, (c) a decrease in solid volume inside the reactor, hence particle number, caused by the sampling of the reaction suspension over the course of the semi-batch operation. An agglomeration of secondary particles (scenario (a)) seems unlikely, since the d_{50} values during stage II increase with $\sqrt[3]{t_{run}}$ (Fig. 2b), following the relationship given by Eq. 6 that is based on assuming a constant $N_{par.}$ value. Furthermore, agglomeration processes are generally a function of agitation,[55,56] so that the largest decrease in particle number would be expected for the semi-batch coprecipitation conducted at n = 550 rpm, while run 3 conducted at n = 1350 rpm should exhibit the lowest change; this is contrary to the observations based on Table II, where the $N_{par.}$ value calculated by Eq. 5 decreases most strongly for n = 1350 rpm ($\sim$29% compared to $\sim$14% for n = 550 rpm).

To examine hypothesis (b), the theoretically resulting particle size at the end of the experiments, i.e., at t_{run} = 8.75 h ($d_{50,8.75 h}^{theo}$), was calculated by assuming that the number of particles would indeed remain constant during stage II, namely between t_{run} of 1.0 h and 8.75 h, which is obtained by rearranging Eq. 7:

$$d_{50,8.75 h}^{theo} = \left(\frac{V_{M(OH)2,8.75 h}}{V_{M(OH)2,1.00 h}} \right)^{1/3} d_{50,1.0 h} \qquad [13]$$

Here, $V_{M(OH)2\ 1.0\ h}$ and $V_{M(OH)2\ 8.75\ h}$ is the total volume of $Ni_{0.8}Co_{0.1}Mn_{0.1}(OH)_2$ particles formed after t_{run} of 1.0 h and 8.75 h, respectively, which was calculated via Eq. 3, while $d_{50\ 1.0\ h}$ is the volume median particle size of the $Ni_{0.8}Co_{0.1}Mn_{0.1}(OH)_2$ particles collected after a t_{run} of 1.0 h, determined by light scattering. A comparison of the thus obtained $d_{50,8.75 h}^{theo}$ values listed in Table II for each semi-batch run to the values obtained by light scattering in Table I reveals that the former are underestimated by $\sim$0.6-0.8 μm. By inspecting Eq. 3, this could be caused by a particle density that is significantly lower than the crystallographic density of $Ni_{0.8}Co_{0.1}Mn_{0.1}(OH)_2$ (ρ_{cryst}) used for the calculation of $V_{M(OH)2}$, which would be the case if the secondary particles have a significant porosity. Therefore, the intra-particle porosity (ε_{intra}) of the $Ni_{0.8}Co_{0.1}Mn_{0.1}(OH)_2$ secondary particles collected after a run time of 8.75 h was determined by nitrogen physisorption. In our previous work it was demonstrated that the internal secondary particle porosity can be determined via N_2 capillary condensation in these pores at a high relative p/p_0 value of 0.995.[7] The resulting ε_{intra} values of $\sim$17%–18% are listed in Table II, indicating a significant secondary particle porosity. It is assumed that the uniformity of the ε_{intra} values stems from a nearly constant volume ratio of the porous secondary particle core to the overall secondary particle irrespective of the stirring speed (see below), which implies

that ε_{intra} in the core and outer regions of the secondary particles are very similar independent of the stirring speed. Using these experimentally determined ε_{intra} values, the volume of the coprecipitated particles ($V_{M(OH)2}$) was recalculated by multiplying the ρ_{cryst} term in Eq. 3 by (1-ε_{intra}) in order to account for the lower secondary particle density on account of their porosity. With the thus corrected $V_{M(OH)2}$ values, the corresponding particle numbers for the different runs ($N_{par.,8.75 h}^{*}$) were calculated from Eq. 5 and are given in Table II. By considering ε_{intra}, the apparent decrease in particle number over the course of stage I (i.e., between t_{run} of 1.0 and 8.75 h) amounts to only $\sim$1%–12%. Thus, within the error of this analysis (e.g., using d_{50} values rather than a size distribution), the number of coprecipitated particles over the course of stage II remains essentially constant.

Even though the continuous withdrawal of solid volume by sampling reaction suspension from the reactor might account for part of the remaining decrease in $N_{par.}$ during stage II (hypothesis (c)), the accumulated amount of sample volume withdrawn by the end of each run amounts to one-fifth of the total suspension volume, whereby the total amount of material lost due to sampling is significantly less. A significant sampling-induced loss of $N_{par.}$ would manifest as a deviation from Eq. 6 by an increase in growth rate, resulting in a continuous increase of the slope of the linear regressions depicted in Fig. 2b. Therefore, an impact on the particle growth kinetics and formation mechanism by sampling can be considered negligible.

In light of the above analysis, it is rationalized that the $Ni_{0.8}Co_{0.1}Mn_{0.1}(OH)_2$ particle formation can be divided in two distinctive stages: Initially, particles with a nearly constant diameter are generated by nucleation until enough solid mass is available in the reactor, so that the process during this period can be denoted as seeding stage (stage I in Fig. 2b). Analogous to seeded batch crystallizations, these particles serve as seed particles in the subsequent growth stage (stage II in Fig. 2b, in which solely particle growth is occurring, without a significant formation of new particles. The applied stirring speed during the semi-batch coprecipitation reaction seems to affect the size and number of particles formed in the seeding phase, which then determines the growth rate (G) during the growth phase, thus, the obtainable particle size after any given run time.

Analysis of the shape of coprecipitated $Ni_{0.8}Co_{0.1}Mn_{0.1}(OH)_2$ particles.—For deeper insights into the particle formation mechanism, the morphology of particles at selected stages of particle growth during the semi-batch coprecipitation of $Ni_{0.8}Co_{0.1}Mn_{0.1}(OH)_2$ was characterized by top-view SEM imaging. Figure 3 displays SEM images and corresponding PSDs of $Ni_{0.8}Co_{0.1}Mn_{0.1}(OH)_2$ particles attained at various points in time for the run conducted at n = 950 rpm, whereby the selected run times are marked by the differently colored data points in Fig. 2. It is worthy to note that the PSDs depicted in Fig. 3a are mono modal, which is also true for the PSDs attained by light scattering for the semi-batch run at n = 950 rpm for run times that are not depicted in Fig. 3a, as well as in the other semi-batch experiments. The particles obtained during the initial phase of the coprecipitation run, i.e., after t_{run} = 5 min exhibit a rather broad PSD (orange line in Fig. 3a) and
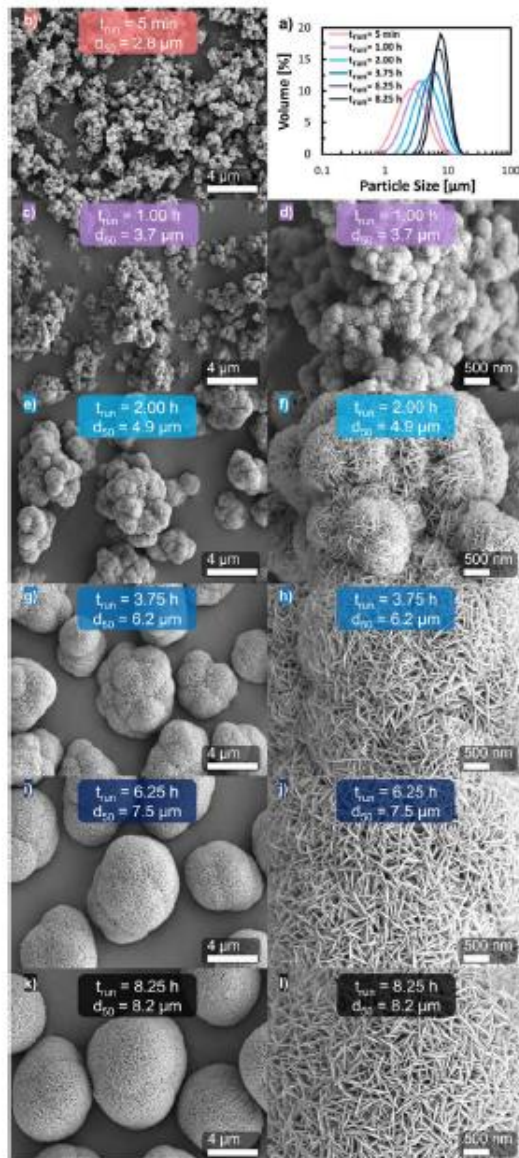
Figure 3. (a) Volume-based particle size distribution of $Ni_{0.8}Co_{0.1}Mn_{0.1}(OH)_2$ secondary particles obtained after different semi-batch coprecipitation run times at a stirring speed of n = 950 rpm. SEM top-view images at 5 k as well as at 20 k magnification of the corresponding $Ni_{0.8}Co_{0.1}Mn_{0.1}(OH)_2$ secondary particles after different run times: (b) 5 min (red), (c) & (d) 1.0 h (purple), (e) & (f) 2.0 h (light blue), (g) & (h) 3.75 h (blue), (i) & (j) 6.25 h (dark blue), and (k) & (l) 8.25 h (black).

are composed of undefined and loose aggregates (see Fig. 3b). After a t_{run} of 1.0 h, consolidation of the inhomogeneous particle clusters into agglomerates has occurred (Fig. 3c), which are comprised of numerous tiny nanospheres and in turn consist of twinned and plate-like shaped primary particles (Fig. 3d) that are characteristic for beta-nickel hydroxide $(Ni(OH)_2)^{[57-61]}$ and $M(OH)_2.^{[7,10,62]}$ Please note that here the term aggregate was chosen as definition for loose

particle assemblages that can be easily ruptured, while the term agglomerate was selected for particle consolidations that are cemented by solid bridges.[63] During that first hour of run time, the PSD span decreased slightly (by ~14%, see Table I), but the PSD still remains comparably broad (see purple line in Fig. 3a). Particles collected at a t_{run} of 2.0 h are aspherical and resemble the initial agglomerate structure with multiple radial extensions (Fig. 3e). At higher magnification (Fig. 3f), the radial orientation of the inter-grown sub-micron sized plate-like shaped primary particles within such extensions becomes evident, whereby the vertical side ("edge") of the primary particles is exposed. This vertical side, which corresponds to the 001-plane[7,60] is pointing away from the center of the corresponding radial extension. With progressing t_{run}, the number of radial extensions for a given aspherical secondary particle is decreased, while the radial extension size is enlarged (Fig. 3g); this further continues with run time, so that the rather heterogeneous structure exhibited by the initially coprecipitated particles (Fig. 3b) cannot be anymore identified after a t_{run} of 6.25 h (Fig. 3i). Interestingly, the primary particles are always radially orientated around the secondary particle perimeter, with the vertical side of the primary particles facing away from the secondary particle center (Figs. 3h, 3j). Simultaneously, a continuous decrease in PSD span from 1.16 at t_{run} = 2.0 h to 1.06 at t_{run} = 3.75 h and to 0.83 at t_{run} = 6.25 h is observed. Close to the end of the semi-batch experiment, i.e., at t_{run} = 8.25 h, the various radial extensions within the secondary particle structure cannot be recognized any more, eventually resulting in spherical secondary particles without any indications of the initial agglomerate structure (Fig. 3k). These particles exhibit a ~2-fold lower PSD span compared to the initially formed particles (0.76 vs 1.4, see Table I), which is reflected by the PSDs shown in Fig. 3 (black vs orange line). These hierarchically structured secondary particles are comprised of numerous sub-micron sized primary particles, as typically reported for NCM hydroxide precursor particles,[6,8–10,62] while the edge of the primary particles is consistently orientated towards the perimeter of the secondary particle (Fig. 3l).

In agreement with the two distinct stages observable in the particle growth profiles depicted in Fig. 2b, the development of the corresponding secondary particle morphology can likewise be divided into two stages:

(i) The initial particles formed during the seeding stage (t_{run} < 1.0 h) exhibit a loose and undefined aggregate-like structure, which is originating from a rapid nucleation of nanospheres. These nanoparticles immediately coagulate to particle clusters and are cemented to agglomerates by the ensuing crystal growth via solid bridge formation. That the particle formation during the seeding stage (between a t_{run} of 5 min and 1.0 h) is governed by an agglomeration mechanism is supported by the inverse correlation of the secondary particle d_{50} values with the stirring speed during the respective semi-batch coprecipitation (Fig. 2, Table I). This result reflects the fact that the turbulence inside the agitated reaction vessel is governing the particle-particle attachment by agglomeration, which can be manipulated by the stirring speed.[55,56]

(ii) During the subsequent growth stage (t_{run} < 1.0 h), the data suggest that the consolidated agglomerates generated during the seeding phase increase in size by lateral crystal growth of individual primary particles ("polycrystallization"), because the vertical side of the primary particles is consistently orientated towards the outer perimeter of the secondary particle during the growth phase (Figs. 3d, 3f, 3h, 3j, and 3l). This seems to result in an overall enhancement of the $Ni_{0.8}Co_{0.1}Mn_{0.1}(OH)_2$ secondary particle sphericity throughout the semi-batch reaction.

To quantitatively verify the increase in secondary particle sphericity over the course of the conducted experiments, SEM top-view images of $Ni_{0.8}Co_{0.1}Mn_{0.1}(OH)_2$ secondary particles at selected

stages of the semi-batch coprecipitations conducted at various stirring speeds were segmented. The SEM images were taken at 1 k magnification and an automated segmentation algorithm was employed, that is analogous to the model employed by other authors.[20,42] By two-dimensional approximation of the segmented secondary particles, the area and perimeter of secondary particles was determined. This allows the calculation of the secondary particle circularity (C) as a two-dimensional descriptor for the secondary particle sphericity, which is a three-dimensional property, according to isoperimetric quotient given in Eq. 10. On average, the C values of 60-100 secondary particles per sample were determined and number-based C value distributions were formulated. Figure 4 exemplary displays a SEM image of $Ni_{0.8}Co_{0.1}Mn_{0.1}(OH)_2$ secondary particles collected at t_{run} of 6.25 h during the semi-batch coprecipitation performed at n = 950 rpm (run 2) before (Fig. 4a) and after automated segmentation (Fig. 4b). The secondary particles in the SEM image that were not considered by the algorithm are encircled in green, while particles for which the C value was determined are additionally colored in blue.

The validity of the algorithm-based segmentation was exemplarily verified by manual segmentation, and the resulting number-based C value distributions extracted from the SEM image displayed in Fig. 4a are compared in Fig. 4c. The obtained distributions are in good agreement, and only minor deviations can be observed for secondary particles exhibiting nearly perfect circularity (C > 0.95) and for rather non-circular particles (C < 0.80). The discrepancy for C > 0.95 might be ascribed to circular secondary particles, which were not considered by the algorithm due to local brightness inhomogeneities across the secondary particle structure that results in a blending with the background brightness. The discrepancy for C < 0.80 might be due to improper segmentation of overlapping secondary particles by the model, which results in an underestimation of the C value for the particle that is being overlapped, whereby such overlapped particles were not considered during manual segmentation. However, these slight discrepancies result in an only minor deviation of ~2% when comparing the number median circularity (C_{50}) determined from the C value distributions obtained by both methods (data not shown). In an analogous manner, the validity of the segmentation was further exemplarily verified for $Ni_{0.8}Co_{0.1}Mn_{0.1}(OH)_2$ secondary particles obtained at a t_{run} of 3.75 h and 8.25 h during the semi-batch coprecipitation conducted at n = 950 rpm. The resulting number-based C value distributions are given in Fig. A.1. Again, the discrepancy between the automated and the manual segmentation based C_{50} values is rather minor, with only ~4% for particles collected at a t_{run} of 3.75 h and ~1% for particles collected at a t_{run} of 8.25 h. It is worthy to note that C values for secondary particles formed at run times shorter than 2.0 h were not determined, due to an excessive deviation of the secondary particles from a circular shape (Figs. 3b–3d). Furthermore, due to the two-dimensional approximation of three-dimensional particles, which is the basis of Eq. 10, some three-dimensional aspherical features of the particle that are not located on or near the perimeter of the particle, are underestimated or even not considered. This, e.g., is the case when radial extensions are orientated towards the camera's line-of-sight in top-view SEM images. Therefore, it is assumed, that values for C obtained via the here presented method as a two-dimensional descriptor for particle sphericity, which is a three-dimensional property, are slightly overestimating the actual sphericity of secondary particles. Regardless, however, it is demonstrated that reasonable results can be obtained by the algorithm-based determination of the secondary particle circularity as descriptor for the secondary particle sphericity from SEM images by the here applied approach. This allows a quantitative assessment of the subjectively observable increase in secondary particle sphericity in Fig. 3.

Figure 5 a depicts the automated SEM image segmentation-based evolution of the C_{50} values of secondary particles collected after similar run times (within t_{run} ± 0.25 h) during semi-batch coprecipitation of $Ni_{0.8}Co_{0.1}Mn_{0.1}(OH)_2$ conducted at three different stirring
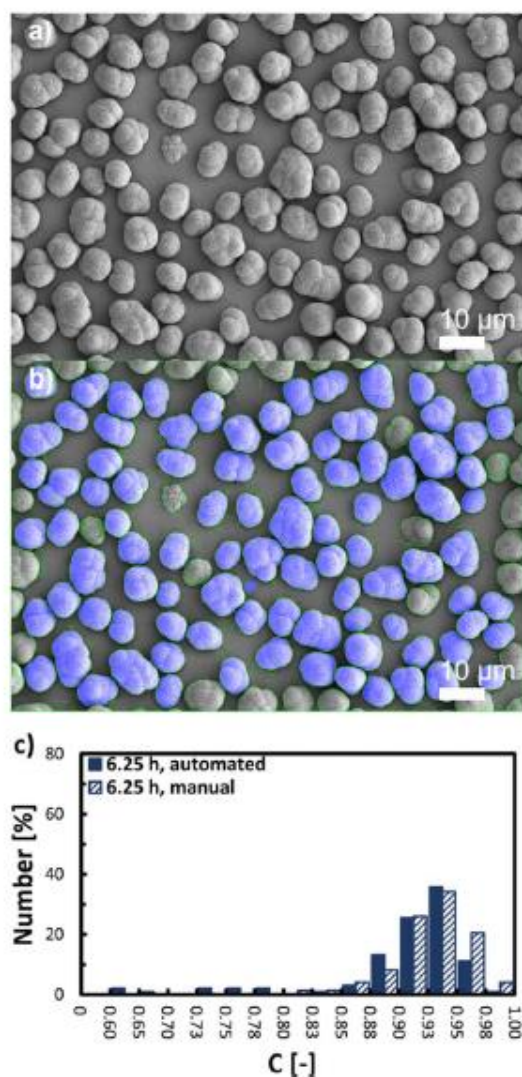
Figure 4. Quantification of particle circularity (C) as descriptor for the sphericity of $Ni_{0.8}Co_{0.1}Mn_{0.1}(OH)_2$ secondary particles by top-view SEM image analysis. (a) Top-view SEM image at 1 k magnification of $Ni_{0.8}Co_{0.1}Mn_{0.1}(OH)_2$ secondary particles obtained from the semi-batch coprecipitation after 6.25 h at a stirring speed of n = 950 rpm. (b) Selection criteria for the automated, algorithm-based secondary particle segmentation, whereby the particles that were selected for automated analysis are highlighted in blue overlay (the other particles were rejected for analysis due to incomplete imaging, insufficient contrast, or partial particle overlap). (c) Comparison of the number-based circularity distribution of $Ni_{0.8}Co_{0.1}Mn_{0.1}(OH)_2$ secondary particles determined by automated (filled) and by manual segmentation (unfilled).

speeds. For all three runs, the relative increase in C_{50} with increasing d_{50} during the growth stage (stage II in Fig. 2b) between t_{run} = 2.0 h and t_{run} = 8.25 h is similar, namely ~20%-30%. Furthermore, the width of the circularity distributions (C_{span}, defined by Eq. 11), that is represented by the error bars in Fig. 5a, decreases by factor of ~4–5 with increasing t_{run} for all three semi-batch experiments.

However, in contrast to the inverse relationship between d_{50} and the stirring speed (Fig. 2), the C_{50} values of the particles at a t_{run} of 2.0 h (left-most data points within each run in Fig. 5a) increase with the stirring speed. It is also interesting to note that even though the slowest stirring speed (n = 550 rpm) yields the largest secondary particles, those particles exhibit the lowest C_{50} (see Fig. 5a). Close to the beginning of stage II, particles with a d_{50} of 8.1 μm and a C_{50} of 0.63 are obtained for n = 550 rpm, growing into particles with a d_{50} of 13.5 μm and a C_{50} of 0.83 at t_{run} = 8.25 h. In comparison, for n = 1350 rpm, much smaller particles with higher circularity are obtained: at t_{run} = 2.0 h, the secondary particles have a d_{50} of only 2.9 μm and a C_{50} of already 0.81, which at t_{run} = 8.0 h increases to a still rather small d_{50} of 5.0 μm and a C_{50} of 0.95. The $Ni_{0.8}Co_{0.1}Mn_{0.1}(OH)_2$ secondary particles produced with n = 950 rpm display comparable particle circularities compared to the experiment with n = 1350 rpm, but with larger particle sizes for any given run time (see Fig. 5a). Further, due to the increase of C_{50} over t_{run} (thus with increasing d_{50}) for all three conducted runs, C_{span} must intrinsically decrease with increasing t_{run} as non-circular particles become more circular over time while already circular particles remain circular. This results in the observed narrowing of C_{span} with increasing t_{run} for all three runs.

The quantitative differences in secondary particle circularity are further visualized by SEM top-view images of the final $Ni_{0.8}Co_{0.1}Mn_{0.1}(OH)_2$ particles obtained by semi-batch coprecipitation after t_{run} = 8.75 h at stirring speeds of 1350 rpm (Fig. 5b), 950 rpm (Fig. 5c), and 550 rpm (Fig. 5d). Identical to the secondary particles throughout the growth phase at n = 950 rpm (Figs. 3e–3l), the secondary particles obtained at 1350 rpm and 550 rpm consist of numerous sub-micron primary particles, which is characteristic for NCM hydroxide precursors.[6–10,62] Furthermore, the vertical side of the primary particles is consistently orientated towards the outer perimeter of the secondary particles, which verifies that independent of the applied stirring speed, the secondary particle size increases by the growth of the individual primary particles. In accordance with the C value analysis conducted above, the $Ni_{0.8}Co_{0.1}Mn_{0.1}(OH)_2$ secondary particles prepared at n = 1350 rpm and n = 950 rpm exhibit an equal sphericity with no radial particle extensions or recognizable traces of the initial agglomerate structure, whereby the secondary particles obtained at 1350 rpm are smaller compared to those obtained at 950 rpm. The secondary particles obtained at 550 rpm are the largest, but still exhibit an aspherical shape, which consists out of multiple radial extensions originating from the initially formed agglomerates, consistent with their still relatively low C_{50} value of ~0.8 (see Fig. 5a).

In summary, one can conclude that the stirring speed during the semi-batch coprecipitation of $Ni_{0.8}Co_{0.1}Mn_{0.1}(OH)_2$ determines the initial agglomerate size and number formed during the seeding stage, which not only governs the growth rate and thus the resulting particle size in the subsequent growth phase, but also the ability of the secondary particles to achieve a high degree of sphericity for a given particle size and run time. Overall, with increasing stirring rate, smaller $Ni_{0.8}Co_{0.1}Mn_{0.1}(OH)_2$ particles with higher sphericity can be obtained (see Fig. 5), while the PSD span is unaffected by the stirring rate (see Table I).

Cross-sectional analysis of $Ni_{0.8}Co_{0.1}Mn_{0.1}(OH)_2$ particles.—Complementary evidence for a two-stage particle formation mechanism was found by evaluation of cross-section SEM images of $Ni_{0.8}Co_{0.1}Mn_{0.1}(OH)_2$ secondary particles obtained by semi-batch coprecipitation after t_{run} = 8.75 h. Exemplary SEM cross-section images of $Ni_{0.8}Co_{0.1}Mn_{0.1}(OH)_2$ secondary particles attained at n = 1350 rpm, 950 rpm, or 550 rpm are displayed in Figs. 6a, 6c, and 6e, respectively. Independent of the stirring speed, the secondary particle structure can be divided into two parts: A particle core consisting of loosely arranged nanometer-sized primary particles, which is followed by a layer of elongated primary particles aligned around the core and orientated towards the outer perimeter of the secondary particle. This coincides well with the above observation
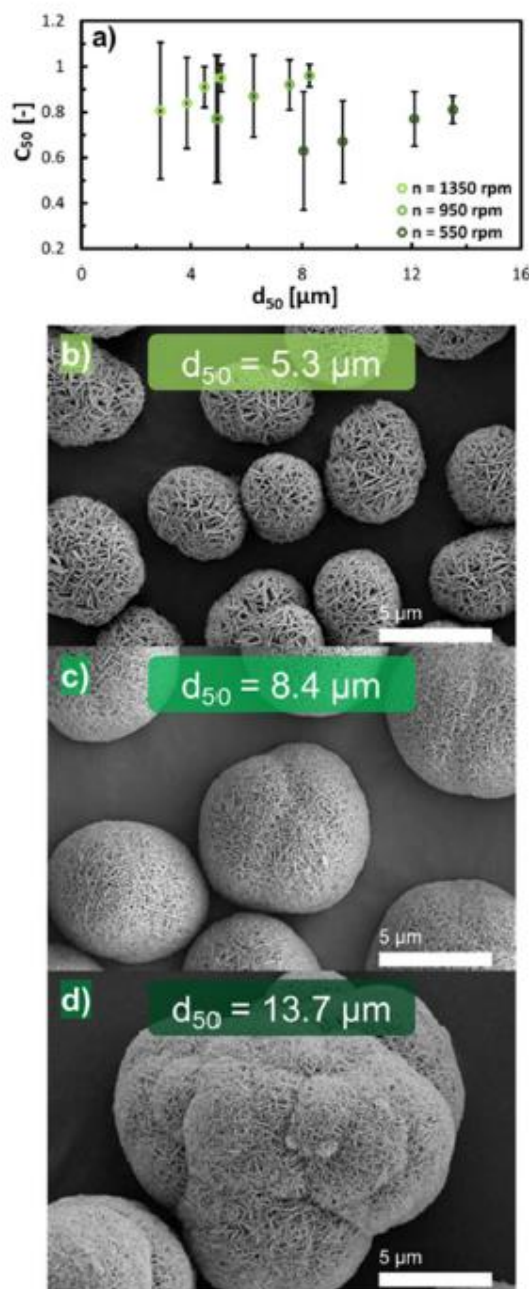
Figure 5. (a) Number median particle circularity (C_{50}) determined from SEM top-view images of secondary particles obtained at various stages of particle growth during semi-batch coprecipitation of $Ni_{0.8}Co_{0.1}Mn_{0.1}(OH)_2$ at various stirring speeds (n). The error bars represent the circularity span (C_{span}, defined by Eq. 11), which indicates the width of circularity distributions that was determined from SEM top-view images. SEM top-view images at 5 k magnification of the dried $Ni_{0.8}Co_{0.1}Mn_{0.1}(OH)_2$ secondary particles obtained after a run time of 8.75 h, with the coprecipitation conducted at different stirring speeds: (b) n = 1350 rpm; (c) n = 950 rpm; and, (d) n = 550 rpm.
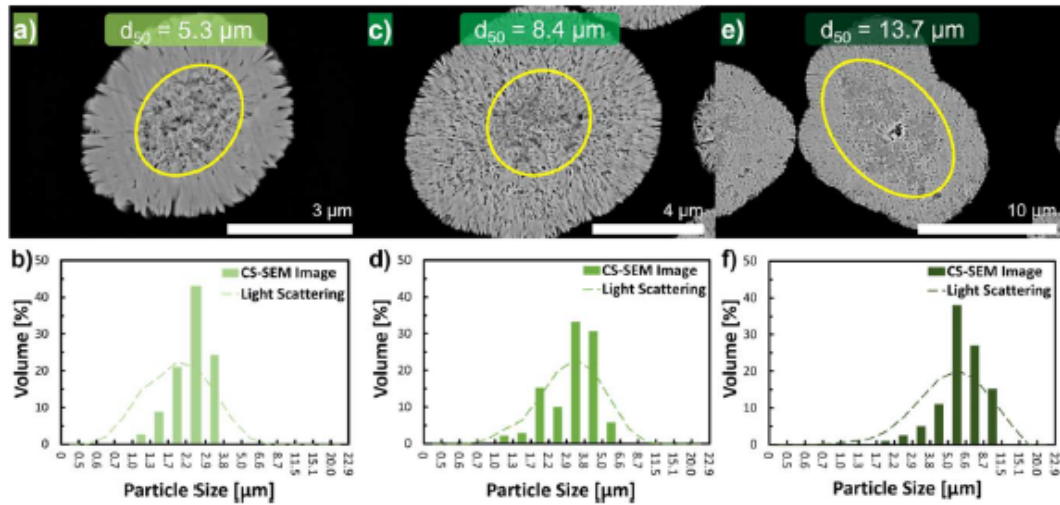
Figure 6. Exemplary cross-sectional SEM images of $Ni_{0.8}Co_{0.1}Mn_{0.1}(OH)_2$ secondary particles obtained after $t_{run} = 8.75$ h for different stirring speeds: (a) n = 1350 rpm (5 k magnification); (c) n = 950 rpm (10 k magnification); and, (e) n = 550 rpm (15 k magnification). The secondary particle core is encircled in yellow, marking the area that was used to quantify the equivalent diameter (d_{eq}, acc. to Eq. 12). The lower panels compare the volume-based particle size distributions of the $Ni_{0.8}Co_{0.1}Mn_{0.1}(OH)_2$ secondary particles obtained by semi-batch coprecipitation after $t_{run} = 1.0$ h, i.e., at the seeding-to-growth transition (dashed line, determined by light-scattering) with the volume-based core size distribution obtained by cross-sectional SEM images of coprecipitated particles (d_{eq} values based on ~50 images per run) obtained after $t_{run} = 8.75$ h (bars) and produced at different stirring speeds: (b) n = 1350 rpm; (d) n = 950 rpm; and, (f) n = 550 rpm.

Table III. The volume-based median core size of $Ni_{0.8}Co_{0.1}Mn_{0.1}(OH)_2$ secondary particles ($d^{core}_{50,8.75\,h}$) determined by the analysis of cross-sectional SEM images of $Ni_{0.8}Co_{0.1}Mn_{0.1}(OH)_2$ secondary particles attained by semi-batch coprecipitation after $t_{run} = 8.75$ h for various stirring speeds (n). This is compared to the volume-based secondary particle diameter obtained after $t_{run} = 1.0$ h ($d_{50,\,1.0\,h}$, based on laser scattering and taken from Table I). The last two columns provide the Reynolds Number (Re) calculated by Eq. 14 as well as the average volume energy input ($E_{avg.}$) calculated by Eq. 15, both being given for the conditions at $t_{run} = 0.0$ h.

Run	n [rpm]	$d^{core}_{50,8.75\,h}$ [μm]	$d_{50,\,1.0\,h}$ [μm]	Re [-]	$E_{avg.}$ [W/l]
1	550	6.2	6.2	41041	1.54
2	950	3.4	3.7	70890	7.94
3	1350	2.5	2.3	100739	22.8

that the vertical side of the plate-like shaped primary particles is consistently pointing towards the outer perimeter of the secondary particles. However, it is noteworthy that these core–shell features exhibiting radial patterns can only be observed by cross-sectional SEM imaging *if* the secondary particle has been perfectly sliced through the equator of the secondary particles during the SEM sample preparation.

Analogous to the size of the initial particles formed during the seeding stage ($t_{run} \leq 1.0$ h), the magnitude of the secondary particle core scales inversely with the applied rotation speed in the respective run. This suggests that the core within the secondary particle structure corresponds to the initial agglomerates formed during the seeding stage, which increase in size by polycrystallization. To quantitatively verify this hypothesis, the size of the core in secondary particles was determined by manual segmentation of cross-sectional SEM images. The area of the porous particle cores of ~50 cross-sectionally sliced $Ni_{0.8}Co_{0.1}Mn_{0.1}(OH)_2$ secondary particles obtained after $t_{run} = 8.75$ h for each semi-batch run was determined. The equivalent particle diameter (d_{eq}) of a circle with the identical area as the measured area of the particle core was calculated by applying Eq. 12. From the resulting d_{eq} values, volume-based core size distributions were constructed. These are shown in Figs. 6b, 6d, and 6f (green colored bars), where they are compared to the PSDs of secondary particles at the transition of the

seeding into the growth stage, i.e., at $t_{run} = 1.0$ h, which were determined by light-scattering (green colored dashed lines). Overall, the size distributions of the secondary particle cores coincide well with the light scattering derived PSDs at the transition point.

This correspondence was further quantitatively verified by determining the volume-based median core size of the $Ni_{0.8}Co_{0.1}Mn_{0.1}(OH)_2$ secondary particles ($d^{core}_{50,8.75\,h}$) from the respective cross-sectional SEM based core size distribution. Table III gives a comparison of these $d^{core}_{50,8.75\,h}$ values with the $d_{50,\,1\,h}$ values of the secondary particles obtained at the seeding-to-growth transition, i.e., at $t_{run} = 1.0$ h (obtained by laser scattering and taken from Table I), revealing an excellent agreement between these two parameters for each of the respective runs (with differences of less than 10%). Consequently, it is reasonable to assume that the core within the secondary particles corresponds to the initial agglomerates formed during the seeding stage and that the core size is inversely proportional to the stirring speed. The somewhat irregular morphology of the core might originate from the inclusion of void spaces during the chaotic aggregation of nanospheres throughout the seeding stage. After the aggregate has solidified to an agglomerate, only primary particles that are in intimate contact with the mother liquor are able to grow, as they are accessible for diffusion of lattice ions towards the solid surface. By contrast, primary particles that are located in the inside of the agglomerate are inaccessible by lattice ions, which could

potentially fill the pores among primary particles with crystallizing matter. This results in void spaces in the core compared to the shell, even though void spaces persist in the entire secondary particle structure. Similar core–shell like features of secondary particles exhibiting radially aligned primary particles were also identified by SEM imaging of cross-sectionally cut secondary particles of precipitated $Ni(OH)_2$,[60,61] $Ni_{0.75}Co_{0.15}Mn_{0.10}(OH)_2$,[64] $Ni_{0.83}Co_{0.07}Mn_{0.10}(OH)_2$,[65] and $Ni_{1/3}Co_{1/3}Mn_{1/3}(OH)_2$.[12]

Characterization of turbulence during coprecipitation of $Ni_{0.8}Co_{0.1}Mn_{0.1}(OH)_2$.—In general, the stirring speed is only an indicator for the turbulence in a stirred-tank reactor, since the turbulent flow caused by stirring also depends on the properties of the stirred fluid as well as the physical dimensions and the other features of the reaction vessel (e.g., stirrer blade configuration). For a better characterization of the prevailing turbulence in an agitated reaction vessel, the dimensionless Reynolds number (Re) and the average volume energy input ($E_{avg.}$) can be used. Both values allow comparing the turbulent motion of a fluid between distinctive reactor setups.[66–68] The Reynolds number represents the ratio of inertial forces to viscous forces of a fluid in a stirred-tank reactor and is defined as:

$$Re = \frac{\rho_{fluid} \cdot n \cdot d^2}{\mu} \quad [14]$$

Here, ρ_{fluid} is the density of the stirred fluid ($=985.0$ kg m^{-3} for H_2O at 55 °C, representing the condition at $t_{run} = 0.0$ h), n is the stirring speed in units of 1/s, d is the stirrer diameter ($=0.05$ m), and μ is the dynamic viscosity of the stirred fluid ($=0.00055$ kg ms^{-1} for H_2O at 55 °C) The parameter $E_{avg.}$ describes the kinetic energy imparted into the stirred liquid and can be calculated according to:

$$E_{avg.} = \frac{Ne \cdot \rho_{fluid} \cdot n^3 \cdot d^5}{V_{total}} \quad [15]$$

Here, Ne is the dimensionless Newton Number, which for the here used 45° pitch-blade stirrer and for the turbulent regime with Re > 10000 equals to Ne = 1.3,[69] and V_{total} is the volume of the reaction suspension ($=200$ ml at a $t_{run} = 0.0$ h).

The Re and $E_{avg.}$ values for the three different stirring rates are listed in Table III. By increasing the stirring speed from 550 rpm to 1350 rpm, Re increases by a factor of ~2.5, while $E_{avg.}$ is increased by factor of ~15. Even though an intensification of turbulence by strong stirring increases the particle collision frequency within the fluid, the shear stress induced by hydrodynamic forces on the aggregates is concomitantly amplified. This in turn results in the breakage of aggregates before cementation occurs via solid bridge formation by the further crystallization reaction. Permanent particle

attachment is additionally reduced due to the higher particle velocities with increasing turbulence, hence higher particle momentum. This leads to higher impact energy upon particle-particle collision and effectively decreases the agglomeration probability. These phenomena overall result in a decrease in the maximum aggregate and/or agglomerate size with increasing turbulence, thus increasing Re and $E_{avg.}$.[55,56] The same inverse relationship between Re and $E_{avg.}$ vs. the aggregate and agglomerate size was observed in this study. Here, during the seeding stage, the $Ni_{0.8}Co_{0.1}Mn_{0.1}(OH)_2$ particle size (i.e., $d_{50, 5 min}$ and $d_{50, 1.0 h}$, see Table I) decreases by a factor of ~2.6–2.7 when n (=input parameter for Re and $E_{avg.}$) is increased from 550 to 1350 rpm, which corresponds to an increase of n by a factor of ~2.5. Since the particle size decreases by a factor of ~2.6-2.7, the particle number ($N_{par., 5 min}$ and $N_{par., 1.0 h}$, see Table II) increases by a factor of ~18-20, which closely corresponds to $2.6-2.7^3$, as is required by a mass balance. Since the number of particles formed during the seeding stage determines the solid surface area, the growth rate (G) during the ensuing growth stage and therefore, the particle size at the end of the semi-batch experiment (i.e., $d_{50, 8.75 h}$), consequently exhibit similar correlations by factor 2.5 and 2.6 (Table I), respectively. Thus, it is rationalized that the degree of turbulence inside the stirred-tank reactor, which can be quantified by Re and $E_{avg.}$, regulates the aggregation and agglomeration during the seeding stage, which governs the size and number of $Ni_{0.8}Co_{0.1}Mn_{0.1}(OH)_2$ secondary particles formed during the seeding stage.

Similar reports on the impact of stirring speed on agglomeration rates, thus agglomerate size, have been reported for the coprecipitation of various material classes in stirred-tank reactors operated in (semi-)batch[70–72] or continuous mode.[73,74] Additionally, a decrease of the final secondary particle size accompanied by an increase in secondary particle sphericity has been observed during the continuous coprecipitation of $Ni_{1/3}Co_{1/3}Mn_{1/3}(OH)_2$,[10] $Ni_{0.90}Co_{0.05}Mn_{0.05}(OH)_2$,[75] and $Ni_{0.80}Co_{0.15}Al_{0.05}(OH)_2$[76] in a Couette Taylor reactor when increasing the rotational speed of the inner cylinder. The analogous observations have been made when increasing the stirring speed in a stirred-tank reactor during the coprecipitation of $Ni(OH)_2$,[77] $Ni_{0.5}Co_{0.2}Mn_{0.3}(OH)_2$,[9] $Ni_{0.6}Co_{0.2}Mn_{0.2}(OH)_2$,[78] and $Ni_{0.225}Co_{0.125}Mn_{0.65}(OH)_2$.[79]

Particle formation mechanism during coprecipitation of $Ni_{0.8}Co_{0.1}Mn_{0.1}(OH)_2$.—Considering the two distinctive stages in the development of the $Ni_{0.8}Co_{0.1}Mn_{0.1}(OH)_2$ secondary particle size (Fig. 2b) and respective morphology (Figs. 3 and 6) as well as the increase in secondary particle circularity as descriptor for particle sphericity (Fig. 5) during the growth phase, the two-step particle formation mechanism of $Ni_{0.8}Co_{0.1}Mn_{0.1}(OH)_2$ secondary particles depicted in Fig. 7 is proposed. Initially nucleation (I) induces the formation of nanosized spheres comprised of several twinned plate-like

Figure 7. Schematic illustration for the proposed two-step secondary particle formation mechanism during coprecipitation of $Ni_{0.8}Co_{0.1}Mn_{0.1}(OH)_2$. Initially nucleation (I) induces the formation of nanosized spheres comprised of several twinned plate-like primary particles (II) that are subjected to rapid and chaotic aggregation to undefined particle clusters (III). Due to solid bridge formation by ensuing lateral crystal growth of individual primary particles, the generated loose aggregates are consolidated to agglomerates, while primary particle growth in direction away of the agglomerate core results in radial extensions leading to aspherical secondary particles (IV). Continuous secondary particle growth by polycrystallization, which is characterized by the lateral crystal growth of individual primary particles leads to a smearing out of the initial irregular agglomerate structure, so that eventually well-defined spherical secondary particles with a core–shell structure (V) are attained.

Results

primary particles (II) that are subjected to rapid and chaotic aggregation to randomly arranged particle clusters (III). Due to solid bridge formation by ensuing lateral crystal growth of individual primary particles, the generated loose aggregates are consolidated to agglomerates, while primary particle growth in direction away of the agglomerate core results in radial extensions leading to aspherical secondary particles (IV). Continuous secondary particle growth by polycrystallization, which is characterized by the lateral crystal growth of individual primary particles leads to a smearing out of the initial irregular agglomerate structure, so that eventually well-defined spherical secondary particles with a core–shell structure (V) are attained. The size of the initial agglomerates can be manipulated by the turbulence, which governs the growth rate and the capability of secondary particles to become spherical after a given run time. Additionally, the particle size increase *within* each run is independent of their size and therefore, the surface mass specific uptake is nearly identical for every particle. This results in a narrowing PSD with progressing particle growth throughout the coprecipitation reaction.

Despite an analogous development of secondary particle morphology from irregular-shaped agglomerates to polycrystalline spherical secondary particles was observed by SEM imaging in several studies,[6,47,61,80,81] the overall proposed particle formation mechanism in this work is in contrast with prevailing theories present in the literature for the coprecipitation of M(OH)$_2$ in a stirred-tank reactor. Numerous studies report that the secondary particle enlargement during coprecipitation of M(OH)$_2$ results from a continuous agglomeration of primary particles.[9,48,75,82–84] In other instances, Ostwald ripening is suggested as the underlying particle growth mechanism, hence dissolution of generated nuclei and/or small primary particles, followed by recrystallization on existing secondary particles,[6,39,85] which is suggested to also result in a decrease in particle size distribution width with progressing coprecipitation time.[86] Others have also been claiming a simultaneous occurrence of agglomeration and Ostwald ripening.[80,81]

Since the particle collision frequency followed by permanent particle attachment during agglomeration is based on a statistic encounter of primary particles due to the isotropic turbulence in stirred vessels,[55,87,88] a random primary particle orientation would be attained as it is in the case for true aggregates and agglomerates.[89,90] Hence, a consistent orientation of the vertical side of the primary particles towards the outer perimeter of the spherical secondary particle as observed for M(OH)$_2$ (co)precipitation, accompanied by a radial alignment of primary particles around the secondary particle core, can hardly be justified by agglomeration. Furthermore, an overall irregular-shaped particle structure would be expected in contrast to spherical secondary particles. An increase in secondary particle sphericity by shear force at higher degrees of turbulence, which makes particles more spherical over time, is also questionable, as this would result in a considerable number of attritional fragments,[91,92] which were not observed by light scattering or SEM imaging, and which would lead to a deviation from the $d_{50} \sim \sqrt[3]{t_{run}}$ relationship during particle growth, due to the formation of new particles. Additionally, the emergence of a second particle modal originating from a second nucleation event after prolonged reaction time, observed by Kim et al. during semi-batch coprecipitation of Ni$_{0.855}$Co$_{0.155}$(OH)$_2$,[93] is difficult to conciliate with an agglomerate mechanism, when considering that there is no driving force for continuously generated primary particles at a certain point throughout the coprecipitation reaction to suddenly form new secondary particle agglomerates instead of agglomeration with already existing secondary particles. A surface charge controlled self-assembly of primary particles in the sense of a controlled agglomeration of primary particles as origin for circular arrangement of primaries is also highly unlikely, because the surface charge results from an electrochemical double layer that is surrounding the particles and that decreases drastically in thickness with increasing ionic strength of the solution. Accordingly, it is reported that above an ionic strength of 0.1 M, the thickness of the electrochemical double layer is below 4.0 nm for a 1:1 electrolyte, and is even further decreased for electrolytes of higher

valency.[94] For the relatively highly concentrated feed solutions (2.6 M MSO$_{4(aq.)}$ and 7.9 M NaOH) as well the volumetric flow rates in this work, the salt concentration of 0.1 M in the reaction mixture is already exceeded after only 20 min of the semi-batch coprecipitation reaction due to Na$_2$SO$_4$ formation according to Eq. 1. At such high ionic concentrations, surface charge driven phenomena become insignificant, as the critical ion concentration above which coagulation was observed to occur for Na$^+$ salt based systems was reported to be already above 0.12 M.[95] This is further emphasized by the fact that during the very early stage of crystallization the agglomeration of nanospheres for the formation of the secondary particle core could not proceed in a controlled manner and resulted in chaotic particle clusters as shown in Figs. 3b–3d.[96]

The size-dependent growth rate induced by Ostwald ripening of a solid depends amongst others on the bulk solubility of the ripening solid.[97] The coprecipitation of M(OH)$_2$ is typically conducted in the pH-regime of 11.0–13.0, in which the solubility of Ni^{2+}, Co^{2+}, and Mn^{2+} is <200 ppm.[5,37] Even though the Ni^{2+} solubility is increased by the formation of [Ni(NH$_3$)$_x$]$^{2+}$ in alkaline media, the solubility of Co^{2+} and Mn^{2+} is only negligibly affected, due to a low affinity for the complexation reaction.[5] Furthermore, since the reactants are continuously fed in the stirred vessel, supersaturation is continuously generated, which creates a steady driving force for M(OH)$_2$ crystallization rather than its dissolution. Therefore, it is rationalized that the essential driving force required for the dissolution of M(OH)$_2$ primary particles on the peripheral regions in the secondary particles and even secondary particles itself is extremely low. Hence, that the occurrence of Ostwald ripening as particle growth mechanism during coprecipitation of Ni$_{0.8}$Co$_{0.1}$Mn$_{0.1}$(OH)$_2$ is rather marginal. The argument that dissolution is unlikely to occur is further supported by the result presented in Fig. 6: Independent of the applied stirring speed for a given run, the PSD at the end of the seeding stage at t_{run} of 1.0 h coincides well with the size distribution of the secondary particle core for particles collected after t_{run} of 8.75 h. A reduction in Ni$_{0.8}$Co$_{0.1}$Mn$_{0.1}$(OH)$_2$ PSD width, i.e., that is σ (see Eq. 9), with progressing coprecipitation time, i.e., that is t_{run}, induced by Ostwald ripening is also unlikely, as it is expected that the dissolution of small particles and recrystallisation on larger particles would actually result in an increase of span instead of a decrease, since the smaller particles would decrease in size due to dissolution over the batch run time (the size of the smaller particles is represented by the d_{10} in Eq. 9), while the large particles increase in size, (the size of the larger particles is represented by the d_{90} in Eq. 9). Since an increase in σ with increasing t_{run} was not observed in this work, the effect of Ostwald ripening on the particle size distribution width can be excluded.

However, nucleation at the contact point of the injected MSO$_{4(aq.)}$ with the bulk alkaline reaction suspension inside the stirred tank reactor followed by an immediate dissolution of thereby formed nuclei and subsequent deposition as dissolved ions on primary particles within already existing secondary particles, thus resulting in crystal growth, cannot be excluded. Nonetheless, this does not interfere with the proposed particle formation mechanism that secondary particle growth occurs by growth of individual primary particles.

Interestingly, Andreassen analogously demonstrated for the precipitation of vaterite that the particle growth mechanism is governed by "spherulitic growth," hence growth of distinctive primary particles from a common core. This lead to the formation of a spherical polycrystalline secondary particle structure.[98,99] Furthermore, spherulitic crystallization as underlying particle growth mechanism was identified for several materials such as Li$_2$CO$_3$,[100] Y$_2$(OH)$_5$(NO$_3$),[101] and l-glutamic acid.[102] This conclusion was in contrast with the formerly assumed agglomeration mechanism of primary particles or nano-crystals resulting in the formation of secondary particles.[103,104] Additionally, polycrystallization can also lead to aspherical secondary particles, which deceivingly looks like an agglomerate structure, even though it does not originate from an agglomeration of primary particles, as it was suggested for Al(OH)$_3$.[105] Considering this, it is rationalized that the particle enlargement during the coprecipitation of Ni$_{0.8}$Co$_{0.1}$Mn$_{0.1}$(OH)$_2$ secondary particles is remarkably similar to spherulitic growth. However, it is worthy to

note that independent of the crystal composition, the particle growth mechanism also depends on the applied process conditions (concentration of reactants, volumetric flow rates etc).[106] Hence, a deviation to the proposed mechanism can be expected if the coprecipitation conditions diverge considerably from the applied process parameter in this work. Nevertheless, the demonstrated relationships in this work allow to optimize the secondary particle sphericity by manipulation of the turbulence in a stirred-tank reactor at otherwise constant process parameters, thereby tailoring M(OH)$_2$ based pCAM particle size and morphology to satisfy the requirements for powder processing on an industrial scale.

Conclusions

To tailor the physical properties of M(OH)$_2$ (M consisting mainly of Ni, Co, and Mn) precursor particles (pCAMs) for the preparation of cathode active materials (CAMs), the particle formation mechanism during the semi-batch coprecipitation of Ni$_{0.8}$Co$_{0.1}$Mn$_{0.1}$(OH)$_2$ in a stirred-tank reactor was investigated by varying the stirring speed between 550, 950, and 1350 rpm. The development of the secondary particle size and morphology throughout the coprecipitation reaction with a total run time of 8.75 h was monitored by light scattering and SEM imaging, respectively.

Independent of the applied stirring speed, the particle growth can be divided into two distinctive stages. Within the first hour of the reaction, the seeding stage, the particle size remains roughly constant and irregular-shaped secondary particle agglomerates are generated. In the subsequent growth phase, i.e., after a run time of 1.0 h, the agglomerates increase in size linearly proportional to the third root of time by crystal growth of individual plate-like shaped primary particles. This results in a smearing out of the initially produced aspherical agglomerate structure and an increase in secondary particle sphericity.

Further proof for a two-step particle formation mechanism was given by SEM imaging of cross-sectionally cut Ni$_{0.8}$Co$_{0.1}$Mn$_{0.1}$(OH)$_2$ secondary particles after a run time of 8.75 h. Independent of the applied stirring speed in the respective run, a secondary particle core consisting of randomly and loosely packed nanometer-sized primary particles was identified, surrounded by a dense layer of elongated plate-like shaped primary particles that are radially aligned around the core. Here, the size of the secondary particle core determined from SEM imaging coincides well with the particle size attained by light scattering at the transition between seeding and growth phase at a run time of 1.0 h. An increase of the turbulence during the coprecipitation reaction (controlled by the stirring speed) decreases the size and increases the number of the agglomerates that are formed during the seeding stage, which not only decreases the final secondary particle size, but also enhances the sphericity of the secondary particles at any given time during the growth stage.

In summary, a two-stage particle formation mechanism comprised of agglomeration and subsequent polycrystalline growth is proposed. This contrasts with the mechanisms proposed in the literature, which suggest that during coprecipitation of M(OH)$_2$ the secondary particles grow by continuous agglomeration of nucleating primary particles and/or Ostwald ripening. However, outside of the lithium-ion battery material related literature, the particle formation mechanism proposed in the present work is known as polycrystallization and closely related to spherulitic crystallization. Finally, the demonstrated relationships in this study allow to optimize secondary particle size and sphericity during coprecipitation of M(OH)$_2$ by manipulation of the turbulence in a stirred-tank reactor at otherwise constant process parameters.

Acknowledgments
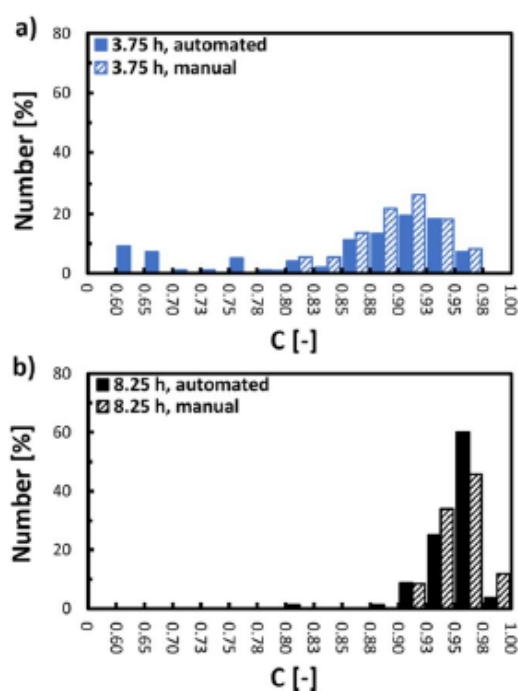
Figure A.1. Quantification of particle circularity C as descriptor for sphericity of Ni$_{0.8}$Co$_{0.1}$Mn$_{0.1}$(OH)$_2$ secondary particles by SEM top-view image analysis. Comparison of number-based circularity distributions obtained by automated (filled) and manual segmentation (unfilled), determined for Ni$_{0.8}$Co$_{0.1}$Mn$_{0.1}$(OH)$_2$ secondary particles attained by semi-batch coprecipitation at n = 950 rpm after different run times: (a) t_{run} = 3.75 h; (b) t_{run} = 8.25 h.

Appendix

ORCID

Rafael B. Berk ⓘ https://orcid.org/0000-0002-9673-9381
Hubert A. Gasteiger ⓘ https://orcid.org/0000-0001-8199-8703

References

1. W. Li, E. M. Erickson, and A. Manthiram, *Nat. Energy*, **5**, 26 (2020).
2. S.-T. Myung, F. Maglia, K.-J. Park, C. S. Yoon, P. Lamp, S.-J. Kim, and Y.-K. Sun, *ACS Energy Lett.*, **2**, 196 (2017).
3. M. H. Lee, Y. J. Kang, S. T. Myung, and Y. K. Sun, *Electrochim. Acta*, **50**, 939 (2004).
4. F. Zhou, X. Zhao, A. van Bommel, A. W. Rowe, and J. R. Dahn, *Chem. Mater.*, **22**, 1015 (2009).
5. Y. Shen, Y. Wu, H. Xue, S. Wang, D. Yin, L. Wang, and Y. Cheng, *ACS Appl. Mater. Interfaces*, **13**, 717 (2021).
6. A. van Bommel and J. R. Dahn, *Chem. Mater.*, **21**, 1500 (2009).
7. R. B. Berk, T. Beierling, L. G. Metzger, and A. Hubert, *J. Electrochem. Soc.* (2023), https://doi.org/10.1149/1945-7111/ad0b42.
8. Y. K. Sun, S. T. Myung, B. C. Park, J. Prakash, I. Belharouak, and K. Amine, *Nat. Mater.*, **8**, 320 (2009).
9. M. Noh and J. Cho, *J. Electrochem. Soc.*, **160**, 105 (2012).
10. J.-M. Kim, S.-M. Chang, J. H. Chang, and W.-S. Kim, *Colloids Surf., A*, **384**, 31 (2011).
11. A. van Bommel and J. R. Dahn, *J. Electrochem. Soc.*, **156**, 362 (2009).
12. X. Ma et al., *Joule*, **5**, 2955 (2021).
13. Y.-K. Sun, D.-H. Kim, H.-G. Jung, S.-T. Myung, and K. Amine, *Electrochim. Acta*, **55**, 8621 (2010).
14. Y.-K. Sun, D.-H. Kim, C. S. Yoon, S.-T. Myung, J. Prakash, and K. Amine, *Adv. Funct. Mater.*, **20**, 485 (2010).
15. Y.-K. Sun, B.-R. Lee, H.-J. Noh, H. Wu, S.-T. Myung, and K. Amine, *J. Mater. Chem.*, **21**, 10108 (2011).

16. Z. Xu, L. Xiao, F. Wang, K. Wu, L. Zhao, M.-R. Li, H.-L. Zhang, Q. Wu, and J. Wang, *J. Power Sources*, **248**, 180 (2014).
17. C.-K. Yang, L.-Y. Qi, Z. Zuo, R.-N. Wang, M. Ye, J. Lu, and H.-H. Zhou, *J. Power Sources*, **331**, 487 (2016).
18. D. Pritzl, T. Teufl, A. T. S. Freiberg, B. Strehle, J. Sicklinger, H. Sommer, P. Hartmann, and H. A. Gasteiger, *J. Electrochem. Soc.*, **166**, A4056 (2019).
19. J. Kim, Y. Hong, K. S. Ryu, M. G. Kim, and J. Cho, *Electrochem. Solid-State Lett.*, **9**, A19 (2006).
20. F. Riewald, P. Kurzhals, M. Bianchini, H. Sommer, J. Janek, and H. A. Gasteiger, *J. Electrochem. Soc.*, **169**, 020529 (2022).
21. L. Hartmann, D. Pritzl, H. Beyer, and H. A. Gasteiger, *J. Electrochem. Soc.*, **168**, 070507 (2021).
22. R. Jung, R. Morasch, P. Karayaylali, K. Phillips, F. Maglia, C. Stinner, Y. Shao-Horn, and H. A. Gasteiger, *J. Electrochem. Soc.*, **165**, A132 (2018).
23. J. W. Mullin, "Crystallizer Design and Operation." *Crystallization (Fourth Edition)* (Butterworth-Heinemann, Oxford) p. 403 (2001).
24. R. Wakeman, *Sep. Purif. Technol.*, **58**, 234 (2007).
25. I. B. Jenssen, S. Ucar, O. M. Dotterud, O. Bøckman, and J.-P. Andreassen, *Hydrometallurgy*, **202**, 105594 (2021).
26. D. Bourcier, J. Férrand, D. Colson, K. Mandrick, D. Ode, E. Brackx, and F. Puel, *Chem. Eng. Sci.*, **144**, 176 (2016).
27. T. Itoh and Y. Wanibe, *J. Japan Soc. Powder Powder Metall.*, **41**, 1111 (1994).
28. T. Oshima, Y.-L. Zhang, M. Hirota, M. Suzuki, and T. Nakagawa, *Adv. Powder Technol.*, **6**, 35 (1995).
29. T. Horio, M. Yasuda, and S. Matsusaka, *Int. J. Pharm.*, **473**, 572 (2014).
30. G. Gai, Y. Yang, L. Jin, X. Zou, and Y. Wu, *Powder Technol.*, **183**, 115 (2008).
31. A. Nouri and A. Sola, *Met. Powder Rep.*, **73**, 276 (2018).
32. T. Matsushita, Y. Akiyama, A. Ouki, T. Sato, and M. Kuratsuka, *Positive-electrode active material, positive electrode, battery, battery pack, electronic device, electric vehicle, electricity storage device, and electric power system*, EP3373367B1 (2021).
33. B. J. H. Bergner and R. B. Berk, *Process for making a particulate (oxy)hydroxide, and electrode active material made therefrom*, WO2021228614A1 (2021).
34. X. Chateau, "Particle Packing and the Rheology of Concrete." *Understanding the Rheology of Concrete* (Elsevier, Amsterdam) p. 117 (2012).
35. C. Meyer, H. Bockholt, W. Haselrieder, and A. Kwade, *J. Mater. Process. Technol.*, **249**, 172 (2017).
36. C. Meyer, M. Kosfeld, W. Haselrieder, and A. Kwade, *Journal of Energy Storage*, **18**, 371 (2018).
37. J. Monhemius, *Transactions Institution of Mining & Metallurgy*, **86**, C202 (1977).
38. G. Bogush, M. Tracy, and C. Zukoski IV, *J. Non-Cryst. Solids*, **104**, 95 (1988).
39. S.-L. Chen, P. Dong, G.-H. Yang, and J.-J. Yang, *J. Colloid Interface Sci.*, **180**, 237 (1996).
40. N. Doki, N. Kubota, A. Sato, M. Yokota, O. Hamada, and F. Masumi, *AIChE J.*, **45**, 2527 (1999).
41. O. Ronneberger, P. Fischer, and T. Brox, *U-Net: Convolutional Networks for Biomedical Image Segmentation, MICCAI 2015*(Springer International Publishing, Cham) p. 234 (2015).
42. P. Kurzhals, F. Riewald, M. Bianchini, S. Ahmed, A. M. Kern, F. Walther, H. Sommer, K. Volz, and J. Janek, *J. Electrochem. Soc.*, **169**, 050526 (2022).
43. D. Sinkhonde, A. Rimbarngaye, B. Kone, and T. C. Herring, *Results in Engineering*, **13**, 100368 (2022).
44. R. Osserman, *Bull. Am. Math. Soc.*, **84**, 1182 (1978).
45. C. A. Schneider, W. S. Rasband, and K. W. Eliceiri, *Nat. Methods*, **9**, 671 (2012).
46. L. M. Anovitz and D. R. Cole, *Rev. Mineral. Geochem.*, **80**, 61 (2015).
47. J. Liu, H. Chen, J. Xie, Z. Sun, N. Wu, and B. Wu, *J. Appl. Electrochem.*, **44**, 225 (2014).
48. Z. Feng, P. Barai, J. Gim, K. Yuan, Y. A. Wu, Y. Xie, Y. Liu, and V. Srinivasan, *J. Electrochem. Soc.*, **165**, A3077 (2018).
49. E. B. Slamovich and F. F. Lange, *J. Am. Ceram. Soc.*, **73**, 3368 (1990).
50. J. Myers and C. Fanelli, *J. Colloid Interface Sci.*, **536**, 98 (2019).
51. J. Garside, *Chem. Eng. Sci.*, **40**, 3 (1985).
52. H. Hojjati and S. Rohani, *Chem. Eng. Process.*, **44**, 949 (2005).
53. Z. Ji, J. Warzywoda, and A. Sacco, *Microporous Mesoporous Mater.*, **81**, 201 (2005).
54. N. Kubota and M. Onosawa, *J. Cryst. Growth*, **311**, 4525 (2009).
55. P. A. Shamlou and N. J. Titchener-Hooker, *Processing of solid-liquid suspensions*, ed. P. A. Shamlou 1 (1993).
56. D. Ilievski and I. Livk, *Chem. Eng. Sci.*, **61**, 2010 (2006).
57. Z.-H. Liang, Y.-J. Zhu, and X.-L. Hu, *J. Phys. Chem. B*, **108**, 3488 (2004).
58. A. Delahaye-Vidal, B. Beaudoin, and M. Figlarz, *React. Solids*, **2**, 223 (1986).
59. G. Sakai, M. Miyazaki, and T. Kijima, *J. Electrochem. Soc.*, **157**, A932 (2010).
60. M.-X. Peng, X.-Q. Shen, L.-S. Wang, and Y.-H. Wei, *Journal of Central South University of Technology*, **12**, 5 (2005).
61. M.-X. Peng and X.-Q. Shen, *Journal of Central South University of Technology*, **14**, 310 (2007).
62. A. van Bommel and J. R. Dahn, *J. Electrochem. Soc.*, **156**, A362 (2009).
63. G. Nichols, S. Byard, M. J. Bloxham, J. Botterill, N. J. Dawson, A. Dennis, V. Diart, N. C. North, and J. D. Sherwood, *J. Pharm. Sci.*, **91**, 2103 (2002).
64. Y. K. Sun, Z. Chen, H. J. Noh, D. J. Lee, H. G. Jung, Y. Ren, S. Wang, C. S. Yoon, S. T. Myung, and K. Amine, *Nat. Mater.*, **11**, 942 (2012).
65. Y.-K. Sun, B.-R. Lee, H.-J. Noh, H. Wu, S.-T. Myung, and K. Amine, *J. Mater. Chem.*, **21** (2011).
66. A. W. Hixson and V. D. Luedeke, *Industrial & Engineering Chemistry*, **29**, 927 (1937).
67. A. W. Nienow, *Chem. Ing. Tech.*, **86**, 2063 (2014).
68. D. Lamberto, M. Alvarez, and F. Muzzio, *Chem. Eng. Sci.*, **54**, 919 (1999).
69. R. L. Bates, P. L. Fondy, and R. R. Corpstein, *Ind. Eng. Chem. Process Des. Dev.*, **2**, 310 (1963).
70. M. Tourbin, F. Brouillet, B. Galey, N. Rouquet, P. Gras, N. Abi Chebel, D. Grossin, and C. Frances, *Powder Technol.*, **360**, 977 (2020).
71. C. Lindenberg, J. Schöll, L. Vicum, M. Mazzotti, and J. Brozio, *Cryst. Growth Des.*, **8**, 224 (2008).
72. A. P. Collier and M. J. Hounslow, *AIChE J.*, **45**, 2298 (1999).
73. S. You, Y. Li, Y. Zhang, C. Yang, and Y. Zhang, *Ind. Eng. Chem. Res.*, **52**, 12710 (2013).
74. A. Kozik, N. Hutnik, K. Piotrowski, A. Mazienczuk, and A. Matynia, *Advances in Chemical Engineering and Science*, **03**, 20 (2013).
75. D. K. Thai, Q.-P. Mayra, and W.-S. Kim, *Powder Technol.*, **274**, 5 (2015).
76. M. Seenivasan, C.-C. Yang, S.-H. Wu, W.-C. Chien, Y.-S. Wu, R. Jose, and S. J. Lue, *J. Alloys Compd.*, **857**, 157594 (2021).
77. E. Weiwei, J. Cheng, C. Yang, and Z. Mao, *Chin. J. Chem. Eng.*, **23**, 860 (2015).
78. D. Ren, Y. Shen, Y. Yang, L. Shen, B. D. A. Levin, Y. Yu, D. A. Muller, and H. D. Abruna, *ACS Applied Material Interfaces*, **9**, 35811 (2017).
79. H.-J. Jeon, S. A. Monim, C.-S. Kang, and J.-T. Son, *J. Phys. Chem. Solids*, **74**, 1185 (2013).
80. W. Hua et al., *Electrochim. Acta*, **232**, 123 (2017).
81. Y. Yang, S. Xu, M. Xie, Y. He, G. Huang, and Y. Yang, *J. Alloys Compd.*, **619**, 846 (2015).
82. D. Wang, I. Belharouak, G. Zhou, and K. Amine, *Adv. Funct. Mater.*, **23**, 1070 (2013).
83. J. Ye, Y. X. Li, L. Zhang, X. P. Zhang, M. Han, P. He, and H. S. Zhou, *ACS Appl. Mater. Interfaces*, **8**, 208 (2016).
84. X. Sun, J. Kim, and W.-S. Kim, *Chem. Eng. J.*, **421**, 129924 (2021).
85. W. Hua et al., *J. Mater. Chem. A*, **5**, 25391 (2017).
86. P. Barai, Z. Feng, H. Kondo, and V. Srinivasan, *J. Phys. Chem. B*, **123**, 3291 (2019).
87. J. Abrahamson, *Chem. Eng. Sci.*, **30**, 1371 (1975).
88. H. Schubert, *Chem. Ing. Tech.*, **51**, 266 (1979).
89. E. R. Leite, J. A. Varela, E. Longo, and C. A. Paskocimas, *Ceram. Int.*, **21**, 153 (1995).
90. J. Thati and Å. C. Rasmuson, *Eur. J. Pharm. Sci.*, **42**, 365 (2011).
91. J. Pohlisch and A. Mersmann, *Chem. Eng. Technol.*, **11**, 40 (1988).
92. C. Gahn and A. Mersmann, *Powder Technol.*, **85**, 71 (1995).
93. H. Kim and Y. Kim, *Ceram. Int.*, **46**, 19476 (2020).
94. P. C. Hiemenz and R. Rajagopalan, *Principles of Colloid and Surface Chemistry, revised and expanded* (CRC press, New York) p. 695 (2016).
95. S. Shrestha, B. Wang, and P. Dutta, *Adv. Colloid. Interface. Sci.*, **279**, 102162 (2020).
96. W. Zhang, "Nanoparticle Aggregation: Principles and Modeling." *Nanomaterial: Impacts on Cell Biology and Medicine*, ed. D. G. Capco and Y. Chen (Springer, Netherlands, Dordrecht) p. 19 (2014).
97. T. Vetter, M. Iggland, D. R. Ochsenbein, F. S. Hänseler, and M. Mazzotti, *Crystal Growth & Design*, **13**, 4890 (2013).
98. J.-P. Andreassen, *J. Cryst. Growth*, **274**, 256 (2005).
99. R. Beck and J.-P. Andreassen, *Crystal Growth & Design*, **10**, 2934 (2010).
100. Y. Wang, S. Du, X. Wang, M. Sun, Y. Yang, and J. Gong, *Powder Technol.*, **355**, 617 (2019).
101. D. K. Aleshin, M. A. Mashkovtsev, V. N. Rychkov, G. M. Bunkov, E. O. Baksheev, and N. V. Zhirenkina, *Powder Technol.*, **376**, 12 (2020).
102. R. Beck, D. Malthe-Sørenssen, and J.-P. Andreassen, *J. Cryst. Growth*, **311**, 320 (2009).
103. J. Park, V. Privman, and E. Matijević, *J. Phys. Chem. B*, **105**, 11630 (2001).
104. V. Privman, D. V. Goia, J. Park, and E. Matijević, *J. Colloid Interface Sci.*, **213**, 36 (1999).
105. B. Gnyra, R. F. Jooste, and N. Brown, *J. Cryst. Growth*, **21**, 141 (1974).
106. R. Beck and J.-P. Andreassen, *J. Cryst. Growth*, **312**, 2226 (2010).

3.2 Impurity content, crystallinity, and secondary particle morphology

This section presents the article "Impact of Sulfate Adsorption on Particle Morphology during the precipitation of Ni-rich Hydroxide Precursors for Li-Ion Cathode Active Material". The manuscript was submitted to the peer-reviewed Journal of the Electrochemical Society in July 2023 and published in November 2023. The article is published open access and distributed under the terms of the Creative Commons Attribution 4.0 License. The permanent web link is: https://iopscience.iop.org/article/10.1149/1945-7111/ad0b42/meta. A summary of the article was presented by Rafael B. Berk as oral presentation (abstract number A06-0596) at the 242nd Meeting of the Electrochemical Society in Atlanta, Georgia, October 9th-13th, 2022.

Nickel-rich layered lithium nickel cobalt manganese oxides (NCMs) have solidified their position as cathode active material (CAM) for lithium-ion batteries in electric vehicle applications, since NCMs exhibit a high energy density at sufficiently low cost.[13, 188] Current industrial manufacturing of NCMs involves the coprecipitation of mixed metal hydroxide ($M(OH)_2$) particles (M consisting mainly of Ni, Co, and Mn) as precursor for CAM (referred to as pCAM) from a mixed metal sulfate solution ($MSO_{4(aq.)}$).[13, 56] The thereby attained secondary particles are comprised of numerous primary particles.[56, 74, 113] After the ensuing calcination reaction of the pCAM with a lithium compound at elevated temperatures to obtain the final NCM, the secondary particle architecture of the pCAM is maintained.[68, 70-72] In this context, it was demonstrated that the morphology and electrochemical performance of NCMs is affected by the physical properties of the respective pCAM utilized for synthesis.[73-75] So far, the relationship between coprecipitation parameters and pCAM morphology were primarily studied in an empirical manner.[43, 121] Therefore, an in-depth knowledge of the coprecipitation reaction and morphology control of the hydroxide precipitate in regard to the process parameters is still missing the literature.

To promote the mechanistic understanding of the $M(OH)_2$ particle formation, ten distinctive $Ni_{0.8}Co_{0.1}Mn_{0.1}(OH)_2$ particle lots were prepared in this study via the coprecipitation method in a stirred tank reactor by adjusting the coprecipitation pH-value at otherwise constant process parameters. Elemental analysis of the resulting $Ni_{0.8}Co_{0.1}Mn_{0.1}(OH)_2$ powders revealed a pH-dependent SO_4^{2-} adsorption equilibrium, which determines the SO_4^{2-} uptake in the $Ni_{0.8}Co_{0.1}Mn_{0.1}(OH)_2$ pCAM during the coprecipitation reaction. Investigation of the precipitates by X-ray diffraction shows that the SO_4^{2-} not only governs the crystallinity of the $Ni_{0.8}Co_{0.1}Mn_{0.1}(OH)_2$ material but also regulates the crystal growth in (001) direction. The latter

in turn affects the vertical primary particle size and the secondary particle porosity, both observable by SEM imaging. The morphological trend is quantitatively verified by extracting the primary particle size distribution from SEM images and by determination of the secondary particle porosity via nitrogen physisorption. As proof-of-concept for the proposed impact of the SO_4^{2-} adsorption, $Ni_{0.8}Co_{0.1}Mn_{0.1}(OH)_2$ was precipitated at constant pH-value but using different metal feed stocks ($MX_{(aq.)}$, with $X = SO_4^{2-}$, $(NO_3^-)_2$, $(CH_3COO^-)_2$). The resulting distinct physical properties of the $Ni_{0.8}Co_{0.1}Mn_{0.1}(OH)_2$ particles obtained from the various anion systems, exhibiting different anion adsorption affinities, can be well understood based on the Fajans-Paneth-Hahn law for crystallization.[187] Further, desorption experiments present options to reduce the amount of residual SO_4^{2-} after the $Ni_{0.8}Co_{0.1}Mn_{0.1}(OH)_2$ particle formation has been completed. In the end, pCAM design rules are discussed based on the findings of this work.

Author contributions

R.B.B. carried out the coprecipitation experiments and the processing of data from analytical measurements. All authors discussed and commented the data, as well as the conclusions. R.B.B. wrote the manuscript. T.B., L.M., and H.A.G. edited the manuscript.

Impact of Sulfate Adsorption on Particle Morphology during the Precipitation of Ni-Rich Hydroxide Precursors for Li-Ion Battery Cathode Active Materials

Rafael B. Berk,[1,2,z] Thorsten Beierling,[3] Lukas Metzger,[4] and Hubert A. Gasteiger[2]

[1]*BASF SE, New Battery Materials and Systems, D-67056 Ludwigshafen, Germany*
[2]*Chair of Technical Electrochemistry, Department of Chemistry and Catalysis Research Center, Technical University of Munich, D-85748 Garching, Germany*
[3]*BASF SE, Battery Materials Process Technology, D-67056 Ludwigshafen, Germany*
[4]*BASF SE, Crystallization and Precipitation, D-67056 Ludwigshafen, Germany*

Nickel-cobalt-manganese-hydroxides ($Ni_xCo_yMn_z(OH)_2$, with $x+y+z = 1$) are utilized as precursor for lithium-ion battery cathode active material (CAM). The physical properties and electrochemical performance of CAM are affected by the morphology, crystallinity and impurity content of the associated $Ni_xCo_yMn_z(OH)_2$ (with $x+y+z = 1$) employed for the CAM synthesis. To promote the mechanistic understanding of the $Ni_xCo_yMn_z(OH)_2$ (with $x+y+z = 1$) formation, the coprecipitation $pH_{23\,°C}$-value was systematically varied from 8.6–12.7 during the synthesis of $Ni_{0.8}Co_{0.1}Mn_{0.1}(OH)_2$, and the obtained powders were characterized by elemental analysis. A dependency of residual sulfur content and crystallinity of the obtained $Ni_{0.8}Co_{0.1}Mn_{0.1}(OH)_2$ on the pH-value in relation to the point-of-zero-charge (pzc) is revealed. This result is rationalized by a pH-dependent sulfate adsorption equilibrium. Furthermore, a suppression of the growth along the (001) plane of the crystallites due to sulfate adsorption is identified. This in turn governs the vertical primary particle size and thus the porosity of the secondary particles, which was verified by substituting the sulfate ion of the metal feed by nitrate or acetate. Adsorption/desorption experiments demonstrate the possibility to decouple secondary particle morphology and residual impurity content. The demonstrated relationships allow formulating design strategies to tailor the $Ni_xCo_yMn_z(OH)_2$ (with $x+y+z = 1$) morphology and its impurity content for its CAM synthesis.

Lithium-ion battery (LIB) technology has established itself as power source for consumer electronics and battery electric vehicles (BEVs).[1–3] One of the key focus areas in LIB research is the cathode active material (CAM), as it is the most cost intensive component of LIBs and as it has significant impact on the overall achievable energy density and lifetime of the cell.[4–6] Layered lithium transition metal (TM) oxides such as lithium-nickel-cobalt-manganese-oxides ($LiNi_xCo_yMn_zO_2$, with $x+y+z = 1$ (NCMs)) present a promising class of materials for next-generation LIBs.[7–9] Especially Ni-rich NCMs with relative nickel contents of $x > 0.8$ are in the focus of academic and industrial research, since they meet the requirements of BEVs due to their high energy density at sufficiently low cost.[10]

The currently used standard industrial manufacturing of CAMs can be divided into two process steps: The first step is the coprecipitation of mixed TM hydroxide particles ($Ni_xCo_yMn_z(OH)_2$, with $x+y+z = 1$) as precursor for the final CAM (referred to as pCAM). In a second step, the pCAM is mixed with a lithium salt (typically lithium hydroxide or carbonate) and then calcined under air or oxygen at elevated temperatures to yield layered lithium TM oxides.[11,12] The coprecipitation of the pCAM is commonly conducted by the simultaneous introduction of an aqueous solution of the mixed TM sulfates ($TMSO_{4(aq.)}$), an aqueous sodium hydroxide solution ($NaOH_{(aq.)}$), and an aqueous ammonia solution ($NH_{3(aq.)}$) into a stirred-tank reactor, which is under nitrogen atmosphere to avoid phase separation in $Ni_xCo_yMn_z(OH)_2$ (with $x+y+z = 1$) induced by the oxidation of Mn^{2+} to Mn^{3+}/Mn^{4+}. The coprecipitated pCAM particles exhibit secondary particle sizes in the μm-range ($\sim$4-16 μm) and a spherical secondary particle morphology that is composed of many hexagonal-plate like primary particles in the sub-μm range.[12–16] It is suggested that these primary particles consist of several $Ni_xCo_yMn_z(OH)_2$ (with $x+y+z = 1$) crystallites[16] that are structurally related to layered brucite-type β-$Ni(OH)_2$.[14,17–20] Despite several phase transitions that occur during calcination of a pCAM with a lithium salt

(shown, e.g., for $LiNiO_2$ (LNO)[21]), the secondary particle structure of the pCAM is generally preserved after the high-temperature calcination in the resulting CAM.[22–24] Recently, correlations of CAM morphology with the electrochemical performance in the cell have been demonstrated for LNO, highlighting the significance of the primary particle size.[25,26] Furthermore, it has been demonstrated that the electrochemical performance of a CAM is affected by the morphology of the associated pCAM.[13,27] For this purpose, empirical optimization studies for the energy density of a CAM were conducted by variation of process parameters during the coprecipitation reaction.[11,28] However, a detailed understanding regarding the impact of the process parameters on the course of the coprecipitation reaction and on the physical properties of the precipitated pCAM (crystal structure, impurity content, primary and secondary particle size, secondary particle porosity, etc.) is still lacking.

In order to gain mechanistic insights into the $Ni_xCo_yMn_z(OH)_2$ with $(x+y+z = 1)$ particle formation, ten distinctive $Ni_{0.8}Co_{0.1}Mn_{0.1}(OH)_2$ particle lots were prepared by the coprecipitation method in a stirred-tank reactor. The coprecipitation pH-value was systematically varied between each experiment, while all other process parameters remained constant. The dependency of the residual sulfate (SO_4^{2-}) content on the coprecipitation pH-value was examined by elemental analysis and related with the point-of-zero-charge (pzc) of nickel hydroxide ($Ni(OH)_2$), suggesting that the SO_4^{2-} content of the pCAM is governed by the pH-dependent SO_4^{2-} adsorption equilibrium. The effect of SO_4^{2-} adsorption on crystallinity and primary particle growth was investigated by X-ray diffraction analysis, while its effect on secondary particle morphology and porosity was followed by SEM imaging. The changes in morphology were quantified by extracting the primary particle size distribution from SEM images and by determination of the secondary particle porosity via nitrogen physisorption. The role of SO_4^{2-} adsorption was further investigated by comparative pCAM coprecipitation experiments with TM nitrate or TM acetate feed solutions as well as SO_4^{2-} adsorption/desorption experiments. Finally, a mechanism for the impact of SO_4^{2-} adsorption on the secondary particle morphology during coprecipitation of $Ni_{0.8}Co_{0.1}Mn_{0.1}(OH)_2$ is proposed, and pCAM design rules are discussed.

zE-mail: rafael-benjamin.berk@basf.com

Experimental

Materials and methods.—The following aqueous TM salt solutions were obtained from BASF SE ($\geqslant$99.0%): Nickel(II) sulfate solution (2.2 mol l^{-1} NiSO$_{4(aq.)}$), cobalt(II) sulfate solution (2.2 mol l^{-1} CoSO$_{4(aq.)}$), manganese(II) sulfate solution (2.2 mol l^{-1} MnSO$_{4(aq.)}$), nickel(II) nitrate solution (2.2 mol l^{-1} Ni(NO$_3$)$_{2(aq.)}$), cobalt(II) nitrate solution (2.2 mol l^{-1} Co(NO$_3$)$_{2(aq.)}$), manganese(II) nitrate solution (2.2 mol l^{-1} Mn(NO$_3$)$_{2(aq.)}$), nickel(II) acetate solution (0.6 mol l^{-1} Ni(CH$_3$COO)$_{2(aq.)}$), cobalt(II) acetate solution (0.6 mol l^{-1} Co(CH$_3$COO)$_{2(aq.)}$), and manganese(II) acetate solution (0.6 mol l^{-1} Mn(CH$_3$COO)$_{2(aq.)}$). From these, a mixed TM sulfate solution TMSO$_{4(aq.)}$, a mixed TM nitrate solution TM(NO$_3$)$_{2(aq.)}$, and a mixed TM acetate solution TM(CH$_3$COO)$_{2(aq.)}$ were prepared by combining the respective TM salt solutions in a molar ratio of M = Ni/Co/Mn = 8/1/1 to achieve an overall metal concentration of 2.2 mol l^{-1}, 2.2 mol l^{-1} and 0.6 mol l^{-1}, respectively. A lower concentration for TM(CH$_3$COO)$_{2(aq.)}$ was utilized due to the solubility limit of the respective TM acetates. Furthermore, sodium hydroxide solution (25 wt% ($\equiv$7.9 mol l^{-1}) and 10 wt% NaOH$_{(aq.)}$ ($\equiv$2.8 mol l^{-1}), $\geqslant$99.0% purity), ammonia solution (25 wt% NH$_{3(aq.)}$ ($\equiv$13.2 mol l^{-1}), $\geqslant$99.0% purity), sulfuric acid solution (6 M H$_2$SO$_{4(aq.)}$, $\geqslant$99.0% purity) and hydrochloric acid solution (2 wt% ($\equiv$0.7 mol l^{-1}) and 5 M HCl$_{(aq.)}$, $\geqslant$99.0% purity) were obtained from Bernd Kraft GmbH (Germany). All solutions were used as they arrived from the chemical suppliers without any further purification.

Coprecipitation of Ni$_{0.8}$Co$_{0.1}$Mn$_{0.1}$(OH)$_2$.—Ni$_{0.8}$Co$_{0.1}$Mn$_{0.1}$(OH)$_2$ particles were prepared semi-batch wise in a 480 ml stirred-tank reactor under nitrogen atmosphere (with a N$_2$ purge flow of 2.0 l h^{-1}), equipped with a temperature control unit and a pH-probe (HA 405-DXK-S8, Mettler Toledo) for monitoring the internal pH-value of the solution (for a sketch of the reactor setup see Fig. A-1). The glass vessel with a double jacket for circulating a heating fluid had an inner diameter of 8 cm, a height of 15 cm, and an outer diameter of 15 cm; it was equipped with baffles, a three-stage 45° pitch-blade stirrer with a diameter of 5 cm, and three dosing tubes for the respective reactant solutions, the mixed TM solutions (TMSO$_{4(aq.)}$, TM(NO$_3$)$_{2(aq.)}$ or TM(CH$_3$COO)$_{2(aq.)}$; referred to as TMX$_{(aq.)}$ in Fig. A-1), the sodium hydroxide solution (NaOH$_{(aq.)}$), and the ammonia solution (NH$_{3(aq.)}$). The three dosing tubes (1 mm inner and 2 mm outer diameter) were introduced through the sealed top of the reactor, separated from each other by 4 cm each (with a total distance of 8 cm between the MX$_{(aq.)}$ and the NaOH$_{(aq.)}$ inlets); the tube outlets were positioned in the reactor 3 cm above the maximum liquid level, which corresponds to 12 cm from the bottom of the reactor.

Before starting the coprecipitation reaction, the vessel was charged with 150 ml deionized H$_2$O and the deionized inside the stirred tank reactor was degassed by purging it for 1 h with nitrogen gas with a flow rate of 2.0 l h^{-1}. This nitrogen gas flow rate was maintained throughout the entire reaction time. Further, 3.2 ml of 25 wt% NH$_{3(aq.)}$ solution were added to achieve an overall NH$_{3(aq.)}$ concentration in the reactor of 0.28 mol l^{-1}. The temperature was set to 55 °C via circulation of tempered silicon oil through the double jacket, while the stirring speed was kept constant at 700 rpm, corresponding to an average energy input of 4.2 W l^{-1} at the start of the reaction with an initial liquid volume of 150 ml. The internal reaction pH-value measured at the solution temperature of 55 °C was referenced to an external pH-value measured at 23 °C (pH$_{23\,°C}$; via an InLab SemI MIcro, Mettler Toledo) by taking solution samples from the reactor and measuring the pH-value at 23 °C. The internal pH electrode was calibrated at 55 °C, while the external electrode was calibrated at 23 °C; in both cases, buffer solutions with pH$_{23\,°C}$ = 7.0 and pH$_{23\,°C}$ = 12.0 were employed (Certipure, Merck KGaA).

The coprecipitation reaction was initiated by simultaneously feeding the TMSO$_{4(aq.)}$ solution at a volumetric flow rate of 40 ml h^{-1} and the NH$_{3(aq.)}$ solution at a volumetric flow rate 2 ml h^{-1} into the reactor, corresponding to a molar NH$_3$/TM ratio of 0.3. The NaOH$_{(aq.)}$ solution flow was controlled by a flow

control-unit (Dulcometer, Prominent) linked to the internal pH-probe to maintain a constant pH-value throughout the reaction; it was close to the predicted volumetric flow rate of 23 ml h^{-1}. The deviation from the set-pH-value was ± 0.03. The coprecipitation pH-value at 23 °C was varied from pH$_{23\,°C}$ = 8.6–12.7, while all other process parameters were kept constant. After 5 h reaction time, the total solution volume was 470 ml and the reactant flows were stopped. The obtained product suspension was collected, filtered with a Buchner funnel, H$_2$O was poured over the filter cake in a 10:1 weight ratio of H$_2$O to solid, and the solid was finally dried in air at 120 °C for 12 h in an oven (universal Oven U, Memmert).

The coprecipitation of Ni$_{0.8}$Co$_{0.1}$Mn$_{0.1}$(OH)$_2$ particles from the mixed TM nitrate solution (TM(NO$_3$)$_{2(aq.)}$) was done analogously as with the mixed TM sulfates (TMSO$_{4(aq.)}$). In the case when the mixed TM acetate solution (TM(CH$_3$COO)$_{2(aq.)}$) was used, all process parameters remained unchanged, except that the initial NH$_{3(aq.)}$ concentration in the reactor was adjusted to 0.12 mol l^{-1}, by adding 1.4 ml NH$_{3(aq.)}$, and the NaOH$_{(aq.)}$ flowrate was 6 ml h^{-1}, while the NH$_{3(aq.)}$ flowrate was 0.7 ml h^{-1}. The initial NH$_{3(aq.)}$ concentration and flowrate were adjusted to achieve the same NH$_3$/TM as for the coprecipitations from TMSO$_{4(aq.)}$ and TM(NO$_3$)$_{2(aq.)}$. The total solution volume after 5 h reaction time was 400 ml. For TM(NO$_3$)$_{2(aq.)}$ and TM(CH$_3$COO)$_{2(aq.)}$, the coprecipitation was conducted at only at pH$_{23\,°C}$ = 12.0, while all other process parameters remained unchanged. An overview of the relevant soluble and insoluble components inside the stirred tank reactor after completed coprecipitation reaction of 5 h is given Table A-I in the Appendix.

Point-of-zero-charge (pzc) determination.—The pzc of the respective TM hydroxide was determined employing a mass titration method described elsewhere.[29,30] In this method, the investigated solid oxide/hydroxide is step wise added to a solution at a defined pH-value. At a certain pH-value, the pH-value will not vary anymore upon solid addition and will remain constant. This pH-value corresponds to the pzc.

Nickel hydroxide Ni(OH)$_2$ and Ni$_{0.8}$Co$_{0.1}$Mn$_{0.1}$(OH)$_2$ for pzc-determination were prepared at pH$_{23\,°C}$ = 11.6 from TMSO$_{4(aq.)}$ as described above. The respective dried precipitate was stepwise added to an aqueous NaOH$_{(aq.)}$ solution at a pH$_{23\,°C}$ = 12.0 (InLab SemI Micro, Mettler Toledo) until the pH-value remained constant after solid addition. That pH-value corresponds to the pzc of the solid. The pzc of Ni(OH)$_2$ was determined to pH$_{23\,°C}$ = 10.6, while for Ni$_{0.8}$Co$_{0.1}$Mn$_{0.1}$(OH)$_2$ the pzc was obtained at pH$_{23\,°C}$ = 10.5.

Sulfate adsorption/desorption and washing experiments.—After the coprecipitation of sulfate based Ni$_{0.8}$Co$_{0.1}$Mn$_{0.1}$(OH)$_2$ at pH$_{23\,°C}$ = 11.6 according to the experimental procedure described above, the adsorption/desorption of sulfate from the precipitate by variation of the solution pH was investigated. For this, the product suspension was kept inside the reactor after the coprecipitation reaction, and the pH-value was adjusted by either addition of the 25 wt% NaOH$_{(aq.)}$ or the 2 wt% HCl$_{(aq.)}$ solution over a time span of 10 s while stirring at 700 rpm until the desired pH-value was achieved. The pH-values were selected in this range, to evaluate the adsorption of sulfate at a pH$_{23\,°C}$-value < pzc of Ni$_{0.8}$Co$_{0.1}$Mn$_{0.1}$(OH)$_2$, namely pH$_{23\,°C}$ = 11.0, and the desorption at pH$_{23\,°C}$-values > pzc of Ni$_{0.8}$Co$_{0.1}$Mn$_{0.1}$(OH)$_2$, namely pH$_{23\,°C}$ = 12.0, 12.5 and 13.0., filtered with a Buchner funnel, and H$_2$O was poured over the filter cake in a 10:1 weight ratio of H$_2$O:solid, and the resulting solid was dried in air at 120 °C for 12 h in an oven (universal Oven U, Memmert). Finally, the sulfur content of the samples was determined (as shown below in elemental analysis).

In addition, washing experiments were performed with an additional batch of sulfate based Ni$_{0.8}$Co$_{0.1}$Mn$_{0.1}$(OH)$_2$ coprecipitated at pH$_{23\,°C}$ = 11.6. The collected product suspension was divided into three equal lots. Subsequently, the suspension was filtered with a Buchner funnel, and 10 wt% NaOH$_{(aq.)}$ was poured

over the filter cake. The weight ratio of applied $NaOH_{(aq.)}$ to the respective $Ni_{0.8}Co_{0.1}Mn_{0.1}(OH)_2$ precipitate was varied between 1/3, 2/3, and 1/1, respectively. After the $NaOH_{(aq.)}$ wash, H_2O was poured over the filter cake in a 10:1 weight ratio of H_2O:solid, and the resulting solids were dried in air at 120 °C for 12 h in an oven (universal Oven U, Memmert). Finally, the sulfur content of the samples was determined (as shown below in elemental analysis).

Elemental analysis.—The elemental composition of the dried pCAM samples was determined by inductively coupled plasma-optical emission spectroscopy (ICP-OES, Agilent Technologies 5100/ICP MS Triple Quad, Agilent Technologies 8800). For this purpose, a small amount of sample (~0.3 g) was dispersed in 5 M aqueous HCl solution. The mixture was stirred and heated in a beaker until the solid powder was completely dissolved. Afterwards, the mixture was cooled down, diluted with deionized H_2O until a concentration of 0.5 M HCl was reached, and the TM content in the sample was determined by ICP-OES.

Residual sulfur content was determined by filling 10 mg of a pCAM sample in a tin capsule and catalytically decomposing any sulfur species over a WO_3/Al_2O_3 catalyst at 1100 °C in a He/O_2 gas stream to SO_2 and SO_3, whereby SO_3 was subsequently reduced to SO_2 by copper granulate. The resulting SO_2 was quantified by a nondispersive infrared-detector system (NDIR, Elementar, Vario Cube). In the following, the residual sulfur content will be referenced to the TM content in terms of $mol_S/(mol_{TM}+mol_S)$ (in mol%), whereby the residual sulfur was ascribed to residual sulfate.

Residual carbon content was quantified by filling 0.2 g of a pCAM sample into a single-use ceramic cup (Eltra GmbH), adding approximately 0.5 g of Fe granulate, and covering the mixture with a layer of 1.5 g W granulate. The mixture was subsequently heated in an induction furnace under oxygen flow to 3000 °C. Residual carbon in the sample was thereby converted into CO_2 and quantified by an NDIR-device coupled to the induction furnace (Eltra GmbH, CS800). In the following, the residual carbon content will be given in terms of $mol_C/(mol_{TM}+mol_C)$ (in mol%), whereby the residual carbon was ascribed to residual acetate.

Residual nitrogen was determined by dispersing 0.2 g of a pCAM sample in 6 M $H_2SO_{4(aq.)}$ in a glass beaker and then performing a modified Kjehldahl digestion to reduce any nitrate species in the sample to NH_3.[31] The developing NH_3 gas representative for residual nitrogen was captured by Nessler's reagent and quantified by UV-VIS spectrometry (Shimadzu). In the following, the residual nitrogen content will be given in terms of $mol_N/(mol_{TM}+mol_N)$ (in mol%), whereby the residual nitrogen was ascribed to residual nitrate.

Powder X-ray diffraction measurements (PXRD).—X-ray Diffraction data were collected using a laboratory diffractometer (D8 Discover, Bruker AXS GmbH). The instrument was set up with a Molybdenum X-ray tube. The characteristic K-alpha radiation ($\lambda = 0.71$ Å) was monochromatized using a bent Germanium Johansson type primary monochromator. Data were collected in the Bragg-Brentano reflection geometry between 5–50° of 2θ, with $0.02°$ and 3 s step^{-1}. A LYNXEYE area detector was utilized to collect the scattered X-ray signal. $Ni_{0.8}Co_{0.1}Mn_{0.1}(OH)_2$ pCAM samples were ground using an IKA tube-mill and an MT40.100 disposable grinding chamber. The resulting powder was placed in a sample holder and flattened using a glass plate. The vertical and lateral crystallite size in the $Ni_{0.8}Co_{0.1}Mn_{0.1}(OH)_2$ samples were calculated based on the (001) reflex (7.8–10.0° of 2θ) and (100) reflex (14.5°–16.0° of 2θ), respectively, by applying the Scherrer equation using the DIFFRAC.EVA V6 software (Bruker AXS GmbH).[32]

$$CS = \frac{K\lambda}{(\cos\theta)B} \qquad [1]$$

where CS is the crystallite size, K is the Scherrer constant ($=0.89$), λ is the wavelength of the Molybdenum K-alpha1 radiation ($=0.71$ Å), θ is the respective reflex position and B is the full width at half maximum (FWHM) of the respective reflection, which amounts to B $= B_{inst.} + B_{cryst.}$. Here $B_{inst.}$ is the reflection broadening originating from the utilized XRD instrument ($=0.05°$ for the Molybdenum K-alpha1), while $B_{cryst.}$ is the reflection broadening caused by the crystal size. The contribution of the crystal strain to reflex broadening was not considered.

Nitrogen physisorption measurements.—Specific surface area and porosity of $Ni_{0.8}Co_{0.1}Mn_{0.1}(OH)_2$ particles were determined by measuring nitrogen physisorption isotherms at 77 K (ASAP2420, Micromeritics). Prior to the measurements, pCAM powders were degassed at 120 °C for three hours. The specific surface area was extracted from the adsorption isotherms in the relative pressure range of $0.05 < p/p_0 < 0.30$ using the Brunauer-Emmet-Teller (BET) theory.

Initially, it was attempted to determine the internal porosity of the $Ni_{0.8}Co_{0.1}Mn_{0.1}(OH)_2$ secondary particles by Mercury intrusion porosimetry, but the structural integrity of the secondary particles could not be maintained during these measurements. However, since the SEM analysis of the pCAM particles showed that internal pores were smaller than ~300–400 nm (see Fig. 5), the internal porosity could be determined via N_2 capillary condensation in these pores at a high relative p/p_0 value of 0.995. Based on the Kelvin equation, the pore diameter d_K describes the maximum pore size at a given relative pressure at which liquid nitrogen can be formed:[33]

$$d_K = \frac{-2\gamma V_m}{R\,T\,\ln\left(\frac{p}{p_0}\right)} \qquad [2]$$

where γ is the surface tension of N_2 at 77 K ($=8.85 \times 10^{-7}$ J cm^{-2}), V_m is the molar volume of liquid N_2 ($=34.7$ cm^3 mol^{-1}), R is the gas constant ($=8.314$ J/(mol·K)), and T is the boiling point of nitrogen ($=77$ K). For a relative pressure of $p/p_0 = 0.995$, the condensation of liquid nitrogen then occurs in pores with diameter below $d_K \approx 380$ nm, so that the amount of condensed nitrogen should closely correspond to the internal volume of the pCAM materials, thereby yielding the intra-particle porosity, ε_{intra} (assuming all pores are smaller than ~380 nm, consistent with the later shown SEM images). The validity of this approach was demonstrated previously by Strehle, who compared the internal porosity values of the secondary particles of several CAMs obtained by Mercury intrusion porosimetry and by nitrogen physisorption.[34]

The specific liquid volume condensed in the pores can then be determined by the following equation:[35]

$$V_{N2,liquid} = V_{N2,STP}\frac{\rho_{N2,STP}}{\rho_{N2,liquid}} \qquad [3]$$

where $V_{N2,liquid}$ is the specific liquid N_2 volume condensed in the pCAM secondary particle pores, $V_{N2,STP}$ is the total amount of measured adsorbed N_2 at a relative pressure of $p/p_0 \approx 0.995$, $\rho_{N2,STP}$ is the density of N_2 at standard temperature 273.15 K and pressure 101325 Pa ($=1.25$ mg cm^{-3}), and $\rho_{N2,liquid}$ is the density of liquid N_2 at 77 K ($=0.809$ g cm^{-3}). The intra-particle porosity can then be calculated according to:[36]

$$\varepsilon_{intra} = \frac{V_{N2,liquid}}{V_{N2,liquid} + \frac{1}{\rho_{cryst.}}} \qquad [4]$$

where $\rho_{cryst.}$ is the crystallographic density of $Ni_{0.8}Co_{0.1}Mn_{0.1}(OH)_2$. Here, a molar averaged crystallographic density of 3.96 g cm^{-3} is assumed, based on the crystallographic density of $Ni(OH)_2$ ($=4.10$ g cm^{-3}), $Co(OH)_2$ ($=3.60$ g cm^{-3}), and $Mn(OH)_2$ ($=3.26$ g cm^{-3}) and the TM ratio of 8/1/1.

Scanning electron microscopy (SEM).—The morphology of the obtained pCAM particles was characterized by attaching the $Ni_{0.8}Co_{0.1}Mn_{0.1}(OH)_2$ powder onto a SEM pin holder (Agar Scientific, Ltd.), which is covered with conducting carbon (Plano GmbH). Subsequently, the sample was coated with a 6 nm platinum layer by sputter deposition (SCD 500 Sputter Coater, Bal-Tec AG). Top-view SEM imaging was performed using a thermal field emission cathode and an Everhat-Thornley secondary electron detector at an operating voltage of 5 kV (Ultra 55, Carl Zeiss Ag).

Samples for cross-section measurements were prepared by mixing 2 g of epoxy resin with 0.5 g of epoxy hardener (Buehler, ITW Test & Measurement GmbH) and then adding a few drops of the mixture to the respective $Ni_{0.8}Co_{0.1}Mn_{0.1}(OH)_2$ pCAM sample in a gelatine capsule (Plano GmbH). The resulting slurry was cast onto an aluminum foil using a manual coater with a gap size of 0.5 mm, followed by drying the coating in an oven at 40 °C overnight. Small sections thereof were transferred to an ion-milling system (ArBlade 5000, Hitachi, Ltd.) equipped with an Ar-ion beam at an operating voltage of 6 kV. Images were taken as described above for the top view measurements.

The vertical size of the primary particles in the pCAM (corresponding to the 001-plane in crystallographic notation) was manually determined from top-view SEM images of the $Ni_{0.8}Co_{0.1}Mn_{0.1}(OH)_2$ secondary particles taken at 50 k magnification, using the ImageJ software.[37] Considering that the curvature of the spherical secondary particle could falsify the vertical primary particle size, only particles were segmented for which the "edge" of primary particles is perpendicularly exposed towards the perspective of the observer.

High resolution-transmission electron microscopy (HR-TEM).—Samples for HR-TEM measurements were prepared by focused ion beam (FIB) milling using a Helios4 instrument (Thermo-Fisher, Waltham, USA). The samples were imaged by TEM using a probe-corrected Themis Z 3.1 instrument (Thermo-Fisher, Waltham, USA) at atomic resolution in high-angle annular dark-field (HAADF) scanning transmission electron microscopy (STEM) mode. Image data were analyzed using the Velox 2.1x software (Thermo-Fisher, Waltham, USA) and image contrast was improved by highpass- as well as Wiener-filtering.

Results and Discussion

pCAM sulfate content as a function of coprecipitation pH-value.—Ten distinctive $Ni_{0.8}Co_{0.1}Mn_{0.1}(OH)_2$ particle lots were prepared semi-batch wise in a stirred-tank reactor, varying the coprecipitation pH-value measured at 23 °C in the range of $pH_{23 °C} = 8.6–12.7$, while all other process parameters were kept constant. It is well-known that $Ni(OH)_2$[19,38–42] and NCM hydroxide precursors that are coprecipitated in aqueous solutions may contain impurities, mostly derived from the counter ion of the employed metal salts.[12,40,43,44] These impurities may even persist after the subsequent lithiation reaction at elevated temperatures, so that they can be present in the cathode active material (CAM).[45] In commercial $Ni_xCo_yMn_z(OH)_2$ (with $x+y+z = 1$) utilized as precursor for CAM, the residual S-content normalized by the TM content (in $mol\%$, in terms of $mol_S/(mol_{TM}+mol_S)$) typically ranges between 0.3–1.0 mol%. Therefore, the residual S-content in the precipitated $Ni_{0.8}Co_{0.1}Mn_{0.1}(OH)_2$ pCAM samples, which was entirely attributed to be residual sulfate (SO_4^{2-}), was investigated and is depicted as a function of $pH_{23° C}$ in Fig. 1a.

In the $pH_{23 °C}$-value range between 8.6 and 10.3 (red), a slight increase in residual SO_4^{2-} normalized by the TM content from 10.29 mol% to 12.60 mol% is observed until it decreases again to 11.10 mol% (see Fig. 1a). Between $pH_{23 °C} = 10.3$ and 10.7, a sharp transition takes place, and the residual S-content is reduced ~4-fold from 11.10 mol% to 2.60 mol%, which even further decreases with increasing pH-value, all the way down to 0.35 mol% at $pH_{23 °C} = 12.7$ (green). Interestingly, the turning point in S-content between
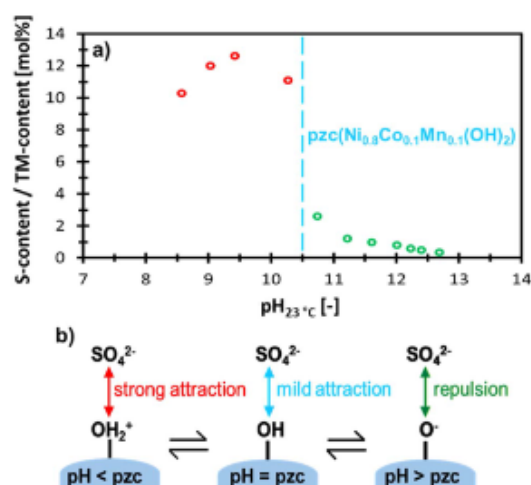
Figure 1. (a) Residual S-content (representative of the residual sulfate (SO_4^{2-}) content) normalized by the transition metal (TM) content in $Ni_{0.8}Co_{0.1}Mn_{0.1}(OH)_2$ pCAM powders depicted as a function of the coprecipitation $pH_{23 °C}$-value (the pH-value measured at 23 °C). The blue dashed line represents the point-of-zero-charge (pzc) of $Ni_{0.8}Co_{0.1}Mn_{0.1}(OH)_2$ synthesized at $pH_{23 °C} = 11.6$ (see Experimental section). (b) Schematic illustration of the interaction of solvated SO_4^{2-} anions in the mother liquor with surface hydroxyl-groups of the $Ni_{0.8}Co_{0.1}Mn_{0.1}(OH)_2$ particles at different degrees of protonation based on the coprecipitation pH-value in relation to the pzc.

$pH_{23 °C} = 10.3$ and $pH_{23 °C} = 10.7$ coincides with the point-of-zero-charge (pzc) of $Ni(OH)_2$ ($pH_{23 °C} = 10.5–10.6$) reported in the literature.[46,47] This value was verified employing the mass titration method introduced by Subramanian et al. and Noh et al. for the pzc determination of composite oxides (see experimental section).[29,30] For this purpose synthesized $Ni(OH)_2$ at $pH_{23 °C} = 11.6$ was stepwise added to an aqueous $NaOH_{(aq.)}$ solution at $pH_{23 °C} = 12.0$ while measuring the pH-value at 23 °C: at a solid content of 40 wt%, the pH-value remained constant after further $Ni(OH)_2$ addition at $pH_{23 °C} = 10.6$, representing the pzc. Applying the identical procedure, the pzc of $Ni_{0.8}Co_{0.1}Mn_{0.1}(OH)_2$ synthesized at $pH_{23 °C} = 11.6$ was found to be at $pH_{23 °C} = 10.5$, which is marked by the dashed blue line in Fig. 1a.

Generally, the pzc is the pH-value at which the net surface charge of a solid equals zero and is therefore an indicator for the surface charge of solids.[29,30,46,48] In case of metal hydroxides such as $Ni_{0.8}Co_{0.1}Mn_{0.1}(OH)_2$, the pzc represents the degree of protonation of hydroxyl-groups as a function of pH-value. Hence, it is rationalized that SO_4^{2-} uptake during the coprecipitation of a Ni-rich hydroxide pCAM follows an adsorptive mechanism that depends on the degree of protonation of surface hydroxyl-groups, which is schematically depicted in Fig. 1b: If the pH is below the pzc, surface hydroxyl-groups are protonated and the $Ni_{0.8}Co_{0.1}Mn_{0.1}(OH)_2$ surface overall bears a positive charge, resulting in a strong attractive interaction with negatively charged SO_4^{2-} (left-most sketch), which is expected to favor a high SO_4^{2-} uptake. If the pH is close to the pzc, the interaction between the surface hydroxyl-groups and SO_4^{2-} is comparably weaker, but some attractive interaction is likely to persist due to hydrogen bridge bonding (middle sketch). On the other hand, if the pH of the solution is higher than the pzc, the electrostatic repulsion between the negatively charged deprotonated surface groups and SO_4^{2-} should significantly reduce the SO_4^{2-} uptake (right-most sketch). This trend is reflected in the S-content vs coprecipitation pH-value data shown in Fig. 1a. An analogous behavior is reported for pure aluminum
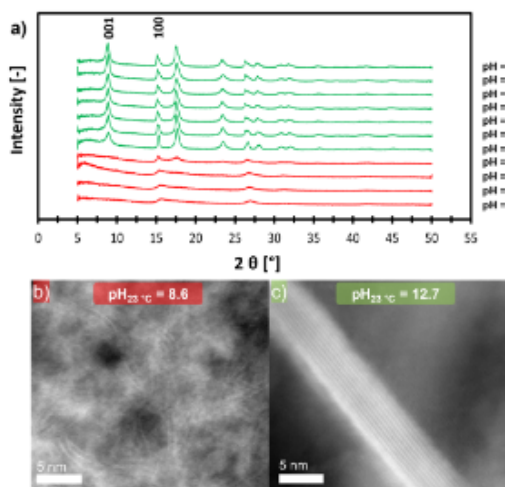
Figure 2. (a) Powder X-ray diffraction patterns (collected at a wavelength $\lambda = 0.71$ Å) of $Ni_{0.8}Co_{0.1}Mn_{0.1}(OH)_2$ pCAMs synthesized at various coprecipitation pH-values (measured at 23 °C). The first two reflexes on the 2θ axis are highlighted by the respective Miller indices. Amorphous α-type $Ni_{0.8}Co_{0.1}Mn_{0.1}(OH)_2$ is obtained for coprecipitation pH-values of $pH_{23\,°C} = 8.6$–10.3 (red), while crystalline β-type $Ni_{0.8}Co_{0.1}Mn_{0.1}(OH)_2$ is obtained in the range of $pH_{23\,°C} = 10.7$–12.7 (green). HR-TEM images of two representative samples: (b) amorphous α-type $Ni_{0.8}Co_{0.1}Mn_{0.1}(OH)_2$ precipitated at $pH_{23\,°C} = 8.6$; (c) crystalline β-type $Ni_{0.8}Co_{0.1}Mn_{0.1}(OH)_2$ coprecipitated at $pH_{23\,°C} = 12.7$.

hydroxide $Al(OH)_3$[49] and mixed layered double hydroxides (LDHs).[50,51] The adsorption and subsequent incorporation of anions into the host structure was mainly depended on the surface charge, which is given by the pH-value in relation to the pzc of the respective solid. Further, a dependency of residual SO_4^{2-} on the precipitation pH-value for $Ni(OH)_2$ synthesized from nickel sulfate $(NiSO_{4(aq.)})$ was also observed by other authors and even linked to an adsorption based mechanism studied by the characteristic SO_4^{2-} vibration bands observable via infrared spectroscopy.[42,52,53]

Sulfate adsorption effect on $Ni_{0.8}Co_{0.1}Mn_{0.1}(OH)_2$ crystallinity.—Ideally, $Ni_xCo_yMn_z(OH)_2$ is structurally related to brucite-type β-$Ni(OH)_2$, which is isostructural to magnesium hydroxide $Mg(OH)_2$ and exhibits a hexagonal layered crystal structure with the *P-3m* space group, where TMs are located in 1a sites and hydroxy-ions in 2d sites.[14,16–20] However, in reality deviations to the brucite-type structure can be expected due to partial oxidation of Mn^{2+}/Co^{2+}, resulting in the oxidation of the hydroxides, the incorporation of foreign ions, and/or H_2O intercalation into the structure.[11,12,40,43,44] Excessive uptake of impurities may even result in the formation of α-$Ni(OH)_2$, an amorphous polymorph of brucite-type β-$Ni(OH)_2$ with random layer orientation. However, the kinetically favored α-phase can be transformed into thermodynamically stable β-$Ni(OH)_2$ by aging in alkaline solutions at high temperatures.[19,38–42]

The microstructural properties of the obtained $Ni_{0.8}Co_{0.1}Mn_{0.1}(OH)_2$ pCAMs was investigated by PXRD, and the resulting patterns are shown in Fig. 2a. Remarkedly, a structural transition of the coprecipitated hydroxides around the pzc is observed: $Ni_{0.8}Co_{0.1}Mn_{0.1}(OH)_2$ precipitated at $pH_{23\,°C} <$ pzc yielded either very broad main reflexes or the reflexes were completely absent (red diffractograms), analogous to what would be the case for amorphous α-$Ni(OH)_2$. In contrast, coprecipitation at $pH_{23\,°C} >$ pzc led to crystalline $Ni_{0.8}Co_{0.1}Mn_{0.1}(OH)_2$, which exhibits characteristic reflexes for brucite-type β-$Ni(OH)_2$ (green).[19,38–42] Complementary

results were obtained by HR-TEM analysis of representative samples precipitated at pH-values below or above the pzc: the $Ni_{0.8}Co_{0.1}Mn_{0.1}(OH)_2$ sample coprecipitated at $pH_{23\,°C} = 8.6$, hence below the pzc exhibits no long-range ordered layers and has only little observable short-range ordering (Fig. 2b), consistent with the absence of reflexes in the PXRD data (Fig. 2a). In contrast, for the $Ni_{0.8}Co_{0.1}Mn_{0.1}(OH)_2$ sample coprecipitated at $pH_{23\,°C} = 12.7$, an ordered layered structure can be identified (Fig. 2c). This can be rationalized by considering that during coprecipitation at $pH_{23\,°C} <$ pzc, the formation of an amorphous α-type $Ni_{0.8}Co_{0.1}Mn_{0.1}(OH)_2$ is dominant due to a positively charged pCAM surface, leading to strong adsorption of negatively charged SO_4^{2-} during the coprecipitation reaction, which in turn results in a high SO_4^{2-} uptake, distortion of the structural layers and thus inhibits the development of an ordered crystal structure. Such disordered features are described in the literature for α-$Ni(OH)_2$, in which layers exhibit little to no propensity to orientate relatively to each other and are instead orientated in a random fashion.[19,54] In contrast, crystalline β-type $Ni_{0.8}Co_{0.1}Mn_{0.1}(OH)_2$ is obtained when coprecipitating at $pH_{23\,°C} >$ pzc, since in this case SO_4^{2-} incorporation is significantly reduced by the negatively charged surface of the metal hydroxide that decreases SO_4^{2-} adsorption. Even though a gradual transformation of the α-phase into the β-phase is reported to occur in alkaline medium, particularly at elevated temperatures,[19,38,41] α-type $Ni_{0.8}Co_{0.1}Mn_{0.1}(OH)_2$ was isolated in the present work, despite the long reaction time ($\sim$5 h). However, the α- to β-phase transformation is generally reported to take place in $\sim$1–4 M NaOH/KOH solution, which would correspond to $pH_{23\,°C} > 14.0$. In this study, the pH-value that resulted in amorphous α-type $Ni_{0.8}Co_{0.1}Mn_{0.1}(OH)_2$ ranged between $pH_{23\,°C} = 8.6$-10.3, so that the hydroxide concentration during $Ni_{0.8}Co_{0.1}Mn_{0.1}(OH)_2$ coprecipitation was at least $\sim$10⁴-fold lower compared to the reported ripening conditions in the literature. The stability of the α-phase under the conditions in this work can thus be ascribed to the much lower hydroxide concentration, consistent with the observation by Faure et al. that ripening of α-$Ni(OH)_2$ in pure H_2O for even four days (vs $\sim$5 h in this work) only leads to a partial transformation of the α- to the β-phase.[38] In addition, the introduction of hetero atoms such as Co, Mn, Al, and Fe to α-$Ni(OH)_2$ stabilizes the amorphous α-phase, as observed for the here synthesized α-type $Ni_{0.8}Co_{0.1}Mn_{0.1}(OH)_2$ at a coprecipitation pH-value below the pzc.[40,53,55,56]

The overall relationship between crystallinity and impurity uptake depending on the coprecipitation pH-value identified in this work for $Ni_{0.8}Co_{0.1}Mn_{0.1}(OH)_2$ was also observed by other authors for the synthesis of $Ni(OH)_2$ from $NiSO_{4(aq.)}$. Faure et al. obtained α-$Ni(OH)_2$ with comparably high residual SO_4^{2-} at pH = 10.0, hence below the pzc at a $pH_{23\,°C} = 10.6$ (see Fig. 1a), while at pH = 13.0, thus above the pzc, the β-phase with lower residual SO_4^{2-} was obtained.[38] Similarly, Song et al. isolated the α-$Ni(OH)_2$ phase at pH = 7.25, whereas above pH = 10.5 the β-$Ni(OH)_2$ was obtained.[42] Interestingly, the discussed nature of crystallinity is not only limited to $Ni(OH)_2$, but also exists for $Co(OH)_2$.[57–60] This strongly suggests that the here observed relationship between the pH-dependent SO_4^{2-} adsorption equilibrium is likely to be relevant for other $Ni_xCo_yMn_z(OH)_2$ (with x+y+z = 1) compositions as well.
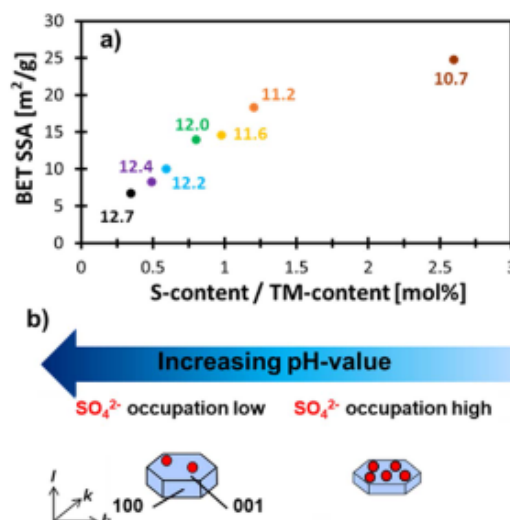
Impact of sulfate adsorption on crystallite growth.—Detailed microstructural differences in the coprecipitated hydroxides were studied by calculating crystallite sizes based on individual diffraction lines in the obtained PXRD patterns shown in Fig. 1c. However, only crystalline β-type $Ni_{0.8}Co_{0.1}Mn_{0.1}(OH)_2$ (green) samples were investigated, since either peak broadening or absence of reflexes made it impossible to refine the amorphous α-type $Ni_{0.8}Co_{0.1}Mn_{0.1}(OH)_2$ materials (red). Two main reflexes are characteristic for brucite-type β-$Ni(OH)_2$ and similarly for Ni-rich $Ni_xCo_yMn_z(OH)_2$ (x+y+z = 1): (001) and (100).[16,38,41,42] The (001) diffraction line is governed by the layering in *l*-direction and therefore is representative for the vertical crystallite size $CS_{vert.}$ (the
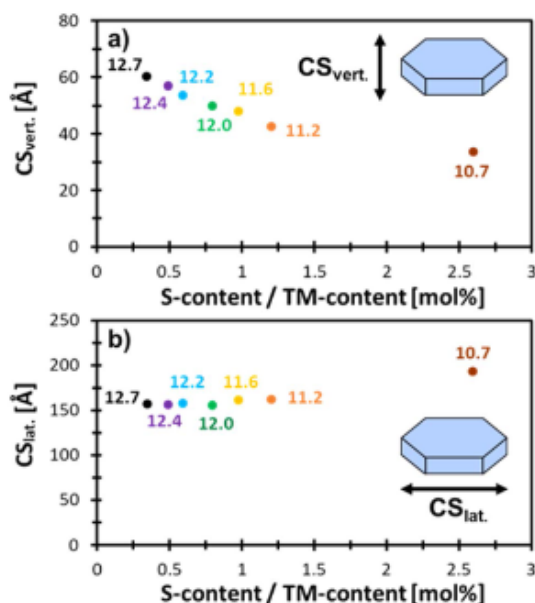
Figure 3. Primary crystallite dimensions determined from the PXRD data (see Fig. 2a) of the β-type $Ni_{0.8}Co_{0.1}Mn_{0.1}(OH)_2$ samples obtained at various coprecipitation pH-values, plotted vs their residual S-content (normalized by the TM-content). The coprecipitation pH-values are given next to the data points: a) vertical crystallite size $CS_{vert.}$ (the "thickness" of the hexagonal crystallite as depicted in the inset) based on the (001) reflex; b) lateral crystallite size $CS_{lat.}$ (the "length" of the hexagonal crystallite as depicted in the inset) based on the (100) reflex.

Figure 4. (a) BET specific surface area (SSA) of β-type $Ni_{0.8}Co_{0.1}Mn_{0.1}(OH)_2$ coprecipitated at various pH-values vs residual S-content (normalized by the TM-content) that is representative for residual SO_4^{2-} impurities. The coprecipitation pH-values are given next to the data points. (b) Schematic illustration of the pH-dependent adsorption equilibrium of SO_4^{2-} on the (001) plane of hexagonal shaped β-type $Ni_{0.8}Co_{0.1}Mn_{0.1}(OH)_2$ crystallites: at comparably low coprecipitation pH-values, high SO_4^{2-} occupation on the (001) plane blocks growth in the l-direction, resulting in crystallites with small $CS_{vert.}$ dimension, while at comparably high coprecipitation pH-values the SO_4^{2-} occupation is reduced and growth in the l-direction can occur, yielding crystallites with enlarged $CS_{vert.}$ dimensions.

"thickness" of the crystallite as shown in Fig. 3a), while the (100) line captures the information about the crystallite size alongside the layers, indicating the lateral crystallite size $CS_{lat.}$ (the "length" of the crystallite as shown in Fig. 3b).[14,16–20]

Figure 3 depicts crystallite sizes calculated by the Scherrer equation based on the individual reflexes extracted from PXRD patterns of β-type $Ni_{0.8}Co_{0.1}Mn_{0.1}(OH)_2$ materials coprecipitated at different pH-values as a function of residual SO_4^{2-} content. An inverse correlation between residual S-content in β-type $Ni_{0.8}Co_{0.1}Mn_{0.1}(OH)_2$ and crystallite size $CS_{vert.}$ based on the (001) reflex can be observed in Fig. 3a: as the coprecipitation pH is decreased from ~12.7 to 10.7, the residual S-content increases from ~0.35 mol% to ~2.60 mol%, while $CS_{vert.}$ is roughly halved, decreasing from ~60.0 Å to ~33.5 Å. On the other hand, $CS_{lat.}$ (based on the (100) reflex) is more or less independent of the coprecipitation pH-value (varying by <4% between pH 11.2–12.7), and thus also of the residual S-content (Fig. 3b); only when the coprecipitation pH-value is decreased from 11.2 to 10.7, the $CS_{lat.}$ slightly increases by about 16%, namely from ~161.6 Å to ~192.6 Å. The here observed crystallite sizes are on the same order of magnitude as reported for $Ni_{0.8}Co_{0.1}Mn_{0.1}(OH)_2$[61] and $Ni(OH)_2$[38,62] and suggest anisotropic growth of the individual crystal faces, with a preferential growth in the lateral dimension, since $CS_{lat.}$ is ~3–6 times larger compared to the $CS_{vert.}$. However, by increasing the pH-value during coprecipitation, vertical crystal growth can be promoted, while lateral crystal growth remains quasi constant. Analogous correlations between synthesis pH-value, residual S-content, crystallinity, and vertical crystallite size derived from the (001) reflex were made for the synthesis of $Ni(OH)_2$ from $NiSO_{4(aq.)}$,[38,42] where it was concluded that crystal growth in the (001) direction is enhanced when raising the synthesis pH-value. In these two studies an adsorption based mechanism for SO_4^{2-} uptake

was proposed, which is consistent with the study by Demourgues-Guerlou et al., who suggested that SO_4^{2-} mainly adsorbs on the surface of the coprecipitated crystallites in case of iron substituted $Ni(OH)_2$.[53]

Since the crystallites coprecipitated in our study are ~3–6 times larger in (100) direction (lateral) than in (001) direction (vertical), the (001) plane exhibits a considerably larger exposed surface area for SO_4^{2-} adsorption compared to the (100) plane. This would justify the high dependency of $CS_{vert.}$ on residual S-content linked to coprecipitation pH-value (Fig. 3a), while $CS_{lat.}$ remained relatively constant (Fig. 3b). Analogous poisoning effects are well-known for various crystal systems, where the growth of certain crystal faces can be drastically reduced by specific adsorption of impurities on the respective plane.[63,64] Nevertheless, for that hypothesis to be valid, a direct correlation between specific surface area (SSA) of the coprecipitated $Ni_{0.8}Co_{0.1}Mn_{0.1}(OH)_2$ powders and residual S-content would be expected. Figure 4a relates the BET SSA of the coprecipitated β-type $Ni_{0.8}Co_{0.1}Mn_{0.1}(OH)_2$ to the respective residual S-content and indeed, a linear relationship between both properties can be observed for $Ni_{0.8}Co_{0.1}Mn_{0.1}(OH)_2$ coprecipitated at $pH_{23\,°C}$ = 11.2–12.7. Only the sample coprecipitated at $pH_{23\,°C}$ = 10.7 deviates from this trend, showing a much higher residual S-content than what would be expected by a linear extrapolation of the trend observed for higher pH-values; this is likely because in this case the majority of SO_4^{2-} is not only bound by adsorption, but rather incorporated into the structure. This is indeed indicated in Fig. A-2, which shows the HR-TEM image analysis of the β-type $Ni_{0.8}Co_{0.1}Mn_{0.1}(OH)_2$ coprecipitated at $pH_{23\,°C}$ = 10.7: the observed distorted layers are indicating α-phase/β-phase interstratifications and/or SO_4^{2-} inclusions, as was reported for pure $Ni(OH)_2$.[12,19,38–44] This could explain the relatively higher residual SO_4^{2-} content compared to the other coprecipitated β-type $Ni_{0.8}Co_{0.1}Mn_{0.1}(OH)_2$

materials and the deviation of the sample coprecipitated at $pH_{23\,°C} = 10.7$ from the general trends observed in Figs. 3 and 4a. In this context, it should be considered that Kolthoff et al. make a fundamental distinction between three general possibilities of impurity uptake during coprecipitation processes, which all are based on impurity adsorption from the solution: (I) impurity incorporation into the crystal lattice; (II) occlusion of impurities in internal crystallite voids; and, (III) surface adsorption of impurities after coprecipitate formation.[65] Considering this, it is proposed that upon coprecipitation at $pH_{23\,°C} <$ pzc all three impurity uptake processes are occurring simultaneously, leading to a significant SO_4^{2-} uptake during coprecipitation that prevents long-range ordering in the crystallites and results in the formation of amorphous α-type $Ni_{0.8}Co_{0.1}Mn_{0.1}(OH)_2$. Slightly above the pzc, i.e., at $pH_{23\,°C} = 10.7$, β-type $Ni_{0.8}Co_{0.1}Mn_{0.1}(OH)_2$ with intercalation faults is obtained due to SO_4^{2-} occlusion between the layers as well as surface adsorption (processes (I) and (III)), which is leading to a comparably high residual SO_4^{2-} content of 2.60 mol% and a deviation from the observed trends regarding crystallite size and SSA in relation to the residual S-content depicted in Figs. 3 and 4a. For β-type $Ni_{0.8}Co_{0.1}Mn_{0.1}(OH)_2$ coprecipitated at $pH_{23\,°C} \geqslant 11.2$ it is deduced that primarily surface adsorption after precipitate formation (process (III)) is contributing to the residual SO_4^{2-} content. This is supported by the correlation between the SSA and the residual S-content in Fig. 4a as well as by the literature that claims that SO_4^{2-} is preferentially adsorptively bound to $Ni(OH)_2$.[42,53]

In light of the pH-dependent SO_4^{2-} adsorption equilibrium, it is concluded that SO_4^{2-} preferably adsorbs on the (001) plane of $Ni_{0.8}Co_{0.1}Mn_{0.1}(OH)_2$ crystallites during coprecipitation, which consequently prevents vertical crystal growth of crystallites. This is schematically conceptualized in Fig. 4b: as the pH-value is decreasing (from left to right), the SO_4^{2-} surface coverage on the (100) plane increases, thereby blocking crystal growth in the l-direction, resulting in decreased $CS_{vert.}$. On the other hand, at comparably high pH-values, the SO_4^{2-} surface coverage on the (001) plane is significantly decreased, implicating unhindered crystal growth in l-direction and enlarged $CS_{vert.}$ values.

Impact of sulfate adsorption on secondary particle morphology.—The secondary particle structure of the coprecipitates was characterized by SEM imaging. Figure 5 displays top-view images at 5 k (upper row) and 50 k (middle row) magnification as well as cross-section images at 12 k magnification (lower row) of the β-type $Ni_{0.8}Co_{0.1}Mn_{0.1}(OH)_2$ particles obtained at $pH_{23\,°C} = 11.2$ (left panels), $pH_{23\,°C} = 12.0$ (middle panels), and $pH_{23\,°C} = 12.7$ (right panels). Independent of the synthesis pH, secondary particles in the size range of $\sim$6-8 μm consisting of numerous sub-μm primary particles are obtained, as typically reported for $Ni_xCo_yMn_z(OH)_2$ (with $x+y+z = 1$).[12–16] Based on the cross-section images in Figs. 5c, 5f, and 5i, the secondary particle structure generally can be divided in two distinctive parts: a $\sim$2-3 μm core consisting of loosely arranged nanometer-sized primary particles, which is surrounded by a denser layer of elongated and radially aligned primary particles, pointing from the core towards the outer perimeter of the secondary particle. Considering both, the magnified top-view (b, e, h) and the cross-section images, the primary particle shape appears to be hexagonal shaped platelets, which are aligned along different crystallographic planes planes: the primary particle planes visible in top-view at 50 k seem to expose the (100) planes, while the planes of the elongated primary particles that extend from the core towards the perimeter in the cross-section images seem to expose the (001) planes. The former corresponds to the vertical primary particle size, while the later can be understood as the lateral primary particle size.

A clear impact of coprecipitation pH-value on the secondary particle morphology and the vertical size of the primary particles can be estimated from the top-view SEM images in Figs. 5b, 5e, and 5h: raising the coprecipitation pH-value from 11.2 to 12.7 leads to an increase of the vertical size of the primary particles, which is accompanied by an apparent decrease of the number of pores between primary particles as well as of their size. The latter can be seen more clearly from the cross-section images (Figs. 5c, 5f, and 5i), which clearly reveal a densification of the secondary particle structure with increasing coprecipitation pH-value. In detail, particles attained at $pH_{23\,°C} = 11.2$ exhibit a porous "Sunflower like" secondary structure with gaps between primary particles that correspond to the pores visible in the top-view images. The porosity decreases when increasing the coprecipitation pH-value to 12.0 and is even further reduced at $pH_{23\,°C}$ 12.7, to the extent that no pores except for the cores are recognizable in neither the cross-section nor the top-view images.

For quantitative verification of the observed trend, vertical primary particle sizes were manually determined from top-view SEM images taken at 50 k magnification of the β-type $Ni_{0.8}Co_{0.1}Mn_{0.1}(OH)_2$ secondary particles using the ImageJ software.[37] This approach is exemplarily visualized in the SEM top-view image shown in the top left corner in Fig. 6a, which also depicts the thus determined vertical primary particle size distribution for β-type $Ni_{0.8}Co_{0.1}Mn_{0.1}(OH)_2$ coprecipitated at $pH_{23\,°C} = 11.2$ (orange), $pH_{23\,°C} = 12.0$ (green), and $pH_{23\,°C} = 12.7$ (black). In agreement with the qualitive trend inferred from Fig. 5, the size distributions are shifted towards larger vertical primary particle sizes when increasing the pH-value from 11.2 to 12.7. The resulting mean vertical primary particle size ($PPS_{vert.}$) obtained from SEM image-based distributions for coprecipitated β-type $Ni_{0.8}Co_{0.1}Mn_{0.1}(OH)_2$ is clearly related to the residual S-content, as shown in Fig. 6b. As the pH-value is decreased from 12.7 to 11.2, the residual S-content increases from 0.35 mol% to 1.20 mol% while the mean $PPS_{vert.}$ decreases by $\sim$4-fold from 139.7 nm to 33.5 nm. Additionally, the width of the size distributions is decreased for larger $PPS_{vert.}$ values, as indicated by the error bars representing the standard deviation from the mean size. In comparison to the $CS_{vert.}$ values derived from the PXRD analysis, the vertical primary particle sizes determined from the SEM images are roughly one order of magnitude larger. This therefore suggests that the primary particles are comprised of stacked crystallite layers along the l-direction.

While the SEM images in Fig. 5 suggest a decrease in secondary particle porosity with increasing coprecipitation pH-value, quantitative information about the porosity of β-type $Ni_{0.8}Co_{0.1}Mn_{0.1}(OH)_2$ secondary particles was acquired by N_2 physisorption. Considering the size of the pores in the secondary particles observable by SEM (Fig. 5), the average pore diameter is estimated to be smaller than $\sim$300-400 nm. As described in the Experimental section, at relative pressures of $p/p_0 \geqslant 0.995$, N_2 liquefaction occurs in pores with diameter of < 380 nm, so that for the materials shown in Fig. 5 the determined intrusion volume of N_2 at $p/p_0 \approx 0.995$ should essentially correspond to the intra-particle porosity (ε_{intra}) of the β-type $Ni_{0.8}Co_{0.1}Mn_{0.1}(OH)_2$ particles. The specific liquid volume intruded in the pores at a given p/p_0 can then be determined Eq. 2, which allows the calculation of ε_{intra} by applying Eq. 3.[35] Figure 6c then relates the $PPS_{vert.}$ values extracted from SEM top-view images to the ε_{intra} values determined by N_2 physisorption. As already suggested by the SEM top-view images in Fig. 5, ε_{intra} is inversely correlated to $PPS_{vert.}$. A decrease in coprecipitation pH-value from 12.7 to 11.2 (corresponding to a residual S-content increase by a factor of $\sim$3-4), also results in an increase of ε_{intra} by a factor of $\sim$4. At the same time, the $PPS_{vert.}$ values are also increased by the same factor, which strongly suggests a correlation between these three parameters. Accordingly, other authors also noticed a densification of the secondary particle structure and/or a "thickening" of primary particles when coprecipitating of $Ni_xCo_yMn_z(OH)_2$ (with $x+y+z = 1$) at increasing coprecipitation pH-value, but they did not conduct any further investigations.[15,17] We hypothesize that secondary particle porosity is linked to the ability of primary particles to grow in the vertical crystallite direction during coprecipitation, which is governed by the pH-dependent SO_4^{2-} adsorption. Assuming that primary particles start growing radially outwards from the secondary particle center during the crystallization
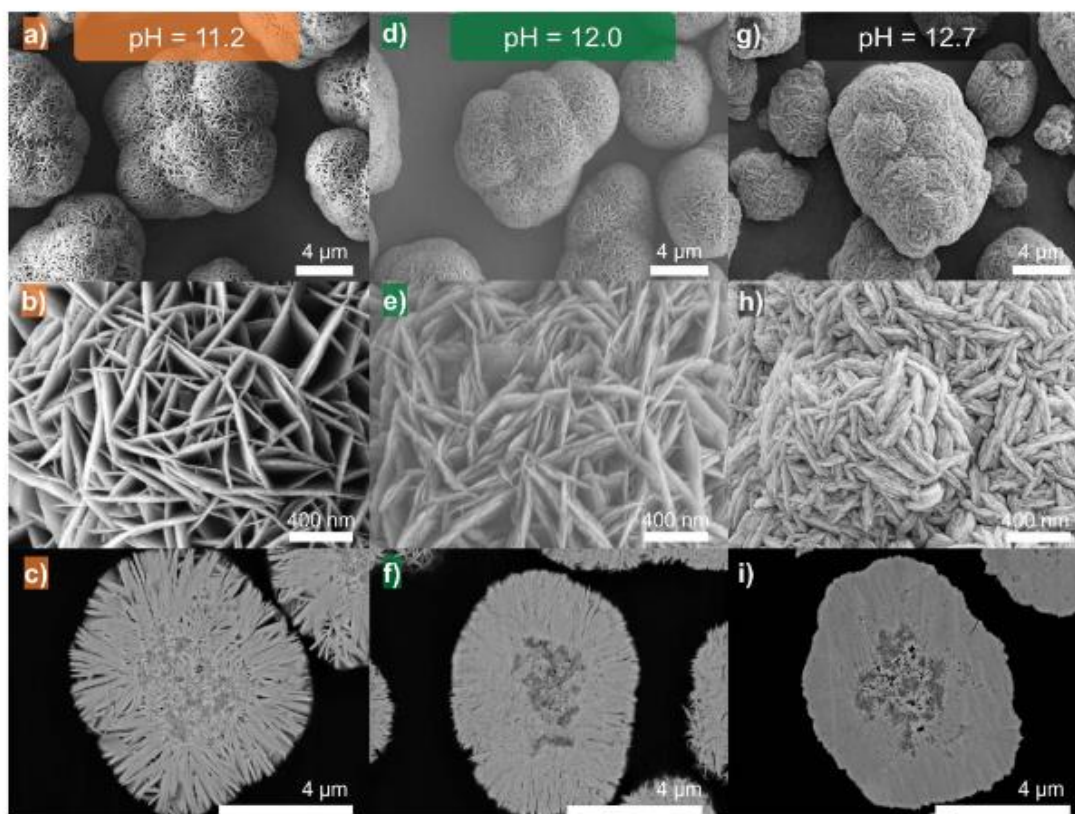
Figure 5. SEM top-view at 5 k (top row) and 50 k (middle row) magnification as well as SEM cross-section images at 12 k of β-type $Ni_{0.8}Co_{0.1}Mn_{0.1}(OH)_2$ secondary particles coprecipitated from $TMSO_{4(aq.)}$ at $pH_{23\,°C} = 11.2$ (left column, a, b, and c), at $pH_{23\,°C} = 12.0$ (middle column, d, e, and f), and at $pH_{23\,°C} = 12.7$ (right column, g, h, and i).

process, as indicated by cross-section images (Figs. 5c, 5f, and 5i), and demonstrated by our previous work,[66] a pronounced vertical growth of these primary particles would result in less void spaces between the primary particles, resulting in the observed overall densification of the secondary particle structure.

Next to the identified SO_4^{2-} adsorption equilibrium, the NH_3 transition metal complex formation rate during the coprecipitation reaction is dependent on the coprecipitation pH-value.[17] Despite keeping the molar ammonia to transition metal ratio NH_3/TM in each experiment constant, the observed changes in the $Ni_{0.8}Co_{0.1}Mn_{0.1}(OH)_2$ secondary particle morphology upon adjusting the coprecipitation pH-value in this work could be next to the identified pH-dependent SO_4^{2-} adsorption equilibrium influenced by changes in the NH_3 transition metal complex formation rate. Nevertheless, such impact by a change in this rate upon adjusting the coprecipitation pH-value is assumed to be minor compared to the pH-dependent SO_4^{2-} adsorption equilibrium, due to the following reasoning: It is suggested that the NH_3 transition metal complex formation rate decreases with increasing coprecipitation pH-value.[17] Combining this with the observation that an increase in $NH_{3(aq.)}$ feed rate at otherwise constant parameters during the coprecipitation of $Ni_{0.90}Co_{0.05}Mn_{0.05}(OH)_2$ (therefore increasing the NH_3 transition metal complex formation rate) resulted in a decrease in secondary particle porosity,[67] an increase in secondary particle porosity with increasing coprecipitation pH-value would be expected if the complex formation rate was mainly

responsible for the development of the secondary particle morphology upon changing the coprecipitation pH-value. Since the opposite was observed in this work, namely a decrease in secondary particle porosity with increasing coprecipitation pH-value, it is rationalized that the impact of the NH_3 complexation rate on the $Ni_{0.8}Co_{0.1}Mn_{0.1}(OH)_2$ physical properties investigated in this work upon changing the coprecipitation pH-value is assumed to be minor compared to the proposed pH-dependent SO_4^{2-} adsorption equilibrium.

If the identified pH-dependent SO_4^{2-} adsorption equilibrium during coprecipitation is indeed governing the resulting $Ni_{0.8}Co_{0.1}Mn_{0.1}(OH)_2$ secondary particle structure, a different morphology would be expected when conducting coprecipitations in the absence of SO_4^{2-}. Therefore, β-type $Ni_{0.8}Co_{0.1}Mn_{0.1}(OH)_2$ particles were also coprecipitated at $pH_{23\,°C} = 12.0$ from either a mixed metal acetate solution ($TM(CH_3COO)_{2(aq.)}$) or a mixed metal nitrate solution ($TM(NO_3)_{2(aq.)}$) instead of from the mixed metal sulfate solution ($TMSO_{4(aq.)}$), while all other process parameters remained unchanged. Figure 7 displays SEM images of $Ni_{0.8}Co_{0.1}Mn_{0.1}(OH)_2$ particles precipitated at $pH_{23\,°C} = 12.0$ from $TM(NO_3)_{2(aq.)}$ (left panels) and from $TM(CH_3COO)_{2(aq.)}$ (right panels). For the coprecipitation with $TM(NO_3)_{2(aq.)}$, secondary particles exhibiting primary particles that are large in vertical size and with almost no pores between the primary particles can be observed by top-view imaging (Fig. 7b), consistent with the cross-section image that shows highly dense secondary particles (Fig. 7c). In contrast, $Ni_{0.8}Co_{0.1}Mn_{0.1}(OH)_2$ particles
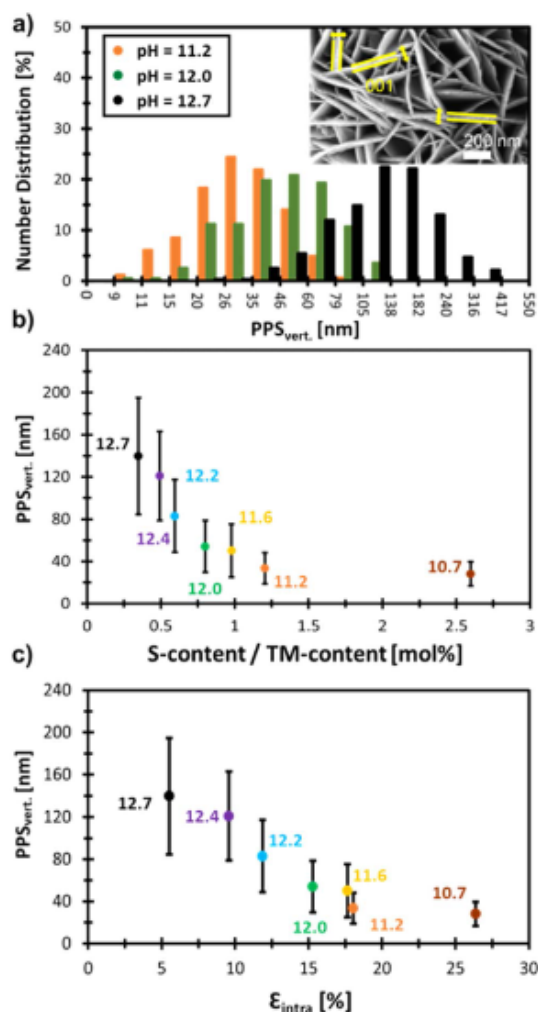
Figure 6. (a) Number distribution histogram of the vertical primary particle size of β-type $Ni_{0.8}Co_{0.1}Mn_{0.1}(OH)_2$ secondary particles coprecipitated from $TMSO_{4(aq.)}$ at $pH_{23\,°C} = 11.2$ (orange), at $pH_{23\,°C} = 12.0$ (green), and at $pH_{23\,°C} = 12.7$ (black). The vertical primary particle size was manually extracted from top-view SEM images at 50 k magnification via Image J,[57] evaluating at least 200 primary particles for each sample. The SEM image in the top right corner of the figure exemplarily depicts the analyzed vertical size between the yellow bars for selected primary particles. b) Mean vertical primary particle size ($PPS_{vert.}$) of the examined β-$Ni_{0.8}Co_{0.1}Mn_{0.1}(OH)_2$ pCAMs coprecipitated at different pH-values, plotted against the S-content (normalized by the TM-content) that is representative for residual SO_4^{2-}. The error bars represent the standard deviation from the mean size. c) Mean vertical primary particle size ($PPS_{vert.}$) of the β-type $Ni_{0.8}Co_{0.1}Mn_{0.1}(OH)_2$ samples vs the intra-particle porosity (ε_{intra}) determined by N_2-physisorption.

obtained from $TM(CH_3COO)_{2(aq.)}$ appear porous in the cross-section image (Fig. 7f) and have a smaller vertical primary particle size (Fig. 7e). The residual impurity content (either N−, S−, or C-content introduced by the anions) and the other morphological properties of the pCAM particles coprecipitated from the respective mixed metal solutions $TMX_{(aq.)}$ (X = NO_3^-, SO_4^{2-}, CH_3COO^-; please note that for the purpose of simplifying the notation the valency of the respective anion X in $TMX_{(aq.)}$ is not considered) at $pH_{23\,°C} = 12.0$

were analogously characterized as above and are compared in Fig. 8. Elemental analysis revealed that the residual N-content in $Ni_{0.8}Co_{0.1}Mn_{0.1}(OH)_2$ particles coprecipitated from $TM(NO_3)_{2(aq.)}$ and residual S-content in $Ni_{0.8}Co_{0.1}Mn_{0.1}(OH)_2$ particles coprecipitated from $TMSO_{4(aq.)}$ was comparable (0.78 mol% N and 0.80 mol% S), while the coprecipitation from $TM(CH_3COO)_{2(aq.)}$ yielded $Ni_{0.8}Co_{0.1}Mn_{0.1}(OH)_2$ particles an almost two-fold higher impurity content of 1.48 mol% C (Fig. 8a). Comparing the $CS_{vert.}$ values based on the (001) PXRD reflex of the $Ni_{0.8}Co_{0.1}Mn_{0.1}(OH)_2$ materials coprecipitated from the different mixed metal solutions, $CS_{vert.}$ decreases by ~40% from 59.7 Å for the nitrates to 49.7 Å for the sulfates all the way to 37.4 Å for the acetates (Fig. 8b). Accordingly, the $PPS_{vert.}$ values extracted by segmentation from SEM top-view images also changes in the same order by a factor of ~4, viz., from 79.4 nm to 54.1 nm all the way to 20.0 nm (Fig. 8c). As one would expect based on the trends in $CS_{vert.}$ and $PPS_{vert.}$, the BET SSA shows the opposite trend (Fig. 8d): the SSA is quadrupled from 8.9 m² g⁻¹ for X = NO_3^- to 14.0 m² g⁻¹ for X = SO_4^{2-} all the way to 39.0 m² g⁻¹ for X = CH_3COO^-. This is accompanied by an increase of ε_{intra} from 10.2% to 15.3% all the way to 32.4% (Fig. 8e). Interestingly, an increase in the SSA of $Ni_{0.90}Co_{0.05}Mn_{0.05}(OH)_2$ particles by the addition of acetate salts during the coprecipitation reaction is also claimed in a patent.[68]

Considering the distinctive properties of the secondary particles obtained at an identical coprecipitation pH-value when using different anions in the mixed metal feeds, in combination with the above established pH-dependent impact of SO_4^{2-} adsorption on the secondary particle morphology, we hypothesize that NO_3^- has a less retarding effect on crystal growth in the *l*-direction, thus the vertical direction of primary particles, so that dense secondary particles are developed during coprecipitation due to a decreased anion adsorption strength/coverage. In contrast, this would suggest that SO_4^{2-} and CH_3COO^- exhibit a higher retardation of the crystal growth in the *l*-direction, yielding porous secondary particles, whereby SO_4^{2-} has a more moderate influence than CH_3COO^-. The argument that the developed secondary particle morphology is linked to the influence of the respective anion on the primary crystallite growth due to its adsorption strength/coverage is supported by the reported adsorption/intercalation affinity sequences for various anions towards layered double hydroxides (LDHs), which increases in the order HPO_4^{2-} > CO_3^{2-} ⩾ SO_4^{2-} > NO_3^- > Cl^-.[50,51,69,70] This series is also followed with regard to the residual impurity level in $Ni(OH)_2$ precipitated from distinctive aqueous nickel sources,[42,52] while analogous adsorption affinities were empirically established for $Al(OH)_3$.[49,71,72] Unfortunately, CH_3COO^- so far was not evaluated and is therefore not included in the adsorption affinity sequence for LDHs. However, a rather fundamental concept for rationalizing the observed phenomena in our present work would be the Fajans-Paneth-Hahn (FPH) Law. It states that the specific adsorption capability of an ion towards a crystalline solid is the higher, the lower the solubility of the salt that would be formed from the respective solvated ion and the oppositely charged ion in the crystal lattice of the solid.[65,73] The applicability of the rule was demonstrated for a variety of systems.[65,74,75] In the case of NO_3^-, SO_4^{2-}, and CH_3COO^- adsorbed on $Ni(OH)_2$, the solubility of $Ni(NO_3)_2$, $NiSO_4$, and $Ni(CH_3COO)_2$ would have to be considered. When comparing the solubilities at 25 °C for the respective nickel salts, the solubility of the salts increases (therefore the adsorption affinity would be expected to decrease) in the following order: $Ni(CH_3COO)_2$ < $NiSO_4$ < $Ni(NO_3)_2$.[76–78] As this sequence reflects the impact on the secondary particle morphology of the respective anion, it suggests that the FPH Law is applicable for the precipitation of hydroxide based pCAMs and that adsorption equilibria are responsible for the development of the primary and secondary particle morphology.

In addition to postulated impact on the secondary particle morphology given by the specific adsorption capability of the respective anion, other factors have to be considered such as the solid content and anion concentration inside the stirred tank reactor,
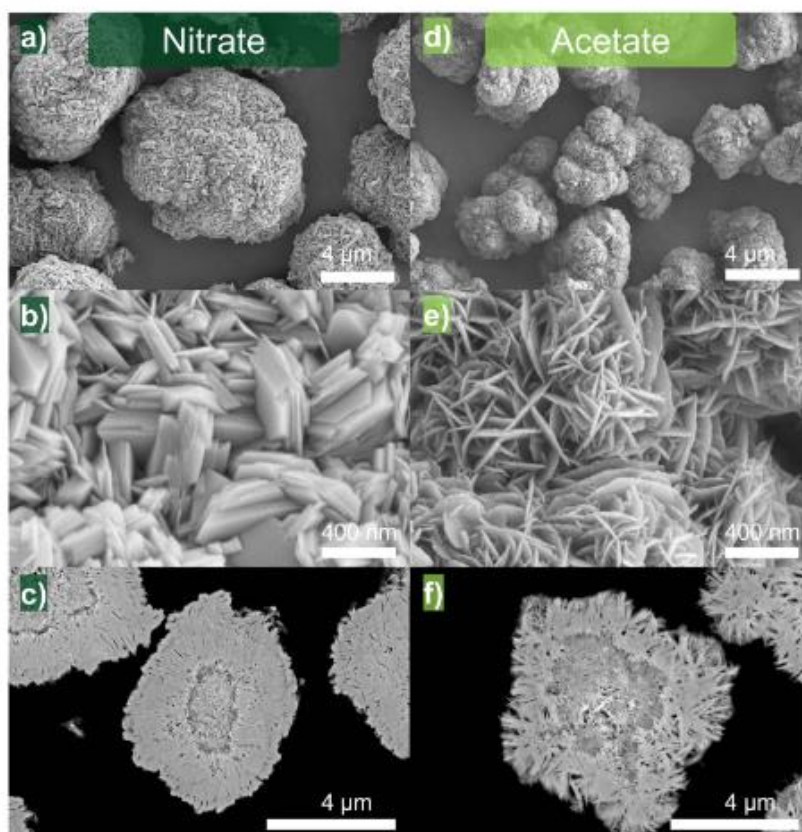
Figure 7. SEM top-view images at 5 k (top row) and 50 k (middle row) magnification as well as SEM cross-section images at 10 k magnification of β-type $Ni_{0.8}Co_{0.1}Mn_{0.1}(OH)_2$ secondary particles coprecipitated at $pH_{23\,°C} = 12.0$ from $TM(NO_3)_{2(aq.)}$ (a, b, and c; dark green) and from $TM(CH_3COO)_{2(aq.)}$ (d, e, and f; light green).

which could potentially influence the $Ni_{0.8}Co_{0.1}Mn_{0.1}(OH)_2$ secondary particle development during the coprecipitation reaction. To evaluate this, the relevant soluble and insoluble components inside the stirred tank reactor after completed coprecipitation reaction of 5 h is given Table A-I in the Appendix. Comparing the final $Ni_{0.8}Co_{0.1}Mn_{0.1}(OH)_2$ solid content inside the after a reaction time of 5 h from various anionic species X in $TMX_{(aq.)}$ ($X = NO_3^-$, SO_4^{2-}, CH_3COO^-) (see column 2 in Table A-I in the Appendix), the coprecipitation from $TM(CH_3COO)_{2(aq.)}$ resulted in a lower amount of the $Ni_{0.8}Co_{0.1}Mn_{0.1}(OH)_2$ solid compared to the coprecipitation reaction from $TMSO_{4(aq.)}$ and $TM(NO_3)_{2(aq.)}$ due to the lower concentration of the $TM(CH_3COO)_{2(aq.)}$ utilized for the coprecipitation of $Ni_{0.8}Co_{0.1}Mn_{0.1}(OH)_2$, namely 0.6 mol l^{-1} compared to 2.2 mol l^{-1} for $TMSO_{4(aq.)}$ and $TM(NO_3)_{2(aq.)}$. This is due to the intrinsically lower solubility of the respective transition metal acetate salts compared to the transition metal sulfate and nitrate salts.[76–78]

Like the lower solid content for the coprecipitation conducted from $TM(CH_3COO)_{2(aq.)}$, the lower final $NH_{3(aq.)}$ concentration compared to the experiments conducted with $TMSO_{4(aq.)}$ and $TM(NO_3)_{2(aq.)}$ as reactant is lower (see column 3 in Table A-I in the Appendix). This variation also stems from the lower concentration of $TM(CH_3COO)_{2(aq.)}$ due to the lower solubility of the respective transition metal acetate salts as discussed above since the target of the experiments was to keep the molar ammonia to

transition metal ratio NH_3/TM constant between all experiments to have comparable NH_3 transition metal complex formation rates. Therefore, an influence of a difference in NH_3 transition metal complexation rate between the coprecipitations from $TMSO_{4(aq.)}$ and $TM(NO_3)_{2(aq.)}$ compared to the coprecipitation conducted from $TM(CH_3COO)_{2(aq.)}$, which could next to the anionic species affect the development of the $Ni_{0.8}Co_{0.1}Mn_{0.1}(OH)_2$ secondary particle morphology, can be considered as neglectable.

In terms of the final concentration of the respective anionic species inside the stirred tank reactor (see column 4 in Table A-I in the Appendix), there is a difference between the trials conducted from different $TMX_{(aq.)}$ ($X = NO_3^-$, SO_4^{2-}, CH_3COO^-) due to the following reasons: (a) the valency of SO_4^{2-}, which is 2−, compared to NO_3^- and CH_3COO^-, which are 1−, is different, and (b) the lower concentration of $TM(CH_3COO)_{2(aq.)}$ utilized for the coprecipitation compared to the concentration of $TMSO_{4(aq.)}$ and $TM(NO_3)_{2(aq.)}$ as discussed above. To evaluate the role of these differences, the ratio of the final concentration of the anionic species to the final $Ni_{0.8}Co_{0.1}Mn_{0.1}(OH)_2$ solid content in the respective experiment was formulated (see column 5 in Table A-I in the Appendix). The attained ratios for the coprecipitation experiments from $TM(NO_3)_{2(aq.)}$ and $TM(CH_3COO)_{2(aq.)}$ are identical but both higher by a factor ~2 compared to the coprecipitations from $TMSO_{4(aq.)}$. If this difference in anion per solid ratio would have a significant impact on the development of the secondary particle
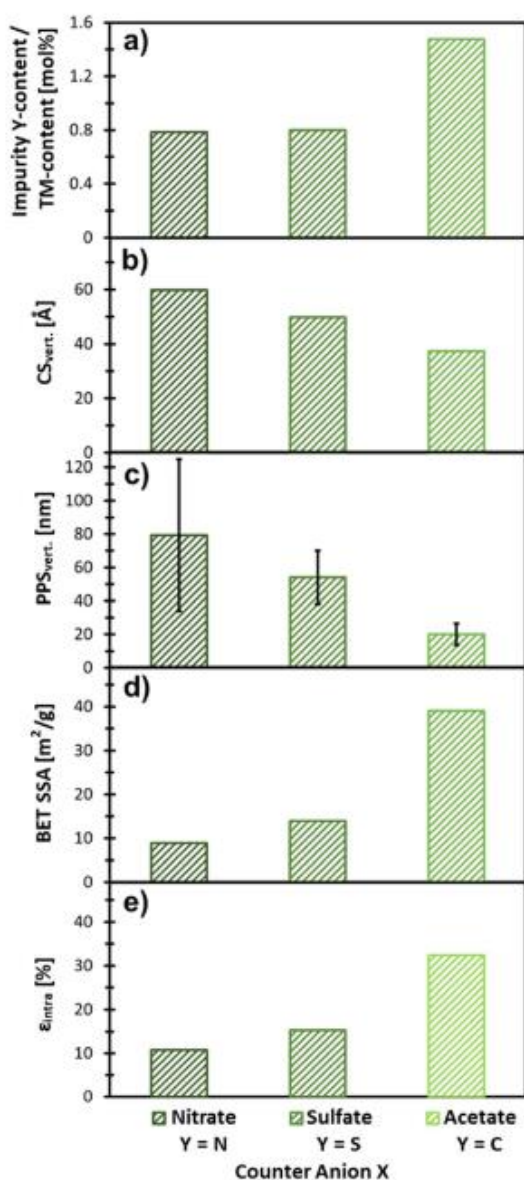
Figure 8. Comparison of the impurity content and the morphological properties of β-type $Ni_{0.8}Co_{0.1}Mn_{0.1}(OH)_2$ coprecipitated from different transition metal feed solutions $TMX_{(aq.)}$ ($X = NO_3^-$, SO_4^{2-}, CH_3COO^-) at $pH_{23\ °C} = 12.0$: a) residual impurity content ($Y = N$, S, C) attributed to originate entirely from the respective anion NO_3^-, SO_4^{2-}, CH_3COO^- of the $TMX_{(aq.)}$ solution, normalized by the TM-content; b) comparison of the vertical crystallite size ($CS_{vert.}$) based on the (001) PXRD reflexes; c) mean vertical primary particle size ($PPS_{vert.}$) determined from SEM top-view images at 50 k magnification as illustrated in Fig. 6a, with the error bars representing the standard deviation from the mean; d) BET specific surface area (SSA); e) intra-particle porosity (ε_{intra}) determined by N_2-physisorption.

morphology during the coprecipitation reaction, a similar $Ni_{0.8}Co_{0.1}Mn_{0.1}(OH)_2$ secondary particle morphology would be expected for the coprecipitation conducted with $TM(NO_3)_{2(aq.)}$ and

the $TM(CH_3COO)_{2(aq.)}$ due to the same anion-solid ratio, while only a different secondary particle morphology would be expected for the $TMSO_{4(aq.)}$ based coprecipitation. However, since clearly distinctive secondary particle morphologies were attained from the different transition metal feeds, the discrepancy in the anion-solid ratio is considered less impactful compared to the impact of the sole anionic species itself. To overcome these differences in solid content and anion to solid ratio one could, in e.g., also additionally dose the respective anion X in $TMX_{(aq.)}$ ($X = NO_3^-$, SO_4^{2-}, CH_3COO^-) as an aqueous sodium salt solution in trying to achieve the same anion to solid ratio. However, this again would then decrease the final $Ni_{0.8}Co_{0.1}Mn_{0.1}(OH)_2$ solid content achieved due to dilution by an additional aqueous reactant solution. To counteract this then an adjustment of the $TMX_{(aq.)}$ ($X = NO_3^-$, SO_4^{2-}, CH_3COO^-) concentration would be necessary, which again influences the anion to solid ratio. Therefore, it is nearly impossible to realize identical solid contents and concentrations of the respective anion due to the differences in valency between the anions.

Despite these slight differences in experimental conditions, it is suggested that the coprecipitations with different anions in $TMX_{(aq.)}$ ($X = NO_3^-$, SO_4^{2-}, CH_3COO^-) still captures the impact of the different anionic species on the secondary particle development, as the main parameter governing the interaction of the metal hydroxide solids in solution with an anionic species in aqueous solution is the surface charge of the solid, which is governed. by the pH-value.[49,50] Since the pH-value was kept constant at $pH_{23\ °C} = 12.0$ for the coprecipitations from $TMSO_{4(aq.)}$, $TM(NO_3)_{2(aq.)}$ and $TM(CH_3COO)_{2(aq.)}$, respectively, it is rationalized that the differences in solid content and anion concentration can be considered as neglectable compared to the impact on the secondary particle morphology of the respective anion itself at identical $pH_{23\ °C}$. This argument is supported by the fact that the clearly distinctive physical properties of the $Ni_{0.8}Co_{0.1}Mn_{0.1}(OH)_2$ secondary particles obtained from the different anion systems with different anion adsorption affinities in this work can be well understood based on the FPH Law for crystallization,[65,73] for which the applicability of this law was demonstrated for a variety of systems.[65,74,75]

Additionally, the role of the overall secondary particle growth rate as a potential factor influencing the development of the $Ni_{0.8}Co_{0.1}Mn_{0.1}(OH)_2$ secondary particle morphology should be considered, as this might also vary upon changing the coprecipitation pH-value. It is worthy to note that this secondary particle growth rate should not be confused with the growth rate of the individual crystal faces of the $Ni_{0.8}Co_{0.1}Mn_{0.1}(OH)_2$ crystallites and primary particles, which considering the results presented above is affected by the adsorption of anionic species.

The development of the secondary particle size was monitored during the coprecipitation of the $Ni_{0.8}Co_{0.1}Mn_{0.1}(OH)_2$ secondary particles by sampling reaction suspension and determining the particle size distribution of the $Ni_{0.8}Co_{0.1}Mn_{0.1}(OH)_2$ secondary particles by light scattering. The volume median particle size d_{50} of the coprecipitated $Ni_{0.8}Co_{0.1}Mn_{0.1}(OH)_2$ secondary particles after a coprecipitation time of 5 h was between 6–8 μm. To evaluate if the secondary particle growth rate could potentially affect the secondary particle morphology, Table A-II lists in the Appendix the values for the d_{50} at a coprecipitation reaction run time of 1 h, $d_{50,1h}$, and 5 h, $d_{50,5h}$, as well as the average growth rate (G_{avg}) of $Ni_{0.8}Co_{0.1}Mn_{0.1}(OH)_2$ secondary particles within the run time of 1 h and 5 h for the "extreme" coprecipitation conditions conducted in this work.

Notably, independent of the $TMX_{(aq.)}$ ($X = NO_3^-$, SO_4^{2-}, CH_3COO^-) applied as feed and $pH_{23\ °C}$ the values obtained for the volume median particle sizes from the respective time interval only differ by 25%–33%, while the G_{avg} varies by 0.32 μm h^{-1} (see Table A-II in the Appendix). Further, when increasing $pH_{23\ °C}$ from 11.2 to 12.0, the $d_{50,\ 1\ h}$ and $d_{50,\ 5\ h}$ increase, while when going from $pH_{23\ °C}$ 12.0 to 12.7, the $d_{50,\ 1\ h}$ and $d_{50,\ 5\ h}$ both decrease again. The same analysis is true for G_{avg}. Based on these results, G_{avg} varies when changing the $pH_{23\ °C}$, however, no logical trend can be found
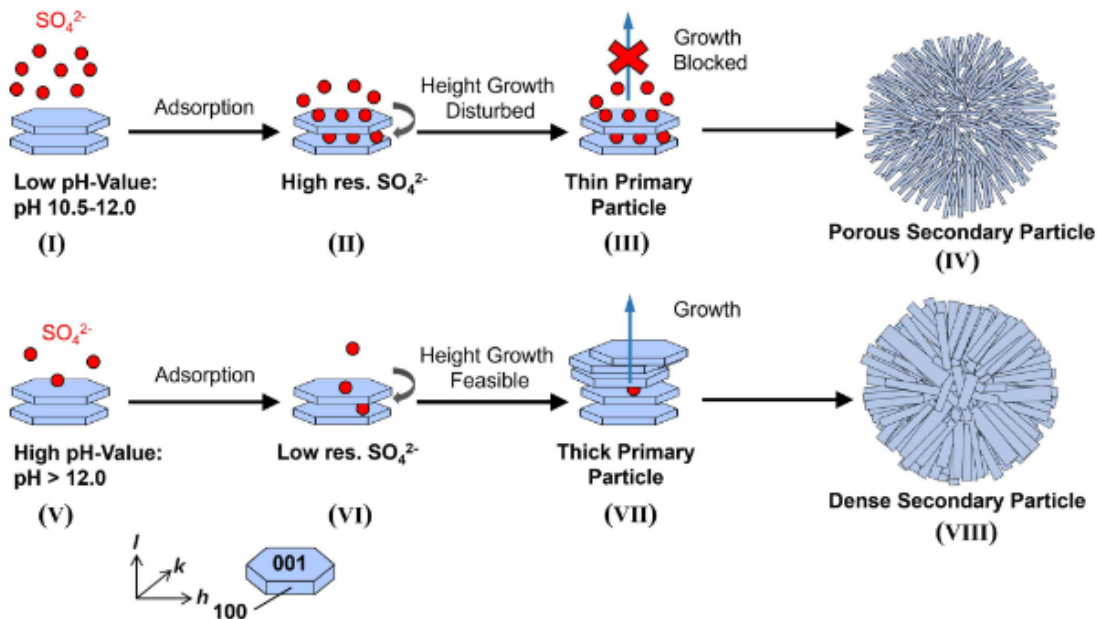
Figure 9. Schematic illustration for the proposed mechanism of the impact of SO_4^{2-} adsorption on the secondary particle formation during the coprecipitation of β-type $Ni_{0.8}Co_{0.1}Mn_{0.1}(OH)_2$ from $TMSO_{4(aq.)}$. At low coprecipitation pH-values ($pH_{23\ °C} = 10.5$–12.0; top row), the crystallite surface is less negatively charged (I) and thus has a high SO_4^{2-} coverage on the (001) crystallite plane (II). This leads to a high SO_4^{2-} uptake and consequently high residual S-content as well as to a suppression of crystallite growth in l-direction (III), which results in primary particles with low vertical size and in porous secondary particles (IV). In contrast, at high pH-values ($pH_{23\ °C} > 12.0$; bottom row), the crystallite surface is highly negatively charged (V), leading to a reduced SO_4^{2-} coverage on the (001) crystallite plane (VI). This results in a lower S-content as well as in a reduced suppression of crystallite growth in l-direction (VII), which leads to primary particles with large vertical size and to denser secondary particles (VIII).

between both values. Therefore, an impact on the $Ni_{0.8}Co_{0.1}Mn_{0.1}(OH)_2$ secondary particle morphology upon changing the $pH_{23\ °C}$ is unlikely. This argument is further supported by the fact that changing the anion in the $TMX_{(aq.)}$ ($X = NO_3^-$, SO_4^{2-}, CH_3COO^-) applied as reactant at constant $pH_{23\ °C}$ resulted in $Ni_{0.8}Co_{0.1}Mn_{0.1}(OH)_2$ secondary particles with clearly distinctive secondary morphologies and different physical properties for which the $CS_{vert.}$ and the $PPS_{vert.}$ increase, while the BET SSA and the ε_{intra} concomitantly decrease in the order $X = (CH_3COO)_2 < X = SO_4 < X = (NO_3)_2$. Such trend is hard to justify by the variations in $G_{avg.}$ as the $G_{avg.}$ increases in the order $X = (NO_3)_2 < X = (CH_3COO)_2 < X = SO_4$. Therefore, it is rationalized that the implications on the development of the $Ni_{0.8}Co_{0.1}Mn_{0.1}(OH)_2$ secondary particle morphology caused by variations in $G_{avg.}$ upon changing the $pH_{23\ °C}$ and the anion in $TMX_{(aq.)}$ ($X = NO_3^-$, SO_4^{2-}, CH_3COO^-) are neglectable compared to the pH-dependent SO_4^{2-} adsorption equilibrium and the adsorptive strength of the respective anion.

Consolidating the above findings and considering the established pH-dependent SO_4^{2-} adsorption equilibrium, we propose the mechanism for the development of the secondary particle morphology during the coprecipitation of $Ni_xCo_yMn_z(OH)_2$ (with $x+y+z = 1$) from $TMSO_{4(aq.)}$ that is depicted in Fig. 9:

• At comparably low coprecipitation pH-values of $pH_{23\ °C} = 10.7$–12.0 (see (I) in Fig. 9), the SO_4^{2-} coverage on the (001) plane of the $Ni_xCo_yMn_z(OH)_2$ (with $x+y+z = 1$) primary crystallites is high (II), which retards the crystal growth on the l-direction (III). As shown in Fig. 6, this leads to high residual SO_4^{2-} content ($>\sim0.8$ mol%) as well as to "thin" primary particles with low vertical size ($PPS_{vert.} < 50$ nm), which in turn results in secondary particles with high intra-particle porosity ($\varepsilon_{intra} > 15\%$), depicted in (IV).

• In contrast, at comparably high coprecipitation pH-values of $pH_{23\ °C} > 12.0$ (V), the SO_4^{2-} coverage on the (001) plane is decreased due to the pronounced negatively charged $Ni_xCo_yMn_z(OH)_2$ (with $x+y+z = 1$) surface (VI), leading to an enhanced crystallite growth in l-direction is enhanced (VII). Hence, the SO_4^{2-} uptake and thus the S-content is reduced (to ~0.3 mol% at pH 12.7, see Fig. 6) and "thick" primary particles with enlarged vertical size are obtained ($PPS_{vert.} \approx 140$ nm at pH 12.7, see Fig. 6), which leads to a densification of the secondary particles (VIII) with intra-particle porosities as low as $\sim5\%$ (see Fig. 6).

Approaches to lower the residual S-content of $Ni_{0.8}Co_{0.1}Mn_{0.1}(OH)_2$.—It was demonstrated above that the pH-dependent SO_4^{2-} adsorption equilibrium is governing the growth of $Ni_{0.8}Co_{0.1}Mn_{0.1}(OH)_2$ primary crystallites coprecipitated from $TMSO_{4(aq.)}$ as well as the secondary particle morphology. In the case where a porous pCAM with a high intra-particle porosity (ε_{intra}) would be desired for the subsequent CAM manufacturing, the here shown synthesis would require a low coprecipitation pH-value (see Fig. 6c) which in turn would result in a high residual S-content (see Fig. 6b). However, a high-purity pCAM is necessary for CAM production, because impurities could negatively affect the subsequent manufacturing steps. Therefore, approaches for the reduction of impurities in precipitated $Ni_xCo_yMn_z(OH)_2$ (with $x+y+z = 1$) pCAMs are required.

Anion desorption in aqueous solution for LDHs can be achieved by either ion exchange with an anion exhibiting a higher adsorption affinity than the presently adsorbed species or by increasing the pH-value far above the pzc, thereby promoting a negatively charged surface of the mixed hydroxide that leads to electrostatic repulsion of the anion.[49,50,79] Inspired by the latter method, the pH-value of a
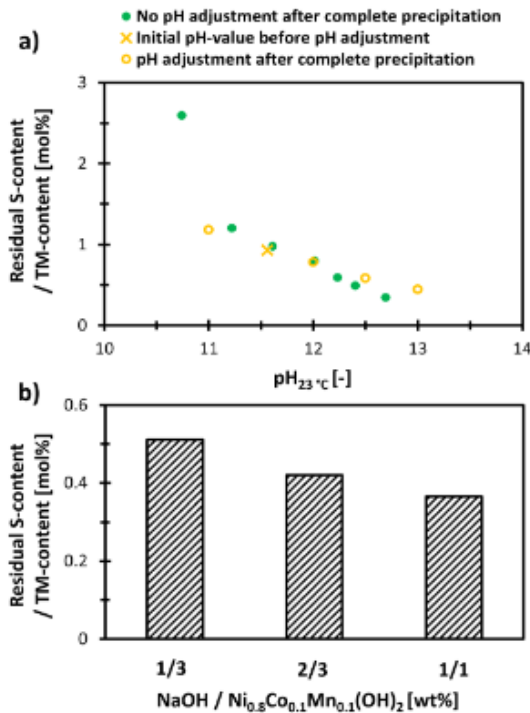
Figure 10. (a) Comparison of residual S-content normalized by the TM-content in β-type $Ni_{0.8}Co_{0.1}Mn_{0.1}(OH)_2$ obtained by coprecipitation at a given $pH_{23\,°C}$-value without any subsequent pH-adjustment (green circles, corresponding to the green circles shown in Fig. 1a) vs that obtained by coprecipitation at $pH_{23\,°C} = 11.6$ (yellow cross) followed by adjusting the pH-value of the suspension after completion of the coprecipitation reaction by addition of either $NaOH_{(aq)}$ or $HCl_{(aq)}$ (yellow circles). b) Residual S-content normalized by the TM-content after washing β-type $Ni_{0.8}Co_{0.1}Mn_{0.1}(OH)_2$ coprecipitated at $pH_{23\,°C} = 11.6$ with 10 wt% $NaOH_{(aq)}$ solution in different $NaOH_{(aq)}/Ni_{0.8}Co_{0.1}Mn_{0.1}(OH)_2$ weight ratios.

SO_4^{2-}-based β-type $Ni_{0.8}Co_{0.1}Mn_{0.1}(OH)_2$ particle suspension was adjusted after the completion of the coprecipitation reaction by the addition of $NaOH_{(aq)}$ or $HCl_{(aq)}$. Figure 10a compares the residual S-content of $Ni_{0.8}Co_{0.1}Mn_{0.1}(OH)_2$ coprecipitated at various pH-values without pH-adjustment (green circles; corresponding to the green circles in Fig. 1a) with that obtained for $Ni_{0.8}Co_{0.1}Mn_{0.1}(OH)_2$ that was first coprecipitated at $pH_{23\,°C} = 11.6$ (yellow cross) followed by a pH-adjustment of the pCAM suspension to different values (yellow circles). Increasing the pH-value of the pCAM suspension from the coprecipitation pH-value of 11.6 to 13.0 results in a ~2-fold decrease of the residual S-content from 0.93 mol% to 0.45 mol%. This, however, is still ~30% higher than the S-content of the $Ni_{0.8}Co_{0.1}Mn_{0.1}(OH)_2$ coprecipitate that was obtained when the pH-value was fixed to $pH_{23\,°C} = 12.7$ throughout the entire reaction. On the other hand, lowering the pH-value of the final pCAM suspension from the coprecipitation pH-value 11.6 to an adjusted pH of 11.0 leads to an increase of the S-content by ~27% (from 0.93 mol% to 1.18 mol%, see Fig. 10a). These observations are consistent with a pH-dependent SO_4^{2-} coverage and suggest an at least partial reversibility of SO_4^{2-} removal and uptake by adjusting the pH of the $Ni_{0.8}Co_{0.1}Mn_{0.1}(OH)_2$ pCAM suspension after completion of the coprecipitation reaction: for $pH_{adjustment} > pH_{coprecipitation}$, the S-content decreases, while it increases for $pH_{adjustment} < pH_{coprecipitation}$. However, the S-content obtained by

adjusting the pH after coprecipitation to a higher value (yellow circles to the right of the yellow cross in Fig. 10a) is still higher than that of a material that was directly coprecipitated at that higher pH (green dots in Fig. 10a). This indicates that some minor fraction of the residual SO_4^{2-} might simply not be able anymore to desorb, which according to Kolthoff et al.[65] likely originates from either SO_4^{2-} incorporation into the lattice and/or occlusion in the crystal during the coprecipitation reaction. This would also explain that the S-content obtained by adjusting the pH after coprecipitation to a lower value remains below that of a material that was directly coprecipitated at that lower pH (the yellow circles to the left of the yellow cross in Fig. 10a are below the green dots).

As alternative impurity reduction approach, washing of β-type $Ni_{0.8}Co_{0.1}Mn_{0.1}(OH)_2$ coprecipitated at $pH_{23\,°C} = 11.6$ with 10 wt% $NaOH_{(aq)}$ in various $NaOH_{(aq)}/Ni_{0.8}Co_{0.1}Mn_{0.1}(OH)_2$ weight ratios was investigated. The S-contents in the thus washed coprecipitates is depicted in Fig. 10b. By washing in a $NaOH_{(aq)}/Ni_{0.8}Co_{0.1}Mn_{0.1}(OH)_2$ weight ratio of 1/3, the S-content is lowered by 44%, i.e., from 0.93 mol% to 0.51 mol%, while for a 1/1 weight ratio the residual S-content could even be lowered by 60%, down to 0.37 mol%. A reduction of the residual S-content was also shown also for Ni-rich $NiCoAl(OH)_2$ coprecipitated from $TMSO_{4(aq)}$ by washing the precipitate with 1.0 M $NaOH_{(aq)}$, while the morphology of the particles remained unchanged.[80] Complementary to increasing the pH-value of the suspension after completion of the coprecipitation reaction (see Fig. 10a), washing of the $Ni_{0.8}Co_{0.1}Mn_{0.1}(OH)_2$ pCAM with $NaOH_{(aq)}$ provides an additional leverage to reduce the residual S-content and to thereby effectively decouple impurity content from attainable particle morphology.

Derivation of pCAM design strategies.—As shown and discussed above, the residual S-content, the crystallinity, and the morphological properties of $Ni_xCo_yMn_z(OH)_2$ (with $x+y+z = 1$) pCAM particles can be manipulated by adjusting the pH-value during coprecipitation due to the pH-dependent SO_4^{2-} adsorption equilibrium. In light of this, pCAM design strategies can be formulated.

Generally, coprecipitation above the pzc of the mixed metal hydroxide in $Ni_xCo_yMn_z(OH)_2$ is recommended to drastically reduce its S-content and to attain ($Ni_xCo_yMn_z(OH)_2$ with $x+y+z = 1$) with reasonable crystallinity. It is assumed that excessive SO_4^{2-} adsorption during the coprecipitation process not only disturbs the growth of the NCM crystallites during the subsequent calcination reaction with lithium salts conducted at elevated temperatures, but also leads to lithium consumption due to lithium sulfate (Li_2SO_4) formation.[81] This could eventually lead to the formation of an under-lithiated CAM (i.e., to Li_xMO_2 with $x < 1.00$) with a decreased specific capacity. Additionally, Li_2SO_4 does not decompose at typical CAM calcination temperatures, hence it could be carried over into the cathode electrode as electrochemically inactive "dead weight," further decreasing the specific capacity of the electrode. In addition, it was suggested that sulfuric residuals may cause nanopores in NCM crystallites, which can promote degradation mechanisms during cycling.[45] These detrimental effects can be minimized by reducing the residual S-content in the pCAM, which can be achieved by increasing the pH-value of the pCAM suspension after completion of the coprecipitation reaction and/or by washing the pCAM filter cake with $NaOH_{(aq)}$. This allows to decouple the S-content from the pCAM particle morphology, which is particularly important if a porous pCAM is desired.

Regarding the desired pCAM morphology, it must be considered that the secondary particle structure of the pCAM is partially transferred to the CAM after the high-temperature calcination. For lithium- and manganese-rich NCMs (LMR-NCMs), it has been shown that the CAM/electrolyte interface area is governing their electrochemical performance, concluding that porous materials exhibiting high BET surface area are preferable for achieving high discharge capacities.[82] However, in order to maximize the volumetric energy density in a battery, densely packed electrodes are required, so that the

internal void volume in CAM particles must be minimized.[83] Therefore, these properties have to be carefully counterbalanced, which can be already influenced during pCAM synthesis.

Additionally, it was demonstrated in this study that particle morphology can be further modified depending on the employed metal feed solution $TMX_{(aq.)}$ and on the respective anion adsorption affinity towards $Ni_xCo_yMn_z(OH)_2$ (with $x+y+z = 1$). This suggests that the crystal growth during coprecipitation and thus the resulting morphology can likewise be tuned by additives (e.g., organic acids), provided that the additive exhibits a higher adsorption affinity than the anion X in the $TMX_{(aq.)}$ feed. Accordingly, addition of acetate salts during $Ni_xCo_yMn_z(OH)_2$ (with $x+y+z = 1$) crystallization in the presence of nitrate ions was claimed in a patent to attain porous particles.[68] However, attention has to be paid to residual impurities (e.g., C from organics) during the subsequent lithiation reaction and manufacturing steps. Analogous to SO_4^{2-}, impurities could not only affect crystal growth, but also consume lithium during calcination, resulting in under-lithiated NCMs accompanied by undesired residual lithium salt impurities (e.g., Li_2CO_3). Furthermore, impurities could also decompose depending on the calcination temperature and atmosphere, leading to the formation of hazardous gases (e. g., CO_X or NO_x), which entails expensive exhaust emission treatment for industrial-scale CAM manufacturing. In the event that residual impurities are remaining in the CAM, they may cause ink-gelation during electrode manufacturing,[84] and/or deteriorating side-reactions in the final LIB application.[85]

Expanding the implications of this work, future studies could investigate, e.g., the impact of reaction temperature at constant coprecipitation pH-value on the $Ni_xCo_yMn_z(OH)_2$ (with $x+y+z = 1$) particle formation. Since adsorption processes are exotherm, a decrease in SO_4^{2-} coverage would be expected with increasing coprecipitation temperature, potentially resulting in the densification of secondary particles.

Conclusions

In this study, the $Ni_xCo_yMn_z(OH)_2$ (with $x+y+z = 1$) particle formation mechanism during the coprecipitation reaction in a stirred-tank reactor was studied by preparing semi-batch wise ten particle lots of $Ni_{0.8}Co_{0.1}Mn_{0.1}(OH)_2$ as precursor for lithium-ion battery cathode materials. The coprecipitation pH-value between the batch syntheses was adjusted over a range of $pH_{23\ °C} = 8.6–12.7$, while keeping other process parameters constant. The residual S-content in the resulting $Ni_{0.8}Co_{0.1}Mn_{0.1}(OH)_2$ powders was characterized by elemental analysis and was entirely attributed to be SO_4^{2-}, which originates from the $TMSO_{4(aq.)}$ feed used as reactant. The implications of the SO_4^{2-} adsorption on the microstructural properties of the $Ni_{0.8}Co_{0.1}Mn_{0.1}(OH)_2$ samples was investigated by X-ray diffraction, while the impact on the $Ni_{0.8}Co_{0.1}Mn_{0.1}(OH)_2$ secondary particle morphology was analyzed by SEM imaging. Furthermore, the qualitative trends observed by SEM imaging were quantified by determination of the primary particle size distributions from SEM images and by determination of the secondary particle porosity via nitrogen physisorption. As a proof of concept, comparative semi-batch coprecipitations of $Ni_{0.8}Co_{0.1}Mn_{0.1}(OH)_2$ particles were also conducted with $TM(NO_3)_{2(aq.)}$ and $TM(CH_3COO)_{2(aq.)}$ as reactant feed, along with adsorption/desorption experiments of SO_4^{2-} from coprecipitated $Ni_{0.8}Co_{0.1}Mn_{0.1}(OH)_2$ produced with metal sulfate reactant feeds.

Elemental analysis of the $Ni_{0.8}Co_{0.1}Mn_{0.1}(OH)_2$ particle lots revealed a dependency of their residual S-content on the coprecipitation pH-value in relation to the pzc of $Ni_{0.8}Co_{0.1}Mn_{0.1}(OH)_2$ (at a $pH_{23\ °C}$ of $\sim$10.5), which was rationalized by a pH-dependent SO_4^{2-} adsorption equilibrium. Coprecipitation at $pH_{23\ °C} <$ pzc resulted in $Ni_{0.8}Co_{0.1}Mn_{0.1}(OH)_2$ particles with high residual SO_4^{2-} content, while at $pH_{23\ °C} <$ pzc the SO_4^{2-} uptake is significantly reduced by a factor of $\sim$10. Thereby, the SO_4^{2-} adsorption equilibrium regulates additionally the crystallinity of the resulting $Ni_{0.8}Co_{0.1}Mn_{0.1}(OH)_2$ powder, as it was proven by X-ray diffraction that amorphous α-type $Ni_{0.8}Co_{0.1}Mn_{0.1}(OH)_2$ was obtained when

coprecipitating at $pH_{23\ °C} <$ pzc while a coprecipitation at $pH_{23\ °C} >$ pzc resulted in crystalline β-type $Ni_{0.8}Co_{0.1}Mn_{0.1}(OH)_2$. Furthermore, it was demonstrated by X-ray diffraction that the specific SO_4^{2-} adsorption on the (001) plane of the β-type $Ni_{0.8}Co_{0.1}Mn_{0.1}(OH)_2$ crystallites affects the vertical crystal growth of the primary particles, which results in an enlargement of the vertical primary particle size (determined by SEM image analysis) with increasing coprecipitation pH-value concomitant with a decrease in secondary particle porosity (determined by nitrogen physisorption).

For concept validation, β-type $Ni_{0.8}Co_{0.1}Mn_{0.1}(OH)_2$ was coprecipitated using $TM(NO_3)_{2(aq.)}$ or $TM(CH_3COO)_{2(aq.)}$ reactant feeds, and the physical properties of the resulting particles were analogously characterized and compared to the properties of an $TMSO_{4(aq.)}$ based precipitate obtained at the identical coprecipitation pH-value of $pH_{23\ °C} = 12.0$. Here, the vertical primary particle size increased, while intra-particle porosity of the secondary particles decreased depending on the mixed transition metal solution in the following order: $TM(CH_3COO)_{2(aq.)} < TMSO_{4(aq.)} < TM(NO_3)_{2(aq.)}$. This trend is rationalized in the light of the Fajans Paneth-Hahn Law by the distinctive impact on crystal growth of the respective anion in the mixed metal solution, which originates from the specific adsorption strength of the respective anion.

Further, adsorption/desorption experiments demonstrate the possibility to decouple the β-type $Ni_{0.8}Co_{0.1}Mn_{0.1}(OH)_2$ secondary particle morphology that is attained by the coprecipitation from the intrinsically related residual S-content: By raising the pH-value after completion of the coprecipitation reaction above the respective coprecipitation pH-value ($pH_{adjustment} > pH_{coprecipitation}$), the S-content decreases, while if the pH-value is lowered below the coprecipitation pH-value ($pH_{adjustment} < pH_{coprecipitation}$), the S-content increases. In addition to manipulating the S-content after the solid formation, the S-content can also be decreased by washing β-type $Ni_{0.8}Co_{0.1}Mn_{0.1}(OH)_2$ with $NaOH_{(aq.)}$ during filtration.

Based on the implications of this study, the following design rules for Ni-rich $Ni_xCo_yMn_z(OH)_2$ (with $x+y+z = 1$) can be formulated.

- To attain Ni-rich $Ni_xCo_yMn_z(OH)_2$ (with $x+y+z = 1$) pCAM coprecipitates with sufficiently low residual S-content and crystallinity for subsequent CAM preparation, the coprecipitation should be conducted above the pH-value corresponding to the pzc of the respective $Ni_xCo_yMn_z(OH)_2$ (with $x+y+z = 1$), which is in the case of $Ni_{0.8}Co_{0.1}Mn_{0.1}(OH)_2$ above the $pH_{23\ °C}$-value of 10.5.
- The secondary particle porosity of coprecipitated $Ni_xCo_yMn_z(OH)_2$ (with $x+y+z = 1$) as pCAM can be tuned according to the requirements of the respective CAM application by either manipulating the coprecipitation pH-value and/or by varying the anions present during the coprecipitation reaction.
- The residual S-content in $Ni_xCo_yMn_z(OH)_2$ (with $x+y+z = 1$) can be lowered after the coprecipitation reaction has completed by increasing the pH-value above the coprecipitation pH-value and/or by applying a $NaOH_{(aq.)}$ wash, which effectively decouples secondary particle morphology from impurity content.

Acknowledgments

Appendix

Stirred tank reactor setup.—A schematic illustration of the employed stirred-tank reactor setup for preparing $Ni_{0.8}Co_{0.1}Mn_{0.1}(OH)_2$ particles is given in Fig. A-1.
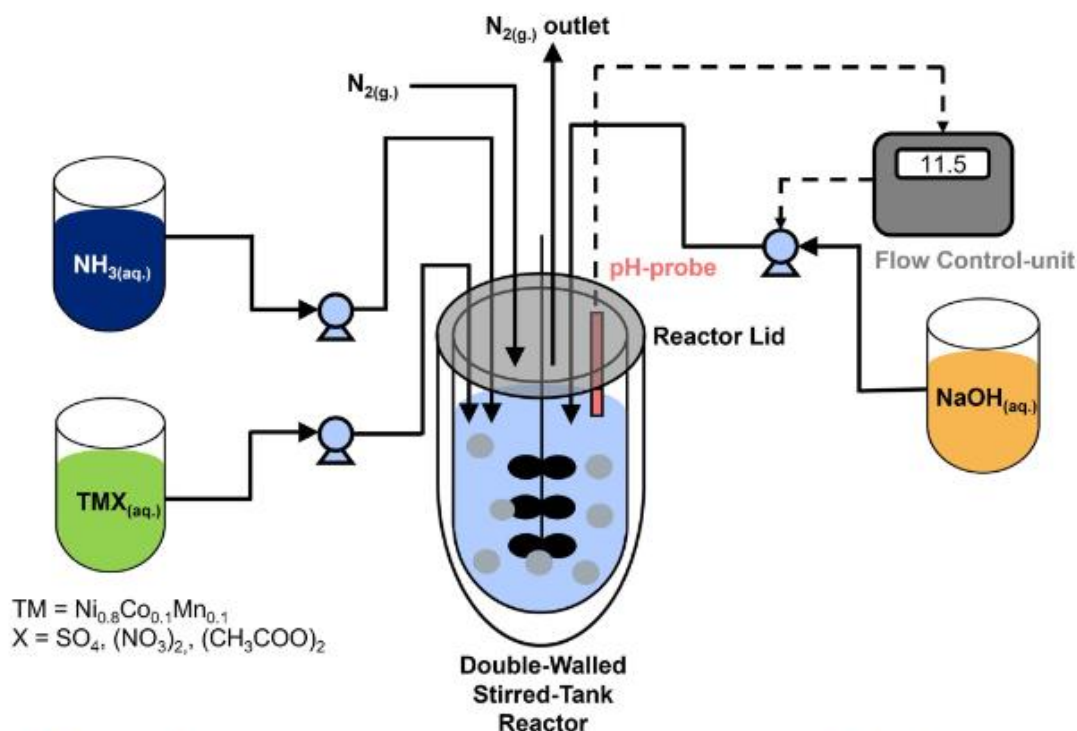
Figure A·1. Schematic illustration of the employed stirred-tank reactor setup for preparing $Ni_{0.8}Co_{0.1}Mn_{0.1}(OH)_2$ particles. The flow rates of the aqueous ammonia solution ($NH_{3(aq.)}$) and the mixed transition metal salt solution ($TMX_{(aq.)}$), with the molar transition metal composition TM of Ni/Co/Mn of 0.8/0.1/0.1 and with X representing either SO_4, $(NO_3)_2$, or $(CH_3COO)_2$ remained constant throughout the coprecipitation reaction, while the $NaOH_{(aq.)}$ flow was automatically regulated by a flow control-unit that controlled the solution pH measured by the pH-probe inside the reactor to a set constant pH-value throughout the coprecipitation reaction.
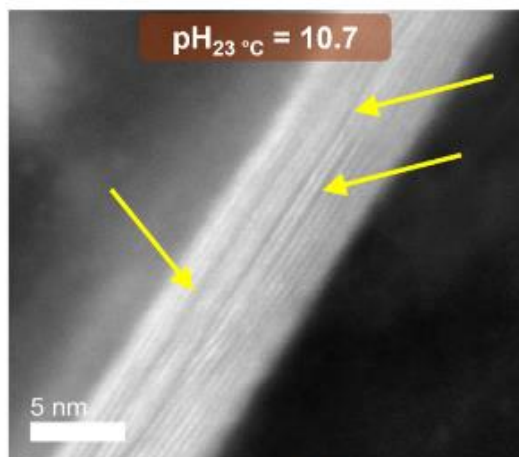
Figure A·2. HR-TEM image of β-type $Ni_{0.8}Co_{0.1}Mn_{0.1}(OH)_2$ coprecipitated at $pH_{23\,°C} = 10.7$.

Final concentrations of components inside the reactor.—An overview of the relevant soluble and insoluble components inside the stirred tank reactor after completed coprecipitation reaction of 5 h is given in Table A-I. Please note that the listed concentrations for $MSO_{4(aq.)}$ are representative for all coprecipitation experiments from $MSO_{4(aq.)}$ despite being conducted at different coprecipitation pH-values as the volumetric flow rate of the $NaOH_{(aq.)}$ for adjusting the coprecipitation pH-value was nearly identical.

HR-TEM image of $Ni_{0.8}Co_{0.1}Mn_{0.1}(OH)_2$ coprecipitated at $pH_{23\,°C} = 10.7$.—For better visual investigation, the HR-TEM image of β-type $Ni_{0.8}Co_{0.1}Mn_{0.1}(OH)_2$ coprecipitated at $pH_{23\,°C} = 10.7$ is given Fig. A-2. The yellow arrows are highlighting layer distortions, which indicate α-phase interstratifications and/or SO_4^{2-} incorporation.

Secondary particle size and secondary particle growth rate.—In desired time intervals, the coprecipitation reaction progress was controlled by withdrawing 4–5 ml of reaction suspension from the reactor, cooling it to 23 °C, measuring the pH-value at 23 °C and determining the secondary particle size distribution by laser diffraction. For this purpose, the reactor suspension sample was homogenously dispersed, and a small amount of the particle slurry was transferred into the particle size analyzer (Mastersizer 2000, Malvern Panalytical GmbH) until a light obscuration between 4.0%-14.0% was achieved. The respective volume-based secondary particle size distribution (PSD) was determined by laser diffraction based on Mie's scattering theory. A refractive index of 1.33 for H_2O as dispersant was selected, while a refractive index of 2.19, identical to the refractive index of NiO, was assumed for the $Ni_{0.8}Co_{0.1}Mn_{0.1}(OH)_2$ secondary particles. The intensity of the

Table A-I. The mixed transition metal solution $TMX_{(aq.)}$ ($X = NO_3^-$, SO_4^{2-}, CH_3COO^-) with anion X applied as feed for the coprecipitation of $Ni_{0.8}Co_{0.1}Mn_{0.1}(OH)_2$ secondary particles, the final $Ni_{0.8}Co_{0.1}Mn_{0.1}(OH)_2$ solid content inside the stirred tank reactor, the final ammonia $NH_{3(aq.)}$ concentration inside the stirred tank reactor, the final concentration of the respective anionic species X and the ratio of the anionic species X and the $Ni_{0.8}Co_{0.1}Mn_{0.1}(OH)_2$ solid.

$TMX_{(aq.)}$	Final $Ni_{0.8}Co_{0.1}Mn_{0.1}(OH)_2$ solid content [g/l]	Final $NH_{3(aq.)}$ concentration [mol/l]	Final concentration of anionic species X [mol/l]	Anion species X to $Ni_{0.8}Co_{0.1}Mn_{0.1}(OH)_2$ solid ratio [mol/g]
$X = SO_4^{2-}$	85.9	0.28	0.93	0.01
$X = NO_3^-$	85.9	0.28	1.87	0.02
$X = CH_3COO^-$	28.8	0.09	0.62	0.02

Table A·II. The mixed transition metal solution $TMX_{(aq.)}$ ($X = NO_3^-$, SO_4^{2-}, CH_3COO^-) with anion X applied as feed for the coprecipitation of $Ni_{0.8}Co_{0.1}Mn_{0.1}(OH)_2$ secondary particles, the coprecipitation pH-value at measured at 23 °C $pH_{23\,°C}$, the volume median particle size d_{50} of the corresponding PSDs determined by light scattering from $Ni_{0.8}Co_{0.1}Mn_{0.1}(OH)_2$ reaction suspension sampled at run time of 1 h and 5 h during the coprecipitation of $Ni_{0.8}Co_{0.1}Mn_{0.1}(OH)_2$ secondary particles and the average growth rate $G_{avg.}$ between the run time of 1 h and 5 h in the respective coprecipitation experiment calculated according to Eq. 5.

$TMX_{(aq.)}$	$pH_{23\,°C}$ [−]	$d_{50,\,1\,h}$ [μm]	$d_{50,\,5\,h}$ [μm]	$G_{avg.}$ [$\mu m/h$]
$X = SO_4^{2-}$	11.2	3.3	6.0	0.68
$X = SO_4^{2-}$	12.0	4.3	7.7	0.85
$X = SO_4^{2-}$	12.7	4.0	6.1	0.53
$X = NO_3^-$	12.0	4.1	6.9	0.70
$X = CH_3COO^-$	12.7	3.0	6.0	0.75

scattered laser beam was collected as a function of the scattering angle for particle sizes in the range of 0.05–70.0 μm by applying a combination of red and blue light. Based on three measurements per sample, the median volume-based percentile secondary particle sizes d_{50} was determined. The average $Ni_{0.8}Co_{0.1}Mn_{0.1}(OH)_2$ secondary particle growth rate $G_{avg.}$ between a coprecipitation run time of t_{run} of 1 h and 5 h was calculated according to the following equation.

$$G_{avg.} = \frac{d_{50,\,2} - d_{50,\,1}}{t_{run,\,2} - t_{run,\,1}} \quad [5]$$

To evaluate the role of the secondary particle growth rate, Table A·II lists the values for the d_{50} at a coprecipitation reaction run time of 1 h, $d_{50,\,1\,h}$ and 5 h, $d_{50,\,5\,h}$ as well as the average $_{avg.}$ of $Ni_{0.8}Co_{0.1}Mn_{0.1}(OH)_2$ secondary particles within the run time of 1 h and 5 h for the "extreme" coprecipitation conditions conducted.

ORCID

Rafael B. Berk https://orcid.org/0000-0002-9673-9381
Hubert A. Gasteiger https://orcid.org/0000-0001-8199-8703

References

1. A. Masias, J. Marcicki, and W. Paxton, *ACS Energy Lett.*, **6**, 621 (2021).
2. Y. Ding, Z. P. Cano, A. Yu, J. Lu, and Z. Chen, *Electrochemical Energy Reviews*, **2**, 1 (2019).
3. B. Dunn, H. Kamath, and J.-M. Tarascon, *Science*, **334**, 928 (2011).
4. G. Berckmans, M. Messagie, J. Smekens, N. Omar, L. Vanhaverbeke, and J. Van Mierlo, *Energies*, **10**, 1314 (2017).
5. A. Manthiram, *Nat. Commun.*, **11**, 1 (2020).
6. D. Andre, S.-J. Kim, P. Lamp, S. F. Lux, F. Maglia, O. Paschos, and B. Stiaszny, *J. Mater. Chem. A*, **3**, 6709 (2015).
7. S. S. Zhang, *Energy Storage Mater.*, **24**, 247 (2020).
8. F. Schipper, E. M. Erickson, C. Erk, J.-Y. Shin, F. F. Chesneau, and D. Aurbach, *J. Electrochem. Soc.*, **164**, A6220 (2016).
9. H.-J. Noh, S. Youn, C. S. Yoon, and Y.-K. Sun, *J. Power Sources*, **233**, 121 (2013).
10. S.-T. Myung, F. Maglia, K.-J. Park, C. S. Yoon, P. Lamp, S.-J. Kim, and Y.-K. Sun, *ACS Energy Lett.*, **2**, 196 (2017).
11. M. H. Lee, Y. J. Kang, S. T. Myung, and Y. K. Sun, *Electrochim. Acta*, **50**, 939 (2004).
12. F. Zhou, X. Zhao, A. van Bommel, A. W. Rowe, and J. R. Dahn, *Chem. Mater.*, **22**, 1015 (2009).
13. Y. K. Sun, S. T. Myung, B. C. Park, J. Prakash, I. Belharouak, and K. Amine, *Nat. Mater.*, **8**, 320 (2009).
14. A. van Bommel and J. R. Dahn, *J. Electrochem. Soc.*, **156**, A362 (2009).
15. M. Noh and J. Cho, *J. Electrochem. Soc.*, **160**, A105 (2012).
16. J.-M. Kim, S.-M. Chang, J. H. Chang, and W.-S. Kim, *Colloids Surf., A*, **384**, 31 (2011).
17. A. van Bommel and J. R. Dahn, *Chem. Mater.*, **21**, 1500 (2009).
18. V. Y. Kazimirov, M. B. Smirnov, L. Bourgeois, L. Guerlou-Demourgues, L. Servant, A. M. Balagurov, I. Natkaniec, N. R. Khasanova, and E. V. Antipov, *Solid State Ionics*, **181**, 1764 (2010).
19. D. S. Hall, D. J. Lockwood, C. Bock, and B. R. MacDougall, *Proc Math Phys Eng Sci*, **471**, 20140792 (2015).
20. S. Bette, B. Hinrichsen, D. Pfister, and R. E. Dinnebier, *J. Appl. Crystallogr.*, **53**, 76 (2020).
21. M. Bianchini, F. Fauth, P. Hartmann, T. Brezesinski, and J. Janek, *J. Mater. Chem. A*, **8**, 1808 (2020).
22. Y.-K. Sun, D.-H. Kim, H.-G. Jung, S.-T. Myung, and K. Amine, *Electrochim. Acta*, **55**, 8621 (2010).
23. Y.-K. Sun, D.-H. Kim, C. S. Yoon, S.-T. Myung, J. Prakash, and K. Amine, *Adv. Funct. Mater.*, **20**, 485 (2010).
24. Y.-K. Sun, B.-R. Lee, H.-J. Noh, H. Wu, S.-T. Myung, and K. Amine, *J. Mater. Chem.*, **21**, 10108 (2011).
25. P. Kurzhals, F. Riewald, M. Bianchini, H. Sommer, H. Gasteiger, and J. Janek, *J. Electrochem. Soc.*, **168**, 110518 (2021).
26. F. Riewald, P. Kurzhals, M. Bianchini, H. Sommer, J. Janek, and H. A. Gasteiger, *J. Electrochem. Soc.*, **169**, 020529 (2022).
27. Z. Xu, L. Xiao, F. Wang, K. Wu, L. Zhao, M.-R. Li, H.-L. Zhang, Q. Wu, and J. Wang, *J. Power Sources*, **248**, 180 (2014).
28. D.-L. Vu and J.-w Lee, *Korean J. Chem. Eng.*, **33**, 514 (2015).
29. J. S. Noh and J. A. Schwarz, *J. Colloid Interface Sci.*, **130**, 157 (1989).
30. S. Subramanian, J. S. Noh, and J. A. Schwarz, *J. Catal.*, **114**, 433 (1988).
31. C. F. H. Liao, *Soil Sci. Soc. Am. J.*, **45**, 852 (1981).
32. M. Casas-Cabanas, M. R. Palacín, and J. Rodríguez-Carvajal, *Powder Diffr.*, **20**, 334 (2005).
33. Q. Instruments, Gas Sorption System Operating Manual, Vol. P/N 05098-1.1 Rev D, p. 337. Quantachrome Instruments, Florida, USA (2009).
34. B. Strehle, "Degradation Mechanisms of Layered Oxides Used as Cathode Active Materials in Lithium-Ion Batteries." *PhD Thesis*, Technical University of Munich (2022), chapter 2.3.
35. P. Klobes and R. G. Munro, (2006)23Porosity and specific surface area measurements for solid materials, Special Publication (NIST SP), National Institute of Standards and Technology.
36. L. M. Anovitz and D. R. Cole, *Rev. Mineral. Geochem.*, **80**, 61 (2015).
37. C. A. Schneider, W. S. Rasband, and K. W. Eliceiri, *Nat. Methods*, **9**, 671 (2012).
38. C. Faure, C. Delmas, and M. Fouassier, *J. Power Sources*, **35**, 279 (1991).
39. P. Oliva, J. Leonardi, J. F. Laurent, C. Delmas, J. J. Braconnier, M. Figlarz, F. Fievet, and A. d Guibert, *J. Power Sources*, **8**, 229 (1982).
40. L. Guerlou-Demourgues, C. Denage, and C. Delmas, *J. Power Sources*, **52**, 269 (1994).
41. A. Delahaye-Vidal, B. Beaudoin, N. Sac-Epée, K. Tekaia-Elhsissen, A. Audemer, and M. Figlarz, *Solid State Ionics*, **84**, 239 (1996).
42. Q. Song, Z. Tang, H. Guo, and S. L. I. Chan, *J. Power Sources*, **112**, 428 (2002).
43. W. Luo and J. R. Dahn, *Chem. Mater.*, **21**, 56 (2009).
44. A. Liu and J. Dahn, *ChemEngineering*, **3**, 3852 (2019).
45. S. Ahmed et al., *ACS Nano*, **13**, 10694 (2019).
46. M. Kosmulski, *Adv. Colloid Interface Sci.*, **152**, 14 (2009).
47. Y. Wang and H. Gao, *J. Colloid Interface Sci.*, **301**, 19 (2006).
48. J. Park and J. R. Regalbuto, *J. Colloid Interface Sci.*, **175**, 239 (1995).
49. J. S. Geelhoed, T. Hiemstra, and W. H. Van Riemsdijk, *Geochim. Cosmochim. Acta*, **61**, 2389 (1997).
50. K. H. Goh, T. T. Lim, and Z. Dong, *Water Res.*, **42**, 1343 (2008).
51. M. Islam and R. Patel, *J. Hazard. Mater.*, **190**, 659 (2011).
52. C. Coudun, F. Grillon, and J.-F. Hochepied, *Colloids Surf., A*, **280**, 23 (2006).
53. L. Demourgues-Guerlou and C. Delmas, *J. Power Sources*, **45**, 281 (1993).
54. R. S. McEwen, *J. Phys. Chem.*, **75**, 1782 (1971).
55. L. Guerlou-Demourgues and C. Delmas, *J. Power Sources*, **52**, 275 (1994).
56. C. Faure, C. Delmas, and P. Willmann, *J. Power Sources*, **35**, 263 (1991).
57. A. Gaunand and W. Lim, *Powder Technol.*, **128**, 332 (2002).
58. H. El-Batlouni, H. El-Rassy, and M. Al-Ghoul, *J. Phys. Chem. A*, **112**, 7755 (2008).
59. J. Rahbani, M. Ammar, and M. Al-Ghoul, *J. Phys. Chem. A*, **117**, 1685 (2013).
60. J. Rahhani, N. M. Khashab, D. Patra, and M. Al-Ghoul, *J. Mater. Chem.*, **22**, 16361 (2012).
61. M. L. Para, M. Alidoost, M. Shica, G. Boccardo, A. Buffo, A. A. Barresi, and D. Marchisio, *Chem. Eng. Sci.*, **254**, 117634 (2022).
62. T. Cao, W. Zhang, J. Cheng, and C. Yang, *Chin. J. Chem. Eng.*, **26**, 196 (2018).
63. R. J. Davey and J. W. Mullin, *J. Cryst. Growth*, **26**, 45 (1974).
64. N. Kubota, J. Fukazawa, H. Yashiro, and J. W. Mullin, *J. Cryst. Growth*, **149**, 113 (1995).
65. I. Kolthoff, *J. Phys. Chem.*, **36**, 860 (2002).
66. R. B. Berk, T. Beierling, L. Metzger, and H. A. Gasteiger, "Investigation of the Particle Formation Mechanism during Coprecipitation of Ni-Rich Hydroxide Precursor for Li-Ion Cathode Active Material." *Journal of The Electrochemical Society*, **170**, 110513 (2023).
67. X. Sun, J. Kim, and W.-S. Kim, *Chem. Eng. J.*, **421**, 129924 (2021).

68. F. Z. Y. Liu, Vol. WO 2021/50935 A1. Springpower International Inc., 2021*Process to produce cathode materials for rechargeable li batteries*, WO2021050935A1 (2020).

69. J. He, M. Wei, B. Li, Y. Kang, D. G. Evans, and X. Duan, "Preparation of Layered Double Hydroxides." *Layered Double Hydroxides* (Springer, Berlin, Heidelberg)p. 89 (2006).

70. Y. You, G. F. Vance, and H. Zhao, *Appl. Clay Sci.*, **20**, 13 (2001).

71. C. Colombo, M. Ricciardella, A. Di Cerce, L. Maiuro, and A. Violante, *Clays Clay Miner.*, **52**, 721 (2004).

72. A. Violante, L. Gianfreda, and P. Violante, *Clays Clay Miner.*, **41**, 353 (1993).

73. W. Gibson, "The Radiochemistry of Lead." *NAS-NS-3040*, National Academy of Sciences (1961).

74. S. Van Der Sluis, G. J. Witkamp, and G. M. Van Rosmalen, *J. Cryst. Growth*, **79**, 620 (1986).

75. K. Sangwal and E. Mielniczek-Brzóska, *Cryst. Res. Technol.*, **42**, 531 (2007).

76. K. S. Egorova and V. P. Ananikov, *Angew. Chem. Int. Ed.*, **55**, 12150 (2016).

77. J. Rumble, *CRC Handbook of Chemistry and Physics*, ed. J. Rumble (CRC Press, Boca Raton, FL) Vol. 102 (2021).

78. A. Apelblat and E. Manzurola, *The Journal of Chemical Thermodynamics*, **31**, 1347 (1999).

79. H. Hatami, A. Fotovat, and A. Halajnia, *Appl. Clay Sci.*, **152**, 333 (2018).

80. A. M.-M. Olbrich, *Beta-nickel hydroxide doped with aluminum*, WO2018234112A1 (2018).

81. J. Lee, S. Park, M. Beak, S. R. Park, A. R. Lee, S. H. Byun, J. Song, J. S. Sohn, and K. Kwon, *Materials*, **14**, 6672 (2021).

82. B. Strehle, J. Yoon, F. Friedrich, and H. Gasteiger, *J. Electrochem. Soc.*, **169**, 060521 (2022).

83. D. Schreiner et al., *J. Electrochem. Soc.*, **168**, 030507 (2021).

84. L. Hartmann, D. Pritzl, H. Beyer, and H. A. Gasteiger, *J. Electrochem. Soc.*, **168**, 070507 (2021).

85. R. Jung, R. Morasch, P. Karayaylali, K. Phillips, F. Maglia, C. Stinner, Y. Shao-Horn, and H. A. Gasteiger, *J. Electrochem. Soc.*, **165**, A132 (2018).

4 Conclusions and outlook

The goal of this PhD thesis was to deepen the understanding of the NCM pCAM coprecipitation mechanism by detailed investigation of process-parameter-product-property relationships. The $Ni_{0.8}Co_{0.1}Mn_{0.1}(OH)_2$ particle formation and growth were studied with an in-house-designed STR by monitoring the course of the coprecipitation reaction and characterizing the properties of intermediates and products. The key findings of this work are summarized in Figure 17 marking the sections in which the findings are described.
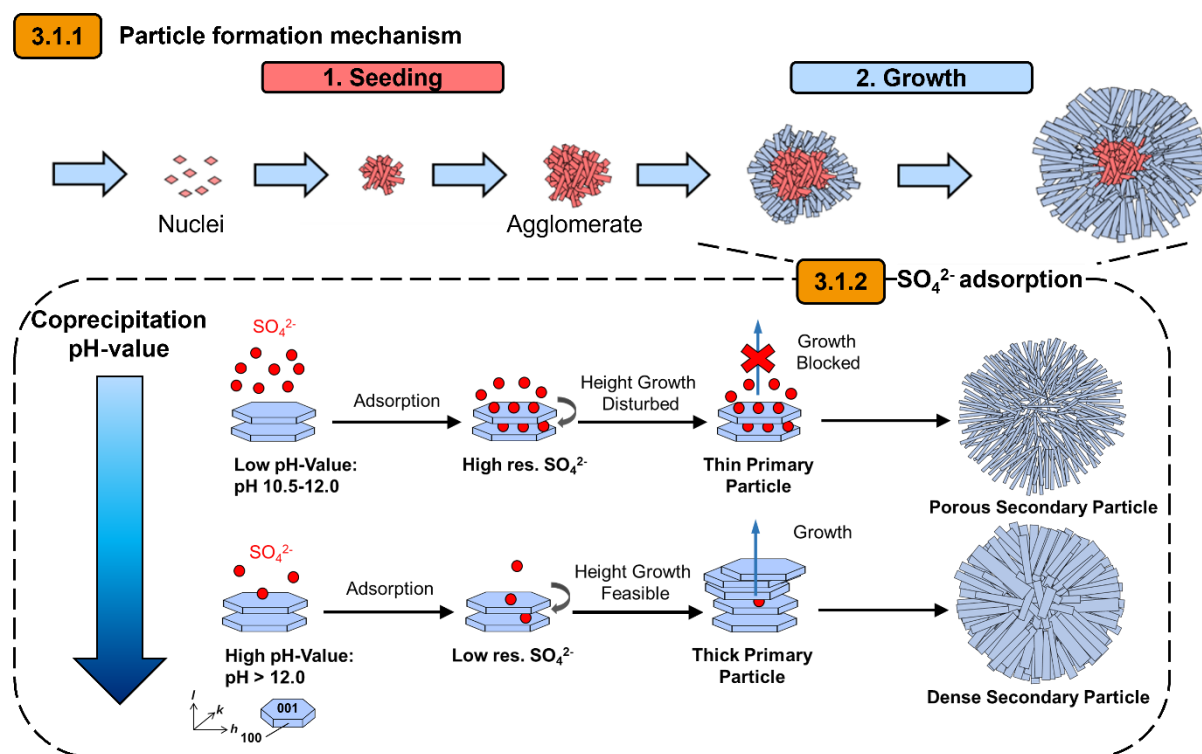
Figure 17: Graphical summary of the key results of this PhD thesis. The discovery of a two-stage $N_{0.8}Co_{0.1}Mn_{0.1}(OH)_2$ secondary particle formation mechanism comprising the seeding of agglomerates and the subsequent growth thereof described in section 3.1.1, and the identification of a pH-dependent SO_4^{2-} adsorption equilibrium governing the secondary porosity of the resulting $N_{0.8}Co_{0.1}Mn_{0.1}(OH)_2$ secondary particles, described in section 3.1.2.

At the outset, in section 3.1.1, the particle development during the semi-batch coprecipitation of $Ni_{0.8}Co_{0.1}Mn_{0.1}(OH)_2$ in an STR at stirring speeds of 550-1350 rpm was monitored by laser scattering and SEM imaging. Independent of the synthesis conditions, a two-step particle formation mechanism consisting of a seeding and growth phase was identified. During the seeding phase, rapid agglomeration of nucleating nanospheres results in the

generation of irregular-shaped secondary particles, while the overall secondary particle size remains constant. In the ensuing growth phase, the agglomerates increase in size with the third root of time by lateral crystal growth of the individual plate-like shaped primary particles, which eventually leads to spherical secondary particles. Complementary evidence for a two-stage mechanism was found in CS-SEM images of $Ni_{0.8}Co_{0.1}Mn_{0.1}(OH)_2$ secondary particles, revealing a secondary particle center comprising of randomly aligned primary particles followed by radially aligned primary particles elongated towards the outer perimeter of the secondary particle. Thereby, the extent of the turbulence in the STR, controllable by the stirring speed, governs at otherwise constant process parameters the agglomerate size and number formed during seeding, which dictates the growth rate and the secondary particle sphericity. This relationship provides control over the pCAM physical properties of the secondary particles such as size and sphericity during the coprecipitation reaction. In this context a high degree of turbulence (quantified by the Reynolds number and average energy input) during the seeding stage is necessary to achieve spherical pCAM secondary particles. This is imperative for cost-effective processing of pCAM and CAM powders in tonnage quantities during NCM manufacturing, as the fluidity and filterability of powders generally suffers for non-spherical particles.[84-89]

In section 3.1.1, the secondary particle growth during semi-batch coprecipitation of $Ni_{0.8}Co_{0.1}Mn_{0.1}(OH)_2$ with respect to the coprecipitation pH-value was investigated in detail by manipulation of the coprecipitation pH-value between 8.7-12.7. Elemental analysis of the obtained precipitates revealed a pH-dependent SO_4^{2-} adsorption equilibrium that governs the SO_4^{2-} uptake during the coprecipitation reaction. This in turn affects the crystallinity of the resulting $Ni_{0.8}Co_{0.1}Mn_{0.1}(OH)_2$ powders determined by X-ray diffraction. Further, it is shown by examination of individual reflexes in the diffraction patterns of crystalline $Ni_{0.8}Co_{0.1}Mn_{0.1}(OH)_2$ that the SO_4^{2-} adsorption also regulates the vertical crystal growth crystallites due to preferred SO_4^{2-} adsorption on the (001)-plane. This effect influences the $Ni_{0.8}Co_{0.1}Mn_{0.1}(OH)_2$ secondary particle morphology and porosity, as with increasing coprecipitation pH-value an enlargement of the vertical primary particle size concomitant with an increase in secondary particle density was identified by SEM imaging and nitrogen physisorption. As proof-of-concept, the physical properties of $Ni_{0.8}Co_{0.1}Mn_{0.1}(OH)_2$ precipitated from different $MX_{(aq.)}$ (with $X = SO_4^{2-}$, $(NO_3^-)_2$, $(CH_3COO^-)_2$) feed solutions at constant coprecipitation pH-value, was compared. The obtained secondary particle morphologies are rationalized by the distinctive impact on the crystal growth of the respective anion (X) during the coprecipitation reaction based on the individual adsorption affinity of the

respective anion towards $Ni_{0.8}Co_{0.1}Mn_{0.1}(OH)_2$ according to the Fajans-Paneth-Hahn Law. Finally, desorption experiments demonstrate options to reduce the impurity content in the pCAM particles after its formation is completed. Making use of the here discovered pH-dependent SO_4^{2-} adsorption equilibrium, design rules for NCM pCAM can be formulated. Generally, it is recommend to conduct the pCAM coprecipitation process at pH-values above the pzc-value of the structurally dominating metal hydroxide in $Ni_xCo_yMn_z(OH)_2$. This limits the residual SO_4^{2-} uptake during the coprecipitation reaction and yields a product with a reasonable crystallinity. While SO_4^{2-} itself is electrochemically inactive, thus not causing undesired side-reactions in the LIB application, residual SO_4^{2-} in the pCAM results in undesired Li consumption during the calcination reaction due to the formation of lithium sulfate $Li_2SO_{4(s.)}$.[189] This leads to an under-lithiated CAM as well as a carryover of $Li_2SO_{4(s.)}$ to the electrode as inactive weight, both decreasing eventually the achievable specific capacity. Additionally, it was shown that the control of pCAM secondary particle porosity provided by adjusting the coprecipitation pH-value of the pCAM is intrinsically linked to the residual SO_4^{2-} content in the resulting precipitate. This inherent relationship can be decoupled by increasing the pH-value after the solid formation has been completed and/or washing the pCAM precipitate with $NaOH_{(aq.)}$, which is particularly useful if a porous secondary particle structure is desired. Further, the act of counterbalancing the CAM's electrode density to achieve a high volumetric energy density[66] against the CAM-to-electrolyte interface area, which governs the electrochemical performance,[67] can be already influenced during the pCAM synthesis by adjusting the coprecipitation pH-value. Likewise, the pCAM secondary particle morphology can be tuned by additives (e.g., organic acids). However, in this case the additive residuals in the pCAM must be considered regarding their reactivity with Li and decomposition temperature of the resulting Li salt, as the formation of hazardous gases would entail expensive exhaust emission treatment during CAM manufacturing on an industrial scale.

Expanding the topic of this work, future studies could address the role of the remaining coprecipitation parameters such as feed flow rates, $NH_{3(aq.)}$ concentration, and temperature. For the latter, an increase in $Ni(OH)_2$ secondary particle density with increasing coprecipitation temperature at otherwise constant parameters was reported without further investigation.[124] This agrees well to the in this work demonstrated pH-dependent SO_4^{2-} adsorption equilibrium that governs the $Ni_{0.8}Co_{0.1}Mn_{0.1}(OH)_2$ secondary particle porosity during coprecipitation reaction. Since adsorption processes are exothermic, a decrease in SO_4^{2-} occupation would be expected, resulting in the densification of secondary particles, as the vertical crystal growth of primary particles can freely occur. This hypothesis could be verified by variation of the reaction

temperature during the coprecipitation reaction at otherwise constant parameters and by an analogous characterization of the thereby attained precipitates as used in section 3.1.2. Alternatively, the influence of impurities in the $MSO_{4(aq.)}$ feed originating from a LIB recycling process on the coprecipitation reaction and the resulting pCAM properties in light of the Fajans-Paneth-Hahn law[187] for adsorption affinities can be explored. Such studies can be even extended to investigate the mode of action of the impurities in the pCAM during the subsequent calcination reaction with a lithium salt and impact on the CAM physical properties as well as electrochemical performance. Regardless, it has to be considered that LIB related research like pCAM and CAM development is rather novel compared to the actual underlying scientific field for pCAM coprecipitation, crystallization. Therefore, a vast amount of the insights available in the field of crystallization can be transferred and applied in pCAM research.

Finally, pCAM-property-CAM-property/performance relationships could be tackled in detail by forthcoming researchers. While it is known that the physical properties[69-72] and the electrochemical performance[73-75] of an NCM CAM is affected by the associated pCAM utilized for the synthesis thereof, a mechanistic understanding is still missing in literature. In e.g., it was phenom logically demonstrated for NCM424 and NCM111 that comparably large primary particles in the pCAM secondary particles yielded comparably smaller primary particles in the resulting NCM CAM secondary particles after calcination at equal conditions. This resulted in distinctive electrochemical performance differences in the final LIB application of the synthesized NCMs from various pCAM morphologies.[73] However, the precise details of the crystal growth during the calcination of various pCAM morphologies as well as the mechanistic transfer from pCAM properties to CAM properties should be elucidated for a wide spectrum of NCM chemistries (e.g., Ni-rich, Mn-rich, Co-free, etc.) to establish an in-depth knowledge of NCM synthesis to enable high performing CAMs for LIBs.

5 Appendix

Reactants are continuously added during a semi-batch coprecipitation in an STR, while the reaction suspension is unable to leave the stirred vessel. This results in a steady increase of the total reaction volume (V_{total}) and mass of formed mixed metal hydroxide, hence volume of formed mixed metal hydroxide ($V_{M(OH)2}$), with progressing batch run time (t_{run}). Due to solubilities of the respective metal hydroxides being < 200 ppm in the coprecipitation pH-range of 11.0-13.0,[44, 55] a complete conversion of the aqueous mixed metal sulfate solution ($MSO_{4(aq.)}$, here M = Ni/Co/Mn in a molar ratio 8/1/1) can be assumed. Further, considering that across the entire run time (t_{run}) the total volumetric flow rate ($\dot{V}_{in}$) remained constant, then $V_{M(OH)2}$ of the formed $Ni_{0.8}Co_{0.1}Mn_{0.1}(OH)_2$ particles is a function of t_{run} and the following expression is valid.

$$V_{M(OH)_2} = \frac{\dot{V}_{MSO4}\, t_{run}\, c_{MSO4}\, M_{M(OH)2}}{\rho_{cryst.}} \tag{13}$$

where $\dot{V}_{MSO4}$ is the volumetric flow rate of $MSO_{4(aq.)}$ ($= 18.0$ mL/h), c_{MSO4} is the concentration of the $MSO_{4(aq.)}$ solution ($= 2.6$ mol/L), $M_{M(OH)2}$ is the molar averaged molar mass of $Ni_{0.8}Co_{0.1}Mn_{0.1}(OH)_2$ ($= 91.93$ g/mol), and $\rho_{cryst.}$ is the crystallographic density of $Ni_{0.8}Co_{0.1}Mn_{0.1}(OH)_2$. A molar composition averaged crystallographic density of 3.96 g/cm^3 is assumed based on the crystallographic density of $Ni(OH)_2$ ($= 4.1$ g/cm3), $Co(OH)_2$ ($= 3.6$ g/cm^3) and $Mn(OH)_2$ ($= 3.26$ g/cm^3) as well as considering the transition metal ratio of 8/1/1.

By approximation of the $Ni_{0.8}Co_{0.1}Mn_{0.1}(OH)_2$ particle's shape as spherical, the volume of individual particles ($V_{par.}$) can be defined as the volume of a sphere with a diameter corresponding to the determined volume median particle size (d_{50}) by light scattering.

$$V_{par.} = \frac{4}{3}\pi\left(\frac{d_{50}}{2}\right)^3 \tag{14}$$

Given that $\dot{V}_{SO4}$ remains constant throughout the batch coprecipitation, and considering equation 13 and 14, the determined d_{50} of $Ni_{0.8}Co_{0.1}Mn_{0.1}(OH)_2$ particles at any t_{run} should then correlate linearly with the third root of t_{run}, as given by the ensuing relationship.

$$d_{50} = \sqrt[3]{\frac{6}{\pi} \cdot \frac{\dot{V}_{MSO4}\ c_{MSO4}\ M_{M(OH)2}}{\rho_{cryst.}}} \cdot \sqrt[3]{\frac{t_{run}}{N_{par.}}} \ \propto \ \sqrt[3]{t_{run}} \ \ (\text{for } N_{par.} = \text{constant}) \tag{15}$$

List of figures

References

<div align="center">Literature</div>

1. Fit for 55, European council for an energy efficient economy, *accessed 01.08.2022*, https://www.consilium.europa.eu/en/policies/green-deal/fit-for-55-the-eu-plan-for-a-green-transition/.

2. EU nations approve end to combustion engine sales by 2035, European Council and Council of the European Union, *accessed 01.08.2022*, https://www.euractiv.com/section/transport/news/eu-countries-approve-end-to-combustion-engine-sales-by-2035/.

3. Global EV Outlook 2021, *accessed 01.08.2022*, https://www.iea.org/reports/global-ev-outlook-2021.

4. R. Kawamoto, H. Mochizuki, Y. Moriguchi, T. Nakano, M. Motohashi, Y. Sakai, and A. Inaba, Estimation of CO_2 Emissions of Internal Combustion Engine Vehicle and Battery Electric Vehicle Using LCA, *Sustainability,* **11** (9), 2690 (2019).

5. W. Li, E. M. Erickson, and A. Manthiram, High-nickel layered oxide cathodes for lithium-based automotive batteries, *Nature Energy,* **5** (1), 26 (2020).

6. M. S. E. Houache, C.-H. Yim, Z. Karkar, and Y. Abu-Lebdeh, On the Current and Future Outlook of Battery Chemistries for Electric Vehicle, *Batteries,* **8** (7), 70 (2022).

7. M. S. Whittingham, Electrical Energy Storage and Intercalation Chemistry, *Science,* **192** (4244), 1126 (1976).

8. T. Ohzuku, A. Ueda, and M. Kouguchi, Synthesis and Characterization of $LiAl_{1/4}Ni_{3/4}O_2$ ($R\bar{3}m$) for Lithium-Ion (Shuttlecock) Batteries, *Journal of The Electrochemical Society,* **142** (12), 4033 (1995).

9. P. A. Nelson, S. Ahmed, K. G. Gallagher, and D. W. Dees, Modeling the performance and cost of lithium-ion batteries for electric-drive vehicles, Argonne National Lab. (ANL), Argonne, IL (United States), 2019.

10. A. Manthiram, A reflection on lithium-ion battery cathode chemistry, *Nature Communications,* **11** (1), 1550 (2020).

11. A. Masias, J. Marcicki, and W. Paxton, Opportunities and Challenges of Lithium Ion Batteries in Automotive Applications, *ACS Energy Letters,* **6** (2), 621 (2021).

12. Y. Ding, Z. P. Cano, A. Yu, J. Lu, and Z. Chen, Automotive Li-Ion Batteries: Current Status and Future Perspectives, *Electrochemical Energy Reviews,* **2** (1), 1 (2019).

13. S.-T. Myung, F. Maglia, K.-J. Park, C. S. Yoon, P. Lamp, S.-J. Kim, and Y.-K. Sun, Nickel-Rich Layered Cathode Materials for Automotive Lithium-Ion Batteries: Achievements and Perspectives, *ACS Energy Letters,* **2** (1), 196 (2017).

14. J.-H. Kim, H.-H. Ryu, S. J. Kim, C. S. Yoon, and Y.-K. Sun, Degradation Mechanism of Highly Ni-Rich Li[$Ni_xCo_yMn_{1-x-y}$]O_2 Cathodes with x > 0.9, *ACS Applied Materials & Interfaces,* **11** (34), 30936 (2019).

15. H.-J. Noh, S. Youn, C. S. Yoon, and Y.-K. Sun, Comparison of the structural and electrochemical properties of layered Li[$Ni_xCo_yMn_z$]O_2 (x = 1/3, 0.5, 0.6, 0.7, 0.8 and 0.85) cathode material for lithium-ion batteries, *Journal of Power Sources,* **233**, 121 (2013).

16. The Role of Critical Minerals in Clean Energy Transitions, *accessed 15.08.2022*, https://www.iea.org/reports/the-role-of-critical-minerals-in-clean-energy-transitions.

17. Panasonic to build EV battery plant for Tesla in Kansas, The Japan Times, *accessed 17.08.2022*, https://www.japantimes.co.jp/news/2022/07/14/business/corporate-business/panasonic-tesla-battery-plant/.

18. Mineral Commodity Summaries 2021, *accessed 17.08.2022*, http://pubs.er.usgs.gov/publication/mcs2021.

19. C. Banza Lubaba Nkulu, L. Casas, V. Haufroid, T. De Putter, N. D. Saenen, T. Kayembe-Kitenge, P. Musa Obadia, D. Kyanika Wa Mukoma, J.-M. Lunda Ilunga, and T. S. Nawrot, Sustainability of artisanal mining of cobalt in DR Congo, *Nature sustainability,* **1** (9), 495 (2018).

20. J. D. Donaldson, Cobalt and Cobalt Compounds, in *Ullmann's Encyclopedia of Industrial Chemistry*, Wiley-VCH, (2000).

21. D. G. E. Kerfoot, Nickel, in *Ullmann's Encyclopedia of Industrial Chemistry*, Wiley-VCH, (2000).

22. M. Azevedo, N. Campagnol, T. Hagenbruch, K. Hoffman, A. Lala, and O. Ramsbottom, A Tale of Two Commodities*, McKinsey & Company,* (2018).

23. N. Campagnol, K. Hoffman, A. Lala, and O. Ramsbottom, The future of nickel: A class act, *Basic Materials, McKinsey & Company,* (2017).

24. Political stability - Country rankings 2021, *accessed 17.08.2022*, https://www.theglobaleconomy.com/rankings/wb_political_stability/.

25. Tesla to invest $1bn on Australian-mined battery raw materials, *accessed 17.08.2022*, https://www.mining-technology.com/news/tesla-invest-australian-battery-materials/.

26. D. B. Wellbeloved, P. M. Craven, and J. W. Waudby, Manganese and Manganese Alloys, in *Ullmann's Encyclopedia of Industrial Chemistry*, Wiley-VCH, (2000).

27. A. H. Reidies, Manganese Compounds, in *Ullmann's Encyclopedia of Industrial Chemistry*, Wiley-VCH, (2000).

28. A. Mayyas, D. Steward, and M. Mann, The case for recycling: Overview and challenges in the material supply chain for automotive Li-ion batteries, *Sustainable materials and technologies,* **19**, e00087 (2019).

29. T. Punt, S. M. Bradshaw, P. van Wyk, and G. Akdogan, The Efficiency of Black Mass Preparation by Discharge and Alkaline Leaching for LIB Recycling, *Minerals,* **12** (6), 753 (2022).

References

30. Z. J. Baum, R. E. Bird, X. Yu, and J. Ma, Lithium-Ion Battery Recycling—Overview of Techniques and Trends, *ACS Energy Letters,* **7** (2), 712 (2022).

31. X. Wang, G. Gaustad, C. W. Babbitt, and K. Richa, Economies of scale for future lithium-ion battery recycling infrastructure, *Resources, Conservation and Recycling,* **83**, 53 (2014).

32. BASF to build new battery recycling prototype plant in Schwarzheide, Germany, *accessed 17.08.2022,* https://www.basf.com/global/en/media/news-releases/2021/06/p-21-216.html.

33. T. Schmidt, M. Buchert, and L. Schebek, Investigation of the primary production routes of nickel and cobalt products used for Li-ion batteries, *Resources, Conservation and Recycling,* **112**, 107 (2016).

34. J. Kyle, Nickel laterite processing technologies–where to next?, *in* "ALTA 2010 Nickel/Cobalt/Copper Conference". ALTA Metallurgical Services, Perth, 2010.

35. S. Stanković, S. Stopić, M. Sokić, B. Marković, and B. Friedrich, Review of the past, present, and future of the hydrometallurgical production of nickel and cobalt from lateritic ores, *Metallurgical and Materials Engineering,* **26** (2), 199 (2020).

36. K. Lascelles, L. G. Morgan, D. Nicholls, D. Beyersmann, and N. Institute, Nickel Compounds, in *Ullmann's Encyclopedia of Industrial Chemistry*, Wiley-VCH, (2000).

37. T. W. Ellis and A. H. Mirza, Battery recycling: defining the market and identifying the technology required to keep high value materials in the economy and out of the waste dump, National Institute of Standards and Technology, 1188 (2014).

38. Y. Zhao, X. Yuan, L. Jiang, J. Wen, H. Wang, R. Guan, J. Zhang, and G. Zeng, Regeneration and reutilization of cathode materials from spent lithium-ion batteries, *Chemical Engineering Journal,* **383**, 123089 (2020).

39. T. H. Cho, S. M. Park, M. Yoshio, T. Hirai, and Y. Hideshima, Effect of synthesis condition on the structural and electrochemical properties of Li[Ni$_{1/3}$Mn$_{1/3}$Co$_{1/3}$]O$_2$ prepared by carbonate co-precipitation method, *Journal of Power Sources,* **142** (1-2), 306 (2005).

40. N. Ngoepe, A. Gutierrez, P. Barai, J. Chen, P. E. Ngoepe, and J. R. Croy, The effects of process parameters on the properties of manganese-rich carbonate precursors: A study of co-precipitation synthesis using semi-batch reactors, *Chemical Engineering Science,* **241**, 116694 (2021).

41. D. Wang, I. Belharouak, G. M. Koenig, G. Zhou, and K. Amine, Growth mechanism of Ni$_{0.3}$Mn$_{0.7}$CO$_3$ precursor for high capacity Li-ion battery cathodes, *Journal of Materials Chemistry,* **21** (25), 9290 (2011).

42. J. Paulsen, H. Hong, and O. JinDoo, Impurity containing cathode material with preferred morphology and method to prepare from impurity containing metal carbonate, US20190386303A1 (2019).

43. M. H. Lee, Y. J. Kang, S. T. Myung, and Y. K. Sun, Synthetic optimization of Li[Ni$_{1/3}$Co$_{1/3}$Mn$_{1/3}$]O$_2$ via co-precipitation, *Electrochimica Acta,* **50** (4), 939 (2004).

44. Y. Shen, Y. Wu, H. Xue, S. Wang, D. Yin, L. Wang, and Y. Cheng, Insight into the Coprecipitation-Controlled Crystallization Reaction for Preparing Lithium-Layered Oxide Cathodes, *ACS Appl Mater Interfaces,* **13** (1), 717 (2021).

45. M. N. Obrovac, L. Zheng, and M. D. L. Garayt, Engineered Particle Synthesis by Dry Particle Microgranulation, *Cell Reports Physical Science,* **1** (6), 100063 (2020).

46. L. Zheng, J. C. Bennett, and M. N. Obrovac, All-Dry Synthesis of Single Crystal NMC Cathode Materials for Li-Ion Batteries, *Journal of The Electrochemical Society,* **167** (13), 130536 (2020).

47. H. Tokoro, T. Nakabayashi, S. Takano, A. Gunji, T. Tooyama, and S. Takahashi, Method for producing positive electrode active material for lithium ion secondary batteries, positive electrode active material for lithium ion secondary batteries, and lithium ion secondary battery, WO2017221554A1 (2017).

48. H. Tokoro, A. Gunji, T. Tooyama, S. Takahashi, S. Takano, and T. Nakabayashi, Method for producing cathode active material used for lithium secondary battery, WO2017213002A1 (2017).

49. H. Tokoro, T. Nakabayashi, S. Takano, S. Takahashi, A. Gunji, and T. Toyama, Cathode active substance used for lithium ion secondary battery, cathode including same, and lithium ion secondary battery provided with cathode, WO2017208703A1 (2017).

50. S. Takano, A. Gunji, H. Tokoro, G. Nakajima, T. Toyama, and S. Takahashi, Cathode active material for lithium ion secondary battery, method for manufacturing cathode active material for lithium ion secondary battery, and lithium ion secondary battery, WO2019131779A1 (2019).

51. M. Zhang, J. Shen, J. Li, D. Zhang, Y. Yan, Y. Huang, and Z. Li, Effect of micron sized particle on the electrochemical properties of nickel-rich LiNi$_{0.8}$Co$_{0.1}$Mn$_{0.1}$O$_2$ cathode materials, *Ceramics International,* **46** (4), 4643 (2020).

52. E. Gratz, Q. Sa, D. Apelian, and Y. Wang, A closed loop process for recycling spent lithium ion batteries, *Journal of Power Sources,* **262**, 255 (2014).

53. P. Liu, X. Yang, L. Xiao, H. Chen, and H. Chen, Preparation of Ternary Precursor Derived from Spent LiNi$_x$Co$_y$Mn$_{1-x-y}$O$_2$ Materials, *The Journal of The Minerals, Metals & Materials Society,* **71** (12), 4492 (2019).

54. A. van Bommel and J. R. Dahn, Analysis of the Growth Mechanism of Coprecipitated Spherical and Dense Nickel, Manganese, and Cobalt-Containing Hydroxides in the Presence of Aqueous Ammonia, *Chemistry of Materials,* **21** (8), 1500 (2009).

55. J. Monhemius, Precipitation diagrams for metal hydroxides, sulphides, arsenates and phosphates, *Transactions Institution of Mining & Metallurgy,* **86**, C202 (1977).

56. F. Zhou, X. Zhao, A. van Bommel, A. W. Rowe, and J. R. Dahn, Coprecipitation Synthesis of $Ni_xMn_{1-x}(OH)_2$ Mixed Hydroxides, *Chemistry of Materials,* **22** (3), 1015 (2009).

57. X. Zhao, F. Zhou, and J. R. Dahn, Phases Formed in Al-Doped $Ni_{1/3}Mn_{1/3}Co_{1/3}(OH)_2$ Prepared by Coprecipitation: Formation of Layered Double Hydroxide, *Journal of The Electrochemical Society,* **155** (9), A642 (2008).

58. K. Martinelle and L. Häggström, On the dissociation constant of ammonium: effects of using an incorrect pK_a in calculations of the ammonia concentration in animal cell cultures, *Biotechnology Techniques,* **11** (8), 549 (1997).

59. J. Hoigne and H. Bader, Ozonation of water: kinetics of oxidation of ammonia by ozone and hydroxyl radicals, *Environmental Science & Technology,* **12** (1), 79-84 (1978).

60. H. Dong, A. Wang, and G. M. Koenig Jr, Role of coprecipitation and calcination of precursors on phase homogeneity and electrochemical properties of battery active materials, *Powder Technology,* **335**, 137 (2018).

61. P. Kurzhals, F. Riewald, M. Bianchini, S. Ahmed, A. M. Kern, F. Walther, H. Sommer, K. Volz, and J. Janek, Deeper Understanding of the Lithiation Reaction during the Synthesis of $LiNiO_2$ Towards an Increased Production Throughput, *Journal of The Electrochemical Society,* **169** (5), 050526 (2022).

62. P. Kurzhals, F. Riewald, M. Bianchini, H. Sommer, H. Gasteiger, and J. Janek, The $LiNiO_2$ Cathode Active Material: A Comprehensive Study of Calcination Conditions and their Correlation with Physicochemical Properties. Part I. Structural Chemistry, *Journal of The Electrochemical Society,* **168** (11), 110518 (2021).

63. S. Ahmed, P. A. Nelson, K. G. Gallagher, N. Susarla, and D. W. Dees, Cost and energy demand of producing nickel manganese cobalt cathode material for lithium ion batteries *Journal of Power Sources,* **342**, 733 (2017).

64. H. Beyer, S. Meini, N. Tsiouvaras, M. Piana, and H. A. Gasteiger, Thermal and electrochemical decomposition of lithium peroxide in non-catalyzed carbon cathodes for Li–air batteries, *Physical Chemistry Chemical Physics,* **15** (26), 11025-11037 (2013).

65. S. Hy, H. Liu, M. Zhang, D. Qian, B.-J. Hwang, and Y. S. Meng, Performance and design considerations for lithium excess layered oxide positive electrode materials for lithium ion batteries, *Energy & Environmental Science,* **9** (6), 1931 (2016).

66. D. Schreiner, T. Zünd, F. J. Günter, L. Kraft, B. Stumper, F. Linsenmann, M. Schüßler, R. Wilhelm, A. Jossen, G. Reinhart, and H. A. Gasteiger, Comparative Evaluation of LMR-NCM and NCA Cathode Active Materials in Multilayer Lithium-Ion Pouch Cells: Part I. Production, Electrode Characterization, and Formation, *Journal of The Electrochemical Society,* **168** (3), 030507 (2021).

67. B. Strehle, J. Yoon, F. Friedrich, and H. Gasteiger, Specific Surface Area and Bulk Strain: Important Material Metrics Determining the Electrochemical Performance of Li-and Mn-Rich Layered Oxides, *Journal of The Electrochemical Society,* **169** (6), 060521 (2022).

68. X. Ma, M. Chen, Z. Zheng, D. Bullen, J. Wang, C. Harrison, E. Gratz, Y. Lin, Z. Yang, Y. Zhang, F. Wang, D. Robertson, S.-B. Son, I. Bloom, J. Wen, M. Ge, X. Xiao, W.-K. Lee, M. Tang, Q. Wang, J. Fu, Y. Zhang, B. C. Sousa, R. Arsenault, P. Karlson, N. Simon, and Y. Wang, Recycled cathode materials enabled superior performance for lithium-ion batteries, *Joule,* **5** (11), 2955 (2021).

69. M. Hietaniemi, T. Hu, J. Välikangas, J. Niittykoski, and U. Lassi, Effect of precursor particle size and morphology on lithiation of $Ni_{0.6}Mn_{0.2}Co_{0.2}(OH)_2$, *Journal of Applied Electrochemistry,* **51** (11), 1545 (2021).

70. Y.-K. Sun, D.-H. Kim, H.-G. Jung, S.-T. Myung, and K. Amine, High-voltage performance of concentration-gradient $Li[Ni_{0.67}Co_{0.15}Mn_{0.18}]O_2$ cathode material for lithium-ion batteries, *Electrochimica Acta,* **55** (28), 8621 (2010).

71. Y.-K. Sun, D.-H. Kim, C. S. Yoon, S.-T. Myung, J. Prakash, and K. Amine, A Novel Cathode Material with a Concentration-Gradient for High-Energy and Safe Lithium-Ion Batteries, *Advanced Functional Materials,* **20** (3), 485 (2010).

72. Y.-K. Sun, B.-R. Lee, H.-J. Noh, H. Wu, S.-T. Myung, and K. Amine, A novel concentration-gradient $Li[Ni_{0.83}Co_{0.07}Mn_{0.10}]O_2$ cathode material for high-energy lithium-ion batteries, *Journal of Materials Chemistry,* **21** (27), 10108 (2011).

73. Z. Xu, L. Xiao, F. Wang, K. Wu, L. Zhao, M.-R. Li, H.-L. Zhang, Q. Wu, and J. Wang, Effects of precursor, synthesis time and synthesis temperature on the physical and electrochemical properties of $Li(Ni_{1-x-y}Co_xMn_y)O_2$ cathode materials, *Journal of Power Sources,* **248**, 180 (2014).

74. Y. K. Sun, S. T. Myung, B. C. Park, J. Prakash, I. Belharouak, and K. Amine, High-energy cathode material for long-life and safe lithium batteries, *Nature Materials,* **8** (4), 320 (2009).

75. C.-K. Yang, L.-Y. Qi, Z. Zuo, R.-N. Wang, M. Ye, J. Lu, and H.-H. Zhou, Insights into the inner structure of high-nickel agglomerate as high-performance lithium-ion cathodes, *Journal of Power Sources,* **331**, 487 (2016).

76. M. Obrovac, O. Mao, and J. Dahn, Structure and electrochemistry of $LiMO_2$ (M= Ti, Mn, Fe, Co, Ni) prepared by mechanochemical synthesis, *Solid State Ionics,* **112** (1-2), 9 (1998).

77. T. Ohzuku and M. Yoshinari, Layered Lithium Insertion Material of $LiCo_{1/3}Ni_{1/3}Mn_{1/3}O_2$ for Lithium-Ion Batteries, *Chemistry Letters,* **30** (7), 642 (2001).

78. T. Ohzuku and M. Yoshinari, Layered Lithium Insertion Material of $LiNi_{1/2}Mn_{1/2}O_2$: A Possible Alternative to $LiCoO_2$ for Advanced Lithium-Ion Batteries, *Chemistry Letters,* **30** (8), 744 (2001).

79. A. Ueda and T. Ohzuku, Solid-State Redox Reactions of $LiNi_{1/2}Co_{1/2}O_2$ ($R\bar{3}m$) for 4 Volt Secondary Lithium Cells, *Journal of The Electrochemical Society,* **141** (8), 2010 (1994).

80. T. Maki and I. Sekiguchi, Study for Evaluation and Optimization of Iron Ore Granulation with Consideration of Dynamics and Particle Conditions, *ISIJ International,* **49** (5), 631 (2009).

81. P. G. Smith and A. W. Nienow, Stirring and stirred-tank reactors, *Chemical Engineering Science,* **38** (8), 1223 (1983).

82. F. Riewald, P. Kurzhals, M. Bianchini, H. Sommer, J. Janek, and H. A. Gasteiger, The $LiNiO_2$ Cathode Active Material: A Comprehensive Study of Calcination Conditions and their Correlation with Physicochemical Properties Part II. Morphology, *Journal of The Electrochemical Society,* **169** (2), 020529 (2022).

83. L. Zou, W. Zhao, H. Jia, J. Zheng, L. Li, D. P. Abraham, G. Chen, J. R. Croy, J.-G. Zhang, and C. Wang, The role of secondary particle structures in surface phase transitions of Ni-rich cathodes, *Chemistry of Materials,* **32** (7), 2884 (2020).

84. J. W. Mullin, Crystallizer design and operation in *Crystallization (Fourth Edition)*, p. 403, Butterworth-Heinemann, Oxford, (2001).

85. T. Itoh and Y. Wanibe, Effect of Particle Characteristics on Fluidity of Metallic Powders, *Journal of the Japan Society of Powder and Powder Metallurgy,* **41** (9), 1111 (1994).

86. T. Oshima, Y.-L. Zhang, M. Hirota, M. Suzuki, and T. Nakagawa, The effect of the types of mill on the flowability of ground powders, *Advanced Powder Technology,* **6** (1), 35 (1995).

87. T. Horio, M. Yasuda, and S. Matsusaka, Effect of particle shape on powder flowability of microcrystalline cellulose as determined using the vibration shear tube method, *International Journal of Pharmaceutics,* **473** (1-2), 572 (2014).

88. G. Gai, Y. Yang, L. Jin, X. Zou, and Y. Wu, Effect of particle shape on powder flowability of microcrystalline cellulose as determined using the vibration shear tube method, *Powder Technology,* **183** (1), 115 (2008).

89. A. Nouri and A. Sola, Metal particle shape: A practical perspective, *Metal powder report,* **73** (5), 276 (2018).

90. T. Thien Nguyen, U.-H. Kim, C. S. Yoon, and Y.-K. Sun, Enhanced cycling stability of Sn-doped $Li[Ni_{0.90}Co_{0.05}Mn_{0.05}]O_2$ via optimization of particle shape and orientation, *Chemical Engineering Journal,* **405**, 126887 (2021).

91. G.-T. Park, N.-Y. Park, T.-C. Noh, B. Namkoong, H.-H. Ryu, J.-Y. Shin, T. Beierling, C. S. Yoon, and Y.-K. Sun, High-performance Ni-rich $Li[Ni_{0.9-x}Co_{0.1}Al_x]O_2$ cathodes via multi-stage microstructural tailoring from hydroxide precursor to the lithiated oxide, *Energy & Environmental Science,* **14** (9), 5084 (2021).

92. B. Namkoong, N. Y. Park, G. T. Park, J. Y. Shin, T. Beierling, C. S. Yoon, and Y. K. Sun, High-Energy Ni-Rich Cathode Materials for Long-Range and Long-Life Electric Vehicles, *Advanced Energy Materials,* **12** (21), 2200615 (2022).

93. J. Li, A. R. Cameron, H. Li, S. Glazier, D. Xiong, M. Chatzidakis, J. Allen, G. A. Botton, and J. R. Dahn, Comparison of Single Crystal and Polycrystalline $LiNi_{0.5}Mn_{0.3}Co_{0.2}O_2$ Positive Electrode Materials for High Voltage Li-Ion Cells, *Journal of The Electrochemical Society,* **164** (7), A1534 (2017).

94. A. Liu, N. Zhang, J. E. Stark, P. Arab, H. Li, and J. R. Dahn, Synthesis of Co-Free Ni-Rich Single Crystal Positive Electrode Materials for Lithium Ion Batteries:

Part I. Two-Step Lithiation Method for Al- or Mg-Doped LiNiO₂, *Journal of The Electrochemical Society,* **168** (4), 040531 (2021).

95. S. Oswald, M. Bock, and H. A. Gasteiger, Elucidating the Implications of Morphology on Fundamental Characteristics of Nickel-Rich NCMs: Cracking, Gassing, Rate Capability, and Thermal Stability of Poly- and Single-Crystalline NCM622, *Journal of The Electrochemical Society,* **169** (5), 050501 (2022).

96. J. E. Harlow, X. Ma, J. Li, E. Logan, Y. Liu, N. Zhang, L. Ma, S. L. Glazier, M. M. Cormier, and M. Genovese, A wide range of testing results on an excellent lithium-ion cell chemistry to be used as benchmarks for new battery technologies, *Journal of The Electrochemical Society,* **166** (13), A3031 (2019).

97. H.-H. Ryu, B. Namkoong, J.-H. Kim, I. Belharouak, C. S. Yoon, and Y.-K. Sun, Capacity Fading Mechanisms in Ni-Rich Single-Crystal NCM Cathodes, *ACS Energy Letters,* **6** (8), 2726 (2021).

98. L. Zheng, C. Wei, M. Garayt, J. MacInnis, and M. Obrovac, Spherically smooth cathode particles by mechanofusion processing, *Journal of The Electrochemical Society,* **166** (13), A2924 (2019).

99. Q. Sa, E. Gratz, J. A. Heelan, S. Ma, D. Apelian, and Y. Wang, Synthesis of Diverse LiNixMnyCozO2 Cathode Materials from Lithium Ion Battery Recovery Stream, *Journal of Sustainable Metallurgy,* **2** (3), 248 (2016).

100. Y. Yang, G. Huang, M. Xie, S. Xu, and Y. He, Synthesis and performance of spherical LiNi$_x$Co$_y$Mn$_{1-x-y}$O$_2$ regenerated from nickel and cobalt scraps, *Hydrometallurgy,* **165** 358 (2016).

101. Z. Zheng, M. Chen, Q. Wang, Y. Zhang, X. Ma, C. Shen, D. Xu, J. Liu, Y. Liu, P. Gionet, I. O'Connor, L. Pinnell, J. Wang, E. Gratz, R. Arsenault, and Y. Wang, High Performance Cathode Recovery from Different Electric Vehicle Recycling Streams, *ACS Sustainable Chemistry & Engineering,* **6** (11), 13977 (2018).

102. H. Zou, E. Gratz, D. Apelian, and Y. Wang, A novel method to recycle mixed cathode materials for lithium ion batteries, *Green Chemistry,* **15** (5), 1183 (2013).

103. J. Ren, R. Li, Y. Liu, Y. Cheng, D. Mu, R. Zheng, J. Liu, and C. Dai, The impact of aluminum impurity on the regenerated lithium nickel cobalt manganese oxide cathode materials from spent LIBs, *New Journal of Chemistry,* **41** (19), 10959 (2017).

104. Q. Sa, J. A. Heelan, Y. Lu, D. Apelian, and Y. Wang, Copper Impurity Effects on LiNi$_{1/3}$Mn$_{1/3}$Co$_{1/3}$O$_2$ Cathode Material, *ACS Applied Materials & Interfaces,* **7** (37), 20585 (2015).

105. M. Jo, H. Ku, S. Park, J. Song, and K. Kwon, Effects of Residual Lithium in the precursors of Li[Ni$_{1/3}$Co$_{1/3}$Mn$_{1/3}$]O₂ on their lithium-ion battery performance, *Journal of Physics and Chemistry of Solids,* **118**, 47 (2018).

106. Y. Weng, S. Xu, G. Huang, and C. Jiang, Synthesis and performance of Li[(Ni$_{1/3}$Co$_{1/3}$Mn$_{1/3}$)$_{1-x}$Mg$_x$]O₂ prepared from spent lithium ion batteries, *Journal of Hazardous Materials,* **246-247**, 163 (2013).

107. Wolfson Electrostatic Unit, Guidelines on the electrostatic hazards during pneumatic conveying and storage of flammable powders, *Journal of Loss Prevention in the Process Industries,* **4** (4), 211-216 (1991).

108. G. Joseph, Combustible dusts: A serious industrial hazard, *Journal of Hazardous Materials,* **142** (3), 589-591 (2007).

109. D. Ham, Cathode active material precursor, cathode active material formed therefrom, method of preparing the cathode active material, and cathode and lithium battery each including the cathode active material, US20190074513A1 (2019).

110. Y. Kawakami, Production method of lithium nickel composite oxide, JP2018193296A (2018).

111. S. Taniguchi, Roller hearth kiln, JP2009103331A (2007).

112. Y. F. Jun Yokoyama, Tetsufumi Komukai, Positive electrode active material for nonaqueous electrolyte secondary batteries, production method thereof, and nonaqueous electrolyte secondary battery, WO2017073682 (2017).

113. A. van Bommel and J. R. Dahn, Synthesis of Spherical and Dense Particles of the Pure Hydroxide Phase $Ni_{1/3}Mn_{1/3}Co_{1/3}(OH)_2$, *Journal of The Electrochemical Society,* **156** (5), 362 (2009).

114. M. Noh and J. Cho, Optimized Synthetic Conditions of $LiNi_{0.5}Co_{0.2}Mn_{0.3}O_2$ Cathode Materials for High Rate Lithium Batteries via Co-Precipitation Method, *Journal of The Electrochemical Society,* **160** (1), 105 (2012).

115. J.-M. Kim, S.-M. Chang, J. H. Chang, and W.-S. Kim, Agglomeration of nickel/cobalt/manganese hydroxide crystals in Couette–Taylor crystallizer, *Colloids and Surfaces A: Physicochemical and Engineering Aspects,* **384** (1-3), 31 (2011).

116. V. Y. Kazimirov, M. B. Smirnov, L. Bourgeois, L. Guerlou-Demourgues, L. Servant, A. M. Balagurov, I. Natkaniec, N. R. Khasanova, and E. V. Antipov, Atomic structure and lattice dynamics of Ni and Mg hydroxides, *Solid State Ionics,* **181** (39-40), 1764 (2010).

117. D. S. Hall, D. J. Lockwood, C. Bock, and B. R. MacDougall, Nickel hydroxides and related materials: a review of their structures, synthesis and properties, *Proceedings of the Royal Society A: Mathematical, Physical and Engineering Sciences,* **471** (2174), 20140792 (2015).

118. S. Bette, B. Hinrichsen, D. Pfister, and R. E. Dinnebier, A routine for the determination of the microstructure of stacking-faulted nickel cobalt aluminium hydroxide precursors for lithium nickel cobalt aluminium oxide battery materials, *Journal of Applied Crystallography,* **53** (Pt 1), 76 (2020).

119. Z. Feng, P. Barai, J. Gim, K. Yuan, Y. A. Wu, Y. Xie, Y. Liu, and V. Srinivasan, In Situ Monitoring of the Growth of Nickel, Manganese, and Cobalt Hydroxide Precursors during Co-Precipitation Synthesis of Li-Ion Cathode Materials, *Journal of The Electrochemical Society,* **165** (13), A3077 (2018).

120. L. Liang, K. Du, Z. Peng, Y. Cao, J. Duan, J. Jiang, and G. Hu, Synthesis and characterization of concentration–gradient $LiNi_{0.6}Co_{0.2}Mn_{0.2}O_2$ cathode material for lithium ion batteries, *Electrochimica Acta,* **130**, 82 (2014).

121. D.-L. Vu and J.-w. Lee, Properties of $LiNi_{0.8}Co_{0.1}Mn_{0.1}O_2$ as a high energy cathode material for lithium-ion batteries, *Korean Journal of Chemical Engineering,* **33** (2), 514 (2015).

122. Y. Yang, S. Xu, M. Xie, Y. He, G. Huang, and Y. Yang, Growth mechanisms for spherical mixed hydroxide agglomerates prepared by co-precipitation method: A case of $Ni_{1/3}Co_{1/3}Mn_{1/3}(OH)_2$, *Journal of Alloys and Compounds,* **619**, 846 (2015).

123. D. Ren, Y. Shen, Y. Yang, L. Shen, B. D. A. Levin, Y. Yu, D. A. Muller, and H. D. Abruna, Systematic Optimization of Battery Materials: Key Parameter Optimization for the Scalable Synthesis of Uniform, High-Energy, and High Stability $LiNi_{0.6}Mn_{0.2}Co_{0.2}O_2$ Cathode Material for Lithium-Ion Batteries, *ACS Applied Material Interfaces,* **9** (41), 35811 (2017).

124. J. Välikangas, P. Laine, M. Hietaniemi, T. Hu, P. Tynjälä, and U. Lassi, Precipitation and Calcination of High-Capacity $LiNiO_2$ Cathode Material for Lithium-Ion Batteries, *Applied Sciences,* **10** (24), 8988 (2020).

125. D. Wang, I. Belharouak, L. H. Ortega, X. Zhang, R. Xu, D. Zhou, G. Zhou, and K. Amine, Synthesis of high capacity cathodes for lithium-ion batteries by morphology-tailored hydroxide co-precipitation, *Journal of Power Sources,* **274**, 451 (2015).

126. X. Sun, J. Kim, and W.-S. Kim, Spherical agglomeration of nickel-manganese-cobalt hydroxide in turbulent Batchelor vortex flow, *Chemical Engineering Journal,* **421**, 129924 (2021).

127. Y. Koshika, H. Kaneda, S. Yoshio, and Y. Furuichi, Precursor Morphology Control and Electrochemical Properties of $LiNi_{0.35}Mn_{0.30}Co_{0.35}O_2$ as a Li-Ion Battery Positive Electrode Material, *ACS Applied Energy Materials,* **5** (7), 8169 (2022).

128. K.-M. Nam, H.-J. Kim, D.-H. Kang, Y.-S. Kim, and S.-W. Song, Ammonia-free coprecipitation synthesis of a Ni–Co–Mn hydroxide precursor for high-performance battery cathode materials, *Green Chemistry,* **17** (2), 1127 (2015).

129. H. Zhou, F. Zhou, Y. Liu, J. Kong, C. Jin, and X. Wu, Enhanced electrochemical performances of $LiNi_{0.8}Co_{0.1}Mn_{0.1}O_2$ synthesized using the new green and low cost preparation process, *Journal of Alloys and Compounds,* **816**, 152563 (2020).

130. B. Bergner, T. Teufl, R. Berk, Process for making precursors for cathode active materials, precursors, and cathode active materials, WO2021083686A1 (2021).

131. B. Bergner, R. Berk, L. Garve, Process for making a particulate (oxy)hydroxide, and particulate (oxy)hydroxide and its use, WO2022078702A1 (2022).

132. N. Zhang, N. Zaker, H. Li, A. Liu, J. Inglis, L. Jing, J. Li, Y. Li, G. A. Botton, and J. R. Dahn, Cobalt-Free Nickel-Rich Positive Electrode Materials with a Core–Shell Structure, *Chemistry of Materials,* **31** (24), 10150 (2019).

133. A. M. Olbrich, Beta-nickel hydroxide doped with aluminum. WO 2018/234112 A1 (2018).

134. B. Bergner, R. Berk, L. Garve, Process for making a particulate (oxy)hydroxide, WO2022157014A1 (2022).

135. A. L. Lipson, J. L. Durham, M. LeResche, I. Abu-Baker, M. J. Murphy, T. T. Fister, L. Wang, F. Zhou, L. Liu, K. Kim, and D. Johnson, Improving the Thermal Stability of NMC 622 Li-Ion Battery Cathodes through Doping During Coprecipitation, *ACS Applied Materials & Interfaces,* **12** (16), 18512 (2020).

136. H. H. Ryu, K. J. Park, D. R. Yoon, A. Aishova, C. S. Yoon, and Y. K. Sun, Li [$Ni_{0.9}Co_{0.09}W_{0.01}$]$O_2$: a new type of layered oxide cathode with high cycling stability, *Advanced Energy Materials,* **9** (44), 1902698 (2019).

137. T. Takahashi, Metal composite hydroxide and its manufacturing method, positive electrode active material for lithium ion secondary battery and its manufacturing method, and lithium ion secondary battery using the same, JP2020050562A (2020).

138. 邱天, Hexavalent element-added nickel-cobalt-manganese composite hydroxide and preparation method thereof, CN110957482A (2019).

139. M. Bianchini, F. Fauth, P. Hartmann, T. Brezesinski, and J. Janek, An in situ structural study on the synthesis and decomposition of $LiNiO_2$, *Journal of Materials Chemistry A,* **8** (4), 1808 (2020).

140. L. Qiu, Y. Song, M. Zhang, Y. Liu, Z. Yang, Z. Wu, H. Zhang, W. Xiang, Y. Liu, G. Wang, Y. Sun, J. Zhang, B. Zhang, and X. Guo, Structural Reconstruction Driven by Oxygen Vacancies in Layered Ni-Rich Cathodes, *Advanced Energy Materials,* **12** (19), 2200022 (2022).

141. 潘五羊, Box bowl for containing materials in high-temperature kiln, CN210400005U (2019).

142. K. H. Song, Method for calcining electrode materials using a rotary kiln, US20140004473A1 (2014).

143. H. Li, J. Li, N. Zaker, N. Zhang, G. A. Botton, and J. R. Dahn, Synthesis of Single Crystal $LiNi_{0.88}Co_{0.09}Al_{0.03}O_2$ with a Two-Step Lithiation Method, *Journal of The Electrochemical Society,* **166** (10), A1956 (2019).

144. L. Li, G. Hu, Y. Cao, Z. Peng, J. Zeng, S. Zhang, and K. Du, Synthesis of micron-sized single-crystalline $LiNi_{0.65}Co_{0.07}Mn_{0.28}O_2$ cathode material for Li-ion batteries via various calcination additives with large ion radius, *Ionics,* **28** (8), 3687 (2022).

145. T. Weigel, F. Schipper, E. M. Erickson, F. A. Susai, B. Markovsky, and D. Aurbach, Structural and Electrochemical Aspects of $LiNi_{0.8}Co_{0.1}Mn_{0.1}O_2$ Cathode Materials Doped by Various Cations, *ACS Energy Letters,* **4** (2), 508 (2019).

146. H.-H. Ryu, N.-Y. Park, J. H. Seo, Y.-S. Yu, M. Sharma, R. Mücke, P. Kaghazchi, C. S. Yoon, and Y.-K. Sun, A highly stabilized Ni-rich NCA cathode for high-energy lithium-ion batteries, *Materials Today,* **36**, 73 (2020).

147. C. Roitzheim, L.-Y. Kuo, Y. J. Sohn, M. Finsterbusch, S. Möller, D. Sebold, H. Valencia, M. Meledina, J. Mayer, U. Breuer, P. Kaghazchi, O. Guillon, and D.

Fattakhova-Rohlfing, Boron in Ni-Rich NCM811 Cathode Material: Impact on Atomic and Microscale Properties, *ACS Applied Energy Materials,* **5** (1), 524 (2022).

148. N. Zhang, J. Stark, H. Li, A. Liu, Y. Li, I. Hamam, and J. R. Dahn, Effects of Fluorine Doping on Nickel-Rich Positive Electrode Materials for Lithium-Ion Batteries, *Journal of The Electrochemical Society,* **167** (8), 080518 (2020).

149. D. Weber, J. Lin, A. Pokle, K. Volz, J. Janek, T. Brezesinski, and M. Bianchini, Tracing Low Amounts of Mg in the Doped Cathode Active Material $LiNiO_2$, *Journal of The Electrochemical Society,* **169** (3), 030540 (2022).

150. T. R. Penki, S. Gilady, P. K. Nayak, H. Sclar, Y. Elias, J. Grinblat, M. Talianker, B. Markovsky, C. Erk, S. Luski, and D. Aurbach, The effect of synthesis and zirconium doping on the performance of nickel-rich NCM622 cathode materials for Li-ion batteries, *Journal of Solid State Electrochemistry,* **25** (5), 1513 (2021).

151. F. Schipper, M. Dixit, D. Kovacheva, M. Talianker, O. Haik, J. Grinblat, E. M. Erickson, C. Ghanty, D. T. Major, B. Markovsky, and D. Aurbach, Stabilizing nickel-rich layered cathode materials by a high-charge cation doping strategy: zirconium-doped $LiNi_{0.6}Co_{0.2}Mn_{0.2}O_2$, *Journal of Materials Chemistry A,* **4** (41), 16073 (2016).

152. D. Goonetilleke, A. Mazilkin, D. Weber, Y. Ma, F. Fauth, J. Janek, T. Brezesinski, and M. Bianchini, Single step synthesis of W-modified $LiNiO_2$ using an ammonium tungstate flux, *Journal of Materials Chemistry A,* **10** (14), 7841 (2022).

153. U.-H. Kim, G.-T. Park, B.-K. Son, G. W. Nam, J. Liu, L.-Y. Kuo, P. Kaghazchi, C. S. Yoon, and Y.-K. Sun, Heuristic solution for achieving long-term cycle stability for Ni-rich layered cathodes at full depth of discharge, *Nature Energy,* **5** (11), 860 (2020).

154. J. Li, R. Doig, J. Camardese, K. Plucknett, and J. R. Dahn, The Effect of Lithium Content and Core to Shell Ratio on Structure and Electrochemical Performance of Core-Shell $Li_{(1+x)}[Ni_{0.6}Mn_{0.4}]_{(1-x)}O_2Li_{(1+y)}[Ni_{0.2}Mn_{0.8}]_{(1-y)}O_2$ Positive Electrode Materials, *Chemistry of Materials,* **27** (22), 7765 (2015).

155. B. Han, T. Paulauskas, B. Key, C. Peebles, J. S. Park, R. F. Klie, J. T. Vaughey, and F. Dogan, Understanding the Role of Temperature and Cathode Composition on Interface and Bulk: Optimizing Aluminum Oxide Coatings for Li-Ion Cathodes, *ACS Applied Materials & Interfaces,* **9** (17), 14769 (2017).

156. S. Liu, Z. Dang, D. Liu, C. Zhang, T. Huang, and A. Yu, Comparative studies of zirconium doping and coating on $LiNi_{0.6}Co_{0.2}Mn_{0.2}O_2$ cathode material at elevated temperatures, *Journal of Power Sources,* **396**, 288 (2018).

157. D. Larcher, M. R. Palacín, G. G. Amatucci, and J. M. Tarascon, Electrochemically Active $LiCoO_2$ and $LiNiO_2$ Made by Cationic Exchange under Hydrothermal Conditions, *Journal of The Electrochemical Society,* **144** (2), 408 (1997).

158. Y. Kim, H. Park, J. H. Warner, and A. Manthiram, Unraveling the Intricacies of Residual Lithium in High-Ni Cathodes for Lithium-Ion Batteries, *ACS Energy Letters,* **6** (3), 941 (2021).

159. R. Jung, R. Morasch, P. Karayaylali, K. Phillips, F. Maglia, C. Stinner, Y. Shao-Horn, and H. A. Gasteiger, Effect of Ambient Storage on the Degradation of Ni-Rich Positive Electrode Materials (NMC811) for Li-Ion Batteries, *Journal of The Electrochemical Society,* **165** (2), A132 (2018).

160. D. Pritzl, T. Teufl, A. T. S. Freiberg, B. Strehle, J. Sicklinger, H. Sommer, P. Hartmann, and H. A. Gasteiger, Washing of Nickel-Rich Cathode Materials for Lithium-Ion Batteries: Towards a Mechanistic Understanding, *Journal of The Electrochemical Society,* **166** (16), A4056 (2019).

161. L. Hartmann, D. Pritzl, H. Beyer, and H. A. Gasteiger, Evidence for Li^+/H^+ Exchange during Ambient Storage of Ni-Rich Cathode Active Materials, *Journal of The Electrochemical Society,* **168** (7), 070507 (2021).

162. L. Hartmann, C. H. Ching, T. Kipfer, M. Koch, and H. A. Gasteiger, Surface-stabilization of LMR-NCM by Washing with Aqueous Buffers to Reduce Gassing and Improve Cycle-Life, *Journal of The Electrochemical Society,* **169** (7), 070516 (2022).

163. F. Klein, J. Bansmann, Z. Jusys, C. Pfeifer, P. Scheitenberger, M. Mundszinger, D. Geiger, J. Biskupek, U. Kaiser, and R. J. Behm, Enhanced Electrochemical Capacity of Spherical Co-Free $Li_{1.2}Mn_{0.6}Ni_{0.2}O_2$ Particles after a Water and Acid Treatment and its Influence on the Initial Gas Evolution Behavior, *ChemSusChem,* **15** (20), e202201061 (2022).

164. M. Yoon, Y. Dong, J. Hwang, J. Sung, H. Cha, K. Ahn, Y. Huang, S. J. Kang, J. Li, and J. Cho, Reactive boride infusion stabilizes Ni-rich cathodes for lithium-ion batteries, *Nature Energy,* **6** (4), 362 (2021).

165. K. Heo, J.-S. Lee, H.-S. Kim, J. Kim, and J. Lim, Ionic Conductor-$LiNi_{0.8}Co_{0.1}Mn_{0.1}O_2$ Composite Synthesized by Simultaneous Co-Precipitation for Use in Lithium Ion Batteries, *Journal of The Electrochemical Society,* **164** (12), A2398 (2017).

166. D. Becker, M. Börner, R. Nölle, M. Diehl, S. Klein, U. Rodehorst, R. Schmuch, M. Winter, and T. Placke, Surface Modification of Ni-Rich $LiNi_{0.8}Co_{0.1}Mn_{0.1}O_2$ Cathode Material by Tungsten Oxide Coating for Improved Electrochemical Performance in Lithium-Ion Batteries, *ACS Applied Materials & Interfaces,* **11** (20), 18404 (2019).

167. X. He, X. Xu, L. Wang, C. Du, X. Cheng, P. Zuo, Y. Ma, and G. Yin, Enhanced Electrochemical Performance of $LiNi_{0.8}Co_{0.15}Al_{0.05}O_2$ Cathode Material via Li_2TiO_3 Nanoparticles Coating, *Journal of The Electrochemical Society,* **166** (2), A143 (2019).

168. S. K. Mylavarapu, F. Ulu Okudur, S. Yari, D. De Sloovere, J. D'Haen, A. Shafique, M. K. Van Bael, M. Safari, and A. Hardy, Effect of TiO_x Surface Modification on the Electrochemical Performances of Ni-Rich (NMC-622) Cathode Material for Lithium-Ion Batteries, *ACS Applied Energy Materials,* **4** (10), 10493 (2021).

169. S. Cangaz, F. Hippauf, R. Takata, F. Schmidt, S. Dörfler, and S. Kaskel, Surface Functionalization of $LiNi_{0.7}Co_{0.15}Mn_{0.15}O_2$ with Fumed Li_2ZrO_3 via a Cost-Effective Dry-Coating Process for Enhanced Performance in Solid-State Batteries, *Batteries & Supercaps,* **5** (9), e202200100 (2022).

170. B. Chen, X. Ma, M. Chen, D. Bullen, J. Wang, R. Arsenault, and Y. Wang, Systematic Comparison of Al^{3+} Modified LiNi$_{0.6}$Mn$_{0.2}$Co$_{0.2}$O$_2$ Cathode Material from Recycling Process, *ACS Applied Energy Materials,* **2** (12), 8818 (2019).

171. S. Yin, H. Chen, J. Chen, A. Massoudi, W. Deng, X. G. Gao, S. Zhang, Y. Wang, T.-W. Lin, C. E. Banks, S.-z. Qiao, G. Zou, H. Hou, and X. Ji, Chemical-Mechanical Effects in Ni-Rich Cathode Materials, *Chemistry of Materials,* **34** (4), 1509 (2022).

172. K. Jaehrling and H. J. Schultz, Flow Fields in Stirred Vessels Depending on Different Internal Heat Exchangers and Vessel Bottoms, *Chemie Ingenieur Technik,* **91** (9), 1281 (2019).

173. V. Hackley, L.-S. Lum, V. Gintautas, and C. Ferraris, Particle Size Analysis by Laser Diffraction Spectrometry: Application to Cementitious Powders, Gaithersburg, USA: National Institute of Standards and Technology, (2004).

174. C. A. Schneider, W. S. Rasband, and K. W. Eliceiri, NIH Image to ImageJ: 25 years of image analysis, *Nature Methods,* **9** (7), 671 (2012).

175. K. Oláh, On the theory of the alkaline error of the glass electrode, *Periodica Polytechnica Chemical Engineering,* **4** (2), 141 (1960).

176. C. F. H. Liao, Devarda's Alloy Method for Total Nitrogen Determination, *Soil Science Society of America Journal,* **45** (5), 852 (1981).

177. X. Liu and L. Yu, Synthesis of nanosized nickel hydroxide by solid-state reaction at room temperature, *Materials letters,* **58** (7-8), 1327 (2004).

178. G. H. Ayres and F. Smith, Colorimetric Determination of Nickel, *Industrial & Engineering Chemistry Analytical Edition,* **11** (7), 365 (1939).

179. O. Ronneberger, P. Fischer, and T. Brox, U-Net: Convolutional Networks for Biomedical Image Segmentation, p. 234. Springer International Publishing, Cham, 2015.

180. R. Osserman, The isoperimetric inequality, *Bulletin of the American Mathematical Society,* **84** (6), 1182 (1978).

181. P. Klobes and R. G. Munro, Porosity and specific surface area measurements for solid materials, *Special Publication (NIST SP),* National Institute of Standards and Technology, 23 (2006).

182. S. Oswald, D. Pritzl, M. Wetjen, and H. A. Gasteiger, Monitoring the Electrochemical Capacitance By in Situ Impedance Spectroscopy As Indicator for Particle Cracking of (Nickel-Rich) Cathode Active Materials: Development of a Simplified Measurement Setup, *Journal of The Electrochemical Society,* **167** (10), 100511 (2020).

183. Q. Instruments, Gas Sorption System Operating Manual, Vol. P/N 05098-1.1 Rev D, p. 337. Quantachrome Instruments, Florida, USA, 2009.

184. L. M. Anovitz and D. R. Cole, Characterization and Analysis of Porosity and Pore Structures, *Reviews in Mineralogy and Geochemistry,* **80** (1), 61 (2015).

185. B. Strehle, Degradation Mechanisms of Layered Oxides Used as Cathode Active Materials in Lithium-Ion Batteries, PhD Thesis, chapter 2.3, Technical University of Munich (2022).

186. M. Casas-Cabanas, M. R. Palacín, and J. Rodríguez-Carvajal, Microstructural analysis of nickel hydroxide: Anisotropic size versus stacking faults, *Powder Diffraction,* **20** (4), 334 (2005).

187. I. Kolthoff, Theory of coprecipitation. The formation and properties of crystalline precipitates, *The Journal of Physical Chemistry,* **36** (3), 860 (2002).

188. S. S. Zhang, Problems and their origins of Ni-rich layered oxide cathode materials, *Energy Storage Materials,* **24**, 247 (2020).

189. J. Lee, S. Park, M. Beak, S. R. Park, A. R. Lee, S. H. Byun, J. Song, J. S. Sohn, and K. Kwon, The Effect of Excessive Sulfate in the Li-Ion Battery Leachate on the Properties of Resynthesized Li[$Ni_{1/3}Co_{1/3}Mn_{1/3}$]O_2, *Materials,* **14** (21), 6672 (2021).

Acknowledgement

First and foremost, I would like to express grateful acknowledgments to **Prof. Dr. Hubert A. Gasteiger** for giving me the opportunity to not only conduct my Masters' Thesis but also my PhD under his professorial chair and supervising my work in cooperation with BASF. During these times your scientific guidance proved as irreplaceable and your simplistic but effective approach for research is second to none. The amount of effort you incur to teach your students the way of analytical, and especially, critical thinking is remarkable. I genuinely appreciate every discussion we had, even though they were either quite early or quite late during the day. Thank you!

Special thanks go also to my former supervisor at BASF **Benjamin Bergner** for bringing me on board of the BASF battery ship and showing me the distinction between industrial and academic research as well as how to survive in a vast company like BASF. Further on I would like to thank **Thorsten Beierling** for semi-voluntarily taking up the liability of supervising me at BASF. Your kind, decent and reasonable attitude made it a pleasure to work every day with you. I am looking forward to maintaining our coprecipitation philosophy meetings.

I especially want to thank **Nhat Long Tran Pham** at TUM for always offering me a place to sleep when I had to travel to Munich on several occasions and being the manager of good vibes at TEC. Additionally, I would like to thank **Felix Riewald**, **Philipp Kurzhals**, **Stefan Oswald**, and **Tim Kipfer** for the good scientific exchange with a shoutout to Felix for being the initiator of my master thesis at BASF as well as to Tim for the excellent cooperation in the last year. My starting point at TEC was the research internship about lithium sulfur batteries, which was kindly supervised by **Qi He**.

Furthermore, I would like to gratefully acknowledge my colleagues at BASF, in particular **Lukas Metzger**, **Michael Kespe**, **Matthias Rauls**, **Daniela Pfister**, and **Murat Yavuz**. Additionally, I would like to express my gratitude to **Thomas Diehl**, **Linda Stark**, **Jochen Gauer**, and **Jürgen Jaeger** for the technical expertise and support in the laboratory.

My sincere gratitude goes to **Masatoshi Matsumoto** for inviting me to BASF Toda Battery Materials LLC in Yamaguchi, Japan. Not only I was able obtain invaluable experience about industrial cathode material manufacturing, but it was also a great pleasure to live and work in Japan once again for some time. Special thanks go to **Kengo Miyamoto**, **Junji**

Kashiwagi, **Daisuke Nishikawa**, **Daisuke Morita**, and **Takahiro Nakanishi** for making the stay an everlasting memory. ありがとうございました!

Extraordinary gratitude goes also to my mother for supporting me throughout my life at any times.

Finally, I would like to express eternal gratitude towards the most important person in my life, my wife, **Kurumi Berk**. Simply put: Without you, I would have not survived the downs of the PhD-life without going mental. Whenever coprecipitation experiments eventually failed after running for 9 h successfully, it was your support, and joy in life, that made the sun shine again. Thank you for all the cheerful moments in our shared life. The strength of our relationship is invaluable to me. いつもありがとうございました! In the end, I would also like to thank my daughter, **Yuna Berk**, for teaching me that it's really the simple things in life that matter.

Scientific contributions

Articles

1. **R. B. Berk**, T. Beierling, L. Metzger, and H. A. Gasteiger, "Investigation of Particle Formation Mechanism during Coprecipitation of Ni-rich Hydroxide Precursor for Li-Ion Cathode Active Material", *Journal Electrochemical Society*, **170**, 110513, (2023).

2. **R. B. Berk**, T. Beierling, L. Metzger, and H. A. Gasteiger, "Impact of Sulfate Adsorption on Particle Morphology during the Precipitation of Ni-rich Hydroxide Precursors for Li-Ion Cathode Active Material", *Journal Electrochemical Society*, **170**, 110530, (2023).

3. I. Kitamura, K. Kato, R. **B. Berk**, T. Nakai, M. Hara, S. Nagano, and T. Seki, "Photo-triggered large mass transport driven only by a photoresponsive surface skin layer", *Scientific Reports*, **10**, 12664, (2020).

Patents

1. T. Beierling, S. Frischhut, M. Rauls, L. Metzger, S. Weiguny, M. Lennartz and **R. B. Berk**, „Method for making precursors of cathode active materials for lithium ion batteries", WO2023285464A1 (2022).

2. T. Beierling, **R. B. Berk**, and L. K. Metzger, "Process for making a particulate (oxy)hydroxide or oxide", WO2022189307A1 (2022).

3. B. J. H. Bergner, **R. B. Berk**, and L. K. Garve "Process for making a particulate (oxy)hydroxide", WO2022157014A1 (2022).

4. B. J. H. Bergner, **R. B. Berk**, and L. K. Garve, "Process for making a particulate (oxy)hydroxide, and particulate (oxy)hydroxide and its use", WO2022078702A1 (2022).

5. B. J. H. Bergner, and **R. B. Berk**, "Process for making a particulate (oxy)hydroxide, and electrode active material made therefrom", WO2021228614A1 (2021).

6. B. J. H. Bergner, T. M. Teufl, and **R. B. Berk**, "Process for making precursors for cathode active materials, precursors, and cathode active materials", WO2021083686A1 (2021).

Oral presentations

1. **R. B. Berk**, L. Metzger, T. Beierling, and M. Rauls, "Vom Keim zum Kathodenmaterial – Fällung von Batteriematerial-Präkursoren", ProcessNet Fachgruppentreffen Kristallisation 2021, Karlsruhe (Germany), 2021.

2. **R. B. Berk**, T. Beierling, L. Metzger, and H. A. Gasteiger, "Impact of Sulfate Adsorption on Secondary Particle Morphology of Ni-rich NCM Cathode Material Precursor", Abstract #A06-0596, 242nd Meeting of the Electrochemical Society, Atlanta, Georgia (USA), 2022.

3. **R. B. Berk,** T. Beierling, L. Metzger, and H. A. Gasteiger, "Investigating the Particle Formation Mechanism during Coprecipitation of Ni-Rich Hydroxide Precursors for Cathode Active Materials for Lithium-Ion Batteries", Abstract #02-0485, 243rd Meeting of the Electrochemical Society, Boston, Massachusetts (USA), 2023.